University of Sussex

Measurement of Muon Neutrino Disappearance with the NOvA Experiment

Luke Vinton

Submitted for the degree of Doctor of Philosophy

University of Sussex

14th February 2018

Declaration

I hereby declare that this thesis has not been and will not be submitted in whole or in part to another University for the award of any other degree.

Signature:

Luke Vinton

UNIVERSITY OF SUSSEX

Luke Vinton, Doctor of Philosophy

Measurement of muon neutrino disappearance with the NOvA experiment

Abstract

The NOvA experiment consists of two functionally identical tracking calorimeter detectors which measure the neutrino energy and flavour composition of the NuMI beam at baselines of 1 km and 810 km. Measurements of neutrino oscillation parameters are extracted by comparing the neutrino energy spectrum in the far detector with predictions of the oscillated neutrino energy spectra that are made using information extracted from the near detector. Observation of muon neutrino disappearance allows NOvA to make measurements of the mass squared splitting Δm^2_{32} and the mixing angle θ_{23}. The measurement of θ_{23} will provide insight into the make-up of the third mass eigenstate and probe the muon-tau symmetry hypothesis that requires $\theta_{23} = \pi/4$.

This thesis introduces three methods to improve the sensitivity of NOvA's muon neutrino disappearance analysis. First, neutrino events are separated according to an estimate of their energy resolution to distinguish well resolved events from events that are not so well resolved. Second, an optimised neutrino energy binning is implemented that uses finer binning in the region of maximum muon neutrino disappearance. Third, a hybrid selection is introduced that selects muon neutrino events with greater efficiency and purity. The combination of these improvements produces an increase in the sensitivity of the analysis equivalent to collecting 40-100% more data across the range of possible values of Δm^2_{32} and $\sin^2\theta_{23}$.

This thesis presents new results using a 14 ktonne detector equivalent exposure of 6.05×10^{20} protons on target. A fit to the far detector data, assuming normal hierarchy, produces $\Delta m^2_{32} = 2.45^{+0.087}_{-0.079} \times 10^{-3}$ eV^2 and $\sin^2\theta_{23}$ in the range 0.429 - 0.593 with two statistically degenerate best fit points at 0.481 and 0.547. This measurement is consistent with maximal mixing where $\theta_{23} = \pi/4$. The data used for this thesis is 1/6 of the total data that NOvA expects to collect.

Acknowledgements

I would like to thank my viva examiners, Dr Iacopo Vivarelli and Dr Evgueni Goudzovski, for both the time they took to read my thesis and the invaluable feedback they provided.

I feel immense gratitude to my supervisor, Professor Jeff Hartnell, for giving me the opportunity to pursue my fascination in neutrino physics. Over the years our discussions have given me new insights and increased my appreciation for the need of precision.

This piece of work would not have been possible without the amazing members of the NOvA collaboration. The members of this collaboration built both the detectors and the fantastic software frameworks used for everything from data collection through to data analysis.

The NOvA post-doctoral researchers at Sussex had to bear the brunt of my many questions and frustrations. I would like to thank Bruno Zamorano, Michael Baird, Jonathon Davies and Matthew Tamsett who all provided unique advice and taught me a lot. I've enjoyed my time in both of the offices I've shared during my time as a student at Sussex. That is thanks to my fellow students including Tristan Blackburn, Diana Méndez, Tyler Alion, Mark Stringer, Fabrizio Miano, Nicola Abraham, Oliver Winston, James Waterfield, Yusufu Shehu, Zara Grout, Ed Leming, James Sinclair and Nicky Santoyo.

In total I have spent a bit over a year stationed at Fermilab. My time there was very enjoyable thanks to all the friendly and interesting people who were also stuck in the wilderness that is the Chicago suburbs. In particular, I would like to thank Martin Frank, Xuebing Bu, Alexander Radovic, Mike Wallbank, Karl Warburton, Rob Ainsworth, and Tristan Blackburn for their friendship.

Throughout this journey I have had the support of my wonderful girlfriend and cheerleader Elizabeth Todd Davies. Last but not least, I have to thank Berni Vinton, Brian Titley and the rest of my family for always being there. The mixture of mocking and enthusiasm for my research has simultaneously kept my feet on the ground and my confidence high.

Preface

The general goals of this thesis were suggested by my supervisor, Jeff Hartnell.

Chapter 1 introduces the thesis and its motivation.

Chapter 2 describes the physics of neutrino oscillations and the experimental status of the field. It has been written from a combination of various sources.

Chapter 3 describes the NOvA experiment. It has been written from a combination of various sources as well as personal experience.

Chapter 4 sets out the reconstruction and analysis chain as well as the systematic uncertainties. The reconstruction and analysis chain, mostly crafted by other members of the NOvA collaboration, is described using various sources. The evaluation of the systematic uncertainties is written from a combination of sources and from my own work.

Chapter 5 explores three new methods to improve the sensitivity of the disappearance experiment. The optimised neutrino energy binning and separation of events based on energy resolution is based on my own work. A hybrid selection method, first introduced by Kirk Bays, is re-optimised by myself and integrated into the disappearance analysis. The combination and optimisation of the above three improvements is based on my own work.

Chapter 6 presents the result of using the improved analysis to measure neutrino oscillation parameters and is based on my own work.

Chapter 7 summarises and concludes the thesis.

Contents

List of Tables

List of Figures

Chapter 1

Introduction

The neutrino was discovered a little over 60 years ago and during the last two decades the ability of neutrinos to change flavour in flight has been well established. The Standard Model of particle physics defines neutrinos to be massless but the observed phenomenon of neutrino oscillations requires that at least two of the neutrinos have mass. This means that the current model is incomplete and neutrino oscillations are physics beyond the Standard Model. Great strides in the understanding of neutrinos have been made but important questions remain. Such as, do neutrinos oscillate in the same way as antineutrinos, what is the ordering of the neutrino masses and what is the octant of the θ_{23} mixing angle? There are also practical issues, for example, the uncertainty on the value of $\sin^2\theta_{23}$ is a significant limitation on our ability to resolve δ_{CP} in future measurements.

The NOvA experiment consists of two detectors which measure the energy and composition of the NuMI beam at baselines of 1 km and 810 km. Neutrino oscillation experiments such as NOvA aim to measure the probability of a neutrino oscillating from one flavour to another. Such measurements probe the neutrino mixing angles and the difference between the squared neutrino masses. Measuring muon neutrino disappearance with NOvA has the potential to make world leading measurements of the mass squared splitting Δm^2_{32} and the mixing angle θ_{23}. Through measuring θ_{23} NOvA will provide insight into the question of whether the third neutrino mass eigenstate is mostly muon ($\theta_{23} > 45^o$) or tau neutrino ($\theta_{23} < 45^o$) or if the two neutrino flavours comprise an equal share ($\theta = 45^o$) of the third mass eigenstate. If $\theta_{23} = 45^o$ then there may be an underlying symmetry. This thesis focusses on improving the sensitivity of the muon neutrino disappearance analysis with particular attention given to improving the sensitivity to distinguish maximal mixing, where $\theta_{23} = 45^o$ exactly.

The history and theory of neutrino oscillations are reviewed in Chapter 2. Particular

focus is given to elements of the neutrino oscillation theory that are directly relevant to the analysis presented in this thesis. The NOvA detectors and neutrino beam are described in Chapter 3. The reconstruction and analysis chain, starting with raw cell hits and ending with selected muon neutrino candidate events, is set out in Chapter 4. Methods with potential to improve the sensitivity of the muon neutrino disappearance analysis are explored in Chapter 5. The result of using the sensitivity improvement techniques to analyse the far detector data is presented in Chapter 6. Conclusions from the work and results presented are given by Chapter 7.

Chapter 2

Neutrino Physics

Let us start in 1914, when Chadwick presented experimental evidence [1] that the energy spectrum of electrons emitted in β decay was continuous instead of being discrete as expected. This meant that either β decay was not a two-body process or conservation of energy was violated. The solution arrived in 1930, when neutrinos were postulated by Wolfgang Pauli [2] as a "desperate remedy" to the apparent non-conservation of energy in nuclear β decay. He suggested that an additional neutral and extremely light particle was produced in β decay which carried away the undetected energy. Pauli referred to this additional particle as a "neutron" but this name did not stick. In 1932 Chadwick discovered a more massive neutral particle and called it the neutron. In 1934 Fermi [3] formulated a theory of β decay and re-named Pauli's additional particle as the "neutrino" (Italian for "the little neutral one").

The neutrino is hard to observe due to its weak interaction with matter. In fact, Bethe and Peierls estimated [4] that the neutrino would travel 10^{16} km through "solid matter" before interacting and described the observation of a neutrino interaction as "absolutely impossible". In 1956, Cowan and Reines [5] overcame the hurdle of experimentally detecting neutrinos[1] and provided the first direct evidence for their existence. The pair setup an experiment to measure the flux of neutrinos emitted from a nuclear reactor. The neutrinos from the reactor were produced via β decay and were detected via inverse β decay ($p + \bar{\nu} \rightarrow n + e^+$). If a neutrino interacted within the detector it would produce a characteristic signal of a pair of photons from electron-positron annihilation and a delayed photon from neutron capture.

[1] They expressed the double edged sword of the validity of Pauli's neutrino proposal and the difficulty of neutrino detection as "the very characteristic of the particle which makes the proposal plausible - its ability to carry off energy and momentum without detection".

At first it was thought that only one type of neutrino existed. This view changed with the subsequent discovery of muon and tau neutrinos, which were discovered several decades apart. In 1962 neutrinos which produce muons but not electrons when interacting with matter were observed [6]. In this paper it was suggested that neutrinos produced in association with a muon are muon neutrinos which are distinct from the electron neutrinos previously observed in β decay. This suggestion of lepton flavour caught on: electron, muon and tau neutrinos are defined by the charged lepton produced in association during charged-current weak interactions. The reverse is also true: a neutrino involved in a charged current interaction with matter producing an electron is necessarily a electron neutrino. Similarly for muon and tau neutrinos. In 1989, The ALEPH collaboration published measurements of the mass and width of the Z boson [7]. Consequently they were able to constrain the number of active light neutrinos to be three at 98% confidence level. Final results from the ALEPH experiment provided conclusive evidence that the number of light active neutrinos is indeed three [8]. In 2000, the DONUT experiment reported an observation of four tau neutrino neutrinos with a background estimation of 0.34 events [9]. This third neutrino completed the set of the three standard model neutrinos associated with the three charged leptons.

The first hints of oscillations between neutrino flavours came from experiments measuring the flux of solar neutrinos. The fusion reactions by which energy is produced in the sun are modelled by the Standard Solar Model. The model predicts three major neutrino emissions: pp neutrinos ($p + p \rightarrow d + e^+ + \nu_e$, $E_{max.} = 420$ keV), ^{7}Be neutrinos ($^7\mathrm{Be} + e^- \rightarrow ^7\mathrm{Li} + \nu_e$, $E_{max.} = 860$ keV) and ^{8}B neutrinos ($^8\mathrm{B} + e^- \rightarrow ^8\mathrm{Be} + e^+ + \nu_e$, $E_{max.} = 14$ MeV) [10]. In 1968 Ray Davis et al. published the "Search For Neutrinos From the Sun" paper [11]. In the same year Bahcall et al. published a prediction for the solar neutrino flux experienced by Ray Davis's experiment based on the standard solar model [12]. Davis used the interaction $^{37}\mathrm{Cl} + \nu \rightarrow e^- + ^{37}\mathrm{Ar}$ to measure the flux of ^{8}B and ^{7}Be solar electron neutrinos. The measured rate of neutrinos was found to be only one third of the rate predicted by Bahcall. At the time of publication this discrepency was generally attributed to errors in either the measurement technique or the standard solar model at high neutrino energies and became known as the "solar neutrino puzzle". In 1989, the Kamiokande-II experiment confirmed the deficit of ^{8}B solar electron neutrinos relative to the standard solar model [13]. In 1991 and 1992, the deficit was further confirmed by two experiments, SAGE [14] and GALLEX [10], which both measured the rate of the less energetic pp solar neutrinos. These experiments showed that the flux deficit

occurred for low energy pp neutrinos as well as the higher energy ^{8}B and ^{7}Be neutrinos measured previously.

Either the standard solar model was incorrect or electron neutrinos produced in the sun do not all survive the journey to the Earth. Neutrino oscillation due to massive neutrinos became accepted as a realistic possibility. Previously, in the years 1962-1968, Pontecorvo, Maki, Nakagawa, and Sakata had formulated a theory including electron and muon neutrinos which were able to transform from one to the other [15, 16, 17].

In 1998, Super Kamiokande reported evidence for the oscillation of atmospheric neutrinos [18]. They measured the rate of muon and electron neutrinos originating from collisions of cosmic rays with nuclei in the upper atmosphere. Electron and muon neutrinos are produced in the upper atmosphere approximately in the ratio 1:2 (electron:muon). This ratio is due to the following: cosmic pions favour the decay to muons over electrons ($\pi^- \rightarrow \overline{\nu_\mu}\mu^-$) due to helicity suppression, the muon produced in this decay will often decay before reaching the ground predominately through the interaction $\mu^- \rightarrow e^-\overline{\nu_e}\nu_\mu$. This results in the estimated neutrino flux of one electron neutrino, one muon neutrino and one muon anti-neutrino. The detector allowed the reconstruction of the direction of the incoming neutrino, which revealed the baseline between production and interaction within the detector and whether the neutrino travelled through the Earth. The asymmetry of upward and downward going events was measured for both electron and muon neutrinos. Since the flux of cosmic rays is isotropic, no asymmetry was expected. The electron neutrino asymmetry was consistent with zero but a energy dependant asymmetry was observed for muon neutrinos at more than 6 standard deviations. The data provided conclusive evidence for neutrino oscillations.

In 2002, SNO published measurements of the flux of solar ^{8}B neutrinos [19], via measurements of the rate of both charged current electron neutrino events and neutral current (NC) events due to all three active neutrinos. The measured neutral current rate was consistent with the flux expected from the standard solar model but the measured flux of electron neutrinos was significantly lower. The theory of neutrino oscillations was again confirmed as the solution to the solar neutrino puzzle.

Since the confirmation of neutrino oscillations, the spotlight has moved on to the determination of the unknown neutrino properties such as: the parameters which govern their oscillations, the nature of neutrinos (whether they are Dirac or Majorana particles), their strength of interaction with matter, their mass, the origin of their mass and the number of neutrino flavours. Experimental and theoretical advances have made progress

on the above questions during the last 6 decades [20] and the observation of neutrino oscillations has opened new fundamental questions regarding the origin of fermion masses and the relationship between quarks and leptons [21].

2.0.1 The Weak Force

Neutrinos interact with matter through the weak force in one of three flavour eigenstates (electron, muon or tau). The weak force is mediated by the electrically charged $W^{\pm}$ and electrically neutral Z bosons. Figure 2.1 shows the Feynman diagrams of neutrinos interacting with the weak force's W (Figure 2.1a) and Z (Figure 2.1b) bosons.

As shown in Figure 2.1a, a neutrino interacting with matter through the W boson will produce a charged lepton corresponding to the lepton flavour, l, of the incoming neutrino. This process can happen in reverse, with a charged lepton producing a neutrino with the same lepton flavour and a W boson. Such processes involving a W boson are known as charged current interactions. As shown in Figure 2.1b, a neutrino interacting with the Z boson will produce a neutrino with the same lepton flavour, l, as the incoming neutrino. Interactions involving the Z boson are known as neutral current interactions. In a detector an incoming neutrino interacting via the neutral current would have the underlying process,

$$\nu_x + Y \rightarrow \nu_x + Y',$$

where x is the lepton flavour, Y is the target and Y' is some excitation of the target.

(a) Charged current. (b) Neutral current.

Figure 2.1: Diagrams showing the interaction of neutrinos with the weak force via the charged current and neutral current mediated by the W and Z bosons respectively. The lepton flavour, l, is conserved for both charged and neutral current interactions.

2.1 Neutrino Eigenstates

Neutrinos interact with matter through the weak force in one of the three eigenstates of lepton flavour (ν_e, ν_μ and ν_τ). However, neutrinos propagate through vacuum in eigenstates of mass (ν_1, ν_2 and ν_3). The eigenstates of mass and flavour are not equivalent,

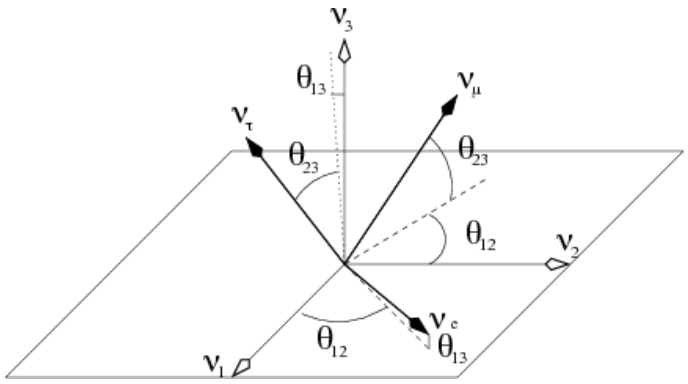

Figure 2.2: Euler angle representation of the neutrino mixing angles. The angles relate the weak flavour eigenstates to the mass eigenstates. Figure taken from [22].

instead the flavour states are a superposition of the mass states (and vice versa). A neutrino of definite weak flavour, α, can be written as a linear combination of the mass states as follows,

$$|\nu_\alpha >= \sum_{i=1}^{3} U^*_{\alpha i} |\nu_i >, \tag{2.1}$$

where $U^*_{\alpha i}$ is the element of the unitary PMNS (Pontecorvo, Maki, Nakagawa, and Sakata) matrix describing the coupling strength between the mass state i and the flavour state α.

In the quark sector, mixing between the weak flavour states is similarly governed by the CKM (Cabibo-Kobayashi-Maskawa) matrix. However, the mixing induced in the lepton sector is large compared to the quark sector because the off-diagonal matrix elements are large.

The standard parametrisation of the PMNS matrix is in terms of a phase δ and three mixing angles, θ_{12}, θ_{13} and θ_{23}. Figure 2.2 shows how the neutrino mixing angles can be represented as Euler angles that relate the weak flavour eigenstates to the mass eigenstates. The PMNS matrix is conventionally written as:

$$U = \begin{pmatrix} U_{e1} & U_{e2} & U_{e3} \\ U_{\mu 1} & U_{\mu 2} & U_{\mu 3} \\ U_{\tau 1} & U_{\tau 2} & U_{\tau 3} \end{pmatrix} \tag{2.2}$$

$$= \begin{pmatrix} c_{13}c_{12} & c_{13}s_{12} & s_{13}e^{-i\delta} \\ -c_{23}s_{12} - s_{13}s_{23}c_{12}e^{i\delta} & c_{23}c_{12} - s_{13}s_{23}s_{12}e^{i\delta} & c_{13}s_{23} \\ s_{23}s_{12} - s_{13}c_{23}c_{12}e^{i\delta} & -s_{23}c_{12} - s_{13}c_{23}s_{12}e^{i\delta} & c_{13}c_{23} \end{pmatrix} \tag{2.3}$$

$$= \begin{pmatrix} 1 & 0 & 0 \\ 0 & c_{23} & s_{23} \\ 0 & -s_{23} & c_{23} \end{pmatrix} \begin{pmatrix} c_{13} & 0 & s_{13}e^{-i\delta} \\ 0 & 1 & 0 \\ -s_{13}e^{i\delta} & 0 & c_{13} \end{pmatrix} \begin{pmatrix} c_{12} & s_{12} & 0 \\ -s_{12} & c_{12} & 0 \\ 0 & 0 & 1 \end{pmatrix} \tag{2.4}$$

where $s_{ij} \equiv \sin\theta_{ij}$, $c_{ij} \equiv \cos\theta_{ij}$ and δ is the CP violating phase. A non-zero and non-π value of δ would indicate charge-parity violation due to the resulting difference in the flavour transformations, for example $\nu_e \to \nu_\mu$ and $\nu_\mu \to \nu_e$ [23].

2.2 Neutrino Oscillation Probability in Vacuum

The following derivation of the neutrino oscillation probability follows [20] and [24] and uses natural units. A neutrino is produced via a weak interaction as a flavour eigenstate. At time $t = 0$ the flavour state, α, can be written as $|\nu_\alpha\,(t=0)>$ and is the sum of the mass states $|\nu_i>$:

$$|\nu_\alpha\,(t=0)> = \sum_{i=1}^{3} U^*_{\alpha i}|\nu_i> . \tag{2.5}$$

As the neutrino propagates the mass states evolve. At a later time, t, we have,

$$|\nu_\alpha\,(t)> = \sum_{i=1}^{3} U^*_{\alpha i} e^{-ip_i.x}|\nu_i>, \tag{2.6}$$

where p_i is the four-momentum and x the four-position of mass state ν_i. At time t the neutrino weakly interacts with matter in flavour state β,

$$\begin{aligned} <\nu_\beta|\nu_\alpha> &= \sum_{j=1}^{3}\sum_{i=1}^{3} U_{\beta j}U^*_{\alpha i}e^{-ip_i.x} <\nu_j|\nu_i> \\ &= \sum_{j=1}^{3} U_{\beta j}U^*_{\alpha j}e^{-ip_j.x}. \end{aligned} \tag{2.7}$$

Assuming all mass states have the same three-momentum $\mathbf{p}^2$,

$$\begin{aligned} p_j.x &= E_j t - \mathbf{p}\cdot\mathbf{x} \\ &= t\sqrt{|\mathbf{p}|^2 + m_j^2} - \mathbf{p}\cdot\mathbf{x} \end{aligned} \tag{2.8}$$

Since neutrinos are extremely light ($m_\nu < 2\ eV$ [20]) and, in the case of accelerator experiments, travel at close to the speed of light we can make the approximations, $m_j << E_j$, $t = L$ and $\mathbf{p}\cdot\mathbf{x} = |\mathbf{p}|L$. Using a binomial expansion we find,

$$p_j \cdot x = |\mathbf{p}|L\left(1 + \frac{m_i^2}{2|\mathbf{p}|^2}\right) - |\mathbf{p}|L = \frac{m_j L}{2E} \tag{2.9}$$

Combining Equations 2.7 and 2.9 we get $< \nu_\beta|\nu_\alpha >= \sum_{j=1}^{3} U_{\beta j}U^*_{\alpha j}e^{-i\frac{m_j L}{2E}}$.

The probability of observing the neutrino in flavour state β after travelling distance L given initial flavour state α is,

$$\begin{aligned} P_{\alpha\to\beta} &= |< \nu_\beta(t)\,|\nu_\alpha(t) >|^2 \\ &= \left(\sum_{j=1}^{3} U_{\beta j}U^*_{\alpha j}e^{-i\frac{m_j L}{2E}}\right)\left(\sum_{i=1}^{3} U^*_{\beta i}U_{\alpha i}e^{i\frac{m_j L}{2E}}\right). \end{aligned} \tag{2.10}$$

Finally, we find:

$$\begin{aligned} P_{\alpha\to\beta} = \delta_{\alpha\beta} &- 4\sum_{i>j}\Re[U^*_{\alpha i}U_{\alpha j}U_{\beta i}U^*_{\beta j}]\sin^2\left(\frac{\Delta m^2_{ij}}{4E}L\right) \\ &+ 2\sum_{i>j}\Im[U^*_{\alpha i}U_{\alpha j}U_{\beta i}U^*_{\beta j}]\sin^2\left(\frac{\Delta m^2_{ij}}{2E}L\right), \end{aligned} \tag{2.11}$$

where $\Delta m^2_{ij} \equiv m_i^2 - m_j^2$ and $\delta_{\alpha\beta}$ is the Kronecker delta. The equation shows that the neutrino oscillation probability depends on the parameters of the PMNS matrix and the value of the two sinusoidal arguments. The probability depends on the mass splittings Δm^2_{21}, Δm^2_{31}, Δm^2_{32}, and varies with the length of the baseline, L, and the energy of the neutrino beam, E. Only two of the mass splittings are independent and (with knowledge of the mass ordering) the third can be described in terms of the other two. The smaller mass splitting, Δm^2_{21}, is often referred to as the "solar mass splitting" due to its role in neutrino oscillation between the Earth and the Sun. The larger weighted average of the

[2] A more exact method is to use the wave packet treatment but this has been shown to produce the same result for our needs [25].

other two, $\Delta m^2_{32/31}$, is often named the "atmospheric mass splitting", Δm^2_{atm}, due to its role in atmospheric neutrino oscillations.

2.3 Neutrino Oscillation Parameter Measurements

The experimentally measured values of the neutrino oscillation parameters are given in Table 2.1. The measurements of the oscillation parameters have been made using reactor, solar, accelerator and atmospheric neutrino experiments.

The two independent mass differences and three mixing angles have all been measured. The sign of the mass difference has been determined for Δm^2_{21} (ν_1 is less massive than ν_2) by measurements of the solar neutrino flux. However, the ordering of Δm^2_{32} has not yet been determined. This means that it is not known whether ν_3 is more or less massive than the two other mass states, the former and later cases are known as Normal Ordering or Inverted Ordering respectively. Tentative measurements of the CP violating phase δ_{CP} have been made [26] but the value essentially remains unknown.

Current measurements [27] suggest that $\sin^2\theta_{23} \simeq 0.5$ which would imply $\cos^2\theta_{23} \simeq 0.5$. In the case where both are equal to 0.5, $U_{\mu 3} = U_{\tau 3} = \frac{1}{2}c_{13}$ (see Equation 2.4). These two PMNS matrix elements define the proportion of ν_μ and ν_τ comprising ν_3. If $\sin^2\theta_{23} = 0.5$ then the third mass state has equal ν_μ and ν_τ parts, this is known as maximal mixing. Current measurements are compatible with maximal mixing and have motivated theoretical models suggesting an underlying muon-tau neutrino symmetry [28, 29, 30]. If nature has chosen non-maximal mixing then discovering the octant (whether $\sin^2\theta_{23}$ is greater or less than 0.5) will determine whether the third mass state is composed of more ν_μ or more ν_τ and exclude the potential underlying muon-tau neutrino symmetry.

2.4 Two-Flavour Approximation

In many experimental cases the neutrino oscillation probability can be approximated as the result of two-flavour mixing. This two flavour oscillation probability and the necessary approximation will be outlined in this section.

For long-baseline neutrino oscillation experiments it is useful to write the phase, $\frac{\Delta m^2_{ij}}{4E}L$, in units of the same scale as the experiment. This is done using units of eV^2 for Δm^2_i, GeV for E and km for L. Restoring the factors of $\hbar$ and c, and applying the appropriate unit conversions, we find,

$$\frac{\Delta m^2_{ij} c^3}{4E\hbar}L \approx 1.27\frac{\Delta m^2_{ij}[\mathrm{eV}^2]}{E[\mathrm{GeV}]}L[\mathrm{km}]. \tag{2.12}$$

Parameter	Average of measurements
$\sin^2\theta_{12}$	0.304 ± 0.014
Δm^2_{21} [10^{-5} eV^2]	7.53 ± 0.18
$\sin^2\theta_{23}$	0.51 ± 0.05 (0.50 ± 0.05)
Δm^2_{32} [10^{-3} eV^2]	2.44 ± 0.06 (-2.51 ± 0.06)
$\sin^2\theta_{13}$ [10^{-2}]	2.19 ± 0.12

Table 2.1: A global best-fit of neutrino oscillation parameter measurements from [20]. The 1 σ uncertainty on each parameter is also shown. Measurements that differ under the assumption of inverted ordering (rather than normal ordering) are provided within parentheses.

Let us use the oscillation channel relevant to this thesis as an example. In the three flavour case (Equation 2.11), the muon neutrino survival probability is,

$$P_{\mu\to\mu} = 1 - 4\sum_{i>j}|U_{\mu i}|^2|U_{\mu j}|^2\sin^2\left(\frac{\Delta m^2_{ij}}{4E}L\right), \tag{2.13}$$

where the imaginary component of Equation 2.11 is zero because in this case $\Im[U^*_{\mu i}U_{\mu i}] = 0$.

The elements of the PMNS matrix, $U_{\mu i}$, can be simplified considering the current measured values. Table 2.1 shows that the value of $\sin^2\theta_{13}$ is very small relative to the two other mixing parameters. Using the approximations $\sin\theta_{13} \approx 0$ and $\cos\theta_{13} \approx 1$ the relevant PMNS elements (see Equation 2.4) can be approximated as,

$$\begin{aligned} |U_{\mu 1}|^2 &\approx s^2_{12}c^2_{23} \\ |U_{\mu 2}|^2 &\approx c^2_{12}c^2_{23} \\ |U_{\mu 3}|^2 &\approx s^2_{23}. \end{aligned} \tag{2.14}$$

Experimental results have shown that the mass splitting, Δm^2_{21}, is very small relative to Δm^2_{31} and Δm^2_{32} (see Table 2.1) [20], which allows the approximation: $\Delta m^2_{31} \simeq \Delta m^2_{32}$. For long-baseline neutrino oscillation experiments, the oscillations associated with the atmospheric and solar mass splittings can be approximated to be de-coupled. This is because the atmospheric mass splitting is approximately 30 times larger than the solar mass splitting. As an example, let us take the NOvA experiment with $L = 810$ km and $E \sim 2$ GeV. For the NOvA experiment the we have:

$$\sin^2\left(\frac{1.27\Delta m^2_{12}}{E}L\right) = \sin^2\left(\frac{1.27\times 7.53\times 10^{-5}}{2}\times 810\right) \approx \sin^2 0.04 \approx 0. \tag{2.15}$$

With the above simplifications, the muon neutrino survival probability can be expressed as:

$$\begin{aligned} P_{\mu\to\mu} &\simeq 1 - 4s_{23}^2 c_{23}^2 (s_{12}^2 + c_{12}^2) \sin^2\left(\frac{1.27\Delta m^2_{atm.}}{E} L\right) \\ &\simeq 1 - \sin^2 2\theta_{23} \sin^2\left(\frac{1.27\Delta m^2_{atm.}}{E} L\right), \end{aligned} \tag{2.16}$$

where $\Delta m^2_{atm.} \equiv \Delta m^2_{32} \simeq \Delta m^2_{13}$. From this equation it can be seen that the disappearance probability has an oscillatory form. The overall magnitude of the oscillation is governed by $\sin^2 2\theta_{23}$ and the period of the oscillation is defined by $\frac{1.27\Delta m^2_{atm.}}{E}$.

The probability of electron neutrino appearance is a more complex expression involving all the PMNS parameters and the three mass splittings. The probability can be approximated as,

$$P\left(\nu_\mu \to \nu_e\right) \sim P_{atm} + 2\sqrt{P_{atm}P_{sol}}\cos(\Delta_{32} + \delta) + P_{sol}, \tag{2.17}$$

where $\Delta_{ij} = \Delta m^2_{ij} L/4E$ [24]. The amplitudes P_{atm} and P_{sol} depend only on Δm^2_{31} and Δm^2_{21} respectively. For neutrinos propagating through vacuum the amplitudes are given by,

$$\begin{aligned} \sqrt{P_{atm}} &\equiv \sin\theta_{23} \sin 2\theta_{13} \sin\Delta_{31} \\ \sqrt{P_{sol}} &\equiv \cos\theta_{23} \cos\theta_{13} \sin 2\theta_{12} \sin\Delta_{21}. \end{aligned} \tag{2.18}$$

For propagation through matter the amplitude terms have to be modified due to phenomena known as matter effects.

2.5 Matter Effects

Neutrinos propagating through matter experience the weak force through coherent forward scattering. Ordinary matter is composed, in part, of electrons but not muons or taus (or the anti-neutrinos). Figure 2.3 shows the Feynman diagrams for scattering of neutrinos on electrons. Subfigure 2.3b shows the neutral current scattering of any type of neutrino on electrons. Neutral current interactions with matter are flavour independent and so do not affect neutrino oscillation probabilities. Subfigure 2.3a shows the charged current coherent forward scattering of electron neutrinos on electrons. Charged current coherent forward scattering on the electrons in ordinary matter is only experienced by electron neutrinos. This additional scattering amplitude causes oscillations involving ν_e or $\bar{\nu}_e$ to have different probabilities relative to oscillation in vacuum. [31, 32]

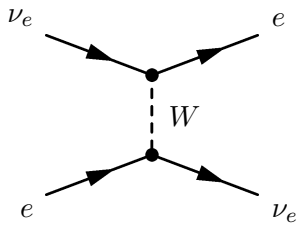

(a) Charged current scattering of an electron neutrino on an electron.

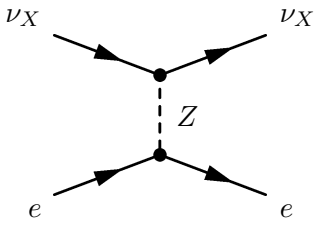

(b) Neutral current scattering of any neutrino flavour on an electron.

Figure 2.3: Feynman diagrams of scattering of neutrinos on the electrons in matter.

The evolution of the neutrino flavour states is given by

$$i\frac{d}{dx}\begin{pmatrix}\nu_e\\ \nu_\mu\\ \nu_\tau\end{pmatrix} = H\begin{pmatrix}\nu_e\\ \nu_\mu\\ \nu_\tau\end{pmatrix}, \tag{2.19}$$

where H is the Hamiltonian. In matter H is given by

$$H = U\begin{pmatrix}\frac{m_1^2}{2E} & 0 & 0\\ 0 & \frac{m_2^2}{2E} & 0\\ 0 & 0 & \frac{m_3^2}{2E}\end{pmatrix}U^\dagger + \begin{pmatrix}\sqrt{2}G_F N_e & 0 & 0\\ 0 & 0 & 0\\ 0 & 0 & 0\end{pmatrix}, \tag{2.20}$$

where U is the PMNS matrix discussed in Section 2.1, G_F is the Fermi constant and N_e is the electron number density of the medium.

Matter effects modify the terms $\sin(\Delta_{31})$ and $\sin(\Delta_{21})$ (where $\Delta_{ij} \equiv \frac{\Delta m_{ij}^2}{4E}L$) in Equation 2.11 by substituting:

$$\sin\left(\Delta_{ij}\right) \to \frac{\Delta_{ij}}{\Delta_{ij} \mp aL}\sin\left(\Delta_{ij} \mp aL\right), \tag{2.21}$$

where $a = \frac{G_F N_e}{\sqrt{2}}$, the top sign refers to neutrinos and the bottom sign to antineutrinos. [24]

For the normal ordering, matter effects enhance the appearance probability $\nu_\mu \to \nu_e$ but suppress the appearance probability $\bar{\nu}_\mu \to \bar{\nu}_e$. Conversely, for the inverted ordering matter effects suppress the ν_e appearance probability and enhance the $\bar{\nu}_e$ probability.

Matter effects have the opposite consequence for neutrinos and antineutrinos and so can be confused with the effect of true CP violation. Figure 2.4 illustrates the ambiguity between CP and matter effects when measuring the neutrino and antineutrino appearance. The figure shows regions of bi-probability where it is possible to disentangle the contributions of matter effects and CP violation. In particular, for the inverted hierarchy and $\delta_{CP} = 3\pi/2$ (shown by the starred point) NOvA would be able to measure

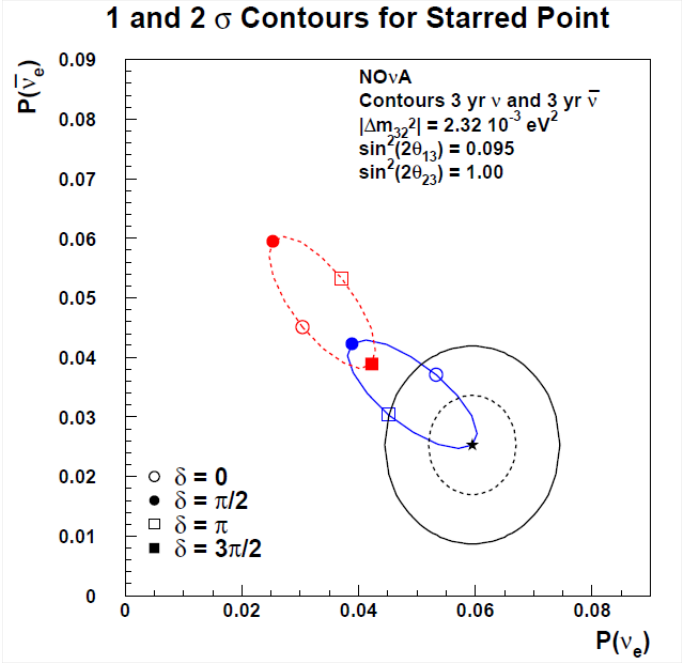

Figure 2.4: Bi-probability plot of ν_e ($\overline{\nu_e}$) appearance for the NOvA experiment. The solid blue and dotted red ellipses show the possible probability measurements for the Normal and Inverted Ordering respectively. The effect of altering δ_{CP} is to trace out the ellipse. Selected values of δ_{CP} are shown by the square and circle markers. Taken from [33].

the mass ordering to be normal with some confidence. This point would correspond to measured probabilities of $P(\bar{\nu}_e) = 0.025$ and $P(\nu_e) = 0.06$. Conversely, if NOvA measures $P(\bar{\nu}_e) = 0.04$ and $P(\nu_e) = 0.04$ then it will not be possible to distinguish between two possible scenarios: either the ordering is normal and $\delta_{CP} \approx \pi/2$ or the ordering is inverted and $\delta_{CP} \approx 3\pi/2$. The two ellipses shown are for fixed values of $\sin^2(2\theta_{13})$, $\sin^2(2\theta_{23})$ and Δm^2_{32}. The effect of increasing (decreasing) θ_{23} is to increase (decrease) both appearance probabilities.

2.6 Recent Results

Over the last two decades many experiments have made significant contributions to the knowledge of neutrino oscillations. Although these experiments deserve recognition, only the experiments currently providing the most precise knowledge of the neutrino oscillation parameters will be discussed in this section.

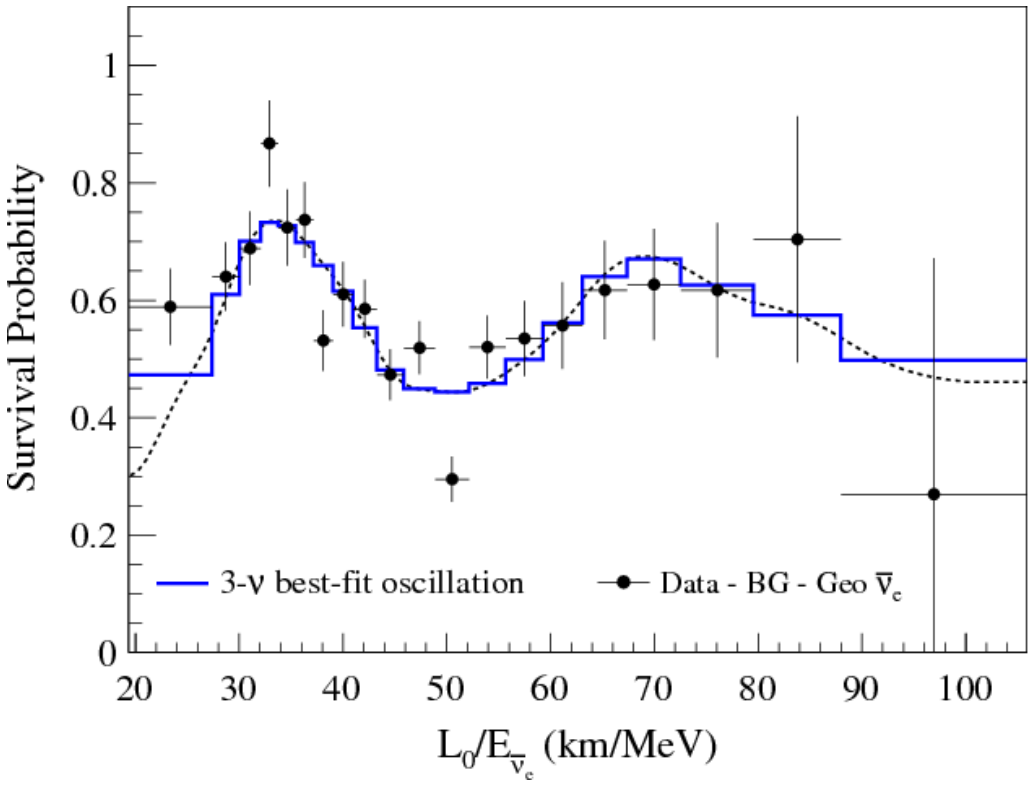

Figure 2.5: Observed survival probability of $\overline{\nu_e}$ vs. the effective baseline divided by the neutrino energy (L_0/E). The KamLAND data are shown by the black data points. A three flavour oscillation fit to the data is shown by the blue histogram. The value of θ_{13} has been constrained in the fit by accelerator and short baseline reactor experiments. Figure taken from [36].

2.6.1 Measurement of θ_{12} and Δm^2_{21}

The KamLAND detector consists of a 13 m diameter transparent balloon filled with 1 ktonne of ultra-pure liquid scintillator and surrounded by non-scintillating oil [34]. The detector measures the electron antineutrino flux from the surrounding 53 nuclear reactors. The flux averaged baseline between the reactors and the detector is approximately 180 km [35].

The observed survival probability of electron antineutrinos versus the effective baseline divided by the neutrino energy (L/E) is shown in Figure 2.5. The range of L/E is large enough to see the oscillatory shape in the survival probability due to neutrino oscillations. A fit of three-flavour oscillations to the data produced the confidence limit contours shown in Figure 2.6. KamLAND measured $\Delta m^2_{12} = 7.53^{+0.18}_{-0.18} \times 10^{-5}$ eV^2 and $\tan^2\theta_{12} = 0.436^{+0.029}_{-0.025}$ [36]. Regions allowed by KamLAND, the Solar experiments and a combined analysis are shown by the black, blue and colour shaded regions respectively.

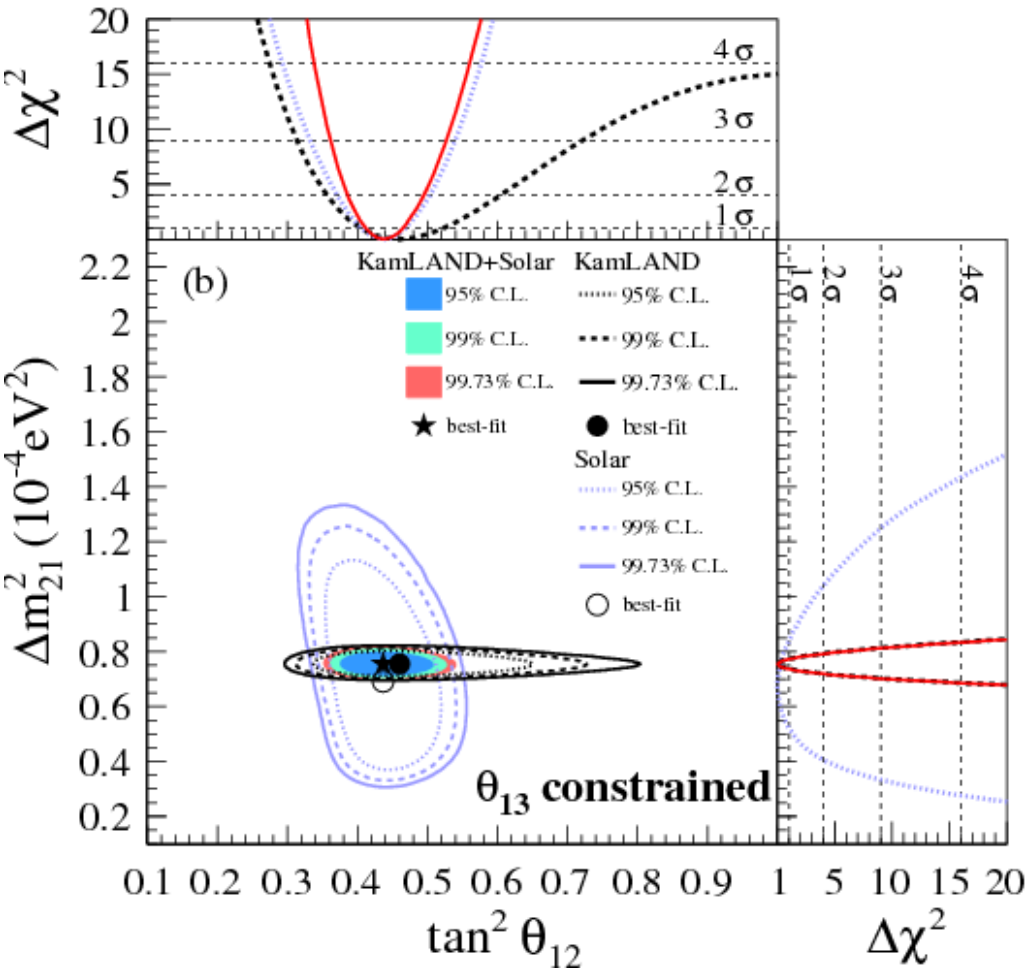

Figure 2.6: Contour plot showing the allowed regions in the Δm^2_{21} vs. $\tan^2\theta_{12}$ plane. The blue and black contours show the regions allowed by the KamLAND and Solar experiments respectively. A combined analysis of the solar and KamLAND data is shown by the colour shaded regions. The value of θ_{13} is constrained by the accelerator and the short baseline reactor experiments. Figure taken from [36].

2.6.2 Measurement of θ_{13}

In 2012 Daya Bay published results [37] measuring a non-zero θ_{13} beyond the 5 σ confidence level. The discovery of a non-zero value for θ_{13} opened a door for measurements of CP violation (through δ_{CP}), the neutrino mass ordering and the octant of θ_{23}.

The Daya Bay experiment consists of three experiment halls containing antineutrino detectors which measure the electron antineutrino flux from 6 nuclear reactor cores. Two of the experiment halls (EH1 and EH2) are situated at short distances from the nuclear cores, with effective baselines of 512 m and 561 m, while the third hall is further away from the nuclear cores, with an effective baseline of 1,579 m. The effective baseline for each detector hall is found by translating the flux received from the 6 nuclear reactor cores into an effective oscillated flux received from a single baseline [38]. The experiment measures the survival probability of electron antineutrinos from the six reactor cores as a function of neutrino energy. A fit to the data is used to extract measurements of the effective mass squared splitting [39], $|\Delta m^2_{ee}|$, and $\sin^2\theta_{13}$. The effective mass squared splitting is used for this Daya Bay measurement because it is independent of the unknown mass ordering and future improvements in the precise measurement of the solar oscillation parameters. This effective mass squared splitting is defined by a combination of the mass splittings, Δm^2_{32} and Δm^2_{21}, the mixing angle, θ_{12}, neutrino energy and baseline. At current experimental precision the effective mass squared splitting is indistinguishable from the mass squared splittings Δm^2_{31} and Δm^2_{32}.

Figure 2.7 shows the electron antineutrino survival probability vs. the effective propagation distance divided by the the antineutrino energy. The effective propagation distance is calculated by equating the actual flux to an effective flux using a single baseline [39]. The measured survival probabilities at experiment halls 1, 2 and 3 is shown by the blue green and black data-points respectively. A best fit to the data measured in the experiment halls is shown by the solid red line. The regions allowed (in the $|\Delta m^2_{ee}|$ vs. $\sin^2\theta_{13}$ plane) by the fit to the data is shown in the contour plot in Figure 2.8. The analysis measured $\sin^2 2\theta_{13} = 0.084 \pm 0.005$ and $|\Delta m^2_{ee}| = (2.42 \pm 0.11) \times 10^{-3}$ eV^2 [39].

2.6.3 Measurement of θ_{23} and $|\Delta m^2_{32}|$

The MINOS experiment consisted of two detectors that measure the atmospheric and accelerator neutrino flux. The muon neutrino beam was produced by the Neutrinos at the Main Injector (NuMI) facility at Fermilab. One detector was placed 1 km from the source of accelerator neutrinos and the other detector was placed at a distance of 735 km from the

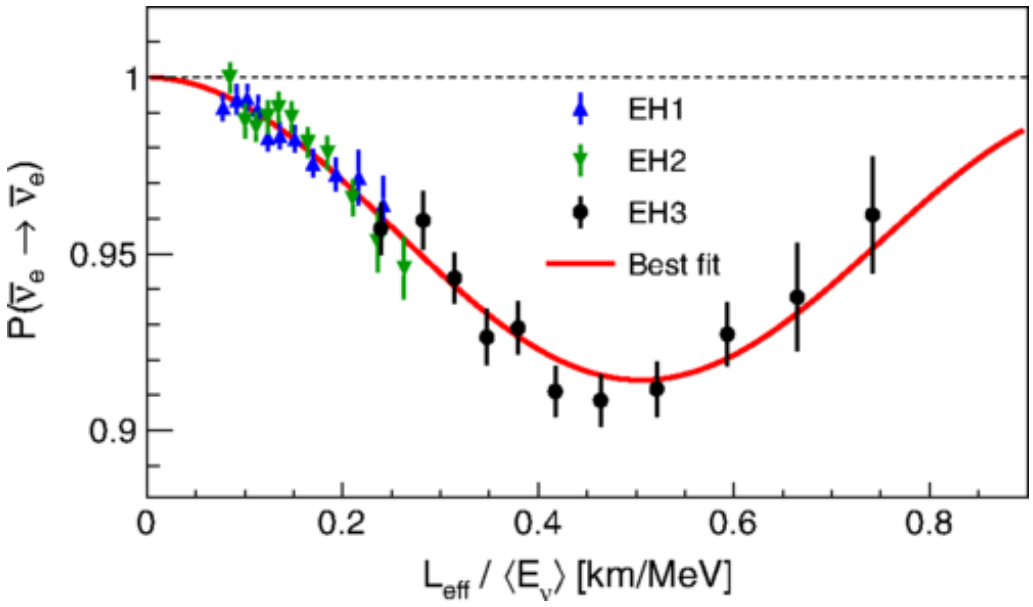

Figure 2.7: Measurement by Daya Bay of the electron antineutrino survival probability vs. the division of the effective propagation distance, $L_{eff.}$, by the average electron antineutrino energy, $< E_\nu >$. The measurements taken with the detectors situated in experiment halls (EH) 1, 2 and 3 are shown by the blue, green and black data points respectively. The best fit to the data is shown by the solid red line. Figure taken from [39].

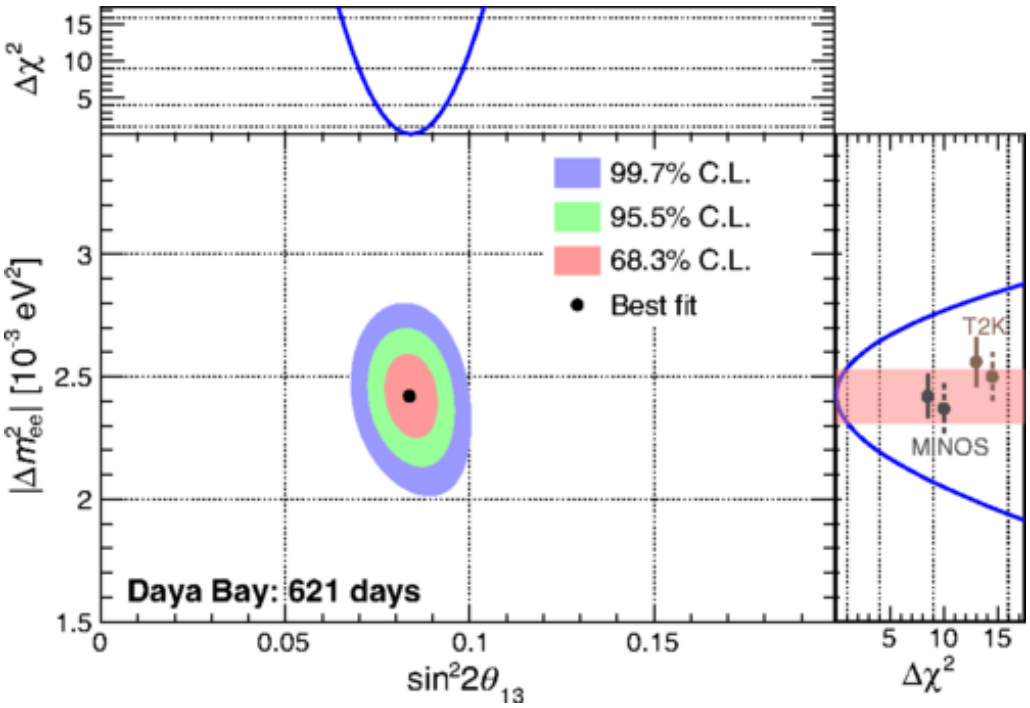

Figure 2.8: Confidence limit contour measured by the Daya Bay experiment. The contour plot shows the allowed regions in the $|\Delta m^2_{ee}|$ vs. $\sin^2\theta_{13}$ plane. Regions allowed with 68.3%, 95.5% and 99.7% confidence levels are shown by the red, green and blue regions. Figure taken from [39].

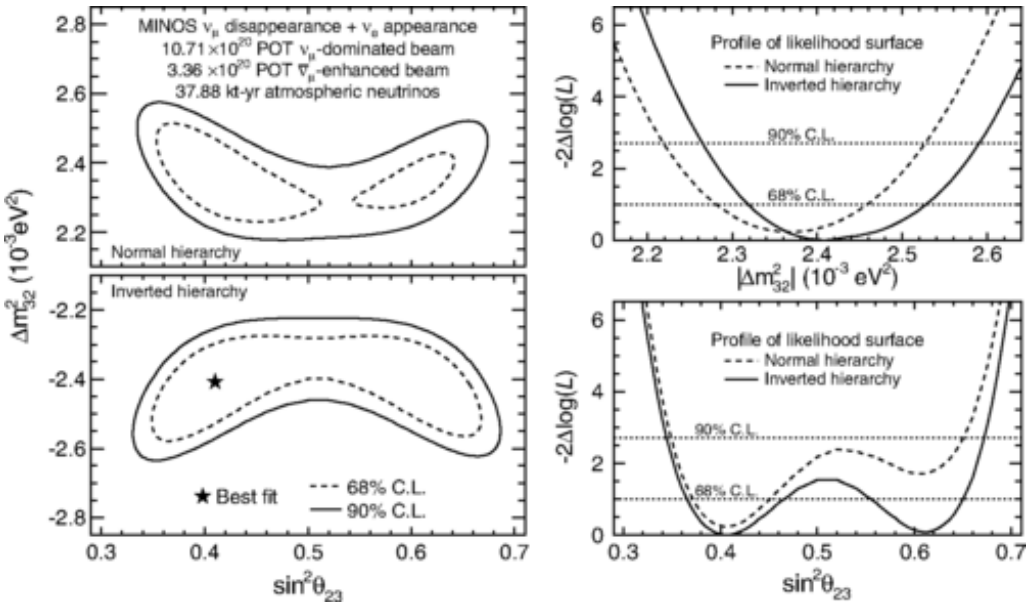

Figure 2.9: Confidence limits measured by the MINOS experiment. The left-hand plots show the confidence contours for Δm^2_{32} vs. $\sin^2\theta_{23}$ for the normal ordering (top) and the inverted ordering (bottom). The best fit point is indicated by the star. The right-hand plots show the one dimensional likelihood profiles as functions of Δm^2_{32} (top) and $\sin^2\theta_{23}$ (bottom), where the normal and inverted ordering are shown by the dotted and solid lines respectively. Figure taken from [40].

source. A joint analysis of the muon neutrino survival and the electron neutrino appearance probabilities was implemented to measure $\sin^2\theta_{23}$ and Δm^2_{32}. Figure 2.9 shows contours indicating the allowed regions from a fit to the measured appearance and disappearance probability distributions. Assuming the normal hierarchy, the experiment measured $|\Delta m^2_{32}| = [2.28 - 2.46] \times 10^{-3}$ eV^2 (68% C.L.) and $\sin^2\theta_{23} = 0.35 - 0.65$ (90% C.L.) [40]. The bottom right plot in Figure 2.9 shows the log likelihood of a fit to the data for each value of $\sin^2\theta_{23}$. As shown by the plot, MINOS prefers the lower octant value of $\sin^2\theta_{23} = 0.41$ with maximal mixing disfavoured by $-2\Delta\log(\mathcal{L}) = 1.54$(or $\sigma = 1.24$) [40].

The Tokai to Kamioka (T2K) experiment consists of three detectors which measure the flux of the predominately muon neutrino beam produced by the J-PARC high-intensity proton accelerator. Two detectors are situated 2.5 degrees from the beam axis and at a distance of 280 m and 295 km from the beam source. The third detector is placed on the beam axis at a distance of 280 m. The two near detectors are used to measure the properties of the neutrino beam both on and off-axis. The experiment measures both the muon neutrino disappearance and electron neutrino appearance probabilities. The confidence limit contour showing the result of a joint disappearance and appearance

analysis is shown in Figure 2.10. The T2K data favours the normal ordering with the inverted ordering slightly disfavoured at 0.86 units of $\Delta\chi^2$ and favours a point close to maximal mixing ($\sin^2\theta_{23} = 0.5$) with $\sin^2\theta_{23} = 0.527$ [27].

This thesis focusses on NOvA's muon neutrino disappearance analysis. The details of the experiment will be described in Chapter 3. NOvA's 2017 disappearance results are presented in [41]. Figures 2.11 and 2.12 show the measured muon neutrino energy spectrum and the resulting contour. Analysis of the disappearance data found $\Delta m^2_{32} = (2.67 \pm 0.11) \times 10^{-3}$ eV^2 and $\sin^2\theta_{23}$ at the statistically degenerate points $0.404^{+0.030}_{-0.022}$ or $0.624^{+0.022}_{-0.030}$. The data disfavour maximal mixing with 2.6 σ significance. To date, this is the highest significance with which maximal mixing has been disfavoured by a neutrino oscillation experiment.

As described in the above text and shown in Figure 2.10, there is some tension between the results published by the MINOS and T2K experiments. Both experiments disfavour the other's best-fit point beyond the 90% confidence limit. However, there are regions of overlap between the two sets of (68% and 90%) confidence limit (C.L.) contours. The 68% C.L. contours only overlap in the inverted hierarchy at approximately $\sin^2\theta_{23} = 0.55$ and $\Delta m^2_{32} = 2.4 \times 10^{-3}$ eV^2. Figure 2.12 shows a comparison of the 90% C.L. contours for the NOvA, T2K and MINOS experiments. When the recent NOvA result is also considered the region of overlap within all the 90% C.L. contours is reduced to two relatively small regions at $\Delta m^2_{32} \approx 2.5$ and $\sin^2\theta_{23} \approx 0.42$ or 0.6.

2.6.4 NOvA's Joint Appearance and Disappearance Result

Due to the non-zero value of θ_{13}, NOvA is able to use fits to the electron neutrino appearance probability to probe the mass ordering, the CP violating phase, δ_{CP}, and the octant of θ_{23}. NOvA's 2017 joint analysis [42] of the electron neutrino appearance and muon neutrino disappearance produced confidence intervals for δ_{CP}, the mass ordering and the octant of θ_{23}. Figure 2.13 shows the regions of $\sin^2\theta_{23}$ vs. δ_{CP} parameter space allowed, to varying degrees of confidence, by a fit to the ν_e and ν_μ spectra. The best fit occurs in the normal ordering contour (Figure 2.13a). In addition, the lower octant in the inverted ordering (Figure 2.13b is disfavoured beyond the 1 σ confidence level.

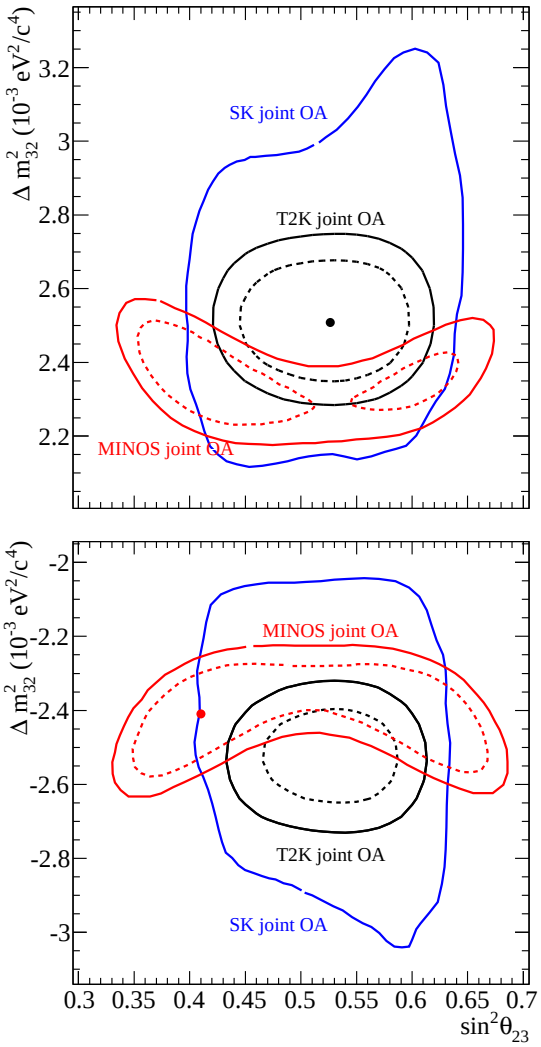

Figure 2.10: Confidence contours in the Δm^2_{32} vs. $\sin^2\theta_{23}$ plane for T2K (black lines), MINOS (red lines) and Super Kamiokande (blue line). The confidence limits in the normal and inverted ordering are shown in the top and bottom plots respectively. Confidence limits of 68% and 90% are shown by the dashed and solid lines respectively. Figure taken from [27].

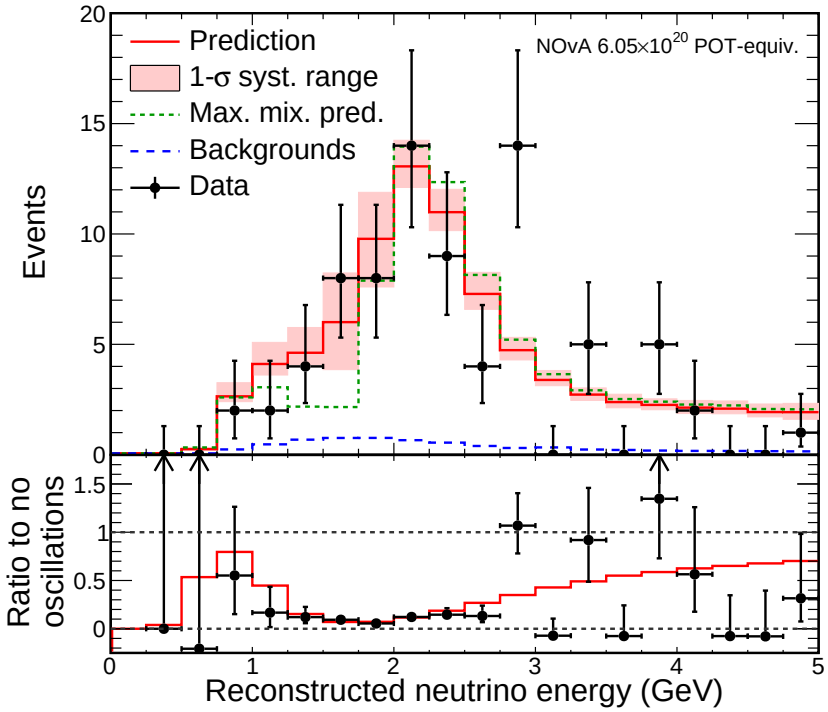

Figure 2.11: NOvA's far detector muon neutrino event rate vs. reconstructed neutrino energy. The data are shown by the black points and the three-flavour oscillation fit to the data is shown by the red histogram. The systematic uncertainty is shown by the red shaded region. The simulated neutrino energy distribution assuming maximal mixing is shown by the dotted green histogram for comparison. The combined background due to the beam and cosmic ray backgrounds is shown by the dashed blue histogram. Figure taken from [41].

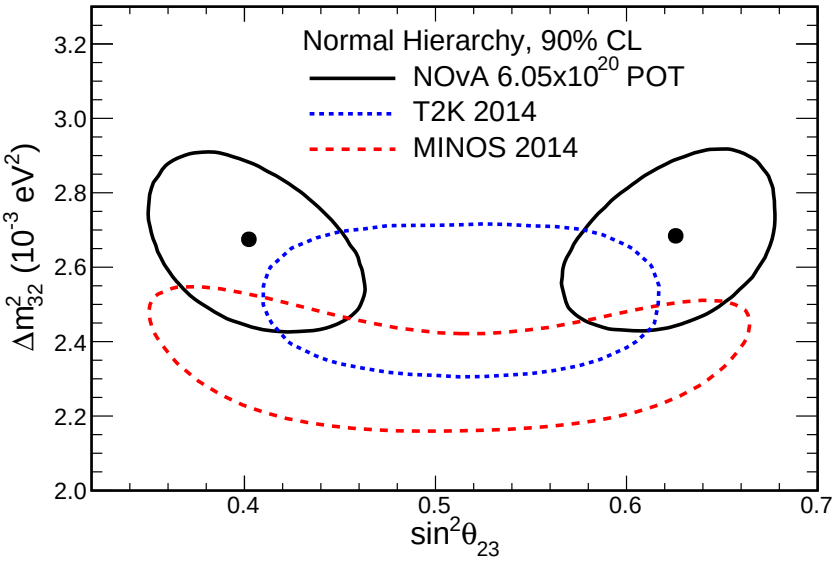

Figure 2.12: Contours showing the 90% confidence limits in the Δm^2_{32} vs. $\sin^2\theta_{23}$ plane. The black, dotted blue and dashed red lines show the measured 90% C.L. contours for the NOvA, T2K and MINOS experiments respectively. Figure taken from [41].

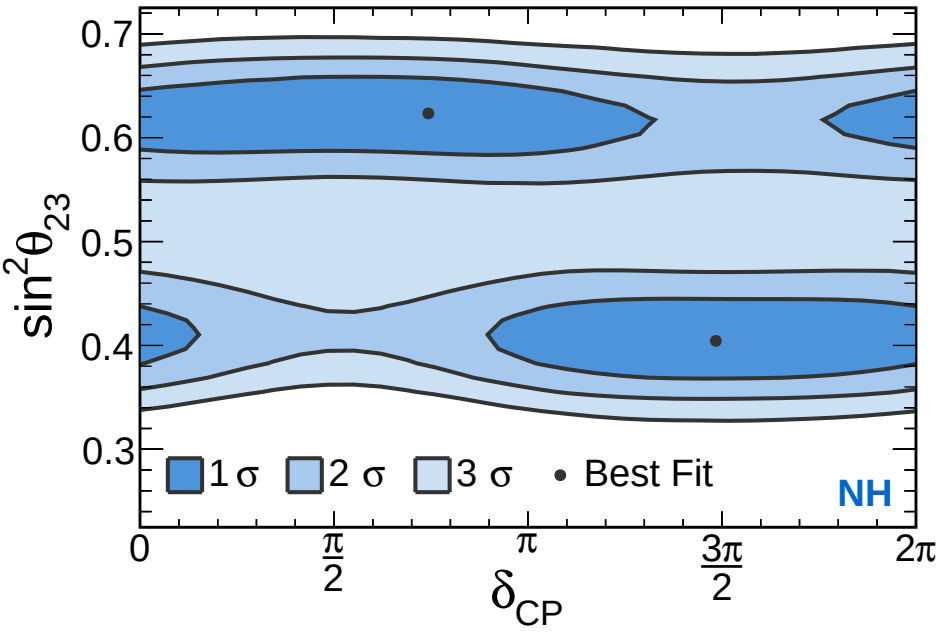

(a) Normal mass ordering.

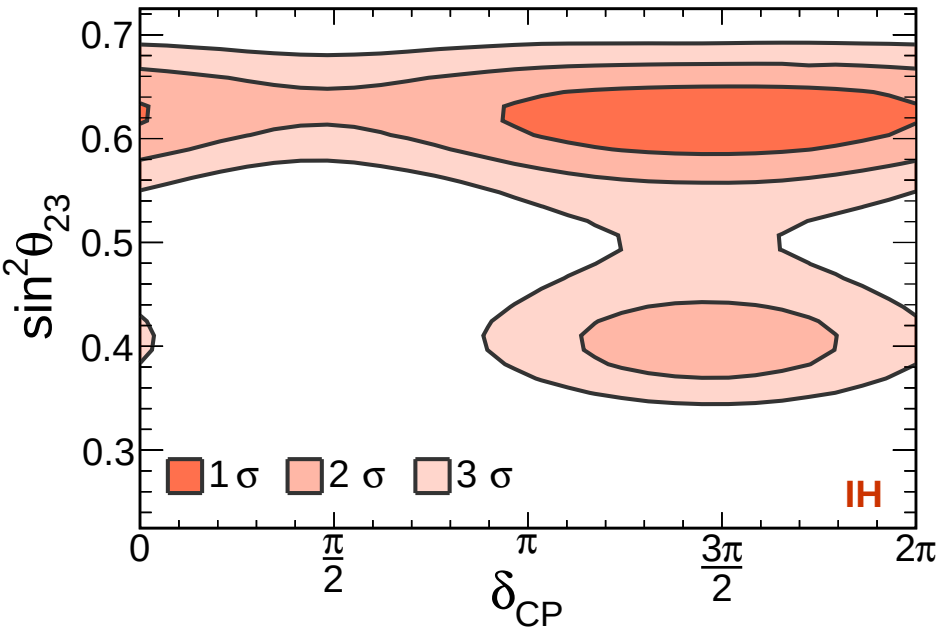

(b) Inverted mass ordering.

Figure 2.13: Confidence limit result contours, in δ_{CP} vs. $\sin^2\theta_{23}$ parameter space, found using a fit to the measured electron neutrino appearance and muon neutrino disappearance data. The confidence with which each combination of parameters in the space is allowed is indicated by the intensity of the colour. Figure taken from [42].

Chapter 3

The NOvA Experiment

The NuMI Off-axis ν_e Appearance (NOvA) experiment is designed to make precise measurements of muon neutrino disappearance and electron neutrino appearance in a muon neutrino beam. The experiment consists of two functionally equivalent detectors which measure the neutrino energy and flavour composition of the Neutrinos at the Main Injector (NuMI) beam. The detectors are constructed from PVC tubes filled with liquid scintillator and are highly granular to distinguish neutrino induced signals and background. The 300 tonne near detector is located on site at Fermilab 1.015 km from the NuMI target. The 14 kilo-tonne far detector is located at a site near Ash River, Minnesota and is 810 km from the NuMI target. The baseline and mean neutrino energy are chosen such that the far detector sees the first oscillation maximum driven by Δm^2_{32}. Both detectors are placed off-axis from the centre of the NuMI beam to enhance the sensitivity to electron neutrino appearance and muon neutrino disappearance.

The original design of the NOvA experiment is laid out in the technical design report (TDR) [43] and the constructed experiment design differs only slightly. The details of the constructed experiment, including the neutrino beam source and the two detectors, are discussed in the following chapter.

3.1 The NuMI Beam

The NOvA experiment's neutrino source is the Neutrinos at the Main Injector (NuMI) beam at Fermilab. The following section briefly describes the process by which the NuMI beam is created. More details are available in Ref [44].

The NuMI beam-line extracts batches of approximately 4.8×10^{13} 120 GeV protons from the Main injector and directs them onto a 0.95 m long graphite target. Each extrac-

tion of protons is known as a beam spill. There is typically an interval of 1.33 s between 10 μs beam spills.

A schematic of the NuMI beam facility is presented in Figure 3.1, which shows the beam components including the target hall, decay pipe, hadron monitor, absorber and muon monitors. Within the target hall, collisions between the accelerated protons and the carbon atoms of the target produce a plethora of secondary particles (mostly pions and kaons). The charged mesons of one sign (or the other) are focused into a beam by two magnetic focussing horns. The resulting beam of charged mesons then enters the 675 m long helium filled decay pipe. Along this length the mesons decay predominantly to charged leptons and neutrinos. The decay pipe is followed by the hadron monitor, the absorber, muon monitors and about 240 m of rock. The remaining muons are absorbed by the rock leaving a beam of neutrinos. After the rock, the beam arrives at the NOvA near detector before continuing through the Earth's crust for 810 km where it reaches the NOvA far detector.

3.1.1 Focusing Horns

Two magnetic horns are used to focus the mesons created by collisions of protons with the NuMI target into a beam. Figure 3.2 shows the NuMI target, horn 1, horn 2 and example meson trajectories. The design of the focusing horns allows different separations between the target, horn 1 and horn 2 to tune the energy of the beam. For NOvA the target is placed 1.3 m upstream from the opening of horn 1 while horn 2 is placed 23 m downstream relative to the front face of horn 1. This is known as the "medium" energy configuration.

The horns act as a lens where the focal length is proportional to the momentum of the mesons. Changing the current direction within the focusing horns, choosing either forward or reverse horn current, changes the direction of the magnetic field and therefore the sign of the mesons that are focused. Operating the horns with forward or reverse horn current selects positively or negatively charged mesons respectively, leading to a predominantly neutrino or antineutrino beam respectively.

3.1.2 Off-axis Experiment Design

The NOvA detectors are both placed 14 mrads off the axis of the NuMI beam. The dominant decay process used to produce a neutrino beam is a two-body decay, where a pion (or kaon) decays to a neutrino and a muon. The two body decay of a pseudo-scalar

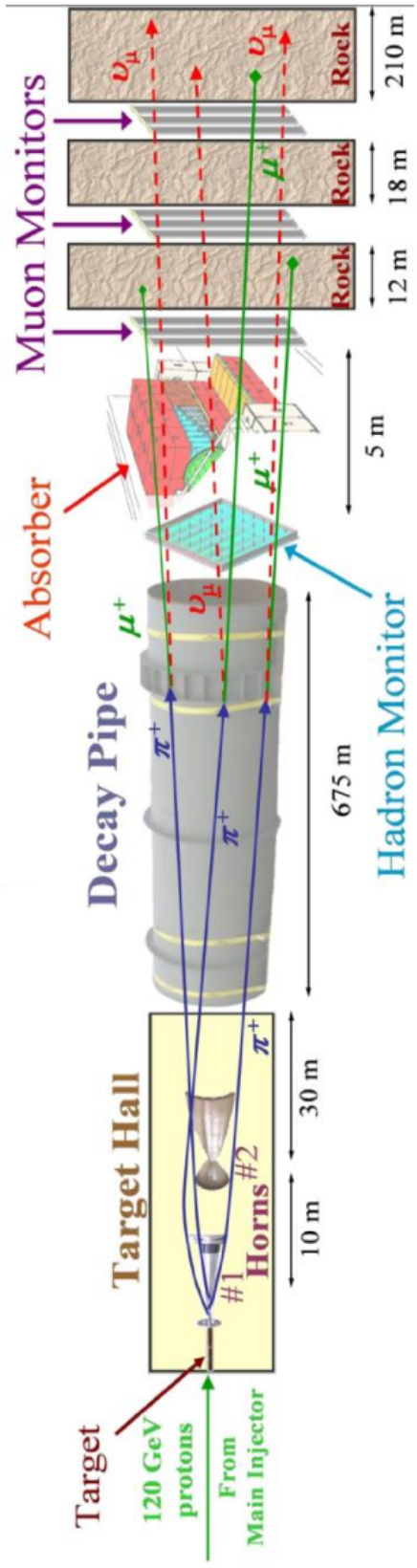

Figure 3.1: A diagram showing the layout of the NuMI beam. [44]

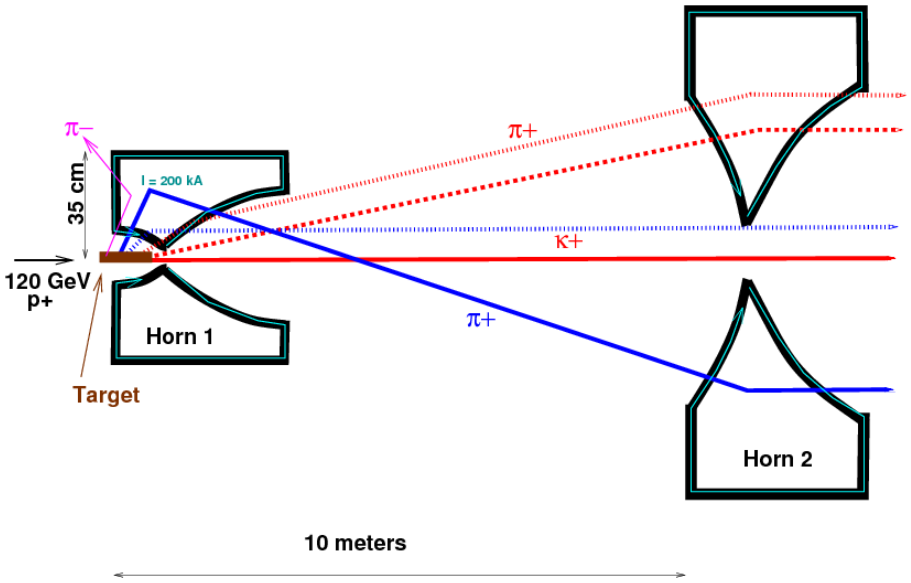

Figure 3.2: A diagram of the magnetic focusing horns operating in forward horn current mode. Positively charged mesons arriving from different directions are focused by the combination of the two horns. The trajectory of positively charged mesons that are over or under focused by horn 1 can be corrected by horn 2. Diagram taken from [44].

meson occurs isotropically in the parent particle's rest frame. In the lab frame the parent particle is not at rest when decaying; for pion and kaon decay this boosts the neutrinos in the direction of the parent particle. For small angles, the flux per decay (Φ) and energy (E_ν) of neutrinos produced by pion decay ($\pi \to \nu_\mu + \mu$) are given by

$$\Phi = \left(\frac{2\gamma}{1+\gamma^2\theta^2}\right)^2 \frac{A}{4\pi z^2}, \tag{3.1}$$

$$E_\nu = \frac{0.43 E_\pi}{1+\gamma^2\theta^2}, \tag{3.2}$$

where E_π is the energy of the parent pion, m_π the mass of the parent pion, $\gamma = E_\pi/m_\pi$, θ the angle between the parent pion and outgoing neutrino directions, A is the cross-sectional area and z is the distance from the pion decay vertex.

Equations 3.1 and 3.2 are shown as functions of pion energy for the medium energy NuMI beam configuration in Figure 3.3. The Figure also shows the effect of four off-axis angles ($\theta = 21$ mrads, $\theta = 14$ mrads, $\theta = 7$ mrads and $\theta = 0$ mrads).

Figure 3.4 shows the number of charged current neutrino events as a function of neutrino energy for the low (Figure 3.4a) and medium (Figure 3.4b) energy beam configuration for various off-axis angles. The plots show that as the off-axis angle is increased the mean and width of the energy distribution decreases.

For the medium energy beam configuration, figure 3.3b shows that at 14 mrad the neutrino energy does not have a strong dependence on the parent pion energy. In addition, figure 3.4b shows that at 14 mrad the medium energy beam configuration produces a narrow energy neutrino beam with approximately 4 times more neutrinos at 2 GeV than the on-axis scenario. This peak at 2 GeV is well matched to the first oscillation maximum which is expected to occur at about 1.6 GeV for NOvA's experiment baseline and for $\Delta m^2_{32} = 2.4 \times 10^{-3}$ eV^2.

As described above, placing the detector off-axis increases the flux at the expected oscillation maximum. In addition, the narrow energy range of the off-axis beam reduces background events. Neutral current, NC, events are an important background source for both the ν_e appearance and ν_μ disappearance analyses. In particular, the topologies of NC events can be hard to distinguish from electron showers produced by ν_e charged current events. For neutral current events, the neutrino carries a significant amount of the energy away and the energy visible within the detector tends to "feed down" to lower energies. For a narrow band off-axis beam, this "feed down" tends to shift the neutral current events towards lower energies outside the ν_e appearance signal energy window. Figure 3.5 shows the number of ν_μ, ν_e and neutral current events as a function of visible energy. The bulk of the neutral current events (black histogram) are shown to shift below the signal region (red-hatched histogram).

The combination of reducing beam backgrounds and increasing the neutrino flux at the oscillation maximum means that placing the NOvA detectors at the off-axis angle of 14 mrads enhances the sensitivity to oscillations driven by Δm^2_{32}.

3.2 The NOvA Detectors

The NOvA collaboration performs measurements of both ν_μ disappearance and ν_e appearance and the NOvA detectors are designed to be able to identify the muons and electrons produced in charged-current neutrino interactions. The ν_e appearance analysis has the potential to be overrun with neutral current background events. A large source of background comes from π^0s produced in neutral current events, which can fake an electron shower. The NOvA detectors are constructed from low Z materials (primarily carbon) to aid in the distinction between neutrino interactions and backgrounds. The constructed detectors have a radiation length [20] of approximately 40 cm which is equivalent to the depth (width) of 7 (10) NOvA cells and the Moliere radius [20] (characteristic scale in the transverse dimension of fully contained electromagnetic showers) is equivalent to the

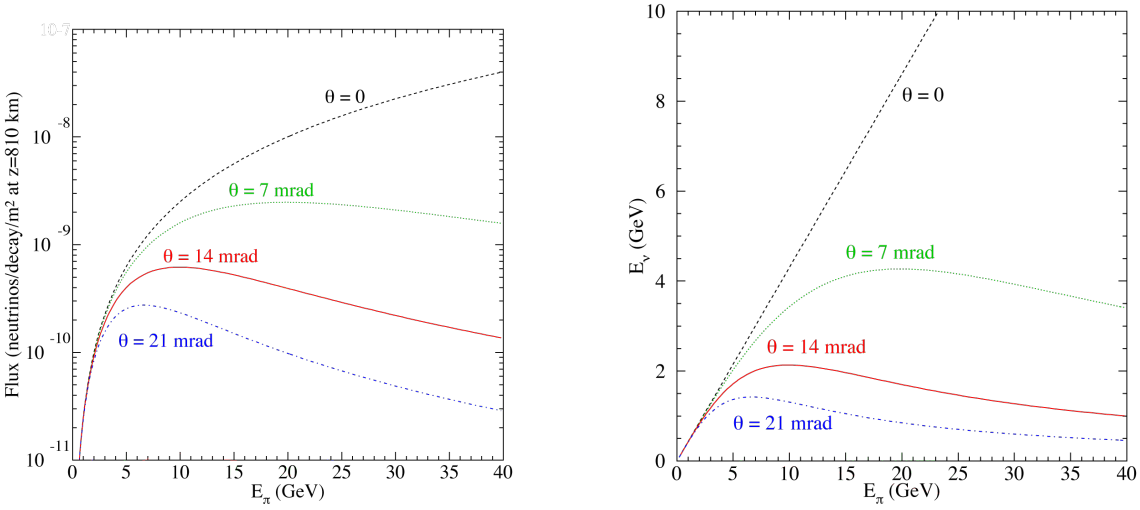

(a) Neutrino flux vs. pion energy.

(b) Neutrino energy vs. pion energy.

Figure 3.3: The above distributions are for the medium energy tune NuMI beam as viewed from a site located 800 km from the NuMI target and off-axis by an angle θ. The left plot shows the neutrino flux as a function of the energy of the parent pion for different off-axis angles. The right plot shows the neutrino energy as a function of the parent pion energy for different off-axis angles. Diagram taken from [43].

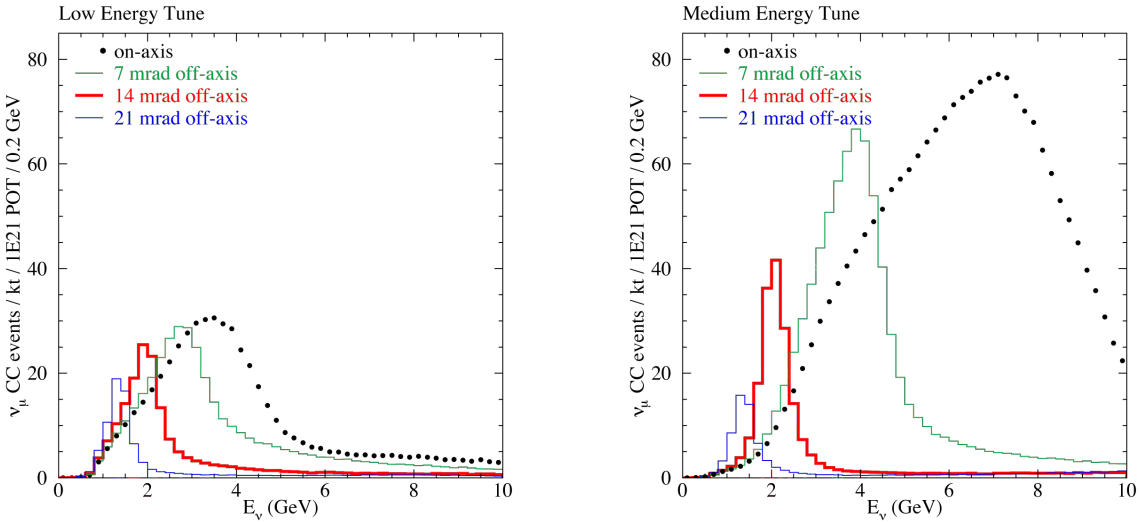

(a) Low energy beam configuration neutrino energy.

(b) Medium energy beam configuration neutrino energy.

Figure 3.4: Charged current ν_μ event rates vs. neutrino energy in the absence of oscillations. The distributions are found for a detector which is 800 km from the NuMI target and for various off-axis angles. Diagram taken from [43].

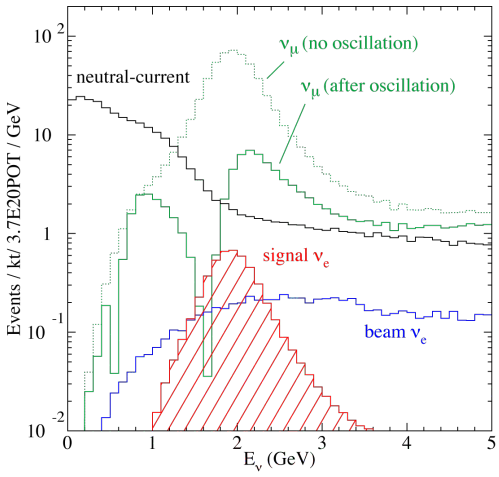

Figure 3.5: Simulated visible energy distributions for ν_μ charged current events with and without oscillations, ν_e oscillation signal events, intrinsic beam ν_e events and neutral current events. The simulation assumes an off-axis position of 12 km at 810 km, $\Delta m^2 = 2.5 \times 10^{-3}$ eV^2, $\sin^2(2\theta_{23}) = 1.0$ and $\sin^2(2\theta_{13}) = 0.1$. Diagram taken from [43].

width of approximately 2 NOvA cells. which means electron showers have sufficient width to be distinguished from muons, charged pions and protons which show up in the detector as non-showering particle tracks.

A diagram of the two detectors is shown in Figure 3.6. The near and far NOvA detectors are functionally identical. Besides the different masses, there are a few physical differences between the two detectors which account for the proximity to the NuMI beam and the depth of the detector relative to ground level. In particular, the smaller near detector has a so called "muon catcher" and has a higher electronic sampling rate. The near detector is 100 m underground and the far detector is constructed on the surface. The construction common among both detectors will be discussed in the following sub-sections. The details specific to the far and near detectors will be discussed in sub-sections 3.2.7 and 3.2.8 respectively.

3.2.1 The Basic NOvA Detector Element

The basic unit of the NOvA detectors is a rectangular rigid PVC (polyvinyl chloride) cell which contains liquid scintillator and a wavelength-shifting fibre. Figure 3.7 shows the NOvA cell, looped wavelength-shifting fibre and an example charged particle. The wavelength-shifting fibre, which is twice the length of the cell, is looped at the bottom of the cell such that the captured light travels in two directions to the instrumented top end of the cell. Both ends of the looped fibre are directed onto one pixel of an Avalanche

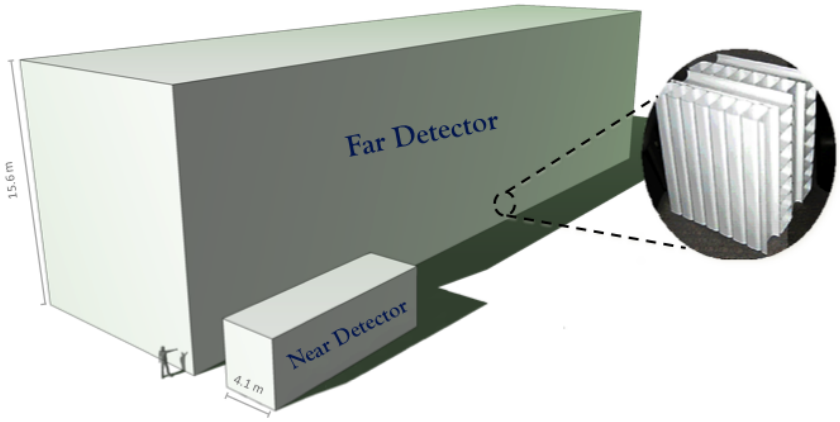

Figure 3.6: Scaled depiction of the near and far NOvA detectors with respect to the average person. The alternating alignment of the NOvA cells is shown by the inset on the right hand side.

Photo Diode (APD) array. The APD converts the light from the fibre into an electronic signal.

The cells have 2 to 4.5 mm thick walls, an interior depth of 5.9 cm along the beam direction and an interior width of 3.8 cm transverse to the beam direction. The thickness of the cell walls varies due to structural considerations. The length of the cells differs between the two detectors, the far detector cells have a length of 15.5 m, whilst the near detector cells are typically 3.6 m long.

3.2.2 Liquid Scintillator

Approximately 65% of the NOvA detector mass is composed of the liquid scintillator held within the cells. The composition of the liquid scintillator is detailed in Table 3.1, which shows that the scintillator is composed mainly of mineral oil along with 5.23% (by mass) pseudocumene as the scintillant. The scintillant emits scintillation light with a spectrum peaked between 360 - 390 nm. Wavelength shifting chemical additives PPO and bis-MSB are added to shift the initial light spectrum to 400 - 450 nm to match the absorption spectrum of the wavelength-shifting fibre.

3.2.3 Wavelength Shifting Fibre

The wavelength-shifting fibre has a diameter of 0.7 mm and a core of polystyrene mixed with R27 dye (as the wavelength shifter) at a concentration of 300 ppm. The fibre has two coatings (contributing about 3% of the fibre diameter) of materials with a lower refractive

Component	Purpose	Mass fraction %
mineral oil	solvent	94.63
pseudocumene	scintillant	5.23
PPO	waveshifter	0.14
bis-MSB	waveshifter	0.0016
stadis-425	anti-static agent	0.0010
tocopherol	antioxidant	0.0010

Table 3.1: Chemical composition of the NOvA liquid scintillator [45].

index than the core which facilitates total internal reflection within the fibre. The fibre is first coated with a thin acrylic layer of PMMA and second with fluor-acrylic.

The 400 - 450 nm light emitted by the liquid scintillator is absorbed by the fibre and then wavelength shifted to 490 - 550 nm. As light travels down the fibre it is attenuated, by a factor of up to about 10 in the far detector, with light in the range 520 - 550 nm preferentially surviving.

3.2.4 Avalanche Photo Diode

The light exiting the fibre ends is detected by an Avalanche Photodiode (APD) and converted into an electronic signal pulse. Figure 3.8 shows a photograph of a NOvA APD containing an array of 32 pixels. Each APD pixel is interfaced with both ends of a single wavelength-shifting fibre, and each APD is connected to a front end board that prepares the signals from the APD for the data acquisition system.

The NOvA APD was chosen because it has an 85% quantum efficiency for the 520 - 550 nm light exiting the fibre ends. The thermal noise generated by each APD is reduced by thermo-electric coolers, which cool the APDs to -15^{o}C.

3.2.5 Data Acquisition System

NOvA's data acquisition system continuously reads out all the information from the APDs. The far detector APDs sample each channel every 500 ns. Differences in the APD sampling rate between the two detectors will be discussed in Section 3.2.8. The information is temporarily stored in a buffer farm and awaits a decision as to whether it should be permanently recorded or rejected. The decision can be made by either online triggering algorithms or by receiving a trigger signal from an external source. The NuMI beam spill signal is an example of an external source trigger.

Each APD is continuously readout by a front end board, which handles the pedestal subtraction and pulse shaping for each signal from the APD. The pedestals are determined for each APD pixel by measuring the baseline noise level. The signal pulses are shaped with a characteristic rise and fall time. When a signal is triggered, the signal sample is read out along with the three immediately preceding samples in a process called "multi-point readout". Once the data is permanently recorded, the known pulse shaping parameters are used to fit the four samples and provide more precise timing resolution. Details of the readout specific to each detector or further described in Section 3.2.8.

The front end board transmits the digitised data to a data concentrator module, which can take inputs from up to 64 front end boards. Each data concentrator module periodically collects all the information from the connected front end boards during a 50 μs window ("microslice"). This data packet is then sent to and stored in the buffer farm until online trigger processes decide whether to record or reject the data.

3.2.6 Detector Assembly

The NOvA detectors are constructed from the cells described in Section 3.2.1, where 16 cells are extruded together in one unit to form an extrusion. Figure 3.9 shows the end-on view of an extrusion with a width of 63.5 cm and depth of 6.6 cm. Two extrusions are placed side by side to form an extrusion module consisting of 32 cells. Figure 3.10 shows an extrusion module consisting of 32 cells, end plate, side seal, manifold cover, snout and electronics box. The module ends are capped by the end plate so that the modules can contain the liquid scintillator. The other end is capped by a manifold cover which contains the liquid scintillator in the horizontal cells and directs the 32 fibre end pairs to the 32 APD pixels in the NOvA APD.

Flat planes of cells are constructed from multiple modules glued together side by side. Figure 3.11 shows a cross-section of multiple plane layers. The planes are layered with alternating orthogonal orientations of the cells making up the plane. This orthogonal orientation of the planes allows for three dimensional reconstruction of tracks passing through multiple planes. Planes are glued together in the orthogonal arrangement described above to form one solid detector piece called a block, consisting of 32 or 24 planes in the far detector or near detector respectively.

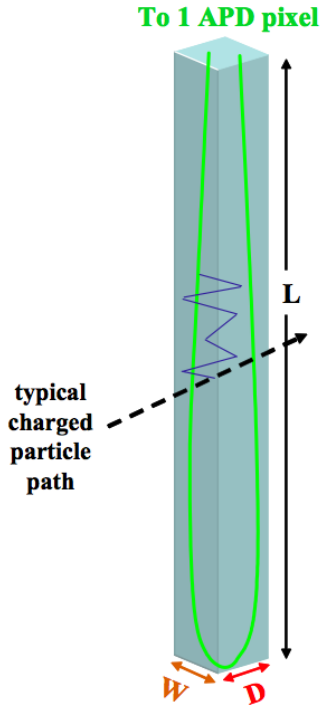

Figure 3.7: A NOvA cell consisting of an extruded PVC tube filled with liquid scintillator and a looped wavelength-shifting fibre. Taken from [43].

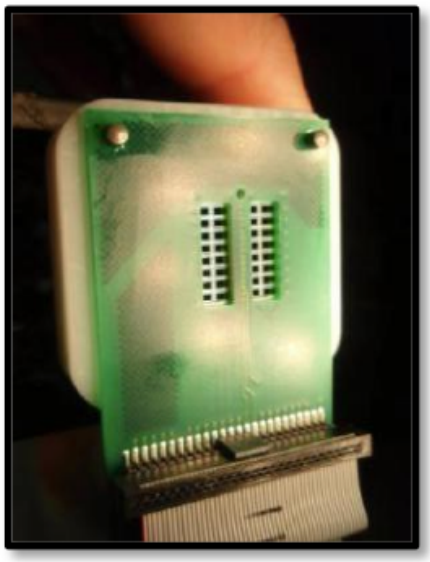

Figure 3.8: The NOvA APD containing an array of 32 pixels.

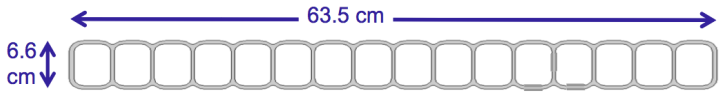

Figure 3.9: An end on view of an extrusion consisting of 16 NOvA cells. Taken from [43].

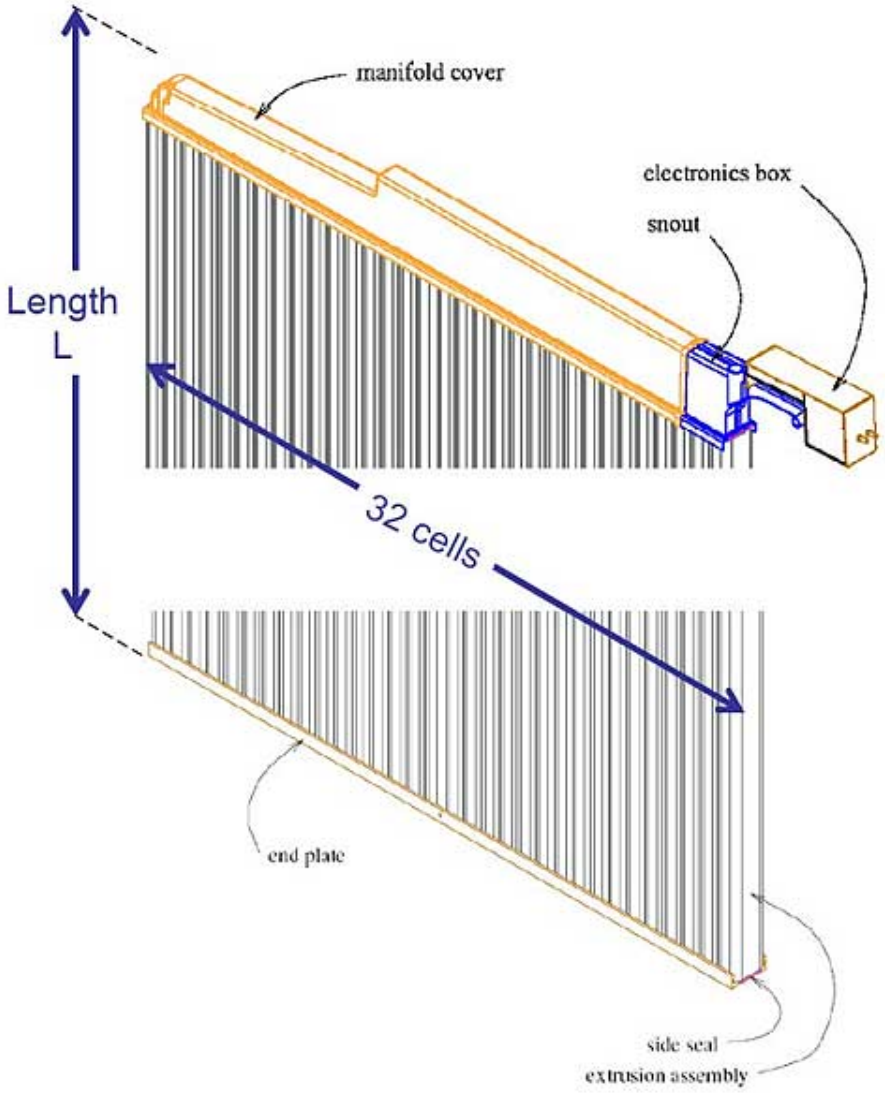

Figure 3.10: A side on view of an extrusion module constructed from two extrusions of 16 cells, an end plate, a side seal, a manifold cover, a snout and an electronics box. Taken from [43].

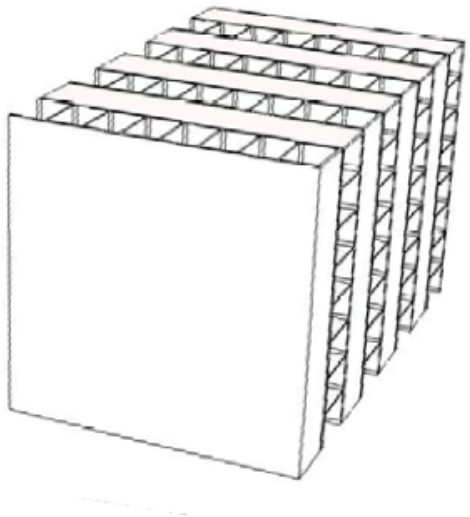

Figure 3.11: A cross section of the NOvA detector showing the alternating orientation of the cells within the stacked planes. Taken from [43].

3.2.7 The Far Detector

The 14 ktonne far detector is located 810 km from the NuMI target, approximately 10 m below ground level and at an elevation of 372 m above sea-level. The neutrino beam enters the detector travelling at an angle of 3^o upwards. The detector is constructed, as described in Section 3.2.6, from 344,064 15.5 m long cells which form 896 planes normal to the beam direction. The detector mass is approximately 65% liquid scintillator and 35% PVC.

As described above, the far detector is built on the surface above sea level so cosmic rays will be a major source of background events. The background due to cosmic rays is mitigated using selection cuts and a shielding overburden above the detector. For the ν_μ disappearance analysis, the background is primarily due to cosmic ray muons which are almost entirely removed using cuts. For the ν_e appearance analysis, the background is primary cosmic ray photons whose interactions within the detector can be mistaken for an electron shower. During a six year run the far detector, without overburden shielding, will see approximately 1600 background events due to cosmic ray photons. In order to reduce this background source to less than one event requires approximately 9 radiation lengths of material above the detector surface. Additional radiation lengths will then help to contain any showers caused by interactions within the overburden. With this in mind, the far detector building was constructed with a 122 cm thick concrete enclosure which supports a 15 cm thick overburden of barite. Together, the concrete enclosure and barite overburden provide 12 radiation lengths of shielding.

3.2.8 The Near Detector

The NOvA near detector is located on site at Fermilab next to the MINOS hall. Figure 3.12 is a diagram of the MINOS hall area showing the MINOS shaft, NuMI beam-line, MINOS hall, 14.6 mrad off-axis beam and the NOvA Near Detector cavern. The near detector is 105 m underground and 1.015 km from the NuMI target. The near detector therefore sees a higher flux of NuMI neutrino events and a lower flux of cosmic rays than the far detector. The neutrino beam enters the detector travelling downwards at an angle of 3^o.

A diagram of the near detector is shown in Figure 3.13. The Figure shows the NOvA Near Detector cavern, access catwalks, and the fully active detector and muon catcher detector sections. The detector is constructed in a similar fashion to the far detector with 20,192 cells arranged in 214 planes, each plane is comprised of 3 extrusion modules (except in the muon catcher). The detector has a width and height (except in the muon catcher) of 4.2 m and a length of 15.8 m. The near detector is functionally equivalent to the far detector with the exception of two distinguishing features.

First, a muon catcher is placed at the downstream end of the near detector in order to help range out muons from few GeV charged current ν_μ interactions which would not otherwise stop within the detector. The muon catcher is constructed from layers of steel and liquid scintillator planes. The steel planes are 10 cm thick and are separated by two (one horizontal and one vertically aligned) scintillator planes. The vertical planes consist of three extrusion modules while the horizontal planes are made from just two extrusion modules. Therefore, the sets of steel and scintillator planes are three extrusion modules wide (the same as the rest of the detector) but only two extrusion modules high. Ten of these steel and liquid scintillator plane sets are stacked to form the muon catcher.

Second, the near detector electronics are setup to sample each channel (APD pixel) four times more frequently (every 125 ns) than in the far detector to help handle the data pileup. The near detector sees approximately 5-10 neutrino interactions per beam spill (10 μs window) while the far detector sees approximately 60-70 cosmic rays per 550 μs window spread out over approximately 17 times more channels. The faster sampling rate improves the timing resolution of hits in the detector. With better timing resolution, pileup events are more easily distinguished from one another.

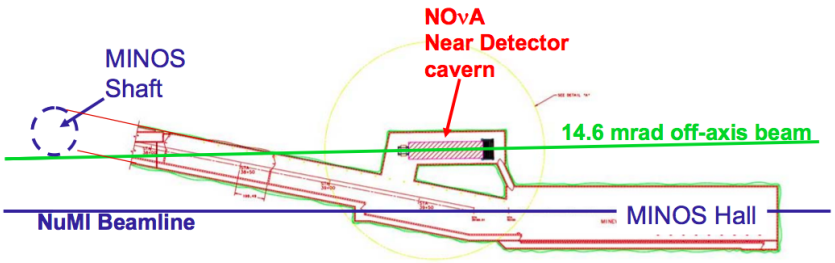

Figure 3.12: Bird's-eye view diagram of the NuMI Beam-line, MINOS Hall, MINOS shaft and the NOvA near detector cavern. Figure taken from [44].

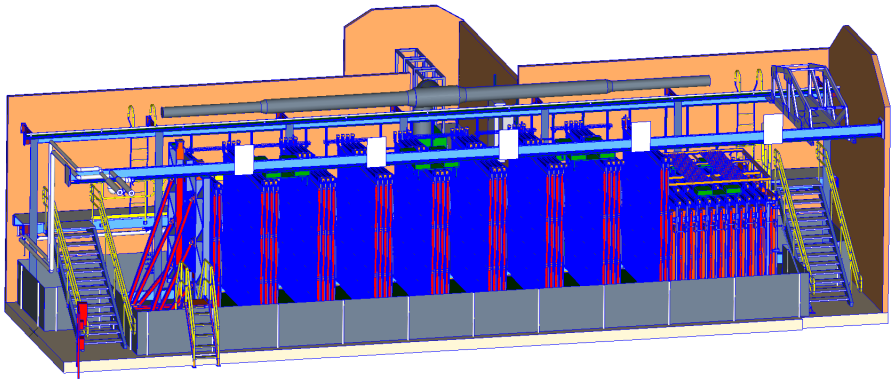

Figure 3.13: Technical drawing of the NOvA near detector and cavern. The NuMI beam enters from the left. The muon catcher planes are shown on the right hand side of the detector. Note that only some of the planes have been drawn to aid visualisation of the detector layout.

3.3 Neutrino Interactions in the NOvA Detectors

In the energy range of the neutrino beam measured by NOvA there are three main types of neutrino interaction: deep inelastic scattering (DIS), quasielastic (QE) scattering and resonance (RES) scattering. These interactions occur via the exchange of either a W boson for charged current interactions or a Z boson for neutral current interactions.

Figure 3.14 shows the charged current neutrino cross section vs. energy. The figure shows the total cross section and the contribution to the cross section from QE, DIS and RES interactions. These interaction types are described as follows:

- In quasielastic scattering interactions the neutrino scatters off a target nucleon, and as a result the nucleon is usually liberated from the nucleus. Charged current QE neutrino interactions can be described as: $\nu_l + n \rightarrow l^- + p$, where l is the lepton flavour, n is a neutron and p is a proton.

- In resonance scattering interactions the incoming neutrino excites the target nucleon to a resonance state: $\nu_l + N \rightarrow l + R$, where N is the target nucleon and R is the resonance state. This resonance then quickly decays, producing combinations of mesons and nucleons.

- In deep inelastic scattering, the incoming neutrino has enough energy to resolve the individual quarks: $\nu_l + N \rightarrow l + X$, where X is the hadronic shower. The interaction with the individual quark produces a hadronic shower.

3.3.1 Backgrounds

There are three beam-induced backgrounds to the disappearance analysis: neutral current, tau neutrino and electron neutrino events. All three background types interact with matter as described above (3.3), with the exceptions of neutral current events where the outgoing lepton remains the same as the incoming neutrino, and tau neutrino interactions which only occur when the neutrino energy is above the threshold energy of 3.5 GeV.

For the case of the NOvA oscillation analysis the neutral current events are considered a background as there is no way of discerning the flavour of the incoming neutrino. In the muon neutrino disappearance analysis the neutral current events are identified by the absence of an outgoing muon from the interaction vertex. However sometimes a neutral current (NC) interaction is mistaken for a charged current (CC) interaction if, for example, the outgoing proton or pion is mistaken for a charged lepton.

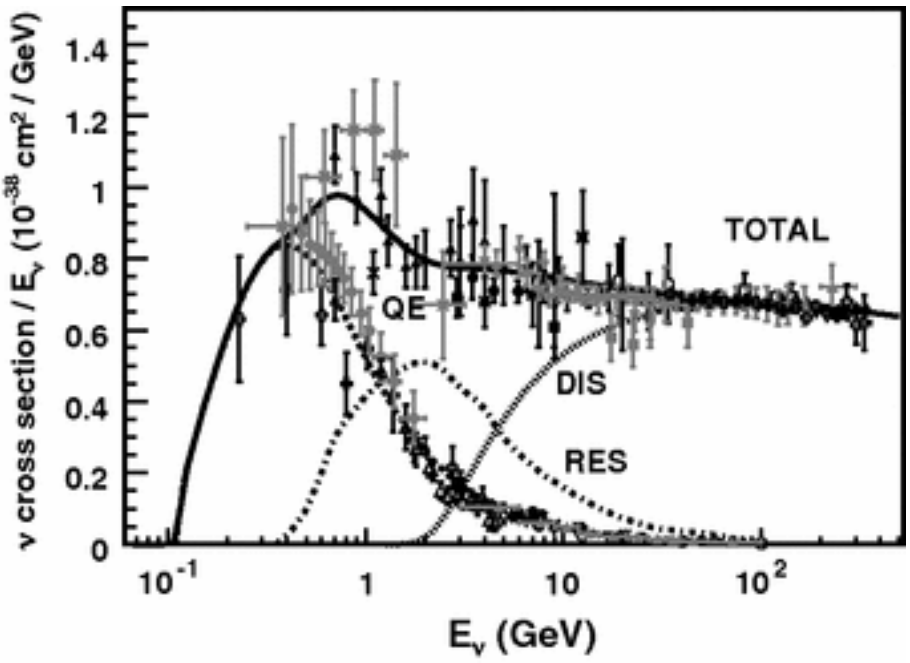

Figure 3.14: Neutrino charged-current cross section vs. neutrino energy. The three main contributing interaction processes are shown. These interactions are: quasielastic (QE), resonance (RES) and deep inelastic scattering (DIS). Figure taken from [46].

The final source of backgrounds is due to cosmic ray particles interacting within the detector. Most of these events are easily deselected by requiring that events are fully contained within the detectors. The methods used to remove the background events from the analysis are discussed in Section 4.3.

3.4 Monte Carlo Simulation

The NOvA experiment is simulated using several Monte Carlo packages. The simulation involves several stages, each using information from the previous step. The simulations model the NuMI beam, subsequent neutrino interactions within the detectors, the propagation of particles through the detector geometry, and the detector response to those particles.

The production and propagation of the NuMI beam is simulated using FLUKA and Geant4 through the FLUGG interface [47, 48, 49]. The beam simulation produces flux files containing simulated neutrinos with given flavour, energy and direction. Details of each neutrino's parent are retained in the flux files.

Neutrino interactions within the detector are simulated with GENIE [50] using the flux files as input. GENIE must decide whether each neutrino interacts within the de-

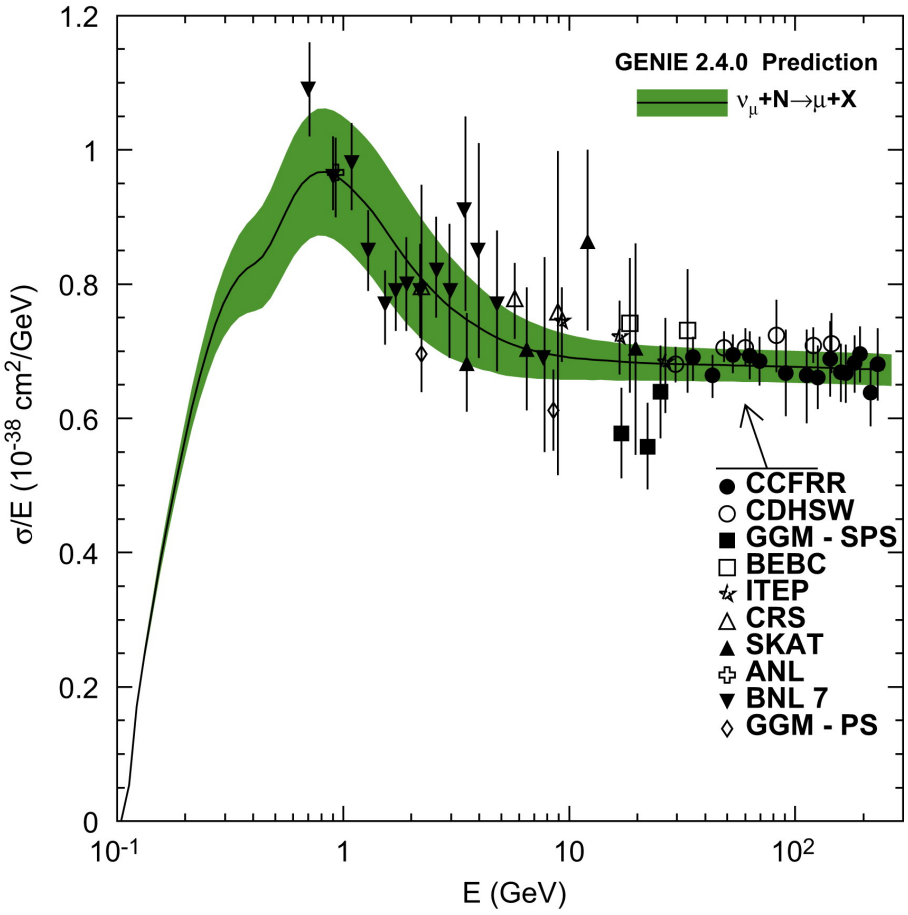

Figure 3.15: Default cross section in GENIE for ν_μ charged current scattering with an isoscalar target. The shaded green band shows the estimated uncertainty on the free nucleon cross section. [50]

tector, the type of interaction, the kinematics of the interaction and the location of the interaction vertex. GENIE uses information regarding interaction cross sections and detector geometry to probabilistically determine whether each neutrino interacts within the detector. Figure 3.15 shows the default ν_μ charged current cross section as a function of neutrino energy used in GENIE. The black data points show the results of experimental measurements, the black curve shows the fit of theory to the data and the green shaded band shows the estimated uncertainty. Note that there is no data recorded below 700 MeV. After an initial simulated neutrino interaction the propagation of the resulting primary particles through the nucleus, including inter-nuclear scattering and absorption, is also simulated by GENIE. Cosmic ray generation in the atmosphere well above the detector is simulated using CRY [51].

Geant4 is used to simulate propagation and energy deposition within the detector of the particles produced by GENIE or CRY. Interactions of the primary particles within the

detector and the resulting secondary particles are also simulated. The resulting energy depositions within the detector's liquid scintillator are stored and are known as Fibre Liquid Scintillator Hits (FLSHits).

Two NOvA specific software modules are used to simulate the response of the NOvA detectors to energy depositions. The first module simulates the processes from energy depositions in a NOvA cell to photons arriving at the APD. The final APD signal is a combination of the photons arriving at the APD and the APDs modelled response to noise. The second module simulates the response of the front end boards to the APD signals.

3.4.1 Modifications to the Simulation

Recently other experiments [52] have presented evidence suggesting an additional process, known as two-particle two-hole (2p2h), contributing to the neutrino interaction event rate. In this additional interaction neutrinos scatter from nucleon pairs within the nucleus via a meson exchange current (MEC) between the nucleons. The model was initially motivated by observations in electron on nucleus scattering [53]. NOvA's near detector data provides supporting evidence for an additional process [54] as shown by Figure 3.16 where there is an excess in data below $E_{had.} = 0.2$ GeV. For NOvA's 2017 [41] analysis the GENIE simulation was adjusted to include a semi-empirical model of the so called 2p2h process.

A reanalysis of the bubble chamber data [55] suggests that the rate of ν_μ charged current non-resonant single pion production (via the process: $\nu_l + X \rightarrow l + X' + \pi$) in GENIE should be reduced by 50%. This reweight is used for the analysis presented in this thesis. This process is a sub-category of the DIS events described in section 3.3.

3.4.2 Matching Running Conditions in Simulation

For this thesis, the data taken by the NOvA detectors is split into three running periods: period 1, period 2 and period 3. The far detector was constructed in a modular fashion, diblocks were installed and instrumented before adding the next diblock. During period 1 the far detector was under construction, data taking occurred using the semi instrumented detector whilst the remaining diblocks were installed. In addition, for period 1 only, single point timing was used to digitise the data read out from the APDs in the far detector. For all other periods and for the near detector multipoint readout is used which provides better resolution of the hit time and reduces the contribution of noise hits to the calorimetric energy. From period 3 onwards the far detector was operated in high gain mode, where the gain was increased from 100 to 150. The gain was increased to reduce the energy

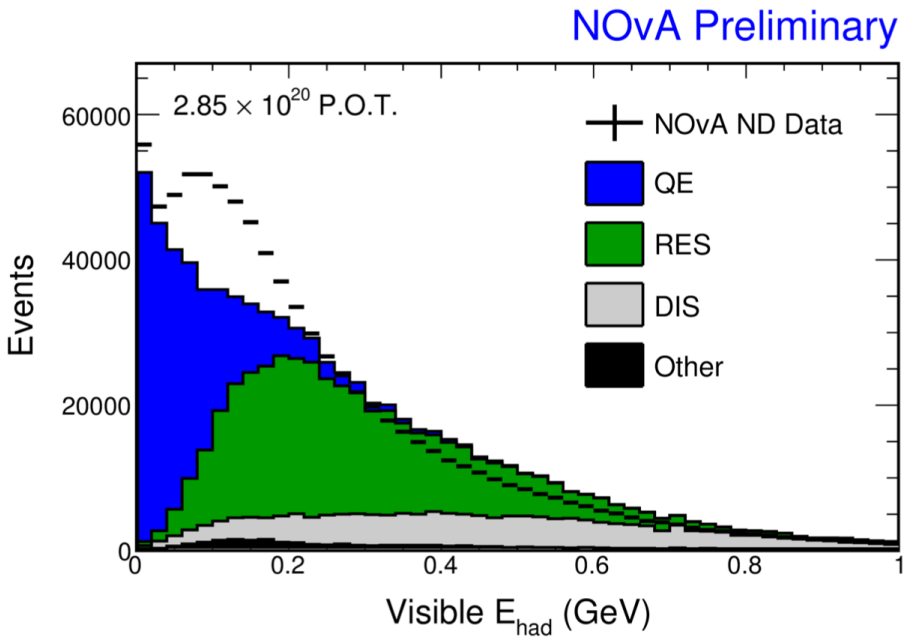

Figure 3.16: Visible hadronic energy of events selected in the first disappearance analysis. The contribution to the simulated distribution from each of the three main interaction types is shown by the stacked histograms and the data is shown by the black points. Figure taken from [54].

threshold in the far detector, particularly at the far end of the cells.

These changes in the running conditions of the detectors are taken into account in the simulation.

Chapter 4

NOvA Analysis Methodology and Systematic Uncertainties

This chapter presents an overview of the methodology used to produce the 2017 muon neutrino disappearance analysis [41]. The methodology represents the event reconstruction and analysis chain starting with raw detector hits and ending with the sensitivity and result contours. Particular focus is given to components of the analysis chain for which the author made a significant contribution. The internal NOvA summary document [56] and the associated paper [41] for the 2017 disappearance analysis are used as references throughout.

4.1 Analysis Software

The analysis presented in this thesis was performed using NOvA's Common Analysis Format Analysis [57] (CAFAna) software framework which provides a set of classes to enable easy plotting and fitting of oscillated neutrino energy spectra. To speed up analysis everything in CAFAna is histogram based. Files containing individual events are read once to produce the required histograms and all further analysis is done in terms of the histograms. This software framework enables a near to far detector extrapolation using the near detector data-MC comparison along with the far detector simulation, more details on the extrapolation are provided in Section 4.5. The framework also enables the application and extrapolation of systematic uncertainties using systematically shifted template spectrums. The fit to the data is performed using Minuit [58] and accounts for the systematic uncertainties using the systematic template spectrums adjusted for oscillations.

4.2 Event Reconstruction Details

The reconstruction of muon neutrino candidate events begins with a collection of above threshold APD signals. These collections of hits are clustered in space and time [59, 60] and then used to reconstruct event candidates [59]. The trajectories of charged particles within an event are reconstructed using a technique based on the Kalman filter algorithm [61, 62]. An example far detector event with tracks found using the NOvA Kalman filter is shown in Figure 4.1. Trackable particles are characterised by trajectories with long straight sections, dominated by small angle multiple scattering, and intermittent large scattering angles caused by electromagnetic or strong interactions [62]. The track finding process initially starts from the downstream end of the detector, where particles emerging from a NuMI beam neutrino interaction will (on average) be the most separated, and proceeds upstream. Track finding and fitting is performed separately in each detector view since the trajectory in each view is independent. Later the views are matched to reconstruct three dimensional tracks [62].

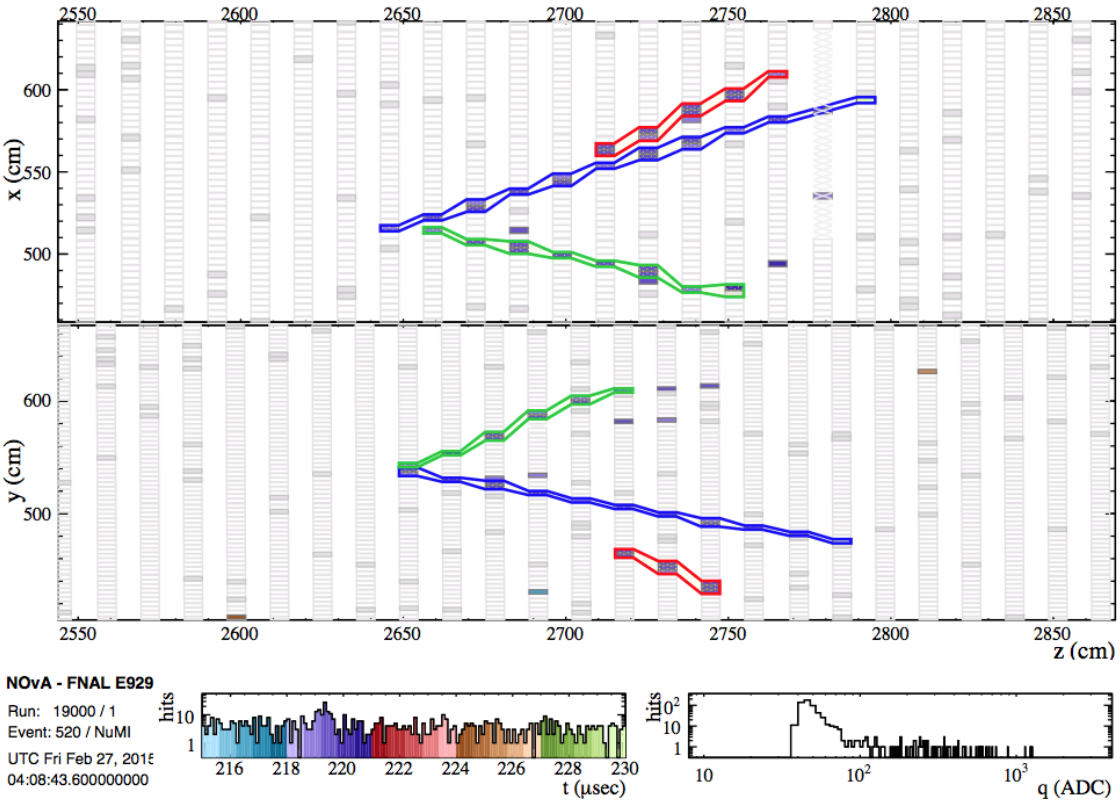

Figure 4.1: Example of reconstructed tracks found using the NOvA Kalman tracker in the far detector simulation. Individual reconstructed tracks are shown by the red, blue and green lines. The x vs. z and y vs. z positions are shown in the top and bottom half of the figure respectively. This figure was taken from NOvA's Kalman track technical note [62].

The ultimate goal of the reconstruction chain is to both identify muon neutrino charged current candidate events in the detectors (see Section 4.3 for details on the selection) and to estimate the energy of the incoming neutrino, E_ν, using the equation,

$$E_{\nu_\mu} = E_\mu + E_{had.}, \tag{4.1}$$

where E_μ is the muon energy and $E_{had.}$ is the hadronic energy which are reconstructed separately.

The muon energy is estimated with a resolution of 3.5% using the length of the track within the detector. As a consequence, the energy of muons that do not stop within the detectors cannot be estimated with the same accuracy. The hadronic energy is estimated in two steps. First, visible hadronic energy in each cell is summed up. Second, the total hadronic energy is estimated, with a resolution of 25%, from the visible energy using a visible-to-total hadronic energy conversion function. The overall neutrino energy has a resolution of approximately 7% as estimated from simulation [41].

4.3 Selection and Background

The two main sources of background to the muon neutrino disappearance analysis are cosmic ray induced events and beam induced backgrounds including neutral current, ν_e charged current and ν_τ charged current events. A series of selection algorithms are used to identify candidate charged-current muon neutrino events within the detector and also to reject background events.

A set of cuts are made with the aim of selecting events that are fully contained within the detector. These cuts have two goals: rejecting background events due to cosmic rays and rock muons (from interactions of neutrinos in the rock upstream of the detector), and improving the accuracy of the reconstructed muon neutrino energy by rejecting events that have particles escaping the detector. As should be expected, neither of these aims is achieved to perfection. Instead, a few background and uncontained muon neutrino events make it into the selected sample. Both the reconstructed Kalman tracks (described in Section 4.2) and the hits are used to select fully contained events. Specifically, the selection requires that: there are no hits in the outer two cells in either view, there are no hits in the first or last two planes of the detector and the forward or backward projection from the end or start of the Kalman track passes through at least 10 cells before exiting the far detector.

The near detector has a slightly different selection to account for the muon catcher and

the much smaller ratio of cosmic events to beam induced neutrino events. As described in Section 3.2.8, the muon catcher at the downstream end of the near detector is 2/3 the height of the fully active detector. Details of the differences with respect to the far detector containment selection are as follows. First, a loosened projection cut requires at least 4 hit-less planes projected forward from the track end and at least 8 hit-less planes projected backwards from the track start to the edge of the detector. The aim of this cut is to only select events whose tracks start and stop within the detector. Second, the start position of the Kalman track must occur in the fully active detector upstream of the muon catcher. Finally, the Kalman track must either end within the fully active detector or the position of the track within the detector at transition from fully active to muon catcher must be below the height of the muon catcher [56].

A k-nearest neighbours (kNN) classifier [63] known as Reconstructed Muon Identification (ReMId) is used to identify muon candidates among the particle trajectories within an event [64]. The Reconstructed Muon Identification algorithm uses the following four variables to distinguish muons from other particles: dE/dx likelihood, scattering likelihood, track length and fraction of planes along the track consistent with additional hadronic energy depositions. The kNN output is a score for each event and the resulting distribution is shown in Figure 4.2. The muon neutrino charged current signal events are shown by the black histogram which peaks close to 1 and the neutral current background events are shown by the red histogram. For each event, the Kalman track with the highest ReMId score is designated as the primary muon track. Events with ReMId > 0.75 are selected as candidate muon neutrino charged current interactions. In the far detector this selection results in a signal efficiency and purity for contained events of 81% and 95% respectively, under the assumption of neutrino oscillations with $\Delta m^2_{32} = 2.5 \times 10^{-3}$ eV^2 and $\sin^2\theta_{23} = 0.5$ [64, 65].

An alternative method called Convolutional Visual Network [66] (CVN) for selecting muon neutrino charged current events has recently been developed. The CVN algorithm identifies muon neutrino charged current events based on the event topology and does not require detailed event reconstruction. The output from the CVN muon neutrino charged current event classifier is shown in Figure 4.3. The signal events are shown by the green histogram. The background neutral current, appearance ν_e and inherent beam ν_e events are shown by the blue, purple and pink histograms respectively [66]. Both the ReMId and CVN selections are responsible for rejecting the neutral current background. The choice of which selection should be used for this thesis is discussed in more detail in Chapter 5

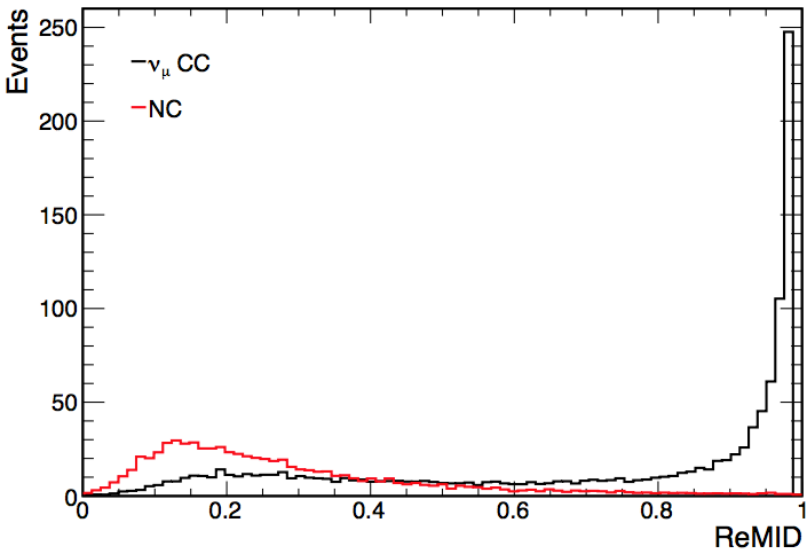

Figure 4.2: Distribution of Reconstructed Muon Identification (ReMId) scores for simulated muon neutrino charged current events (black histogram) and neutral current events (red histogram). For the standard analysis events are required to have a ReMId score of 0.75 or greater. Figure taken from [65].

A good spill selection requires that the NuMI beam is produced within acceptable bounds of spill time (< 0.5 seconds), spill POT ($> 2 \times 10^{12}$), horn current (-202 kA $< I < -198$ kA), proton beam position on NuMI target (-2 mm $< pos(x, y) < 2$ mm) and beam width (0.57 mm $< width(x, y) < 1.58$ mm) [67, 68].

The data quality selection removes events with problems in one or more data concentrator modules. The selection requires that: no data concentrator modules completely drop out during the spill, there is not an excess of tracks stoping at DCM edge boundaries (this signals that the detector is out of sync and uses the DCM edge metric [69]), and the fraction of hits outside the NuMI beam spill window (in cells affected by light leaking) is less than 45% [70].

The cosmic rejection selection utilises a beam spill window cut and a boosted decision tree (BDT) to create a cosmic rejection particle identification variable [71]. The BDT uses the Kalman track with the highest ReMId score and is passed 11 variables including: the angle of the track relative to the NuMI beam direction, the y-direction of the track, maximum height of activity within the detector, the number of hits on the track, length of the track, the number of cells projected from the end (start) of the track forwards

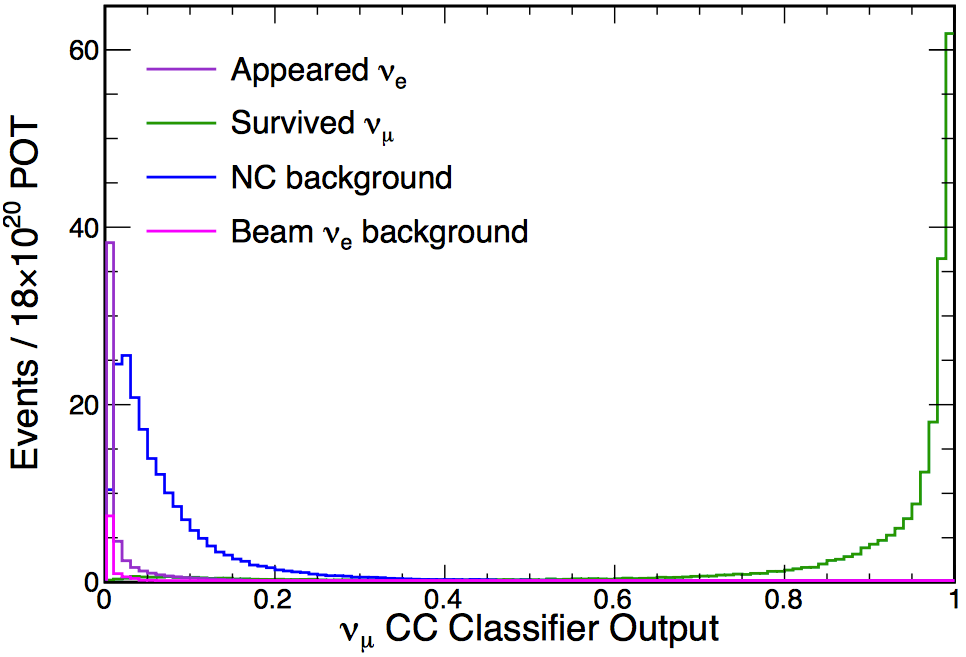

Figure 4.3: Output of the Convolutional Visual Network (CVN) muon neutrino charged current event identification using the MC simulation. Muon neutrino charged current events are shown by the green histogram. The backgrounds of neutral current events are shown by the blue histogram, appearance ν_e events are shown by the purple histogram and the inherent beam ν_e events are shown by the pink histogram. Figure taken from [66].

(backwards) to the edge of the detector, the estimated scattering divided by the track length, number of hits in event, visible calorimetric energy per hit in the event, minimum y-position of activity in the event and the number of 3D Kalman tracks in the event.

The beam background events are estimated using the simulation for each detector. Events passing the selection that do not have a true muon or anti-muon neutrino associated with them are deemed to be background. The cosmic background is estimated using two samples of far detector data which occur outside of the beam spill window. The first sample is taken using the timing sidebands of the data collected with the NuMI spill trigger with a time window of . This sample matches the exposure of the detector to the NuMI beam but is statistically limited . The second sample is recorded at times when there is no beam trigger using a pulser trigger where data is collected during 550 μs intervals. This second sample contains more events but does not so closely match the far detector running conditions. Figure 4.4 shows the estimated number of cosmic background and signal events after each successive selection is applied to the sample.

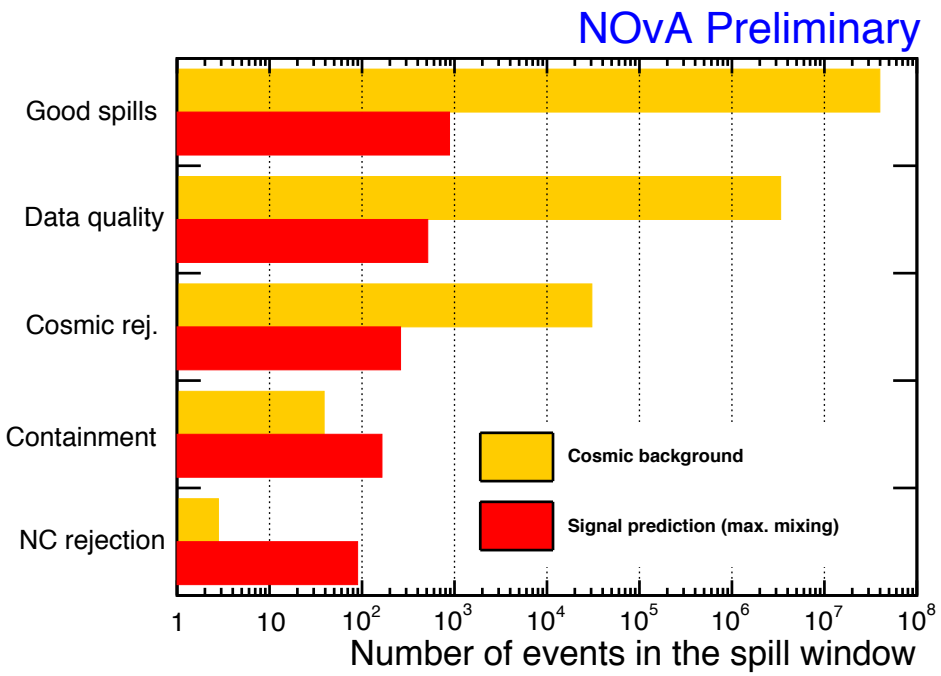

Figure 4.4: The number of signal events (red) and cosmic background events (yellow) surviving each successive analysis selection. The signal is estimated from the simulation and the cosmic background is estimated from the timing sidebands of the NuMI trigger. Figure taken from [72].

4.4 Calorimetric Energy Scale Calibration

NOvA's calorimetric energy calibration is performed in three stages. Firstly, the attenuation calibration corrects the response along each cell using hits from through-going muons. Cell-to-cell response differences are also corrected at this stage. Secondly, an absolute energy calibration uses muons that stop within the detector to convert the attenuation corrected response into physically meaningful units of GeVs. Finally, a drift calibration accounts and adjusts for the variation of the detector response with time. At the time of writing the drift calibration is not used since the observed changes are small enough to have a negligible impact on the analysis.

4.4.1 Attenuation and Threshold Calibration

The attenuation calibration is performed for each cell in both NOvA detectors using the cell-hits from cosmic ray muon energy depositions. The detector response to these cell-hits is divided by the path length through the cell to provide the uncalibrated energy loss per cm. To provide an accurate path length, only cell-hits which have neighbouring hits from the same track in the two directly adjacent cells within the same plane are used for the

calibration. The path-length through a cell can then be precisely calculated from the cell width and the angle of the track. Figure 4.5 shows the uncalibrated detector response per unit path length along the length of a NOvA near detector cell. Data is shown by the black points and a fit to the data is shown by the blue curve. The fit provides the attenuation calibration constants used to correct the detector response [73, 74].

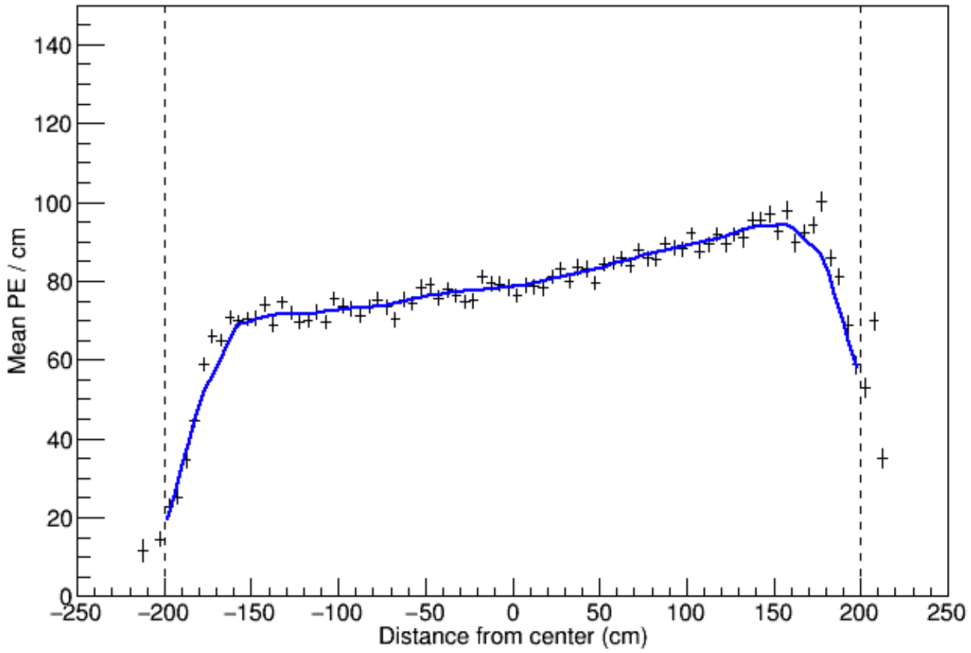

Figure 4.5: An example of how the detector response (PE/cm) varies along the length of a cell in the NOvA near detector. The distance is measured relative to the centre of the cell. The data is shown by the black points with statistical errors. A fit to the data is shown by the blue curve. Figure taken from [73].

4.4.2 Absolute Calibration

The NOvA absolute calibration uses the energy deposited by stopping muons as a standard candle. To reduce systematic uncertainties, for the calibration of the detector, only those energy deposits in a 1-2 m window away from the muon track end point are used where the dE/dx is very close to minimum ionising. The mean of the detector response distribution is found for data and MC in both near and far detectors. The mean of the distribution of true energy deposits in the track window is used to provide a conversion factor between the detector response and the true energy deposited in the scintillator for minimum ionising muons. Figure 4.6 shows the resulting calibrated dE/dx distribution of stopping muons in NOvA's far detector. Remaining residual differences between the data and MC are

accounted for when assessing the systematic errors of the analysis. The absolute calibration method is described in the first analysis absolute calibration technical note [75]. The results of the 2017 [41] calibration and the differences compared to the first analysis [76] are described in the second analysis absolute calibration technical note [77].

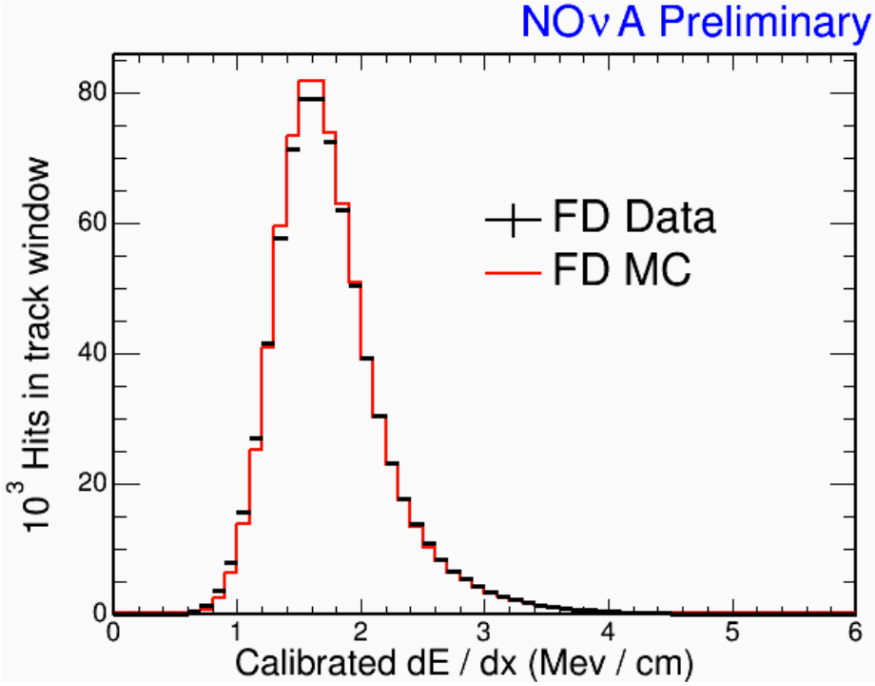

Figure 4.6: Calibrated dE/dx (MeV/cm) for hits within the 100 cm track window in the NOvA far detector. Data and simulation are shown by the black points and red histogram respectively. Figure taken from [75].

4.4.3 Timing Calibration

The aim of the timing calibration is to precisely synchronise each detector externally with the neutrino beam and internally among the electronic detector components. The internal timing calibration measures and accounts for timing offsets between data concentrator modules (see 3.2.5) using hit times from cosmic ray tracks crossing multiple data concentrator modules [78].

4.5 Extrapolation

The NOvA near detector is used to compare the reconstructed energy of muon neutrino charged current candidate events in data and simulation. Predictions of the far detector energy spectrum are created using an extrapolation of the near detector energy spectrum.

Neutrino oscillations, acceptance differences and flux differences between the near and far detector are accounted for.

The extrapolation proceeds in several stages. First, the background (estimated from simulation) is subtracted from the the near detector data spectrum. Second, a reconstructed to true neutrino energy matrix, obtained from the near detector simulation, is used to convert the background subtracted reconstructed neutrino energy into a true spectrum. Third, the near detector true spectrum is multiplied by a far-to-near detector event ratio to produce the far detector true spectrum. The far-to-near detector event ratio accounts for the effect of neutrino oscillations and the different acceptances of the detectors. Fourth, the far detector true spectrum is converted into a reconstructed spectrum using the far detector reconstructed to true energy matrix obtained from the far detector simulation. Finally, background events due to cosmic rays (from data) and beam backgrounds (from MC including neutral current, ν_e and ν_τ interactions) are added to the extrapolated far detector reconstructed neutrino energy distribution to form a prediction that will later be compared to the far detector data. [41]

4.6 Producing Confidence Limit Contours

Measurements of the neutrino oscillation parameters are extracted from the far detector neutrino energy spectrum by comparing the data with the prediction. The log-likelihood for each set of different oscillation parameters is found by comparing the far detector data with a prediction generated at those oscillations parameters using the poisson log-likelihood function [20],

$$\ln\lambda\left(\vec{\theta},\vec{\delta}\right) = -2\sum_{i=1}^{N}\left[\nu_i\left(\vec{\theta},\vec{\delta}\right) - n_i + n_i \ln\frac{n_i}{\nu_i\left(\vec{\theta},\vec{\delta}\right)}\right] + \sum_{i=1}^{M}\frac{\delta_i^2}{\sigma_i^2}, \tag{4.2}$$

where the sums run over all bins, ν_i is the predicted number of events in each bin, $\vec{\theta}$ is the vector of oscillation parameters included in the fit, $\vec{\delta}$ is the vector of systematic nuisance parameters, n_i is the number of events observed in each bin. The second sum term describes the ΔLL due to the systematic pull terms, δ_i is the fitted value of the systematic and σ_i is the error on that systematic.

For the disappearance analysis the LL function described above is used to create a map of ΔLL vs. Δm^2_{32} and $\sin^2\theta_{23}$. The best fit is found where $\lambda(\vec{\theta},\vec{\delta})$ is minimised. The confidence boundaries are found by comparing the value of $\lambda(\vec{\theta},\vec{\delta})$ at each point in the ΔLL map with the value at the best fit. The 90% C.L. boundary is found in the

Δm^2_{32} vs. $\sin^2\theta_{23}$ map where $\Delta LL = 4.61$, this is the Bayesian confidence interval for a two parameter fit. The measured values of Δm^2_{32} and $\sin^2\theta_{23}$ are fitted independently allowing the other oscillation parameter to float as a parameter constrained by other experimental results. As such, the 68% C.L. interval quoted is found using the Bayesian confidence interval for a one parameter fit, this is found to be when $\Delta LL = 1$. The confidence with which particular values of a measured oscillation parameter is rejected is found from the square root of the log likelihood difference at the best fit and the value in question: $\sqrt{\Delta LL}$. Details of the systematic uncertainties included in the fit are provided within the next section.

The sensitivity of the analysis is evaluated before using the far detector data using sensitivity contours. These are created using the a fake-data far detector neutrino energy spectrum. This fake-data spectrum is oscillated with chosen neutrino oscillation parameters to test the sensitivity of the analysis at that chosen point in the oscillation parameter space.

4.7 Evaluation of Systematic Uncertainties

The measurement of the oscillation parameters presented in this thesis takes account of systematic uncertainties in the normalisation, energy scales, neutrino cross sections, final-state interactions, neutrino flux, scintillation model, noise model and background normalisation. The uncertainties are defined as absolute uncertainties that apply to both detectors and as inter-detector (relative) uncertainties due to differences between the two detectors.

Where possible a reweighting approach to evaluating the systematic uncertainties is used to reduce the computational resources required. A simple example is the quasi-elastic charged current cross section normalisation. These events can be reweighted to quantify the effect of the uncertainty on the particular interaction type. For those systematic uncertainties where a simple reweighting is not practical, such as for uncertainties that may effect the reconstruction, simulation samples are produced with shifts according to the systematic uncertainty. In these samples the reconstruction has been performed assuming that either the upper or lower 1 σ bound on the uncertainty is the central value. In the case of uncertainties due to different models (such as the scintillation model) a simulation sample is created for each of the models. The effect of each source of systematic uncertainty is incorporated into the analysis by normalisation reweights and shifts to the neutrino energy spectrum. For a given systematic uncertainty, events are shifted

Systematic sample	Percentage shift in: Mean $E_{had.}$	Mean E_{μ}	Mean E_{ν}	Selected events
ND XY calibration -1 σ shift	-4.97	-0.34	-1.60	+1.16
ND XY calibration $+1$ σ shift	+4.79	+0.82	+2.01	-1.76
ND Y-func. calibration shift	-1.53	-0.10	-0.47	+0.49
FD XY calibration -1 σ shift	-5.02	+0.65	-0.90	-4.02
FD XY calibration $+1$ σ shift	+4.89	-0.15	+1.28	+1.12
FD Y-func. calibration shift	-1.48	+0.16	-0.30	-0.91
ND Birks' B	-3.92	-0.40	-1.37	+3.06
ND Birks' C	-0.26	-0.34	-0.28	+2.51
FD Birks' B	-5.02	+0.20	-1.25	+1.49
FD Birks' C	-0.64	-0.19	-0.32	+1.28
FD noise model	+1.29	-0.02	+0.36	+0.25

Table 4.1: Percentage shifts in the energy variables and normalisation when comparing a systematically shifted sample to the baseline simulation. The XY calibration systematic uncertainty describes the uncertainty in the absolute energy scale in each detector. The Y-func. calibration systematic uncertainty describes the uncertainty along the length of the y-view cells. The normalisation is found using the neutrino energy distribution in the range 0 to 5 GeV.

and reweighted to produce a systematically shifted neutrino energy spectrum. Within the CAFAna framework, a neutrino energy spectrum is created at the ±1, ±2 and ±3 sigma level for each source of systematic uncertainty.

The following subsections describe the systematic uncertainties analysed by the author for NOvA's 2017 [41] ν_{μ} disappearance analysis. These uncertainties are the calibration, scintillation model and noise model systematic. A summary of the percentage shifts in hadronic energy, muon energy, neutrino energy and normalisation due to the uncertainties analysed by the author is shown in Table 4.1. Details of the table are discussed in the following subsections. A summary of the full list of systematic uncertainties used in the disappearance analysis is discussed at the end of this section.

4.7.1 Evaluation of the Calibration Systematic Uncertainties

Systematic uncertainties in the energy calibration are assessed to account for residual differences between data and MC after the full calibration has been performed. The

systematic uncertainty due to the calibration is defined by an overall uncertainty in the energy scale and response shape uncertainties along the length of horizontal and vertical cells. Ratios of data over simulation of calibrated muon energy as a function of distance from the cell centres are used to define the calibration shape systematics for the vertical (x-view) and horizontal (y-view) cells independently. The y-view cells display the most extreme disagreement between data and simulation in terms of calibrated response along the cells. In comparison the disagreement between data and simulation in the x-view cells is negligible and is currently neglected in the analysis of systematics [77].

A comparison of proton energy in the data and simulation is used to define an uncertainty of $\pm 5\%$ on the energy scale of hadronic showers [79]. In this study the profiles of dE/dx vsthe distance to the track end were compared in data and MC for both protons and muons. The study found that the MC best matched the data when scaled by 98% for muons and by 95% for protons. The effect of this energy scale uncertainty is evaluated using two simulation samples generated with a $+5\%$ or -5% shift applied. These samples are referred to as the "XY" shifted samples.

The effect of the calibration uncertainty along the length of the horizontal cells was analysed using a simulation sample generated with a functional shift to the calibration of hits along the cells. This sample is referred to as the "Y-func." shifted sample. The shift in hadron, muon and neutrino energy for each systematically shifted sample was analysed in [80].

Distributions of the hadronic energy, muon energy, neutrino energy and (reconstructed-true)/true energy are shown for the near detector "XY", near detector "Y-func.", far detector "XY" and far detector "Y-func." shifted samples in Figures 4.7, 4.8, 4.9 and 4.10 respectively. For each plot the standard baseline simulation is shown for comparison. In both detectors the "XY" shifted sample causes a larger shift (compared to the "Y-func." sample) to the mean hadronic, muon and neutrino energy and the normalisation as can be seen in Table 4.1 [80]. The table shows that the shifts in the near and far detector normalisation due to the calibration uncertainty samples ("XY" and "Y-func.") are anti-correlated, this is not currently understood and investigation is ongoing.

The "XY" systematic samples shift the mean hadronic energy by about 5% which is expected because the hadronic energy is found using the calibrated cell-hits. Meanwhile, the same systematic samples only have a small effect on the mean muon energy which is expected because the muon energy is found from the track length. The effect on the neutrino energy is about what is expected using the approximation that the hadronic

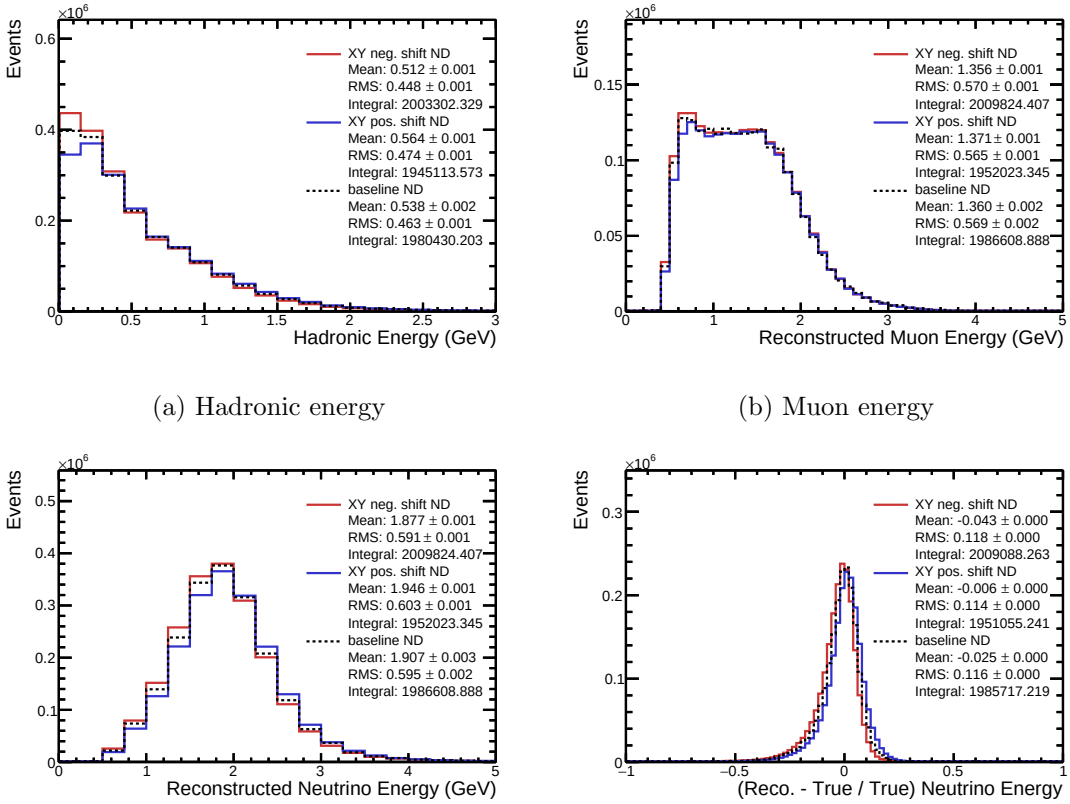

(a) Hadronic energy

(b) Muon energy

(c) Neutrino energy

(d) (Reconstructed - true) / true neutrino energy

Figure 4.7: Energy distributions for the baseline, XY negatively shifted and XY positively shifted near detector simulation shown by the dotted black, solid red and solid blue histograms respectively.

energy contributes about 1/4 of the neutrino energy on average. The impact on the normalisation is largest for the "FD XY neg. shift" systematic sample which reduces the normalisation by 4%. This reduction was shown to be due to a sensitivity of the cosmic rejection algorithm to the calibration scale [81].

4.7.2 Evaluation of the Scintillation Model Systematic Uncertainties

Generally, the observed light yield from a scintillant is proportional to the energy loss of the through going particle. However, at high dE/dx the light yield, L, is often no longer proportional to the energy loss per cm but can be modelled as

$$L \propto \frac{\frac{dE}{dx}}{1 + k_B \frac{dE}{dx} + k_C \left(\frac{dE}{dx}\right)^2}, \tag{4.3}$$

where k_B and k_C are Birks' constant and a higher order correction constant respectively [82].

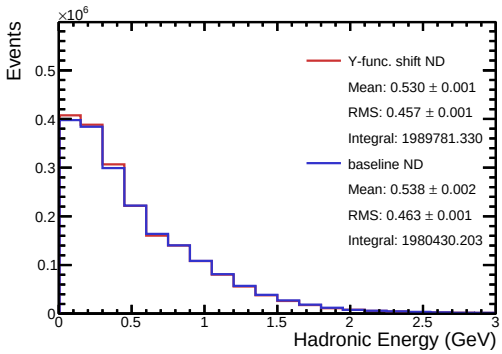

(a) Hadronic energy

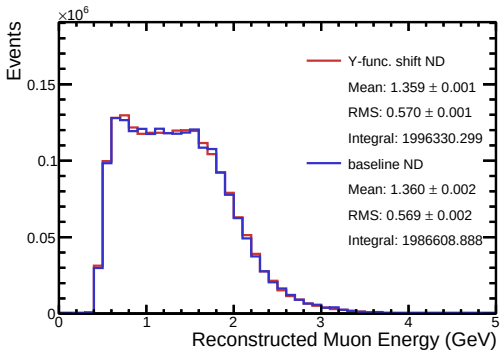

(b) Muon energy

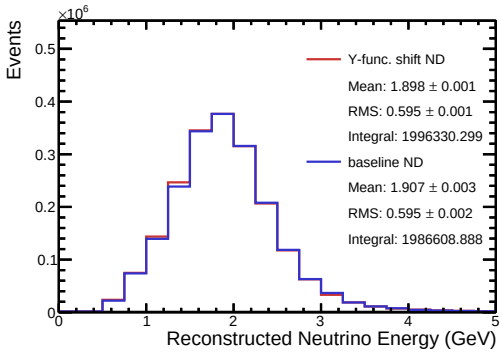

(c) Neutrino energy

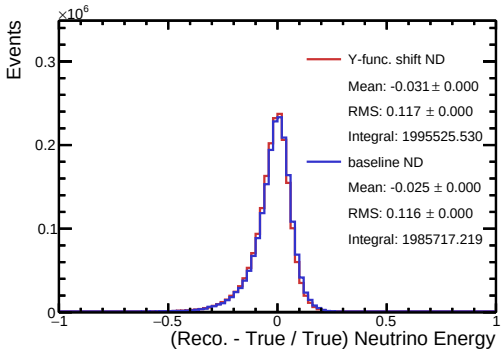

(d) (Reconstructed - true) / true neutrino energy

Figure 4.8: Energy distributions for the baseline and Y-functional (Y-func.) shifted near detector simulation shown by the solid blue and solid red histograms respectively.

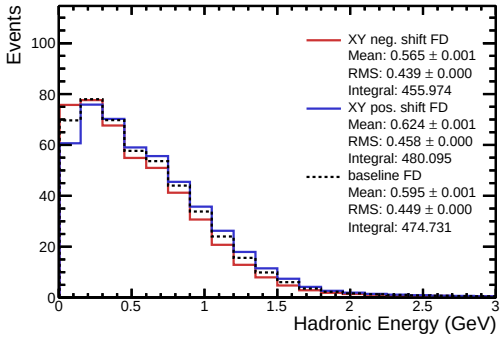

(a) Hadronic energy

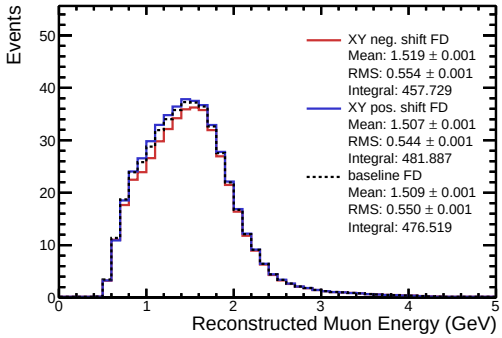

(b) Muon energy

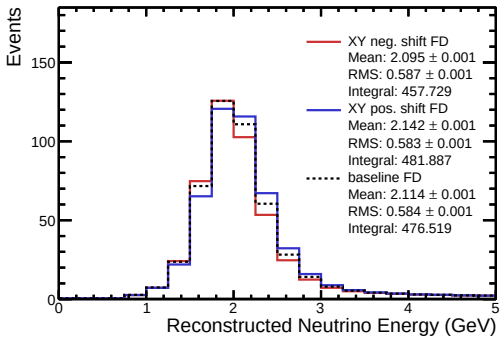

(c) Neutrino energy

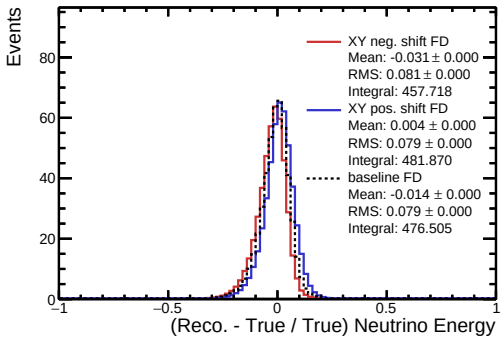

(d) (Reconstructed - true) / true neutrino energy

Figure 4.9: Energy distributions for the baseline, xy negatively shifted and xy positively shifted far detector simulation shown by the dotted black, solid red and solid blue histograms respectively.

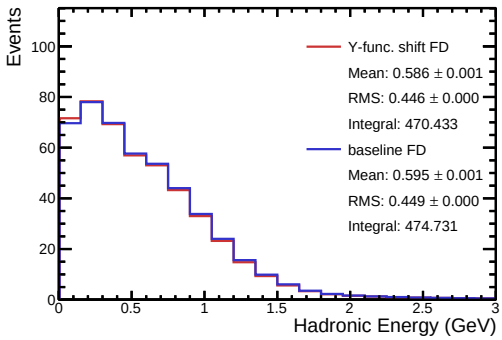

(a) Hadronic energy

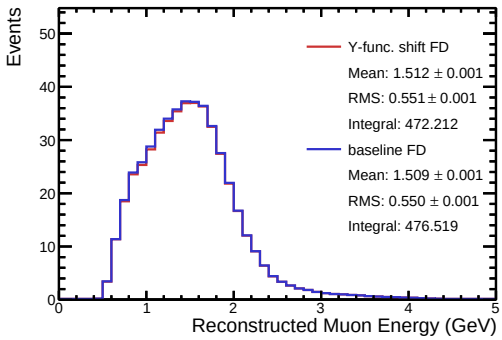

(b) Muon energy

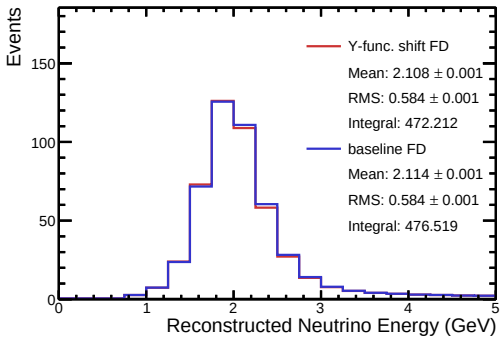

(c) Neutrino energy

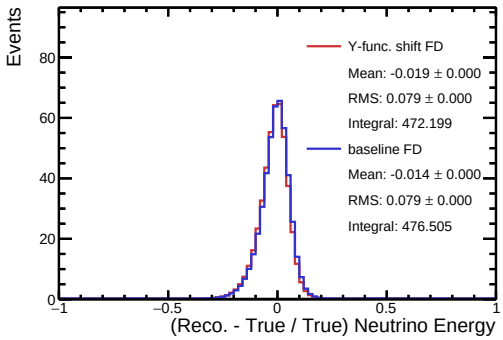

(d) (Reconstructed - true) / true neutrino energy

Figure 4.10: Energy distributions for the baseline and Y-functional (Y-func.) shifted far detector simulation shown by the solid blue and solid red histograms respectively.

A fit of this model to the near detector data gave the constants for the standard simulation used for NOvA's 2017 [41] analysis. This is done by generating MC simulation with the various settings for the model parameters and fitting each new simulation with the data. The fit yielded $k_B = 0.04$ cm / MeV and $k_C = -0.0005$ cm^2/MeV^2 [83]. These values for the constants are not consistent with those often found in the literature[1]. In order to evaluate the effect of the uncertainty in the model parameters on the analyses, two systematic samples (called Birks' B and Birks' C) were created with the constants set to alternative values. The Birks' C sample files are created using values commonly found in the literature, $k_B = 0.01$ cm / MeV and $k_C = 0.0$ cm^2/MeV^2. The Birks' B sample files are created using values approximately halfway between the standard NOvA constants and the Birks' C constants, $k_B = 0.02$ cm / MeV and $k_C = 0.0$ cm^2/MeV^2.

The simulations that used scintillation models with the alternative model parameter settings were produced without an overlay of the neutrino induced activity originating outside the near detector. In these samples there are approximately 10% more selected events per POT than the nominal simulation [85]. It was shown [86] that this increase in events per POT was due to fewer events failing the containment cut. For the study of the systematic uncertainty due to the Birks' parameters a sample of the standard simulation was created that also did not include external neutrino-induced activity to allow a like-for-like comparison.

Plots of hadronic energy, muon energy, neutrino energy and (reconstructed-true)/true energy for the baseline and new noise models in the far detector are shown in Figures 4.11 and 4.12 for the near and far detector respectively. For both detectors the shift due to the Birks' B sample is larger than than the shift due to the Birks' C sample (see Table 4.1). The shifts found using the Birks' B sample are used as the systematic uncertainty due to the the light yield model for the second analysis.

4.7.3 Evaluation of the Noise Model Systematic Uncertainties

Electronic noise in the readout of the NOvA avalanche photo diode is introduced to the simulation in two ways. For cells with physics hits, Gaussian-Markov processes are used to add noise to the signal pulse in the APD. In cells without physics hits the noise is modelled using a distribution of unclustered hits taken from real data [59]. The uncertainty due to the modelling of electronic noise is evaluated using two alternative noise models [87]. NOvA's 2017 [41] analysis uses the initial noise model (version 1) [56]. A new noise model

[1]It has since been understood that this fit was effectively compensating for the absence of Cherenkov light simulation in the MC [84].

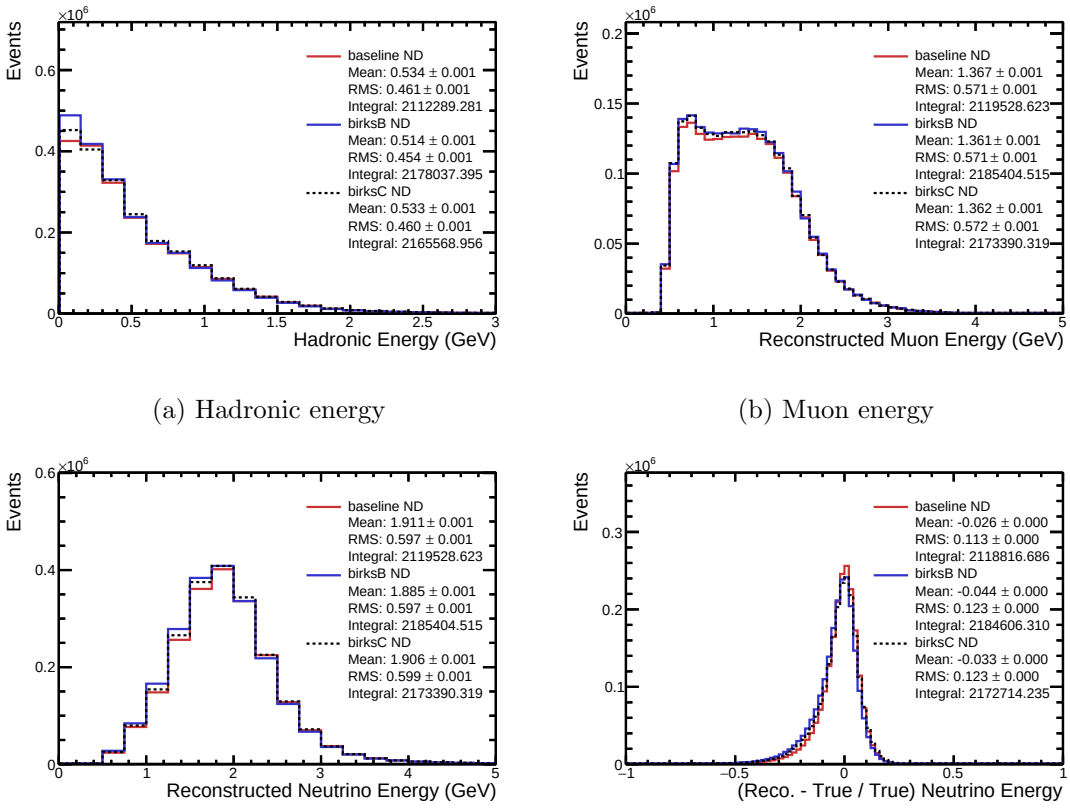

(a) Hadronic energy

(b) Muon energy

(c) Neutrino energy

(d) (Reconstructed - true) / true neutrino energy

Figure 4.11: Energy distributions for the baseline, Birks' B and Birks' C near detector simulation are shown by the solid red, solid blue and dotted black histograms respectively.

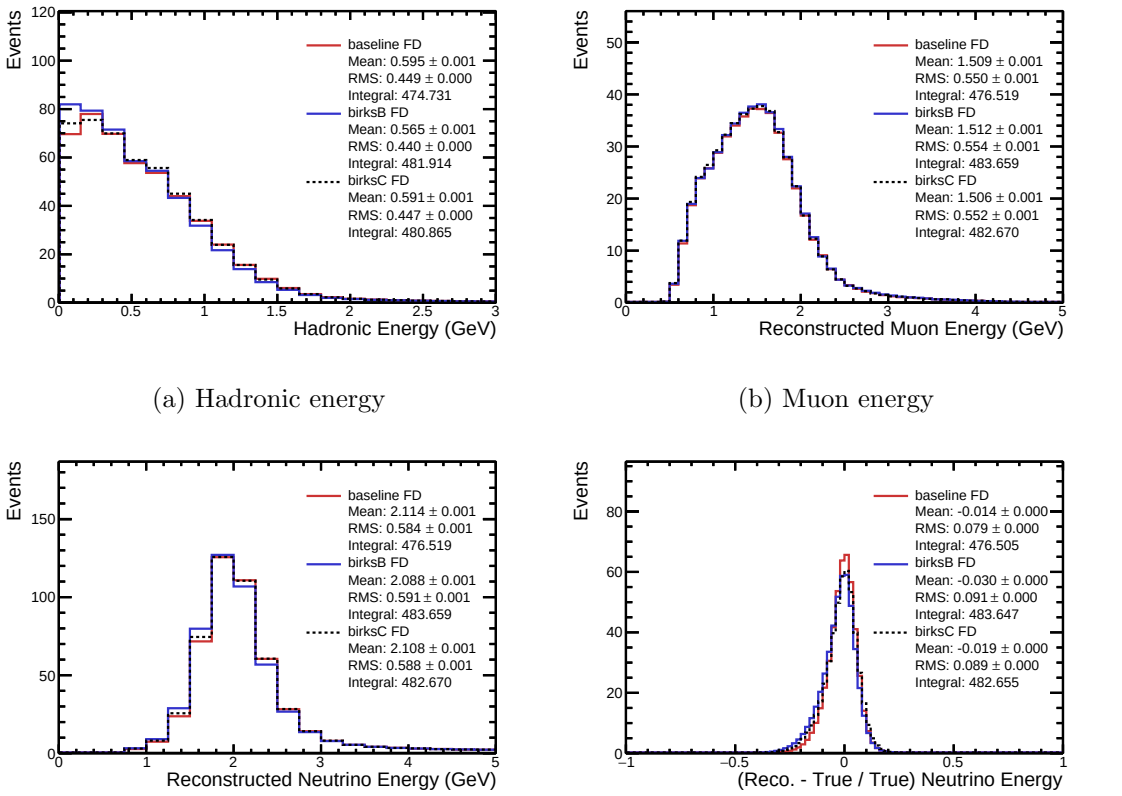

(a) Hadronic energy

(b) Muon energy

(c) Neutrino energy

(d) (Reconstructed - true) / true neutrino energy

Figure 4.12: Energy distributions for the baseline, Birks' B and Birks' C far detector simulation are shown by the solid red, solid blue and dotted black histograms respectively.

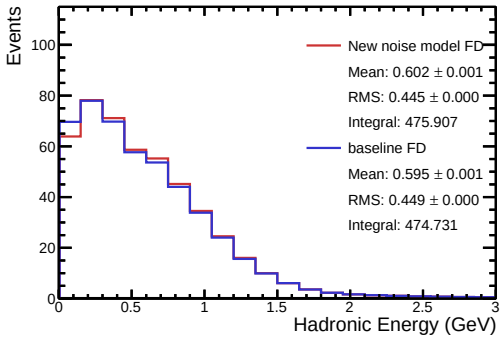

(a) Hadronic energy

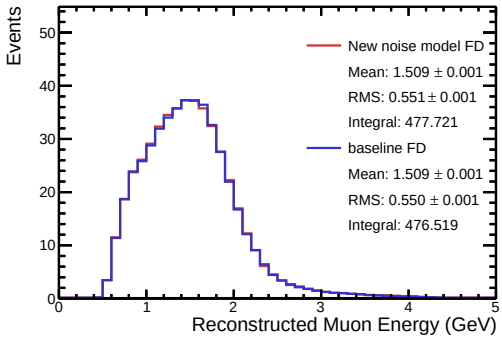

(b) Muon energy

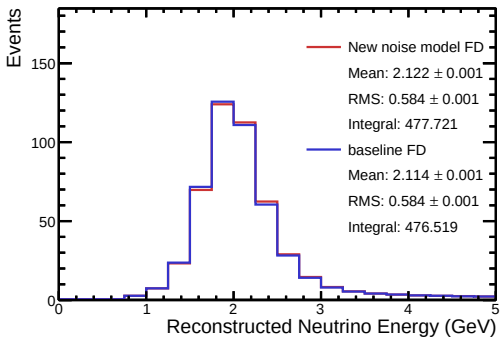

(c) Neutrino energy

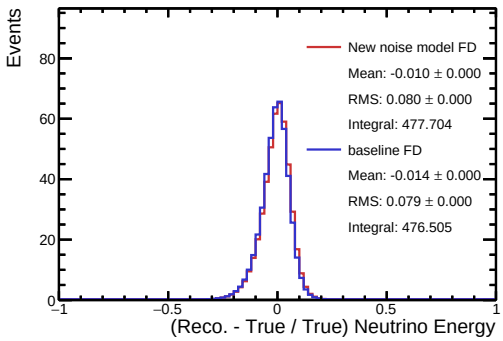

(d) (Reconstructed - true) / true neutrino energy

Figure 4.13: Energy distributions for the baseline and new noise model far detector simulation are shown by the solid blue and solid red histograms respectively.

has since been created (version 2) which provides a better match to the data. A far detector simulation sample was produced with the new model to approximately measure the systematic uncertainty due to noise modelling.

Plots of hadronic energy, muon energy, neutrino energy and (reconstructed-true)/true energy are shown in Figure 4.13. The shifts in mean and normalisation are shown in Table 4.1. The largest shift due to the new noise model is in the mean hadronic energy (+1.3%). The shifts in mean neutrino energy and normalisation are small compared to the other samples analysed in this section. [88]

4.8 Summary of Systematic Uncertainties for the Disappearance Analysis

The systematic uncertainties used in this thesis are the same as those used for NOvA's official 2017 disappearance analysis [41]. A brief summary of each of the systematic uncer-

tainties accounted for in the analysis is as follows. Both the relative and absolute hadronic energy scale uncertainties are estimated as 5% based on the response of the near detector to protons [41]. The relative and absolute muon energy scale uncertainty is 2% due to the uncertainties in simulating energy loss [20] and the uncertainty in the composition of the detectors. The relative normalisation is estimated as 5% and is due to the combination of neutrino induced activity originating outside the near detector and cosmic ray pile up in the far detector. The neutrino cross section uncertainties are taken from GENIE [50], with the exceptions of the charged-current non-resonant single-pion and 2p2h events which are both assigned 50% normalisation uncertainties due to the reweighting described in Section 3.4. The absolute uncertainty in the neutrino flux is estimated as 20% and is mostly due to uncertainties in the model of hadron production at the NuMI target. Since this systematic is correlated between the two detectors it is mitigated by the extrapolation. The uncertainty on the selected beam background events (NC, ν_e-CC and ν_τ-CC) has a conservative uncertainty of 100% and still needs to be precisely analysed. The uncertainty on the light output as a function of dE/dx was estimated by comparing simulations with the Birks' constants applied at three settings (see Section 4.7.2). The uncertainty due to the noise model is estimated by comparing two noise models and is found to be negligible (see Section 4.7.3).

Chapter 5

Analysis Improvements

This chapter discusses three methods to improve the sensitivity of the muon neutrino disappearance analysis to Δm^2 and $\sin^2\theta_{23}$. The first involves separating neutrino events into bins of energy resolution such that well resolved events are not mixed in with less well resolved ones. For the second the neutrino energy binning is altered to provide finer binning in the energy region where maximum disappearance is known to occur. The third utilises a hybrid of two different selection algorithms to identify muon neutrino candidate events with higher efficiency and purity. Optimisation of the improvements is discussed in two parts. First, the optimisation of the improvements individually. Second, a re-optimisation when the the analysis improvements are combined. Systematic uncertainties are included in all the optimisations presented here and the effect of each individual uncertainty is delineated.

5.1 Choice of Sensitivity Test Points in Oscillation Parameter Space

Sensitivity contours are obtained from fitting a simulated far detector spectrum to an oscillated fake data spectrum (constructed according to the "Asimov" approach as described in the PDG [20]). The sensitivity of the experiment is evaluated at different test points in the Δm^2_{32} vs. $\sin^2\theta_{23}$ parameter space to sample the sensitivity across the range of possible neutrino oscillation parameters. This is achieved by changing the values of the oscillation parameters used to construct the fake data spectrum.

The impact of each analysis improvement will be quantified using three metrics: the sensitivity to reject maximal mixing ($\sin^2\theta_{23} = 0.5$) for the NOvA 2017 [41] analysis ν_μ disappearance best fit, the sensitivity to reject maximal mixing for the MINOS 2014 [40]

analysis ν_μ disappearance best fit and finally the sensitivity to reject $\sin^2\theta_{23} = 0.6$ for the T2K 2015 [27] ν_μ disappearance best fit. All best fit points are taken assuming the Normal Ordering hypothesis. MINOS's best fit is taken from the 2014 combined analysis paper [40] which reported measurements of $|\Delta m^2_{32}| = [2.28 - 2.46] \times 10^{-3}$ eV^2 (68% C.L.) and $\sin^2\theta_{23} = 0.35$–0.65(90% C.L.). In the following analyses the test point used to make the sensitivity contours is taken to be $|\Delta m^2_{32}| = 2.36 \times 10^{-3}$ eV^2 and $\sin^2\theta_{23} = 0.41$. T2K's best fit point is extracted from the results of the 2015 paper [27]. The reported measurements are $\sin^2\theta_{23} = 0.528^{+0.055}_{-0.038}$ and $|\Delta m^2_{32}| = (2.51 \pm 0.11) \times 10^{-3}$ eV^2). NOvA's 2017 [41] analysis produced a best fit of $\sin^2\theta_{23} = 0.404^{+0.030}_{-0.022}$ and $|\Delta m^2_{32}| = (2.67 \pm 0.11) \times 10^{-3}$ eV^2. The 3 test points cover the allowed 3 σ range of Δm^2_{32} from the Particle Data Group of 2.37 - 2.63$\times 10^{-3}$ eV^2 (for Normal Ordering) [20]. The Particle Data Group's 2 σ allowed range of $\sin^2\theta_{23}$ (0.379 - 0.616) is almost covered by the 3 test points.

5.2 Analysis Simplifications Made for the Optimisation Procedure

This section provides an overview of two simplifications made for this analysis regarding inclusion of the cosmic ray background and the Feldman-Cousins correction to the coverage.

When making the fit to the actual far detector data the estimated cosmic ray background must be added to the predicted far detector spectrum. This is because the data includes an inherent background from cosmic rays. However, sensitivity plots only use simulation in the far detector so it is possible to not include the cosmic ray background for convenience. Figure 5.1 shows the sensitivity of the standard disappearance analysis to the oscillation parameters Δm^2_{32} and $\sin^2\theta_{23}$. The sensitivity when accounting for the cosmic ray induced background (blue contour) is compared with the sensitivity neglecting the cosmic background (red contour). The contours show that the addition of the cosmic background slightly reduces the sensitivity of the experiment to reject maximal mixing. The cosmic background will not initially be included for the following studies designed to optimise the sensitivity of the analysis due to the large computational requirements. Instead, the impact of the cosmic background on the sensitivity with all the proposed analysis improvements included will be presented later in the chapter.

The Feldman-Cousins [89] correction (where confidence limit boundaries are determined by inspecting the range of log-likelihood ratios found in pseudo-experiments) is used

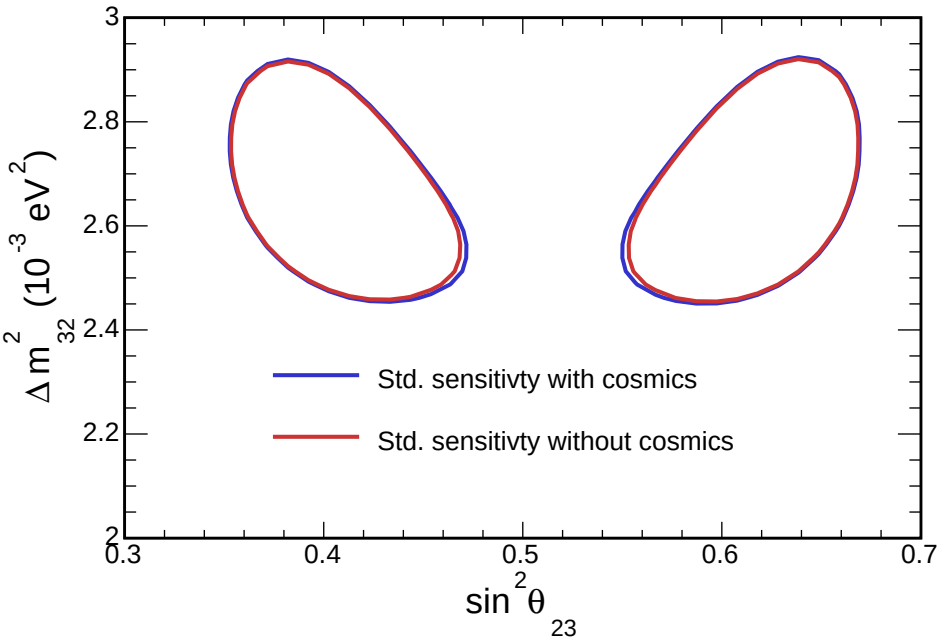

Figure 5.1: Comparison of the sensitivity (90% C.L.) with (blue contour) and without (red contour) accounting for the cosmic background at NOvA's 2017 [41] best fit point and exposure (6.05×10^{20} POT-equivalent).

when making the result contours for the official disappearance analysis but not for the results in this thesis due to the large computational resources required. A comparison of NOvA's 2017 [41] result contour with and without using the Feldman-Cousins technique is shown in Figure 5.2. The contours show that, at NOvA's 2017 best fit point, using the Feldman-Cousins technique causes the contours to shrink and hence the oscillation parameters to be measured with slightly greater precision. It is expected that applying the Feldman-Cousins technique will increase the sensitivity slightly beyond that presented here.

5.3 Hadronic Energy Fraction Binning

The first sensitivity improvement considered is to separate the neutrino events by energy resolution. Events with better energy resolution are less likely to migrate across neutrino energy bin boundaries and this is particularly important for events near the oscillation maximum.

The reconstructed neutrino energy is the sum of the reconstructed muon energy and the reconstructed hadronic shower energy. In the NOvA detectors, muon energy is estimated using the length of the muon track with a resolution of 4% while hadronic energy is

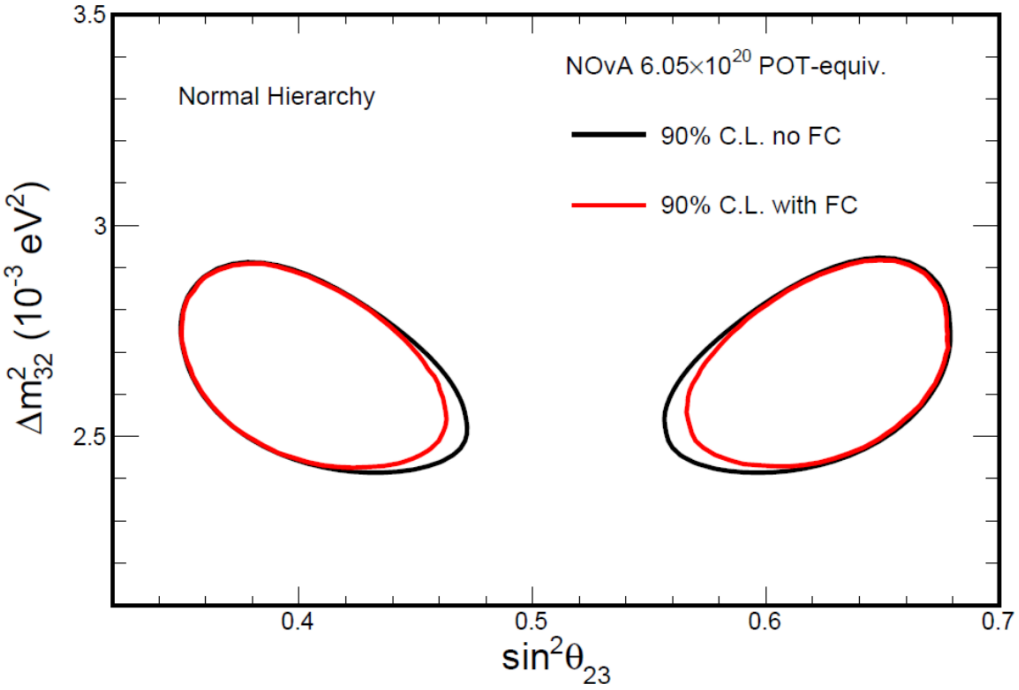

Figure 5.2: Comparison of NOvA's 2017 [41] result (6.05×10^{20} POT-equivalent exposure) contour with (black line) and without (red line) using the Feldman Cousins corrections. Taken from [90].

estimated from calorimetry with an average resolution of about 25% [41]. Therefore, neutrino events with a larger proportion of hadronic activity will be less well resolved by the detector than those with a small proportion of hadronic energy. Hence the hadronic energy divided by neutrino energy (E_{had}/E_ν), is used as a metric to estimate the neutrino energy resolution. The E_{had}/E_ν distribution is obtained for each bin of reconstructed neutrino energy. For each energy bin events are divided into quantiles (containing equal numbers of events) by finding the boundaries in E_{had}/E_ν that divide the sample evenly. The number of E_{had}/E_ν quantiles is varied to optimise the sensitivity. Figure 5.3 shows the distribution of hadronic energy fraction vs. reconstructed neutrino energy for far detector running period two (see Section 3.4). The plots of E_{had}/E_ν vs. neutrino energy are almost identical for all running periods so only one is shown here. The quantile boundaries are formed on a period by period basis to incorporate any changes in the detector performance such as the introduction of a higher APD gain in the far detector since the 2015 summer shutdown. The quantile boundaries for a division into four hadronic energy fraction quantiles are shown by the black lines overlaid on the colour plot.

The resolution information gained by dividing events into quantiles of E_{had}/E_ν is included in the fit by carrying out separate shape fits for each E_{had}/E_ν quantile. The

sensitivity contours for scenarios where the far detector neutrino energy spectrum is split into 2, 3, 4, 5, 6, 7 and 8 quantiles of E_{had}/E_{ν} are compared with the standard analysis at NOvA's 2017 [41] best fit point in Figure 5.4a, at MINOS's 2014 [40] best fit point in Figure 5.5a and at T2K's 2015 [27] best fit point in Figure 5.6a. In addition, the significance of rejection of a point in oscillation parameter space (maximal mixing for the NOvA and MINOS best fit and $\sin^2\theta_{23} = 0.6$ for the T2K best fit) is plotted against the number of E_{had}/E_{ν} quantiles for the NOvA, MINOS and T2K best fit points in Figures 5.4b, 5.5b and 5.6b respectively.

Both the improvement to the sensitivity and the increase in the computational resources required to perform the fit must be considered when deciding upon the number of E_{had}/E_{ν} quantiles used for the analysis of the data. The memory and processing required to produce the fit approximately scales with the number of E_{had}/E_{ν} quantiles. The largest gain in sensitivity at all three best-fit points comes from the initial introduction of splitting events into two E_{had}/E_{ν} quantiles. Further improvements are seen when using three and four quantiles. After four quantiles the improvement seen with each additional E_{had}/E_{ν} is substantially reduced. Considering both the improvements in sensitivity and also the increase in memory use the division of neutrino events into 4 quantiles of E_{had}/E_{ν} was chosen.

5.4 Optimising Neutrino Energy Binning

The neutrino energy binning used for the muon neutrino disappearance analysis presented in the 2016 [76] and 2017 [41] papers consists of 20 0.25 GeV wide bins from 0 to 5 GeV (see Figure 2.11). This section discusses improvements to the sensitivity through optimisation of the energy binning.

Figure 5.7a shows a comparison of the far detector muon neutrino energy spectrum assuming oscillations at the three test points in the oscillation parameter space: NOvA's 2017 [41], MINOS's 2014 [40] and T2K's 2015 [27] best fit points. Figure 5.7b shows the log-likelihood distribution for comparisons between each combination of the test point predictions. The log-likelihood is calculated for each neutrino energy bin using the formula

$$LL = 2\left(e - o + o\log\left(\frac{o}{e}\right)\right),$$

where e is the number of expected events and o is the number of observed events. Almost all of the distinction between the three test points is gained between 1 and 3 GeV.

Information useful in determining the oscillation parameters may be lost if the energy

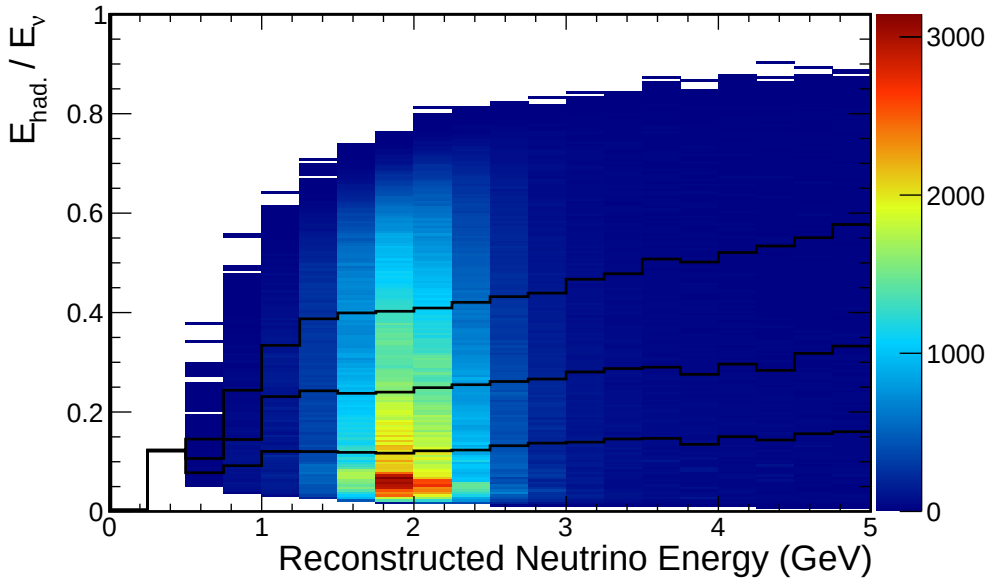

Figure 5.3: Hadronic energy fraction vs. reconstructed neutrino energy in the far detector MC during running period 2. The quantile boundaries are shown for each neutrino energy bin for the choice of 4 hadronic energy fraction bins.

binning is wider than the neutrino energy resolution [91]. Using finer binning could enhance the sensitivity of the disappearance analysis. The advantages of finer binning will diminish as the bin size approaches and goes beyond the neutrino energy resolution. Another point to consider when adjusting the neutrino energy binning is that the number of neutrino energy bins almost proportionally impacts the memory required for the fit. For this reason, the strategies presented below focus specifically on increasing the number of bins in the region of maximum oscillation between 1 and 3 GeV.

To investigate possible enhancements to the sensitivity, three alternative neutrino energy binning strategies are compared with the standard analysis neutrino energy binning. An overview of the standard binning and the three alternative binning strategies is presented in Table 5.1. The table shows that binning schemes "A", "B" and "C", use narrow energy bins in the region of maximum oscillation (1-2 GeV or 1-3 GeV) and wider energy bins in regions with less oscillation information (0-1 GeV and 3-5 GeV). Note that binning scheme "A" requires slightly fewer bins in total (19) than the standard binning (20) whilst retaining more information in the region of interest.

Comparisons of the four binning strategies in terms of sensitivity to Δm^2_{32} and $\sin^2\theta_{23}$ and rejection of maximal mixing are shown for the NOvA, T2K and MINOS best fit points

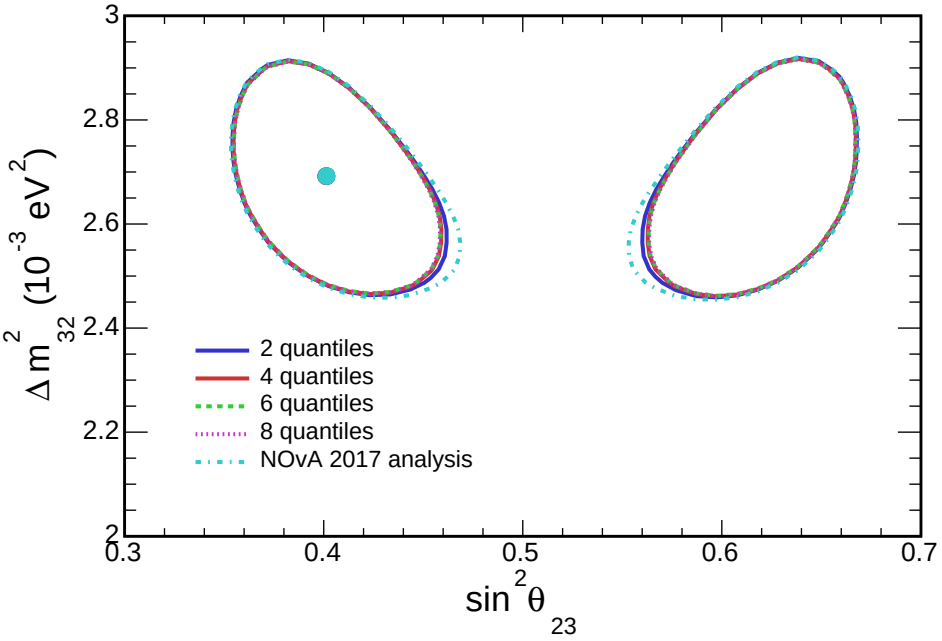

(a) The sensitivity of NOvA's 2017 [41] analysis is shown by the dotted light-blue contour. The best-fit points are shown by the solid circles. In addition, the sensitivity for set of analyses where the events are split 2, 4, 6 and 8 quantiles of E_{had}/E_ν are shown by the solid blue, solid red, dashed green and dotted purple contours respectively.

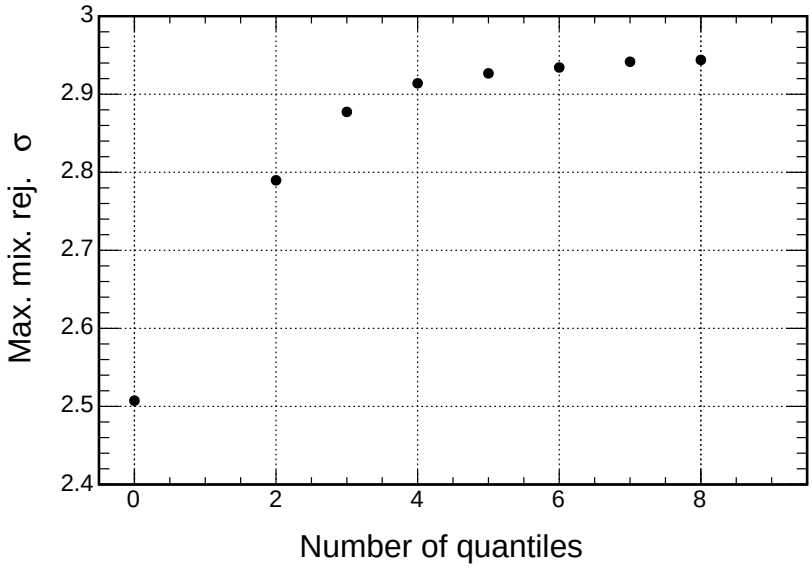

(b) Significance of maximal mixing ($\sin^2\theta_{23} = 0.5$) rejection vs. the number of E_{had}/E_ν quantiles used in the analysis. NOvA's 2017 analysis sensitivity, where the events are not divided into quantiles of E_{had}/E_ν, is shown by the point where quantiles = 0.

Figure 5.4: Sensitivity of the ν_μ disappearance analysis at NOvA's 2017 best-fit and exposure (6.05×10^{20} POT-equivalent) for events split into 1 to 8 quantiles of E_{had}/E_ν.

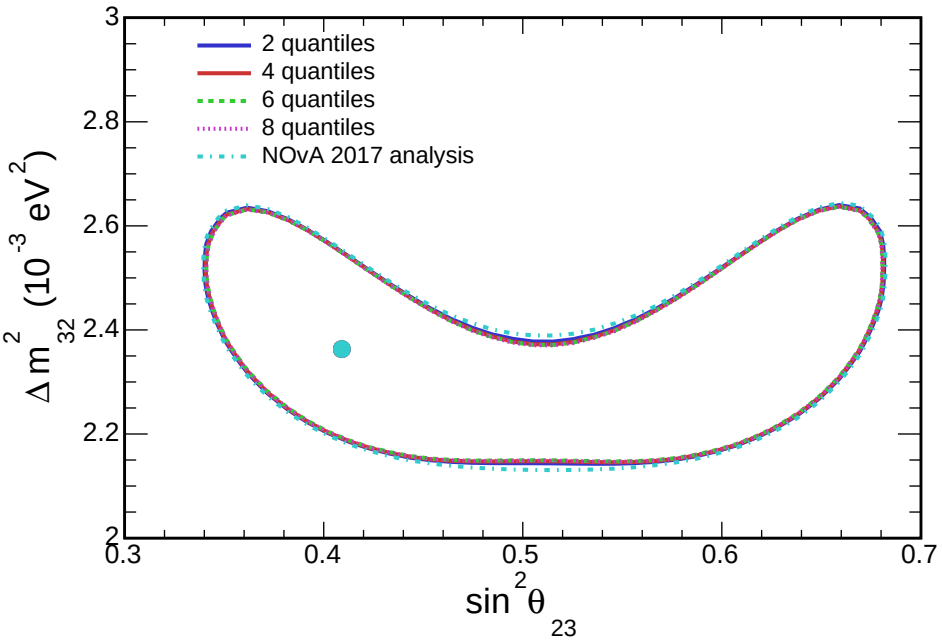

(a) The sensitivity of NOvA's 2017 [41] analysis is shown by the dotted light-blue contour. The best-fit points are shown by the solid circles. In addition, the sensitivity for set of analyses where the events are split 2, 4, 6 and 8 quantiles of E_{had}/E_ν are shown by the solid blue, solid red, dashed green and dotted purple contours respectively.

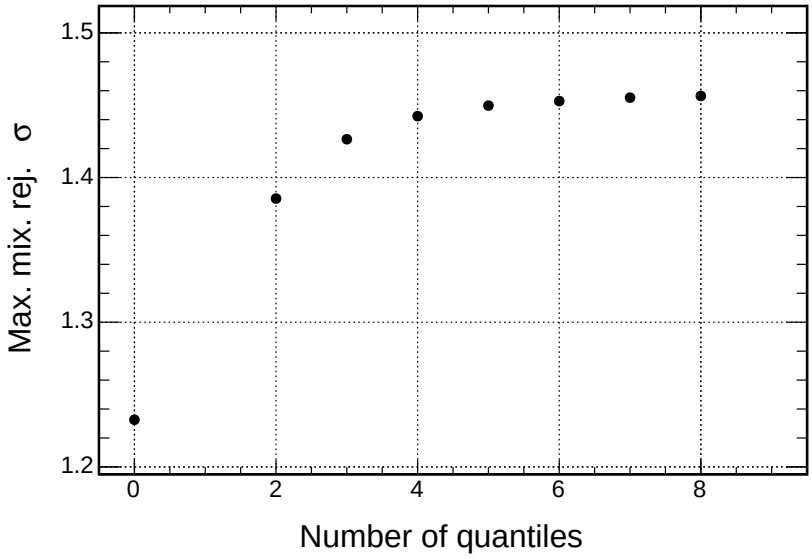

(b) Significance of maximal mixing ($\sin^2\theta_{23} = 0.5$) rejection vs. the number of E_{had}/E_ν quantiles used in the analysis. NOvA's 2017 analysis sensitivity, where the events are not divided into quantiles of E_{had}/E_ν, is shown by the point where quantiles = 0.

Figure 5.5: Sensitivity of the ν_μ disappearance analysis at MINOS's 2014 [40] best-fit and NOvA's 2017 [41] exposure (6.05×10^{20} POT-equivalent) for events split into 1 to 8 quantiles of E_{had}/E_ν.

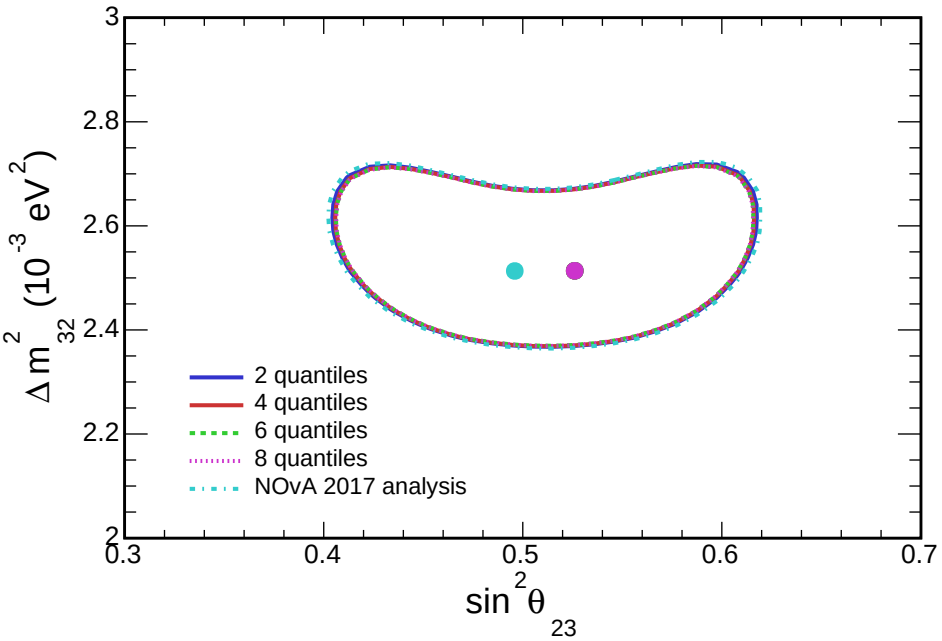

(a) The sensitivity of NOvA's 2017 [41] analysis is shown by the dotted light-blue contour. The best-fit points are shown by the solid circles. Note that the best fit points are either side of maximal mixing, this is caused by degeneracy about $\sin^2\theta_{23} \approx 0.514$. In addition, the sensitivity for set of analyses where the events are split 2, 4, 6 and 8 quantiles of E_{had}/E_ν are shown by the solid blue, solid red, dashed green and dotted purple contours respectively.

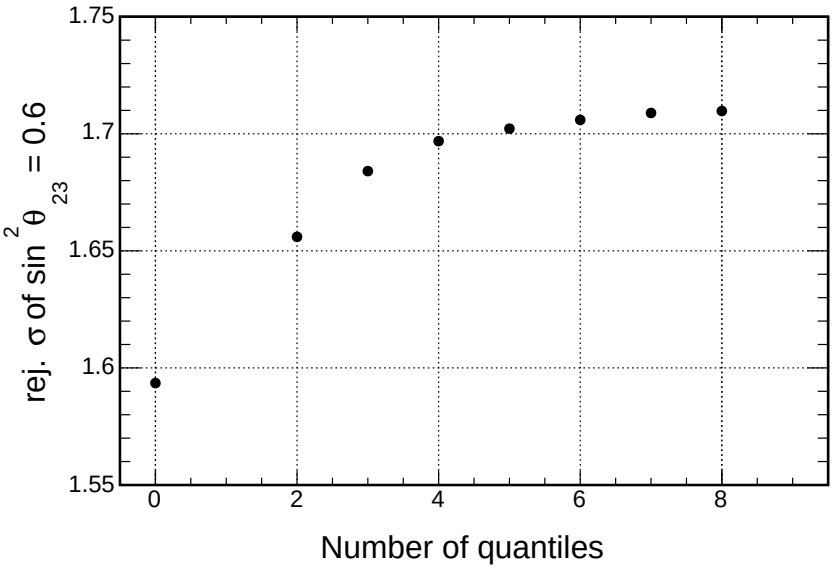

(b) Significance of rejecting $\sin^2\theta_{23} = 0.5$ vs. the number of E_{had}/E_ν quantiles used in the analysis. NOvA's 2017 analysis sensitivity, where the events are not divided into quantiles of E_{had}/E_ν, is shown by the point where quantiles = 0.

Figure 5.6: Sensitivity of the ν_μ disappearance analysis at T2K's 2015 [27] best-fit and exposure NOvA's 2017 [41] exposure (6.05×10^{20} POT-equivalent) for events split into 1 to 8 quantiles of E_{had}/E_ν.

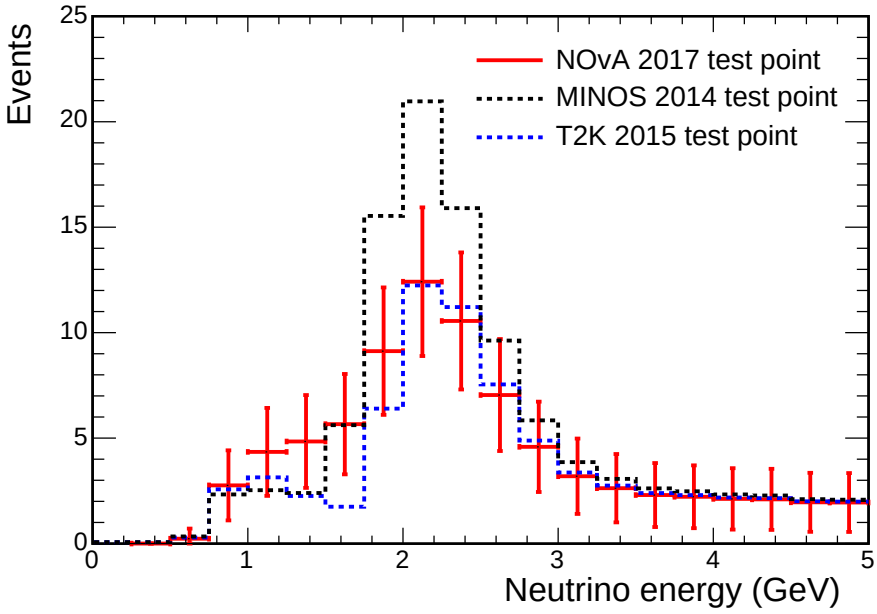

(a) Predicted far detector muon neutrino energy. Spectra with oscillations applied at NOvA's 2017 [41], MINOS's 2014 [40] and T2K's 2015 [27] best fit points are shown by the red error bars, dashed black lines and dashed blue lines respectively.

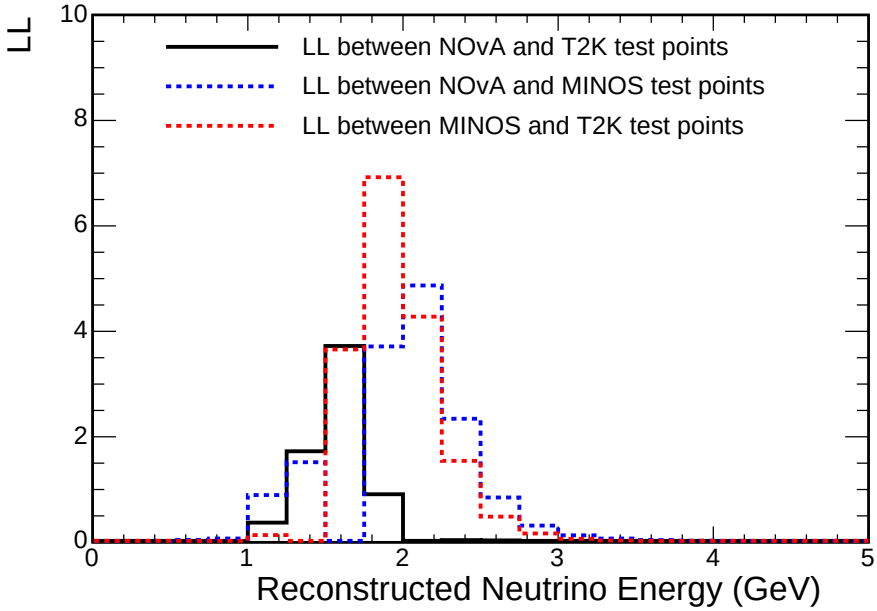

(b) Log-likelihood distributions from comparisons between the energy spectra shown in Figure 5.7a. The result of comparisons between the NOvA and T2K, NOvA and MINOS, and MINOS and T2K spectra are shown by the solid black, dashed blue, and dashed red lines respectively.

Figure 5.7: Comparisons of the simulated muon neutrino energy distributions produced assuming neutrino oscillations with NOvA's 2017 [41], MINOS's 2014 [40] and T2K's 2015 [27] best fit points. The predicted energy spectra are scaled to NOvA's 2017 [41] exposure (6.05×10^{20}POT-equivalent).

	Neutrino Energy Binning Scheme			
Neutrino Energy Range (GeV)	Std.	Scheme A	Scheme B	Scheme C
0 - 0.75	3	1	1	1
0.75 - 1	1	1	1	1
1 - 2	4	10	40	40
2 - 3	4	4	4	40
3 - 4	4	2	2	2
4 - 5	4	1	1	1
Total 0 - 5	20	19	49	85

Table 5.1: Bins per energy range for each neutrino energy binning scheme. The total number of bins required by each scheme is shown in the last row assuming a single E_{had}/E_{ν} quantile.

in Figures 5.8a, 5.8b, 5.9a, 5.9b, 5.10a and 5.10b respectively. The figures show that the sensitivity to reject maximal mixing increases when increasing the number of neutrino energy bins (going from std. through to "C" binning) for all three best fit points. The largest increase in the sensitivity to reject maximal mixing comes when going from the standard binning to the "A" binning. Increasing the number of bins by going from "A" to "B" or "C" binning shows only modest improvements but requires more than double the number of neutrino energy bins. Binning strategy "A" is chosen over the other strategies as it shows a significant improvement in sensitivity (only marginally beaten by "B" and "C") whilst very slightly reducing the number of neutrino energy bins compared to the standard binning.

5.5 Hybrid Combination of Selection Algorithms

NOvA's 2016 [76] and 2017 [41] analyses used the Reconstructed Muon Identification (ReMId) algorithm discussed in Section 4.3 to identify candidate muon neutrino charged current events. A new algorithm called Convolutional Visual Network [66] (CVN) has since been developed. A study [92] showed that the sensitivity of the analysis could be improved by using a hybrid selection combining both ReMId and CVN. Currently the hybrid selection requires events have CVN$>$ 0.5 and ReMId$>$ 0.5. When reducing the cut threshold of ReMId the neutral current background increases along with the signal. However, the addition of CVN reduces the NC bkg beyond that achieved by ReMId alone.

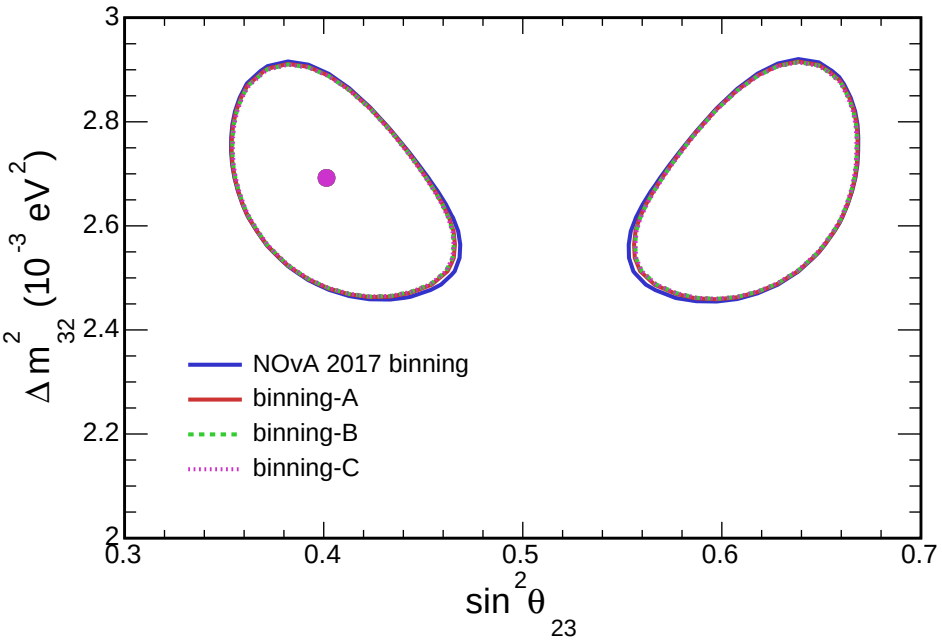

(a) The sensitivity of the standard analysis is shown by the dotted pink contour. The sensitivity when the neutrino energy is binned according to scheme's A, B or C is shown by the solid blue, solid red and dotted green contours respectively.

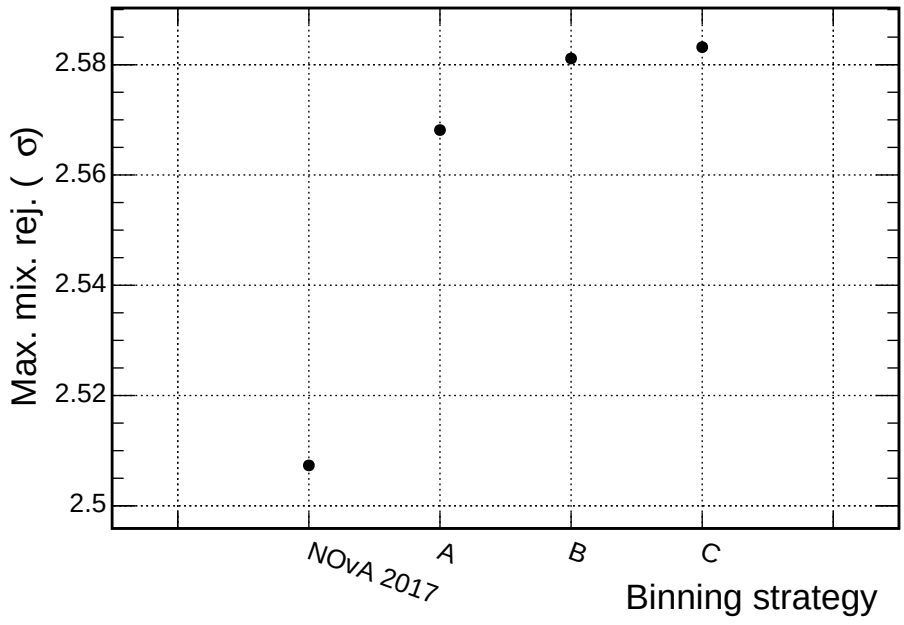

(b) Significance of maximal mixing ($\sin^2\theta_{23} = 0.5$) rejection vs. the neutrino energy binning strategy used in the analysis. p

Figure 5.8: Sensitivity of the ν_μ disappearance analysis at NOvA's 2017 [41] best-fit and exposure (6.05×10^{20} POT-equivalent) when the neutrino energy is binned according to binning scheme A, B, C or standard. A breakdown of each neutrino energy binning scheme is shown in Table 5.1.

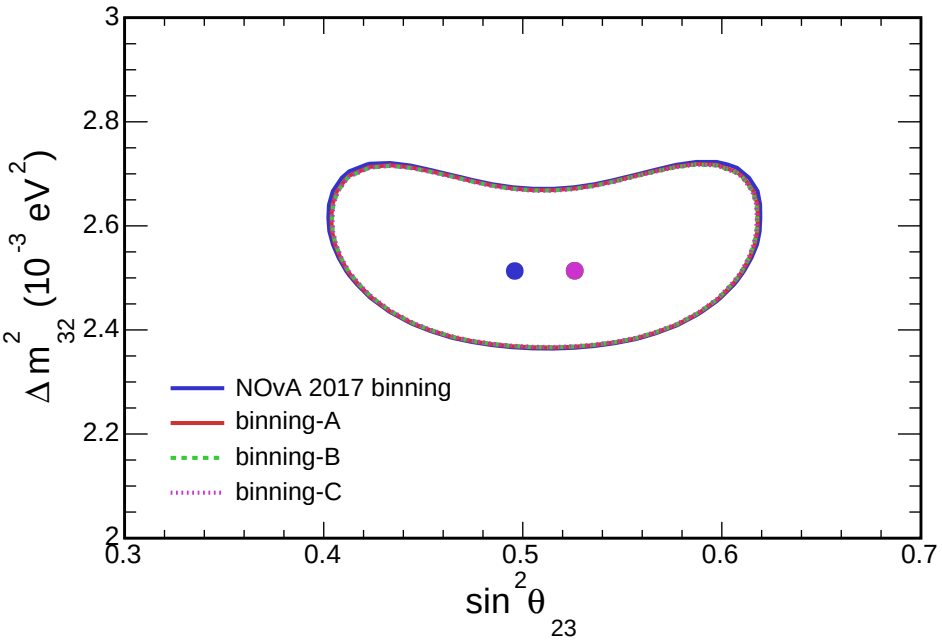

(a) The sensitivity of the standard analysis is shown by the dotted pink contour. The sensitivity when the neutrino energy is binned according to scheme's A, B or C is shown by the solid blue, solid red and dotted green contours respectively.

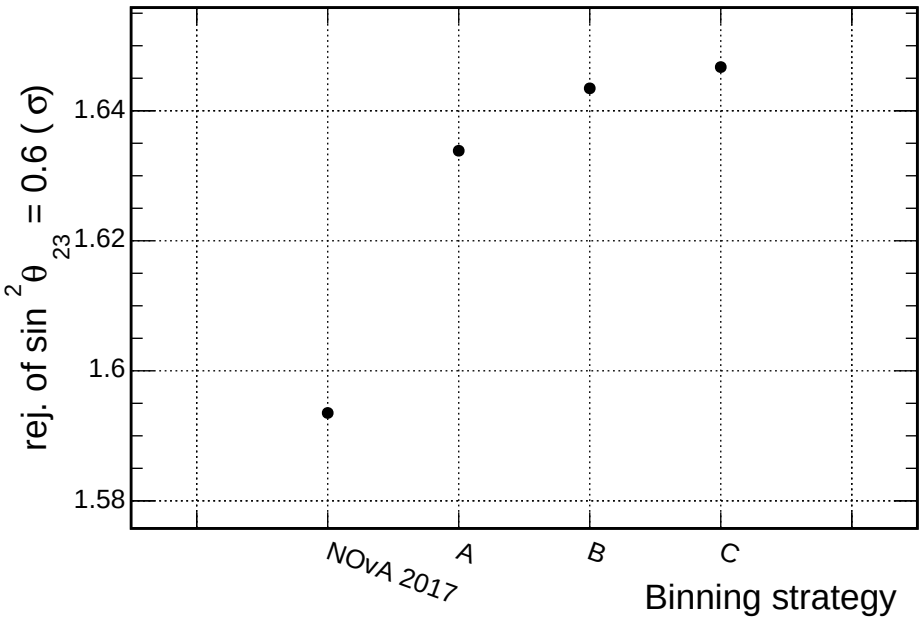

(b) Significance of maximal mixing ($\sin^2\theta_{23} = 0.5$) rejection vs. the neutrino energy binning strategy used in the analysis.

Figure 5.9: Sensitivity of the ν_μ disappearance analysis at T2K's 2015 [27] best-fit and NOvA's 2017 [41] exposure (6.05×10^{20} POT-equivalent) when the neutrino energy is binned according to binning scheme A, B, C or standard. A breakdown of each neutrino energy binning scheme is shown in Table 5.1.

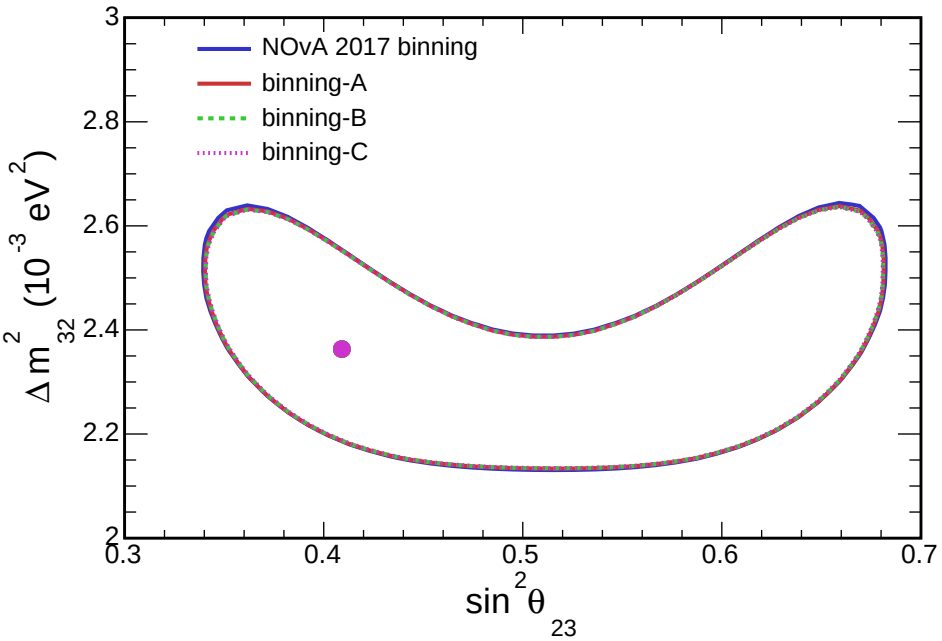

(a) The sensitivity of the standard analysis is shown by the dotted pink contour. The sensitivity when the neutrino energy is binned according to scheme's A, B or C is shown by the solid blue, solid red and dotted green contours respectively.

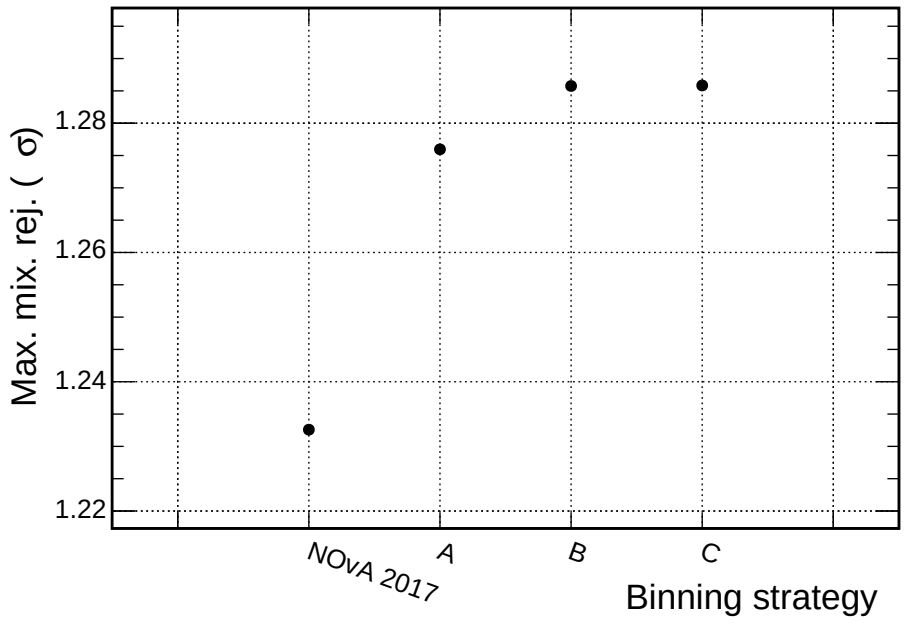

(b) Significance of maximal mixing ($\sin^2\theta_{23} = 0.5$) rejection vs. the neutrino energy binning strategy used in the analysis.

Figure 5.10: Sensitivity of the ν_μ disappearance analysis at MINOS's 2014 [40] best-fit and NOvA's 2017 [41] exposure (6.05×10^{20} POT-equivalent) when the neutrino energy is binned according to binning scheme A, B, C or standard. A breakdown of each neutrino energy binning scheme is shown in Table 5.1.

Overall an 11% increase in signal, a 42% reduction in the cosmic background and a 54% reduction in the beam background is achieved [92].

Figures 5.11, 5.12 and 5.13 show a comparison of the sensitivity using the standard selection and using the hybrid selection for the NOvA, MINOS and T2K best fit points respectively. The hybrid sensitivity contour is created with the standard analysis (standard neutrino energy binning and no division into quantiles of E_{had}/E_{ν}). At all three test points in oscillation parameter space the sensitivity is improved with the introduction of the hybrid selection. In particular the sensitivity at NOvA's 2017 [41] best fit point is improved, the sensitivity to reject maximal mixing increases from 2.5 σ to 3.0 σ.

A study to optimise the hybrid selection was carried out and it was shown that the ability to reject maximal mixing was relatively flat across the ReMId vs. CVN parameter space [93]. There was a slight improvement when loosening both the ReMId and CVN cut level. However, the study did not account for cosmics which would reduce the sensitivity particularly for low values of ReMId and CVN. The decision for this thesis is to leave the hybrid selection at the standard setting as there is not much sensitivity to gain from further tuning of cut values even when not accounting for the cosmic background.

5.6 All Analysis Improvements Combined

This section discusses the improvement to the sensitivity when the individually optimised analysis improvements discussed in Sections 5.3, 5.4 and 5.5 are combined. The combination uses the individually optimised settings for each improvement: 4 E_{had}/E_{ν} quantiles, binning scheme "A" and the default ReMId-CVN hybrid selection.

Figures 5.14, 5.15 and 5.16 show the sensitivity when using all the analysis improvements in combination at the NOvA, MINOS and T2K best-fit points respectively. It is clear that the sensitivity at each best fit point is significantly improved with the introduction of the analysis improvements.

5.7 Re-optimisation when Combining Analysis Improvements

Sections 5.3, 5.4 and 5.5 discussed the individual optimisation for each analysis improvement. When combined the optimal configuration for each improvement may be different from the individual optimisation. This section will discuss a combined optimisation of the improvements using an iterative approach. The individually optimised settings for the analysis improvements will be used as a starting point. One of the improvements (e.g.

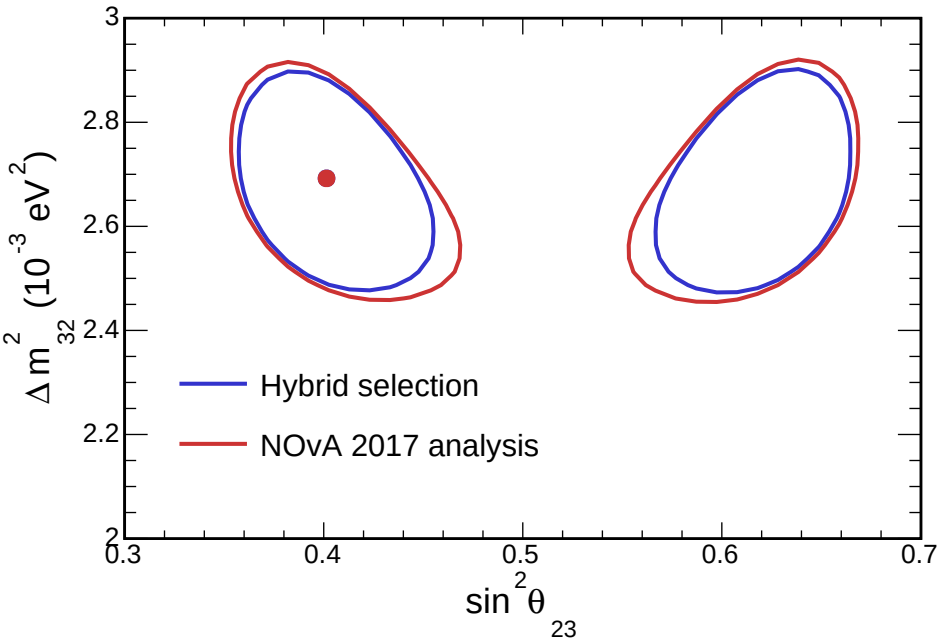

Figure 5.11: Sensitivity contours for the ν_μ disappearance analysis at NOvA's 2017 [41] best-fit and exposure (6.05×10^{20} POT-equivalent). The sensitivity of the standard analysis and an analysis using the hybrid selection are shown by the red and blue contours respectively. The rejection of maximal mixing increases from 2.5 σ to 3.0 σ when using the hybrid selection.

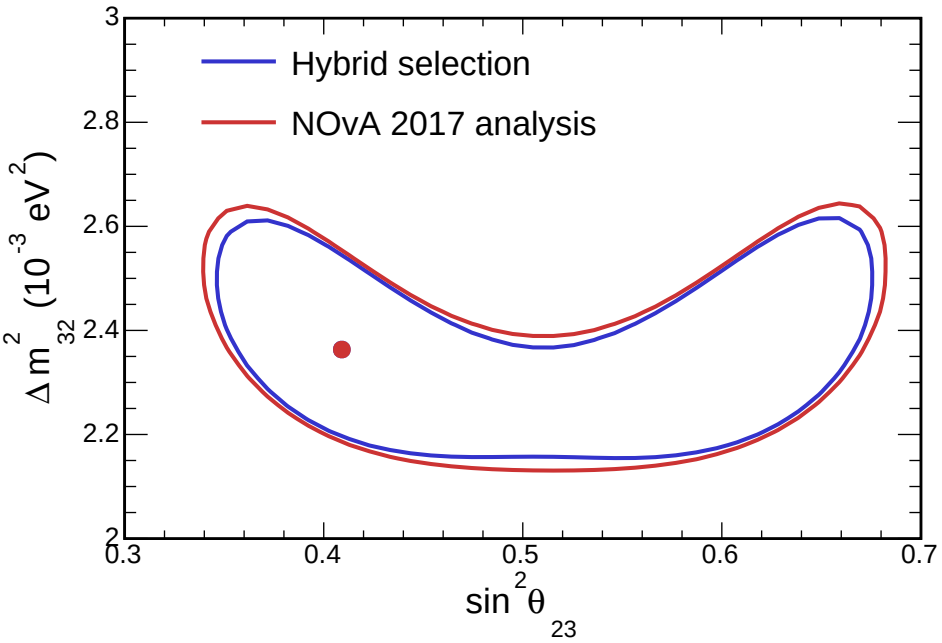

Figure 5.12: Sensitivity contours for the ν_μ disappearance analysis at MINOS's 2014 [40] best-fit and NOvA's 2017 [41] exposure (6.05×10^{20} POT-equivalent). The sensitivity of the standard analysis and an analysis using the hybrid selection are shown by the red and blue contours respectively. The rejection of maximal mixing increases from 1.2 σ to 1.5 σ when using the hybrid selection.

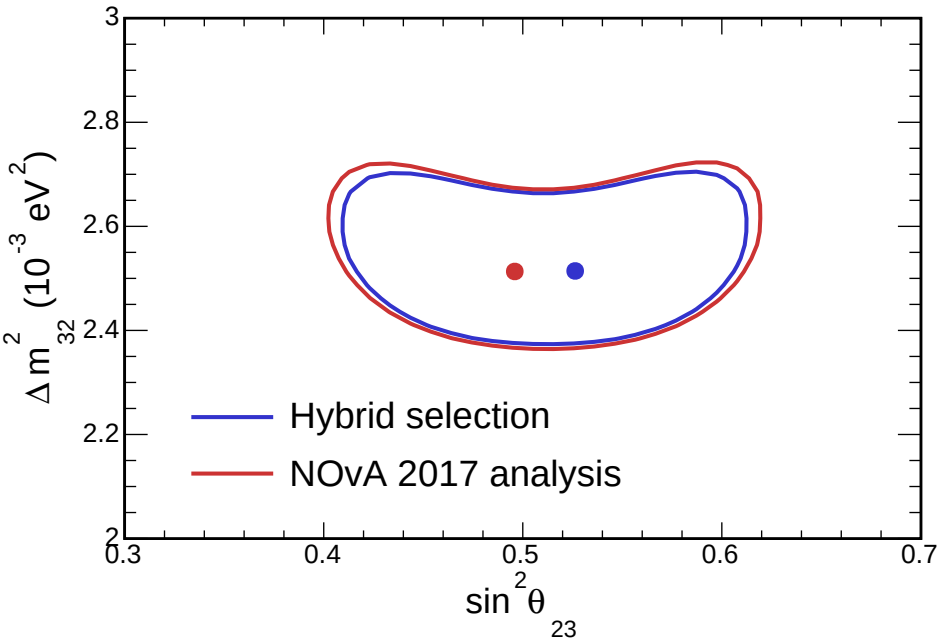

Figure 5.13: Sensitivity contours for the ν_μ disappearance analysis at T2K's 2015 [27] best-fit and NOvA's 2017 [41] exposure (6.05×10^{20} POT-equivalent). The sensitivity of the standard analysis and an analysis using the hybrid selection are shown by the red and blue contours respectively. The rejection of $\sin^2\theta_{23} = 0.6$ increases from 1.6 σ to 1.8 σ when using the hybrid selection.

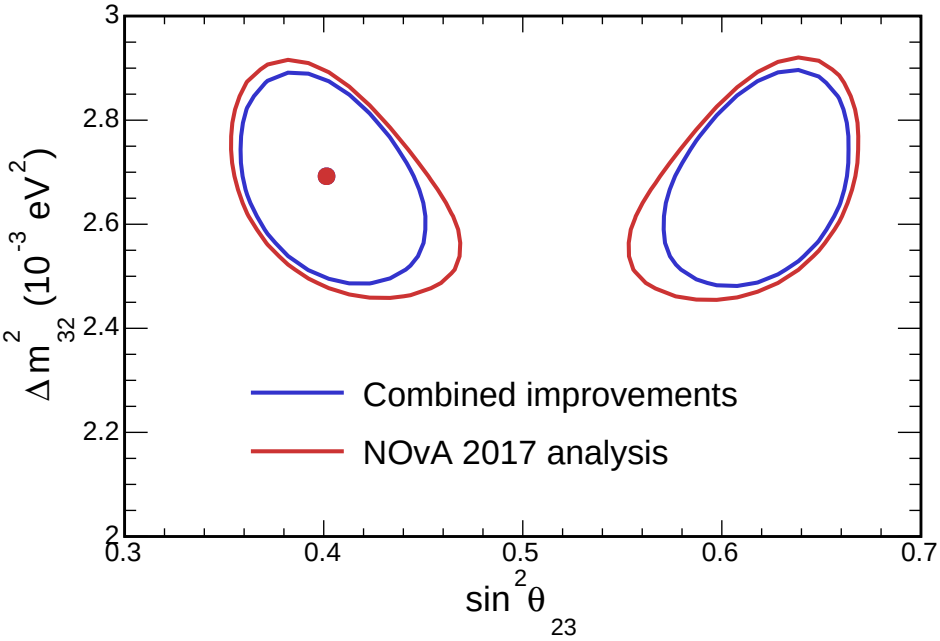

Figure 5.14: Sensitivity contours for the ν_μ disappearance analysis at NOvA's 2017 [41] best-fit and exposure (6.05×10^{20} POT-equivalent). The sensitivity of the standard analysis and an analysis using the individually optimised sensitivity improvements (with 4 E_{had}/E_ν quantiles, neutrino energy binning scheme "A" and the hybrid selection) are shown by the red and blue contours respectively. The rejection of maximal mixing increases from 2.5 σ to 3.3 σ when using all three analysis improvements together.

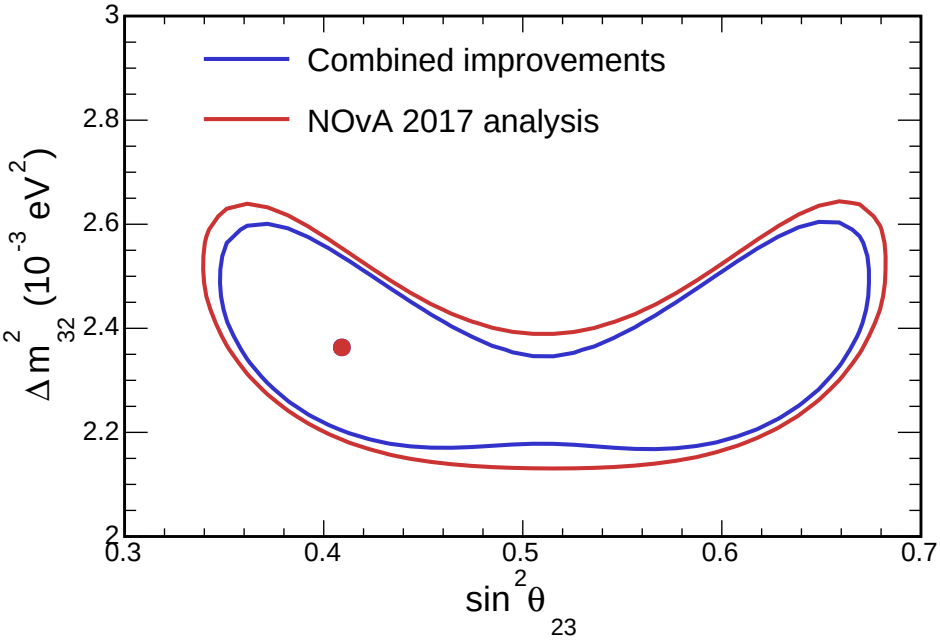

Figure 5.15: Sensitivity contours for the ν_μ disappearance analysis at MINOS's 2014 [40] best-fit and NOvA's 2017 [41] exposure (6.05×10^{20} POT-equivalent). The sensitivity of the standard analysis and an analysis using the individually optimised sensitivity improvements (with 4 E_{had}/E_ν quantiles, neutrino energy binning scheme "A" and the hybrid selection) are shown by the red and blue contours respectively. The rejection of maximal mixing increases from 1.2 σ to 1.7 σ when using all three analysis improvements together.

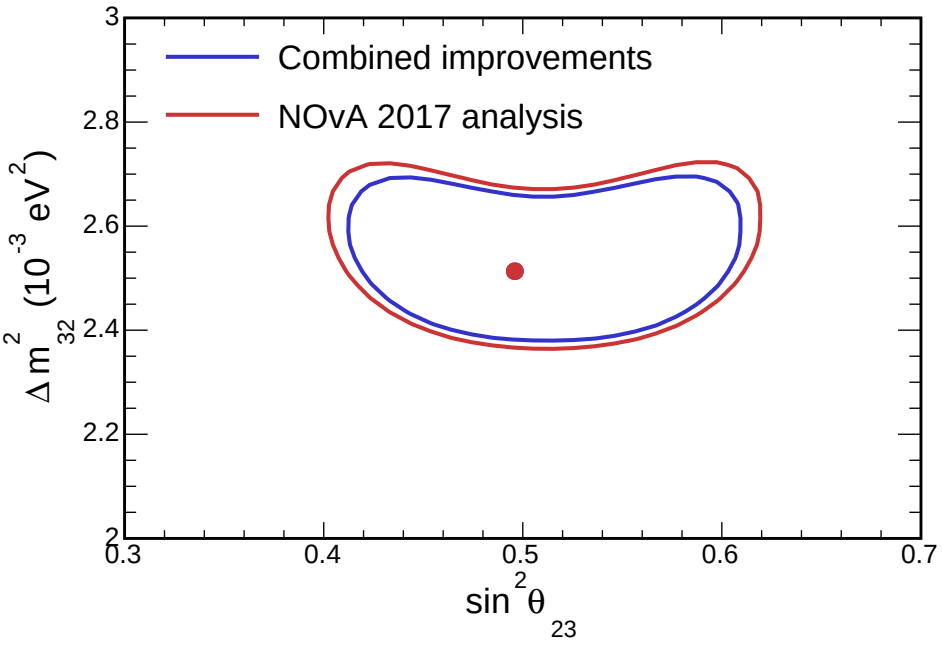

Figure 5.16: Sensitivity contours for the ν_μ disappearance analysis at T2K's 2015 [27] best-fit and NOvA's 2017 [41] exposure (6.05×10^{20} POT-equivalent). The sensitivity of the standard analysis and an analysis using the individually optimised sensitivity improvements (with 4 E_{had}/E_ν quantiles, neutrino energy binning scheme "A" and the hybrid selection) are shown by the red and blue contours respectively. The rejection of $\sin^2\theta_{23} = 0.6$ (marginalised for Δm^2_{32}) increases from 1.6 σ to 1.9 σ when using all three analysis improvements together.

neutrino energy binning) will then be varied to find the new setting that optimises the sensitivity. Afterwards, at the new optimal setting, the other improvement (e.g. splitting the events into E_{had}/E_{ν} quantiles) will be varied to find a new optimal setting. The process will continue until there is no significant gain in sensitivity.

First, the number of E_{had}/E_{ν} quantiles is varied to investigate the optimal number of E_{had}/E_{ν} quantiles when using binning scheme A. Comparisons of the sensitivity when using 4, 5, 6, 7 and 8 E_{had}/E_{ν} quantiles is shown for the NOvA, MINOS and T2K best fit points in Figures 5.17, 5.18 and 5.19. The contours show that, at all three best fit points, there is no significant sensitivity improvement when increasing the number of E_{had}/E_{ν} quantiles beyond 4. Therefore, when implented with the hybrid selection and binning scheme A the optimal number of E_{had}/E_{ν} quantiles remains at 4.

Second, the choice of energy binning scheme is varied whilst maintaining the hybrid selection and the use of 4 E_{had}/E_{ν} quantiles. Comparisons of the sensitivity when using each of the binning schemes (A, B and C) is shown for the NOvA, MINOS and T2K best fit points in Figures 5.20, 5.21 and 5.22. The contours show that there is no significant improvement to the sensitivity when using binning scheme B or C instead of scheme A.

The iterative search presented in this subsection has shown that the sensitivity does not significantly increase when going beyond 4 E_{had}/E_{ν} quantiles or using binning schemes B or C instead of A. The settings for the combination of analysis improvements will therefore remain the same as those found for each improvement independently in Sections 5.3, 5.4 and 5.5.

An increase in the sensitivity of the experiment can be expressed as the exposure required to gain the same sensitivity. At NOvA's 2017 [41] and MINOS's 2014 [40] best fit points the increased sensitivity to reject maximal mixing is equivalent to collecting 74% and 100% more data respectively. At T2K's 2015 [27] best fit point the increased rejection of $\sin^2\theta_{23} = 0.6$ is equivalent to collecting 41% more data.

5.8 Sensitivity Including the Cosmic Ray Background

The far detector is located on the surface of the Earth and as such is exposed to cosmic rays which form a background to the disappearance analysis. As described in Section 4.3, the cosmic ray background is estimated using both the timing sidebands of the data collected with the NuMI trigger and the data collected with the pulser trigger.

An estimate for the number of cosmic background events and the associated Poisson uncertainty is found using the sidebands of the NuMI trigger. The number of events and

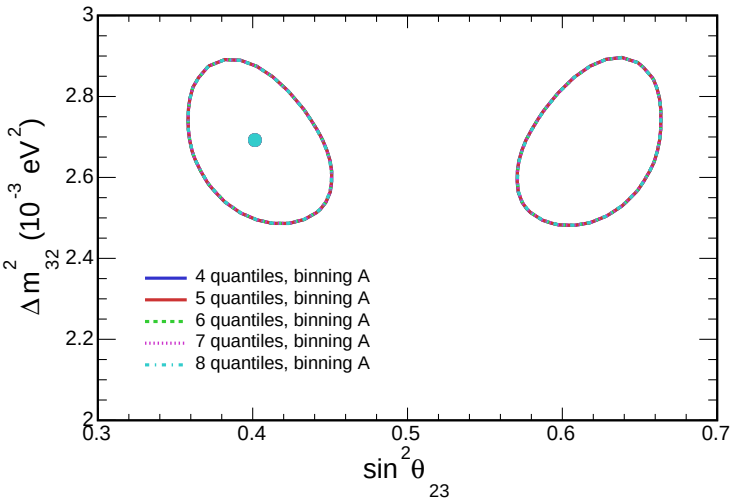

Figure 5.17: Sensitivity contours for the ν_μ disappearance analysis at NOvA's 2017 [41] best-fit and exposure (6.05×10^{20} POT-equivalent). The sensitivity using the individually optimised improvements is shown by the blue contour. The sensitivity for 5, 6, 7 and E_{had}/E_ν quantiles is shown by the red, dashed green, doted magenta and dash-dotted blue curves respectively. These contours are made with the hybrid selection and binning scheme A.

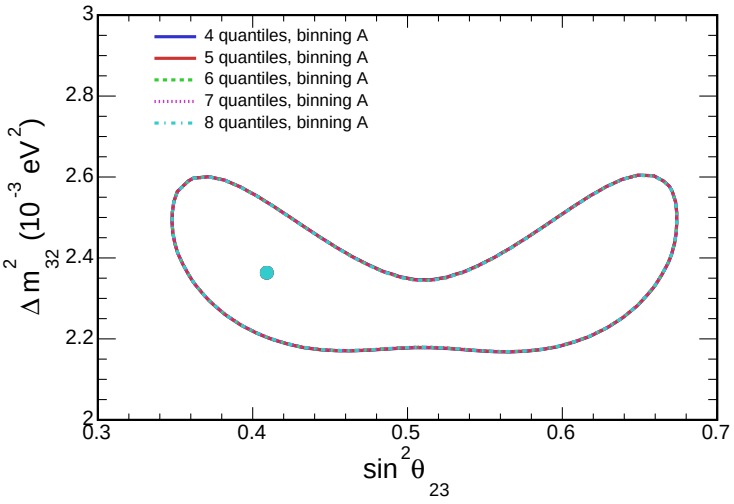

Figure 5.18: Sensitivity contours for the ν_μ disappearance analysis at MINOS's 2014 [40] best-fit and NOvA's 2017 [41] exposure (6.05×10^{20} POT-equivalent). The sensitivity using the individually optimised improvements is shown by the blue contour. The sensitivity for 5, 6, 7 and E_{had}/E_ν quantiles is shown by the red, dashed green, doted magenta and dash-dotted blue curves respectively. These contours are made with the hybrid selection and binning scheme A.

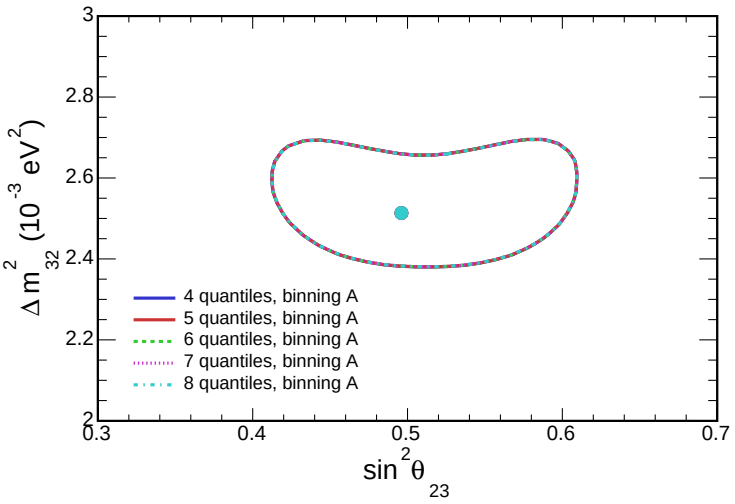

Figure 5.19: Sensitivity contours for the ν_μ disappearance analysis at T2K's 2015 [27] best-fit and NOvA's 2017 [41] exposure (6.05×10^{20} POT-equivalent). The sensitivity using the individually optimised improvements is shown by the blue contour. The sensitivity for 5, 6, 7 and E_{had}/E_ν quantiles is shown by the red, dashed green, doted magenta and dash-dotted blue curves respectively. These contours are made with the hybrid selection and binning scheme A.

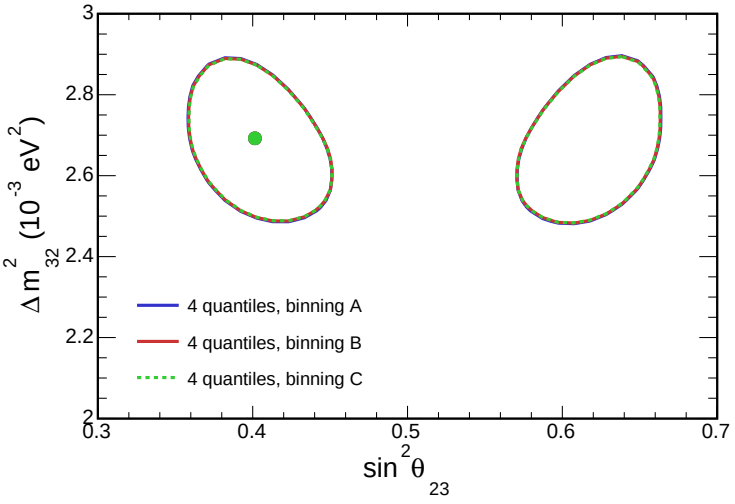

Figure 5.20: Sensitivity contours for the ν_μ disappearance analysis at NOvA's 2017 [41] best-fit and exposure (6.05×10^{20} POT-equivalent). The sensitivity using the individually optimised improvements is shown by the blue contour. The sensitivity for binning schemes B and C is shown by the red and dotted green lines respectively. All three sensitivity contours are made using the hybrid selection and 4 E_{had}/E_ν quantiles.

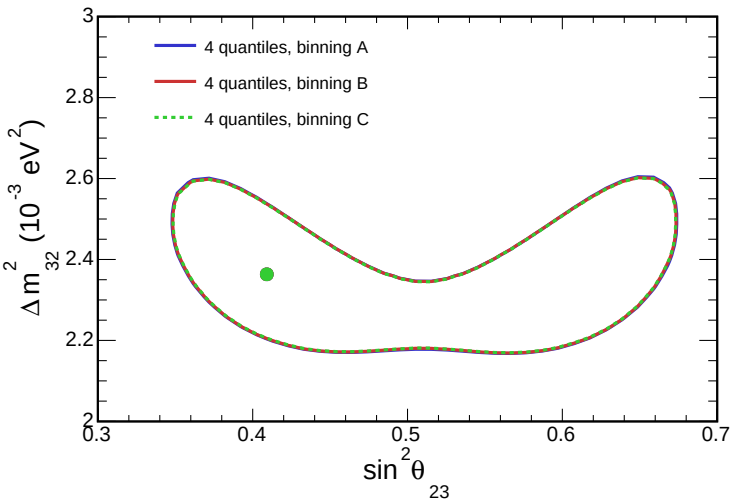

Figure 5.21: Sensitivity contours for the ν_μ disappearance analysis at MINOS's 2014 [40] best-fit and NOvA's 2017 [41] exposure (6.05×10^{20} POT-equivalent). The sensitivity using the individually optimised improvements is shown by the blue contour. The sensitivity for binning schemes B and C is shown by the red and dotted green lines respectively. All three sensitivity contours are made using the hybrid selection and 4 E_{had}/E_ν quantiles.

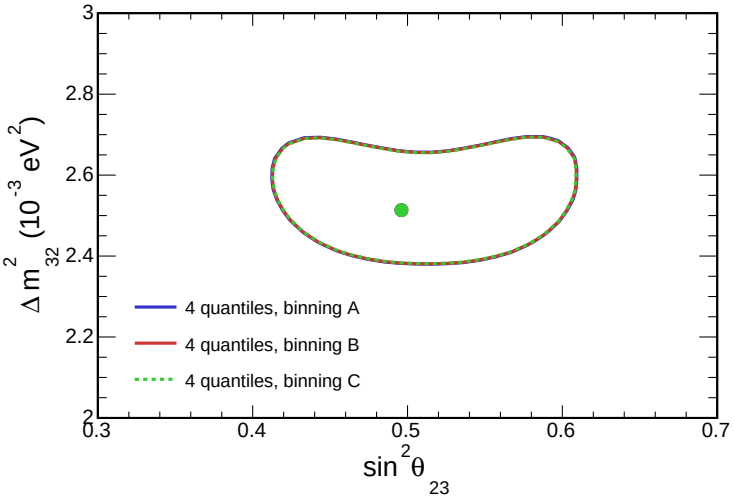

Figure 5.22: Sensitivity contours for the ν_μ disappearance analysis at T2K's 2015 [27] best-fit and NOvA's 2017 [41] exposure (6.05×10^{20} POT-equivalent). The sensitivity using the individually optimised improvements is shown by the blue contour. The sensitivity for binning schemes B and C is shown by the red and dotted green lines respectively. All three sensitivity contours are made using the hybrid selection and 4 E_{had}/E_ν quantiles.

E_{had}/E_ν quantile	Estimated in-time events	Out-of-time events
lowest E_{had}/E_ν	0.032 ± 0.032	1.0 ± 1.0
second lowest E_{had}/E_ν	0.065 ± 0.046	2.0 ± 1.4
second highest E_{had}/E_ν	0.45 ± 0.12	14 ± 4
highest E_{had}/E_ν	2.1 ± 0.3	65 ± 8

Table 5.2: The estimated count and associated Poisson uncertainty of cosmic background events within the NOvA 2017 [41] far detector analysis sample. A simple factor of 0.0324 is used to scale the live-times to produce an event estimate within the NuMI beam timing window from the event count outside the NuMI beam timing window.

error are adjusted to account for the different live-times of the data within the NuMI beam-spill and timing sideband samples. As mentioned in Section 4.3, the energy distribution of the cosmic events within each E_{had}/E_ν quantile is estimated from the data gathered by the pulser trigger. This trigger stream has the advantage of collecting more statistics than the NuMI trigger sideband and so it is used to determine the shape of the energy spectrum. The number of cosmic ray background events, associated uncertainty and energy distribution are estimated for each E_{had}/E_ν quantile individually.

Figure 5.23 shows the distribution of selected cosmic events in data, collected via the pulser trigger (Figure 5.23a) and the NuMI trigger sidebands (Figure 5.23b). In addition, Table 5.2 shows the estimates for the number of cosmic background events within the NuMI beam spill for each E_{had}/E_ν quantile. The distributions for the E_{had}/E_ν quantiles with the lowest, second lowest, second highest and highest E_{had}/E_ν are shown by the blue, dashed red, green and black lines. The large majority of the cosmic background events occur within the highest E_{had}/E_ν quantile. In contrast, the two quantiles with the lowest E_{had}/E_ν contain almost no events. For this reason, the energy distribution of the cosmic events (recorded using the pulser trigger) in the second highest E_{had}/E_ν quantile is used to estimate the shape of the energy distribution within the lowest and second lowest E_{had}/E_ν quantiles.

Sensitivities accounting for the cosmic ray background are shown for the NOvA 2017 [41], MINOS 2014 [40] and T2K 2015 [27] test points in Figures 5.24, 5.25 and 5.26 respectively. For the NOvA 2017 [41] test point, including the background reduces the maximal mixing rejection significance from 3.31 to 3.25 σ.

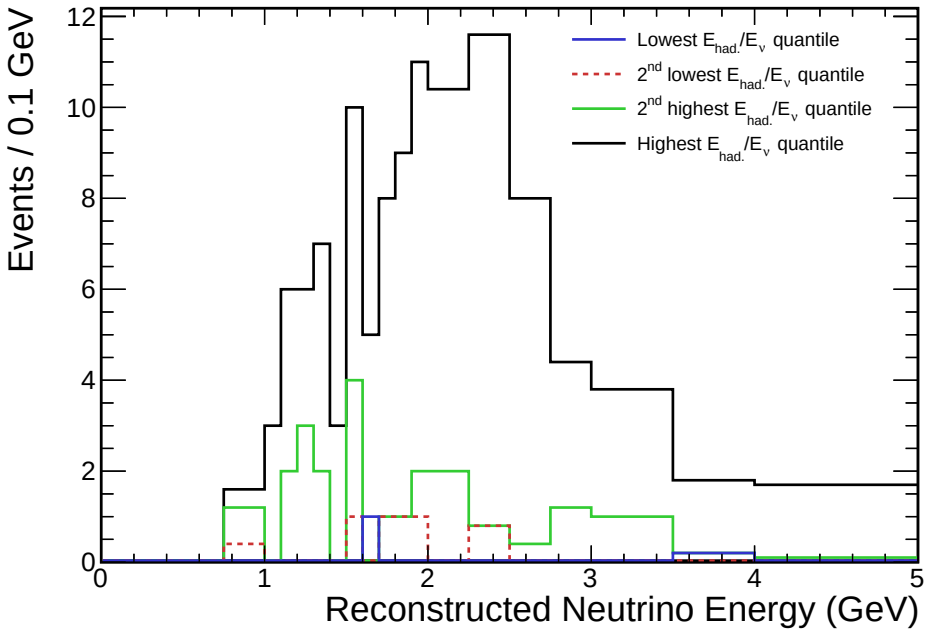

(a) Cosmic events selected as muon neutrino charged current candidates using the high statistics pulser trigger.

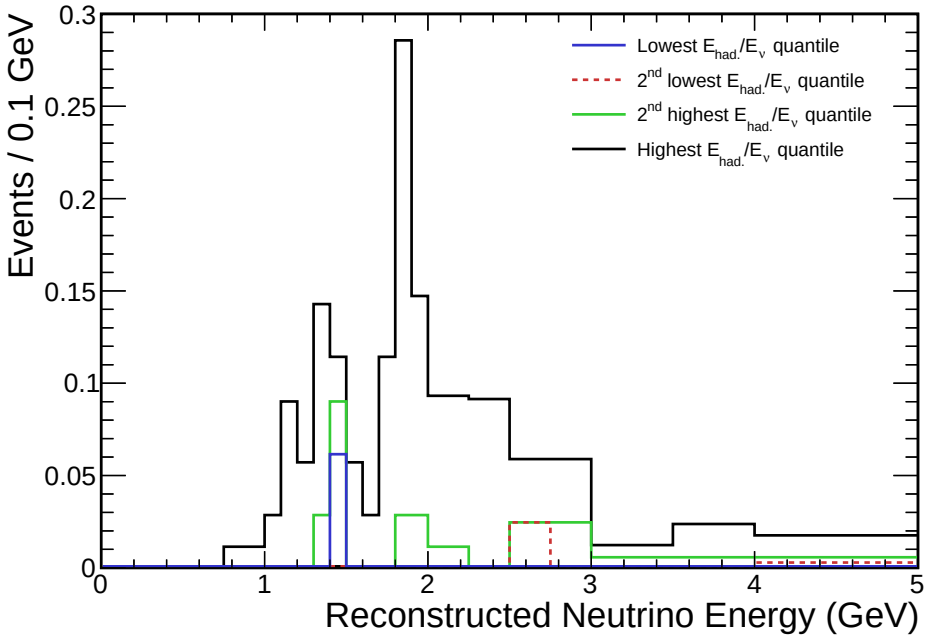

(b) Cosmic events selected as muon neutrino charged current candidates using the timing sidebands of the NuMI beam spill trigger. The distribution is scaled to the live-time of the beam timing window.

Figure 5.23: Muon neutrino energy distributions for cosmic background events collected during NOvA's 2017 [41] far detector live time. The distributions for the quantiles with the lowest, second lowest, second highest and highest E_{had}/E_{ν} are shown by the blue, dashed red, green and black lines respectively.

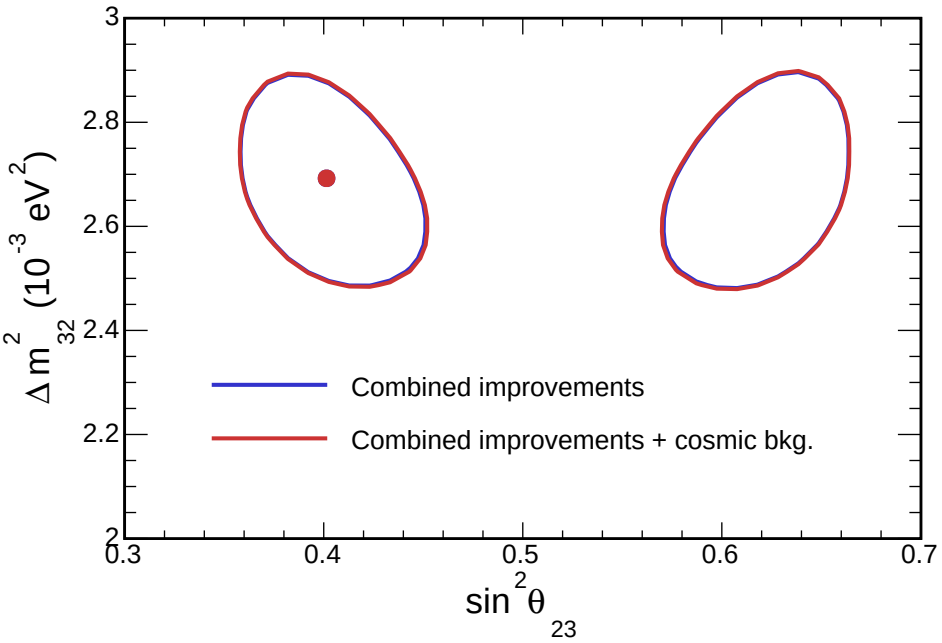

Figure 5.24: Sensitivity contours for the improved ν_μ disappearance analysis at NOvA's 2017 [41] best-fit and exposure (6.05×10^{20} POT-equivalent). The blue line shows the sensitivity of the analysis without accounting for the cosmic ray background. Including the cosmic ray background slightly reduces the sensitivity (shown by the red line). The rejection of maximal mixing is reduced from 3.31 to 3.25 σ.

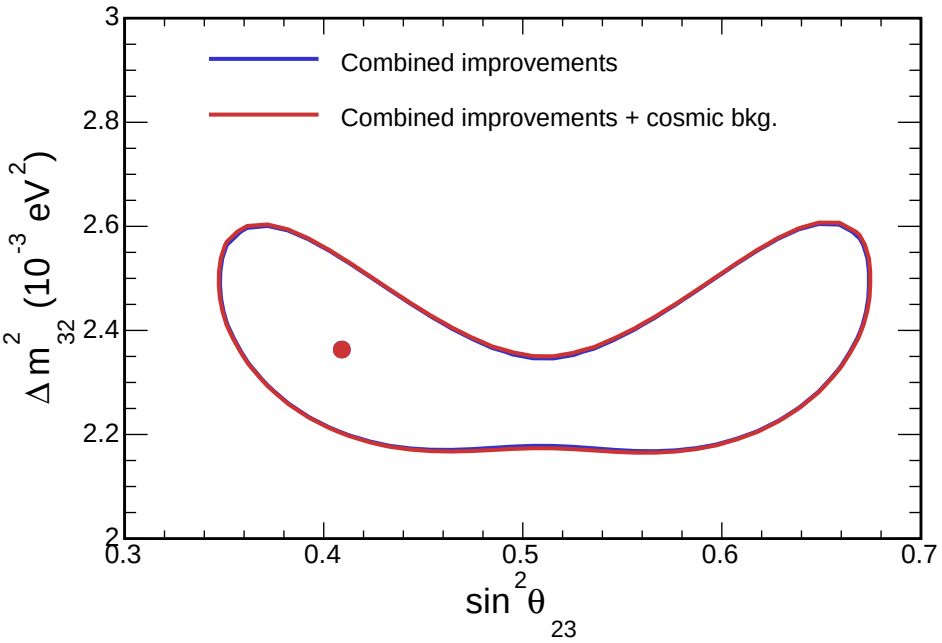

Figure 5.25: Sensitivity contours for the improved ν_μ disappearance analysis at MINOS's 2014 [40] best-fit and NOvA's 2017 [41] exposure (6.05×10^{20} POT-equivalent). The blue line shows the sensitivity of the analysis without accounting for the cosmic ray background. Including the cosmic ray background slightly reduces the sensitivity (shown by the red line). The rejection of maximal mixing is reduced from 1.74 to 1.70 σ.

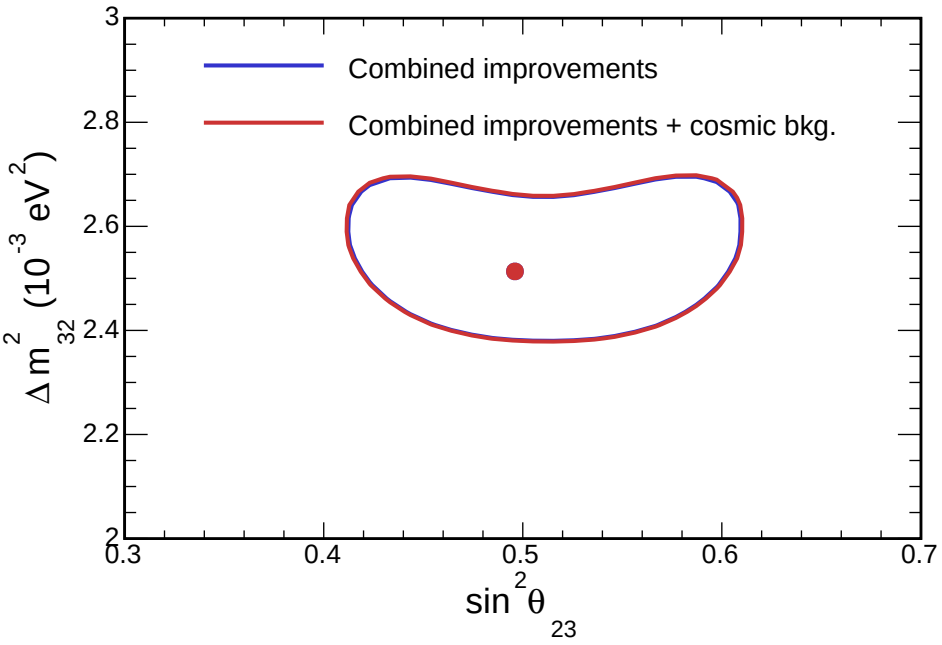

Figure 5.26: Sensitivity contours for the improved ν_μ disappearance analysis at T2K's 2015 [27] best-fit and NOvA's 2017 [41] exposure (6.05×10^{20} POT-equivalent). The blue line shows the sensitivity of the analysis without accounting for the cosmic ray background. Including the cosmic ray background slightly reduces the sensitivity (shown by the red line). The rejection of $\sin^2\theta_{23} = 0.6$ is reduced from 1.91 to 1.87 σ.

5.9 Systematic Uncertainty

The effect of each source of uncertainty on the analysis can be quantified in terms of the contribution to the total uncertainty in the oscillation parameter measurements. Focus is given to those systematic uncertainties that make the largest contribution to the total measurement uncertainty. The systematics uncertainties cover the energy scale, normalisation, GENIE, background and scintillation model systematic uncertainties. An important feature of the new improved analysis is that events are able to migrate between E_{had}/E_{ν} quantiles in response to systematic uncertainties and this was explicitly demonstrated in [94].

Table 5.3 details each source of systematic uncertainty and the corresponding oscillation parameter measurement uncertainty for both NOvA's 2017 [41] analysis and the improved analysis. NOvA's 2017 [41] upper octant best fit point was used to analyse the impact of each systematic uncertainty shown in the table. Each uncertainty shown in the table is evaluated by comparing two fits. The first fit only considers the statistical uncertainty. Whereas, the second fit also includes the systematic uncertainty. Subtraction in quadrature of the 68% C.L. boundaries from the two fits quantifies the systematic uncertainty in the oscillation parameters.

For NOvA's 2017 [41] analysis, the largest sources of systematic uncertainty in $\sin^2\theta_{23}$ are the combined relative and absolute normalisations, the relative and absolute energy scales and the neutral current background. The largest sources of uncertainty in Δm^2_{32} are the energy scales, Birks' suppression, MaCCRES (axial mass for CC resonance) and the neutral current background.

With the introduction of the analysis improvements there are several significant changes to the effect of the systematic uncertainties on the oscillation parameter measurements. In particular:

- The neutral current systematic improves by a factor of 2-4. It goes from being the largest systematic uncertainty on $\sin^2\theta_{23}$ to one of only medium importance. This is thought to be due to the E_{had}/E_{ν} analysis improvement, where almost all NC events fall into the worst energy resolution bin.

- The normalisation systematic has the same value in the new analysis but becomes the joint largest (with the combined energy scale systematics) on $\sin^2\theta_{23}$, due to the other systematics becoming smaller.

- The energy scale systematic uncertainties are the largest uncertainty on Δm^2_{32} and

among the most important for $\sin^2\theta_{23}$. The impact of the absolute energy scale systematic uncertainties on Δm^2_{32} have increased slightly in the new analysis while the relative energy scale systematics have decreased slightly.

- The cross-section systematics are of medium importance for both $\sin^2\theta_{23}$ and Δm^2_{32}. Their impact decreased by about 15% in the new analysis. The individual cross-section systematics that contribute the most are the effective charged current resonance axial mass and vector mass uncertainties as well as the 2p2h-MEC uncertainty.

The uncertainty in δ_{CP} causes a linear shift to the oscillation parameter measurements due to degeneracy between δ_{CP} and Δm^2_{32} [95]. The uncertainty due to δ_{CP} is found in two stages. First, the 1 σ upper and lower bounds are found when allowing δ_{CP} to vary across the whole range of possible values. Second, the linear difference between these bounds and the statistical uncertainty only bounds defines the uncertainty on the oscillation parameter due to δ_{CP} [96]. Before the improvements the uncertainty due to δ_{CP} in the measurement of $\sin^2\theta_{23}$ is small relative to the other sources of uncertainty. However, δ_{CP} is one of the larger contributors to the uncertainty in Δm^2_{32}. The uncertainty due to δ_{CP} does not significantly change when the analysis improvements are introduced as expected because of the inherent degeneracy between δ_{CP} and Δm^2_{32}.

The analysis improvements presented in this chapter decrease the impact of the systematic and statistical uncertainty on the oscillation parameter ($\sin^2\theta_{23}$ and Δm^2_{32}) measurements. The contribution of the systematic uncertainties are reduced from a 2.2% to 2.0% uncertainty on Δm^2_{32} and from a 2.1% to 1.5% uncertainty on $\sin^2\theta_{23}$. The reduced uncertainty in the measurement of $\sin^2\theta_{23}$ is largely due to reducing the impact of the energy scale and neutral current background uncertainties. Whereas, the reduced uncertainty in Δm^2_{32} is due to the decreased contributions of the normalisations, neutral current background, GENIE, MEC and RPA uncertainties.

For the GENIE uncertainties a few abbreviations are used with the following meanings:

- NormCCQE: charged current (CC) quasi-elastic cross-section scale.
- MaCCQEShape: axial mass for CC quasi-elastic.
- MaCCRES: axial mass for CC resonance.
- MvCCRES: vector mass for CC resonance.
- MaNCRES: axial mass for NC resonance.

- CCQEPauliSupViaKF: CC quasi-elastic Pauli suppression via the Fermi level k_F.
- MEC: 2-particle 2-hole meson exchange current scale.

5.10 Summary of Analysis Improvements

In this chapter, three improvements to NOvA's muon neutrino disappearance analysis were discussed and optimised for an exposure of 6.05×10^{20} POT-equivalent. The improvements include introducing a finer neutrino energy binning around the oscillation maximum, separating events by E_{had}/E_ν and using a hybrid of two selection algorithms to reject background. Each improvement was optimised considering both the improvement to the sensitivity and the demand for computational resources. The final optimised setting for each improvement is as follows: events are separated into 4 quantiles of E_{had}/E_ν, neutrino energy is binned using binning scheme "A" and events are selected using the ReMId-CVN hybrid selection. The combination of all three of the improvements significantly increases the sensitivity of the experiment to $\sin^2\theta_{23}$ and Δm^2_{32}. For example, using NOvA's 2017 [41] best-fit point as a test point, the introduction of the improvements increases the rejection of maximal mixing from 2.51 to 3.25 σ (including the cosmic ray background). These improvements are approximately equivalent to accumulating between 40-100% more data (depending on the oscillation test point).

In the next chapter the improvements discussed in this chapter will be used to analyse the far detector data. A fit of a MC prediction to the data will be used to extract measurements of the neutrino oscillation parameters Δm^2_{32} and $\sin^2\theta_{23}$.

Table 5.3: Table of uncertainty in $\sin^2\theta_{23}$ and Δm^2_{32} due to each source of systematic uncertainty when using NOvA's 2017 [41] (upper octant) best fit ($\sin^2\theta_{23} = 0.626$, $\Delta m^2_{32} = 2.67 \times 10^{-3}$ eV^2). The uncertainty when using both NOvA's 2017 [41] analysis and the new improved analysis are shown. The largest uncertainties in the oscillation parameters are shown in bold. Uncertainties that are significantly reduced by the analysis improvements are shown in green while uncertainties that are increased are shown in red. The abbreviations used are described in Section 5.9.

Source of uncertainty	Uncertainty in $\sin^2\theta_{23}(\times 10^{-3})$		Uncertainty in $\Delta m^2_{32}\left(\times 10^{-6}\text{ eV}^2\right)$	
	NOvA '17	New analysis	NOvA '17	New analysis
Normalisations	**+5.4 / -4.7**	**+5.2 / -5.1**	+5.1 / -11	+1.0 / -9.2
Absolute muon energy	**+3.7 / -2.6**	**+2.4 / -1.8**	**+14 / -20**	**+16 / -23**
Relative muon energy	**+4.4 / -4.7**	**+3.1 / -3.3**	**+11 / -9.3**	**+7.7 / -4.4**
Absolute hadronic energy	+1.3 / -1.7	+2.1 / -2.8	**+11 / -13**	**+16 / -19**
Relative hadronic energy	**+5.0 / -5.5**	**+3.0 / -3.2**	**+14 / -11**	**+8.2 / -5.2**
Birks'	+0.47 / -0.11	+0.22 / -0.78	**+10 / -12**	**+12 / -14**
Summed small GENIE	+0.54 / -1.1	+0.19 / -0.38	+1.1 / -2.5	+0.42 / -0.75
NormCCQE	+0.41 / -0.46	+0.81 / -1.1	+1.1 / -1.0	+2.9 / -2.8
MaCCQEshape	+0.49 / -0.32	+0.52 / -0.41	+2.2 / -3.0	+1.6 / -2.7
MaCCRES	+1.1 / -0.41	+0.59 / -0.13	**+13 / -15**	**+11 / -14**
MvCCRES	+0.76 / -0.32	+0.50 / -0.10	+7.6 / -9.2	+7.2 / -9.3
MaNCRES	+0.41 / -0.86	+0.15 / -0.26	+1.5 / -2.7	+0.59 / -0.84
CCQEPauliSupViaKF	+0.61 / -0.42	+0.55 / -0.40	+2.4 / -3.5	+1.9 / -3.1
MEC scale	+0.41 / -0.83	+0.69 / -1.2	+8.2 / -9.0	+8.9 / -9.7
RPA	+0.41 / -0.23	+0.27 / -0.13	+2.7 / -3.0	+2.6 / -3.1
Comb. GENIE+MEC+RPA	+1.8 / -1.9	+1.6 / -1.8	**+18 / -21**	**+15 / -18**
NC background	**+3.3 / -6.6**	**+1.4 / -2.3**	**+9.2 / -17**	**+3.3 / -4.6**
Cosmic background	+0.46 / -0.68	+0.57 / -0.79	+0.35 / -0.00	+0.95 / -1.4
TransportPlusNA49	+1.2 / -2.3	+0.70 / -1.2	+3.0 / -6.4	+3.0 / -4.7
δ_{CP}	+0.2 / -0.3	+0.2 / -0.2	**+14 / -13**	**+14 / -13**
Statistical uncertainty	+21 / -23	+19 / -19	+98 / -95	+86 / -83
Total systematic uncertainty	+11 / -13	+9.6 / -9.3	+57 / -58	+54 / -53
Total uncertainty	+23.9 / -27.1	+21.1 / -22.6	+121 / -118	+109 / -105

Chapter 6

Results

This chapter discusses the result of using the analysis improvements, introduced in Chapter 5, to re-analyse NOvA's 2017 [41] data set and extract a measurement of the neutrino oscillation parameters. The results are produced using the near and far detector data collected between the 6th February 2013 and the 2nd of May 2016. In the far detector this data corresponds to a 14 ktonne equivalent exposure of 6.05×10^{20} protons on target [41].

The chapter proceeds in stages, starting in the near detector and moving onto the far detector. First of all, the data-MC agreement in the near detector is assessed using distributions of variables important to the analysis. Next, the same comparisons are made in the far detector. Finally, a fit to the far detector neutrino energy spectrum is used to extract measurements of the oscillation parameters Δm^2_{32} and $\sin^2\theta_{23}$.

6.1 Near Detector Distributions

In this section, the near detector is used to compare the distribution of the energy variables in data and simulation for each of the E_{had}/E_ν quantiles. These near detector plots are used to assess the agreement between data and MC before opening the box and looking at the far detector data. The MC and data normalisations differ by approximately 1% for selected events. In the ND comparison plots the MC is area-normalised to the data and only the systematics effecting the shape of the distributions are shown. The normalisation systematic uncertainties are included when performing the extrapolation and will be reduced due to the functional equivalence of the near and far detector.

Comparisons between the data and simulation distributions of hadronic, muon and neutrino energy in the near detector are shown for each E_{had}/E_ν quantile in Figures 6.1, 6.2 and 6.3. The data are shown by the black points while the simulation and total

uncertainty on the simulation are shown by the red histogram and red shaded region respectively. The uncertainty is evaluated for each by taking the combination of shifts to the systematics within 1 σ that produces the largest uncertainty band. The combined systematic uncertainties are then combined with the statistical uncertainty (which is relatively low due to the large number of events in the simulation) in quadrature The simulated background passing the selection is shown by the blue histogram. For hadronic energy, the agreement between data and simulation is within errors for the two lowest quantiles but worsens for the two higher E_{had}/E_{ν} quantiles. In the two highest quantiles the data shows a shift to lower energy than the MC beyond the systematic uncertainty bands. The agreement between the data and MC muon energy distributions also worsens as the E_{had}/E_{ν} quantile is increased, showing a similar pattern of data-MC agreement as seen in the hadronic energy. In the two highest E_{had}/E_{ν} quantiles the data is visibly shifted to lower energy than the MC. The data MC agreement is at its worst at low reconstructed muon energies (< 1 GeV) where data rises up above the MC. Section 6.1.1 will discuss a correction to the energy calibration and re-evaluate the data-MC agreement in the three energy variables.

For the MC, the mean muon neutrino energy distribution does not visibly shift which is expected because the events are split into quantiles defined for each bin of neutrino energy. Similarly to the hadronic and muon energy distributions, the data-simulation agreement is within errors for the lowest two quantiles and worsens for the two highest E_{had}/E_{ν} quantiles where the data is shifted lower than the MC. The beam background is concentrated in the highest E_{had}/E_{ν} plot, as can be seen in Figure 6.3e between approximately 1 and 2 GeV. The mean of the MC and data distributions are shown in the legend of each plot. For all the quantiles combined the MC mean is approximately 2% higher than the data mean. In the lowest two quantiles the difference is reduced and the MC is approximately 1% higher. However, in the second highest and highest quantiles the difference increases and the MC mean shifts to 3% and 4% higher than data respectively. Section 6.1.1 discusses these differences and how they are handled in the analysis.

Distributions showing the breakdown into each interaction type are shown for the muon, hadronic and muon neutrino energy in Figures 6.4, 6.5 and 6.6 respectively. Events in the lowest E_{had}/E_{ν} quantile are mostly quasi-elastic (QE) type interactions. These interactions tend to impart most of the neutrino energy to the outgoing muon and only a small fraction of the neutrino energy to the target nucleon. The second lowest E_{had}/E_{ν} quantile consists of a mixture of resonance (RES), quasi-elastic and two-particle-two-hole

	Events per quantile		Events per quantile / total events	
E_{had}/E_{ν} quantile	Data	MC	Data	MC
Lowest	452036	486712	0.233	0.249
Second lowest	514559	487350	0.265	0.249
Second highest	481683	488231	0.248	0.250
Highest	494984	494473	0.255	0.253
Total	1.94326e+06	1.95677e+06	1	1

Table 6.1: Events and share of total events within each quantile in data and MC.

meson exchange current (2p2h-MC) type events. The second highest quantile consists of mostly resonance type events. Finally, the highest quantile contains a mixture of resonance and deep inelastic-scattering (DIS) type events. There is a small amount of coherent scattering (Coh) type events in the highest and second highest E_{had}/E_{ν} quantiles.

The number of candidate neutrino events within each quantile in both data and MC is shown in Table 6.1. Also shown are the events within each quantile divided by the total events. Each quantile should contain close to 25% of the total events in both data and MC. In data, each quantile's share of events differs from 25%, the lowest and second lowest E_{had}/E_{ν} quantiles contain 23.3% and 26.5% of the events respectively. My study [97] considered the effect of a few of the cross-section systematics on the fraction of events within each quantile. The study showed that the divergence of each quantile's fraction of events in data from 25% is covered by 1 σ shifts to two GENIE [50] systematic uncertainties, the normalisation of charged current quasi-elastic events (NormCCQE) and the effective charged current resonance axial mass (MaCCRES).

Data-MC comparisons of the CVN muon neutrino identification scores and the ReMID distributions for each quantile are shown in Figures 6.7 and 6.8 respectively. The data-MC agreement is good for each of the quantiles and also for the combination of all quantiles.

Three of the variables used to create the ReMId selection are also shown. The dE/dx log-likelihood is shown in Figure 6.9, the scattering log-likelihood is shown in Figure 6.10 and the fraction of planes within the event that do not contain hadronic activity is shown in Figure 6.11. The non hadronic plane fraction shows good data-MC agreement but the dE/dx log-likelihood and scattering log-likelihood shows some disagreement between data and MC.

The direction of the leading track relative to the detector z-axis, $\cos\theta_Z$, is shown for each quantile in Figure 6.12. The data and MC agree within the errors for the two lowest

E_{had}/E_ν quantiles. However, in the two highest E_{had}/E_ν quantiles there is significant MC excess at high values of $\cos\theta_Z$ (when the track is close to the beam direction) and a MC deficit at lower values of $\cos\theta_Z$. To investigate further, plots of track length vs. track direction in data are shown in Figures 6.13. For each $\cos\theta_Z$ bin the mean of the profile is shown by the black circles with statistical error bars. In the lowest E_{had}/E_ν quantile the distribution is peaked at high track length and high $\cos\theta_Z$ but with increasing E_{had}/E_ν quantile the distribution shifts to lower values of track length and $\cos\theta_Z$. The difference between the data and MC distributions of track length vs. $\cos\theta_Z$ is shown by the bin colour in Figure 6.14. For each quantile, there is a MC deficit at low track lengths (less than approximately 5 m) for all values of $\cos\theta_Z$. The MC excess appears at higher values of track length and $\cos\theta_Z$. At the time of writing, the discrepency described above is under active investigation. It is suspected that the uncertainty band may not be capturing the effect of all the GENIE systematic uncertainties due to the NOvA implementation. Additionally, there could perhaps be an under estimate in the RES-DIS transition region uncertainty in the simulation.

The number of Kalman tracks is shown for each quantile in Figure 6.15. The agreement between data and MC is good for all quantiles. With increasing E_{had}/E_ν the number of tracks in the slice increases, from predominately single track events in the two lowest quantiles to mostly two or more track events in the highest E_{had}/E_ν quantile. The maximum height of activity within the detector (y-coordinate) in selected events is displayed in Figure 6.16. The distributions display reasonably good agreement between data and MC.

The starting point of the leading track is shown in x, y and z detector coordinates for each quantile in Figure 6.17, 6.18 and 6.19 respectively. Conversely, the stopping point of the leading track in x, y and z detector coordinates is shown in Figure 6.20, 6.21 and 6.22 respectively. The agreement between data and MC is reasonable for all the track start and end point distributions.

In general the distributions described above show good data-MC agreement. However, the vitally important hadronic, muon and neutrino energy distributions show some disagreement between data and MC. For hadronic energy, the data-MC agreement is good in the two lowest E_{had}/E_ν quantiles but the MC is significantly higher than the data in the two highest quantiles. The muon and neutrino energy in data are both visibly shifted to lower energies relative to the MC. A remedy for these discrepancies will be discussed next.

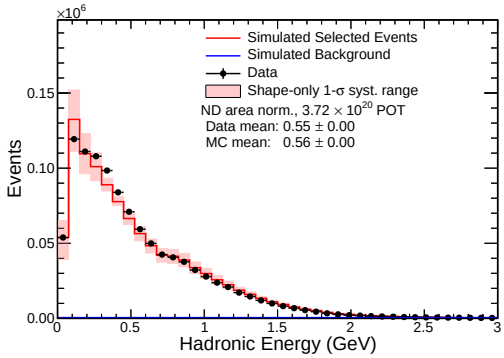

(a) All E_{had}/E_{ν} quantiles combined.

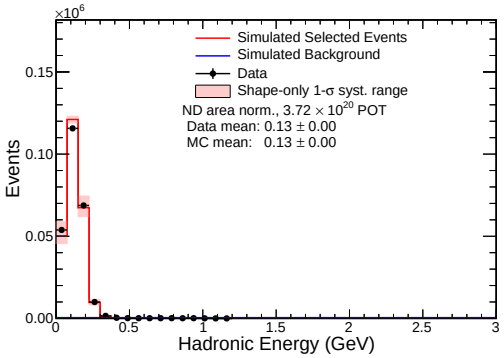

(b) Lowest E_{had}/E_{ν} quantile.

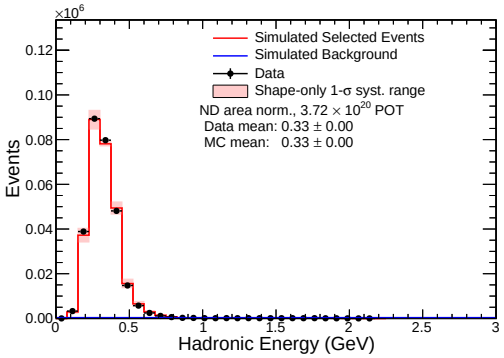

(c) Second lowest E_{had}/E_{ν} quantile.

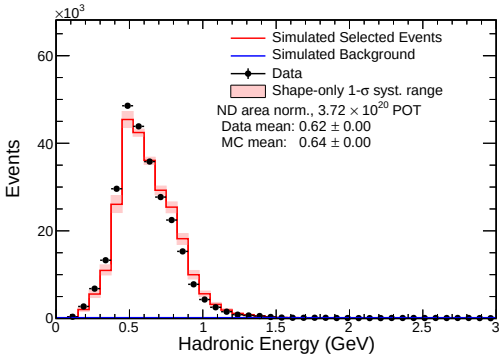

(d) Second highest E_{had}/E_{ν} quantile.

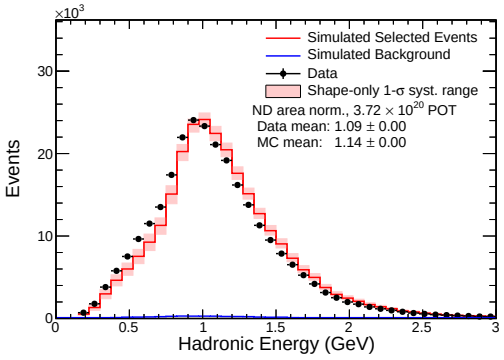

(e) Highest E_{had}/E_{ν} quantile.

Figure 6.1: Plots showing the number of events vs. the hadronic energy for each E_{had}/E_{ν} quantile. The events passing selection for simulation and data are shown by the red histogram and the black data-points respectively. The systematic uncertainty in the distribution of the simulated events is shown by the shaded red region enclosing the red histogram. The simulated background events passing the selection are shown by the blue histogram.

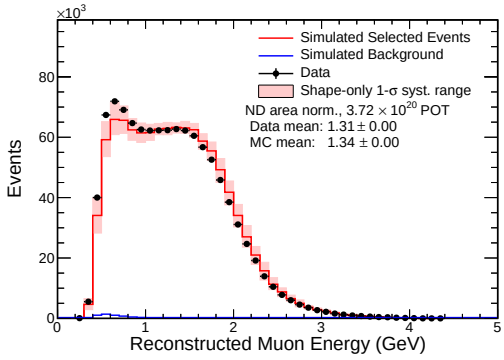

(a) All E_{had}/E_{ν} quantiles combined.

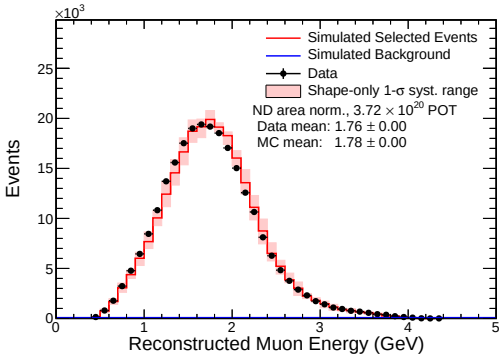

(b) Lowest E_{had}/E_{ν} quantile.

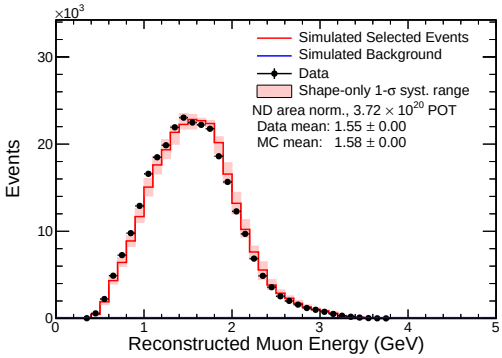

(c) Second lowest E_{had}/E_{ν} quantile.

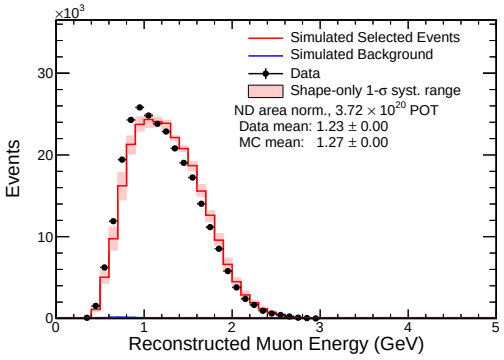

(d) Second highest E_{had}/E_{ν} quantile.

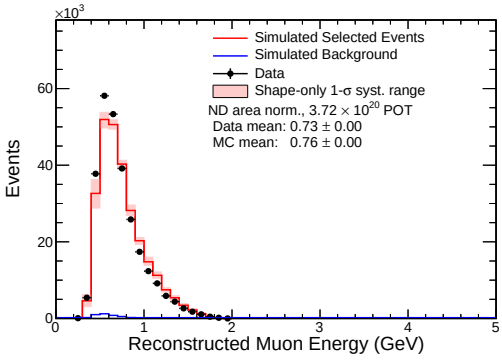

(e) Highest E_{had}/E_{ν} quantile.

Figure 6.2: Plots showing the number of events vs. the muon energy for each E_{had}/E_{ν} quantile. The events passing selection for simulation and data are shown by the red histogram and the black data-points respectively. The systematic uncertainty in the distribution of the simulated events is shown by the shaded red region enclosing the red histogram. The simulated background events passing the selection are shown by the blue histogram.

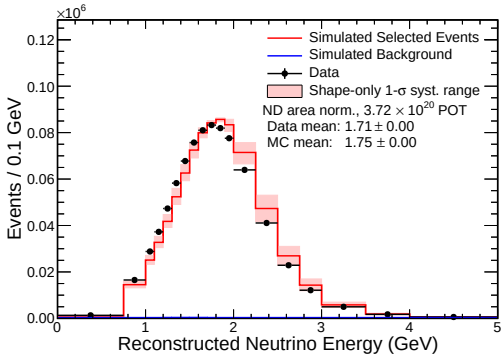

(a) All E_{had}/E_{ν} quantiles combined.

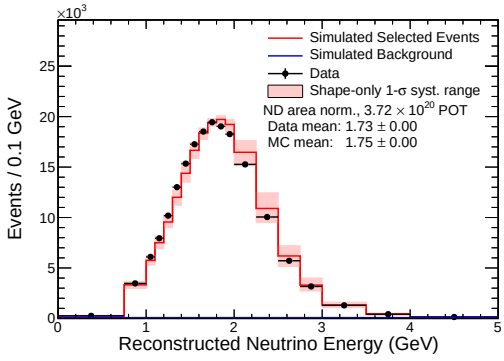

(b) Lowest E_{had}/E_{ν} quantile.

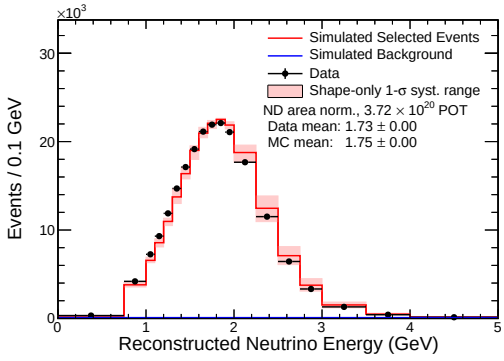

(c) Second lowest E_{had}/E_{ν} quantile.

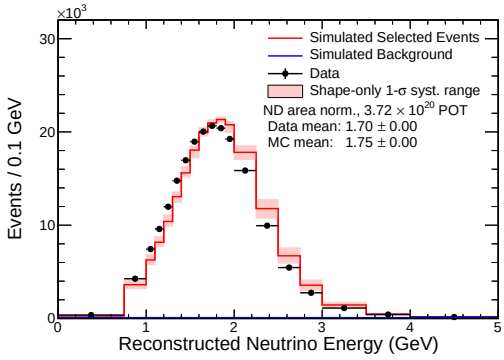

(d) Second highest E_{had}/E_{ν} quantile.

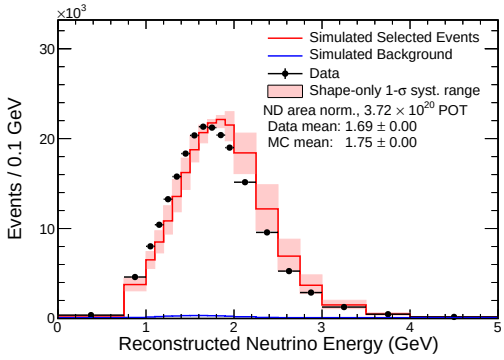

(e) Highest E_{had}/E_{ν} quantile.

Figure 6.3: Plots showing the number of events vs. the muon neutrino energy for each E_{had}/E_{ν} quantile. The events passing selection for simulation and data are shown by the red histogram and the black data-points respectively. The systematic uncertainty in the distribution of the simulated events is shown by the shaded red region enclosing the red histogram. The simulated background events passing the selection are shown by the blue histogram.

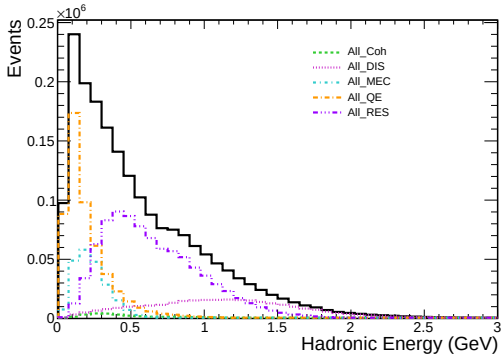

(a) All E_{had}/E_{ν} quantiles combined.

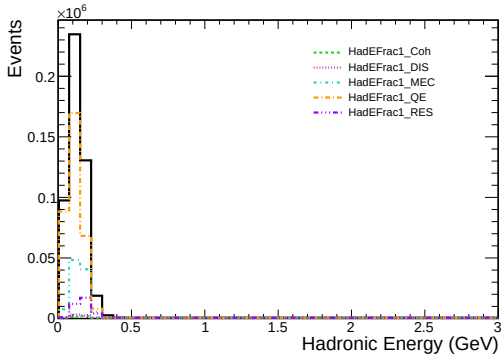

(b) Lowest E_{had}/E_{ν} quantile.

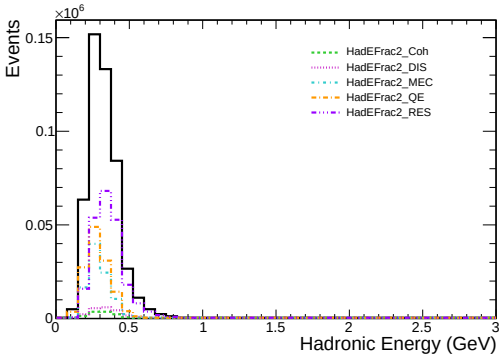

(c) Second lowest E_{had}/E_{ν} quantile.

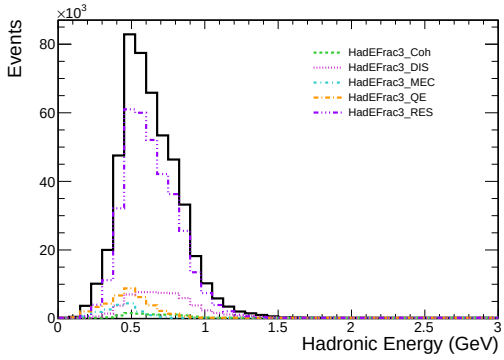

(d) Second highest E_{had}/E_{ν} quantile.

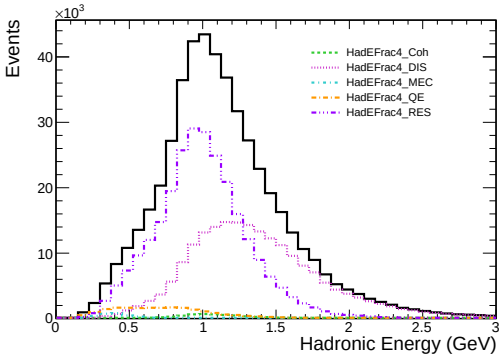

(e) Highest E_{had}/E_{ν} quantile.

Figure 6.4: Plots showing the number of events vs. the hadronic energy for each E_{had}/E_{ν} quantile. The distribution for quasi-elastic (QE), resonance (RES), deep inelastic-scattering (DIS), coherent scattering (Coh) and two-particle-two-hole meson-exchange-current (2p2h MEC) type interactions are shown by the dash-dotted orange, dash-triple-dotted purple, dotted magenta, dashed green and dash-dotted blue lines respectively.

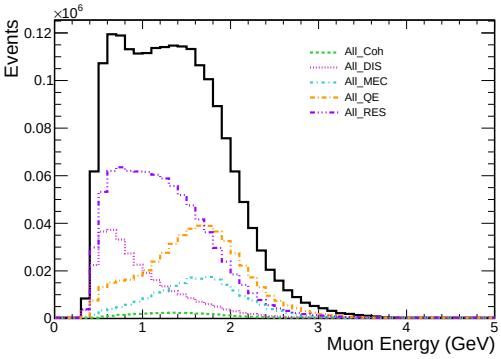

(a) All E_{had}/E_{ν} quantiles combined.

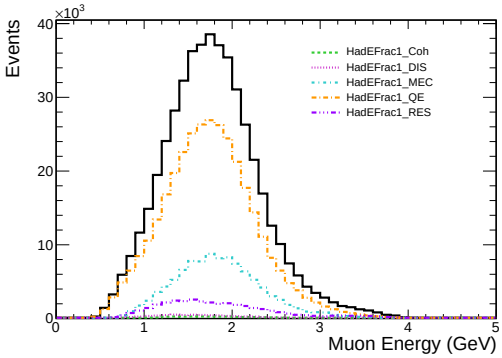

(b) Lowest E_{had}/E_{ν} quantile.

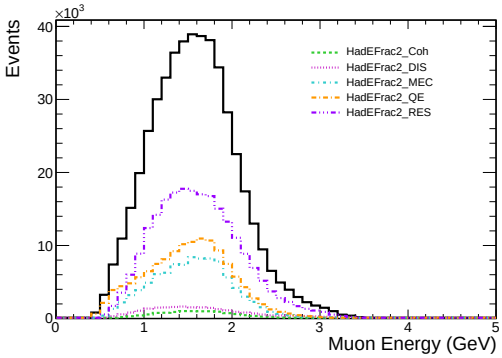

(c) Second lowest E_{had}/E_{ν} quantile.

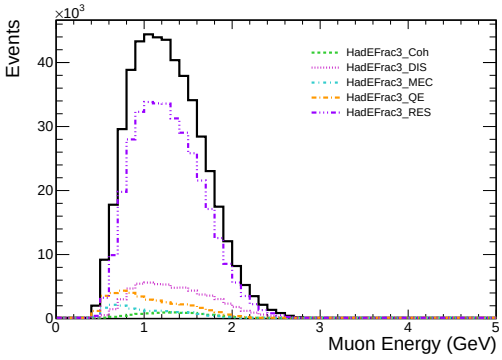

(d) Second highest E_{had}/E_{ν} quantile.

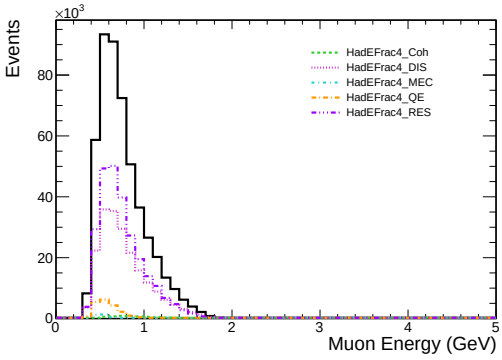

(e) Highest E_{had}/E_{ν} quantile.

Figure 6.5: Plots showing the number of events vs. the muon energy for each E_{had}/E_{ν} quantile. The distribution for quasi-elastic (QE), resonance (RES), deep inelastic-scattering (DIS), coherent scattering (Coh) and two-particle-two-hole meson-exchange-current (2p2h MEC) type interactions are shown by the dash-dotted orange, dash-triple-dotted purple, dotted magenta, dashed green and dash-dotted blue lines respectively.

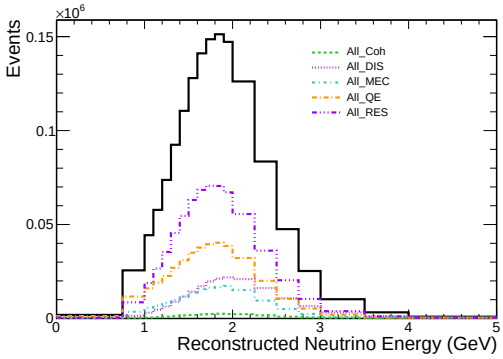

(a) All E_{had}/E_{ν} quantiles combined.

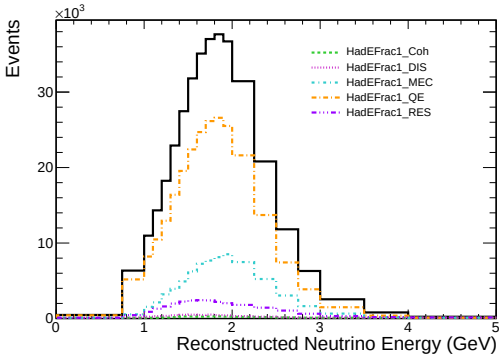

(b) Lowest E_{had}/E_{ν} quantile.

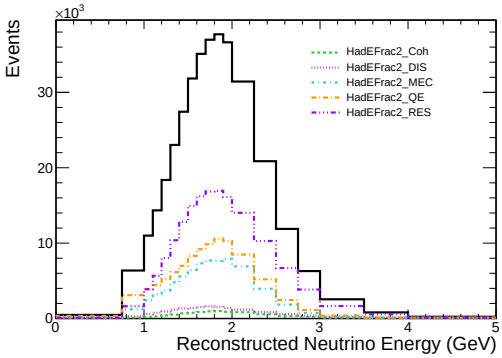

(c) Second lowest E_{had}/E_{ν} quantile.

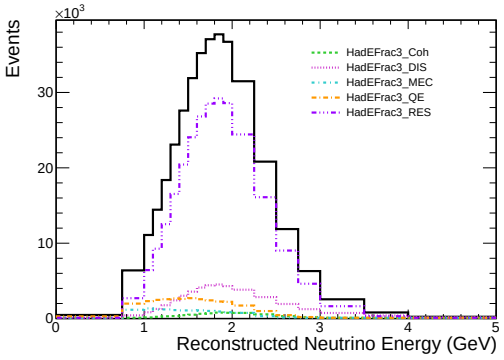

(d) Second highest E_{had}/E_{ν} quantile.

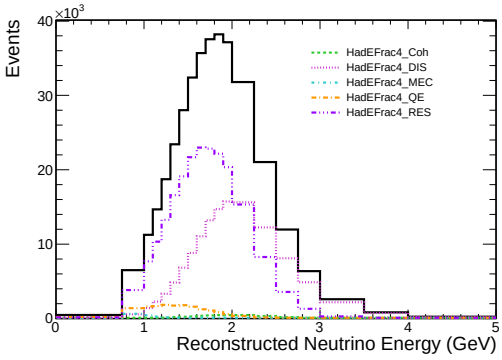

(e) Highest E_{had}/E_{ν} quantile.

Figure 6.6: Plots showing the number of events vs. the muon neutrino energy for each E_{had}/E_{ν} quantile. The distribution for quasi-elastic (QE), resonance (RES), deep inelastic-scattering (DIS), coherent scattering (Coh) and two-particle-two-hole meson-exchange-current (2p2h MEC) type interactions are shown by the dash-dotted orange, dash-triple-dotted purple, dotted magenta, dashed green and dash-dotted blue lines respectively.

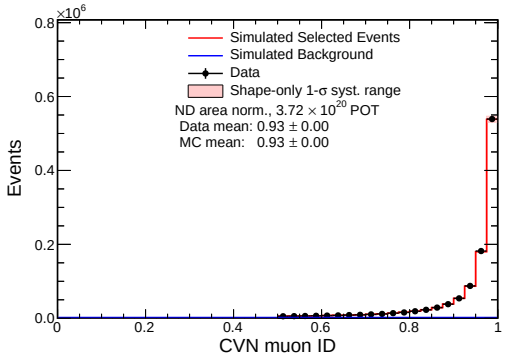

(a) All E_{had}/E_{ν} quantiles combined.

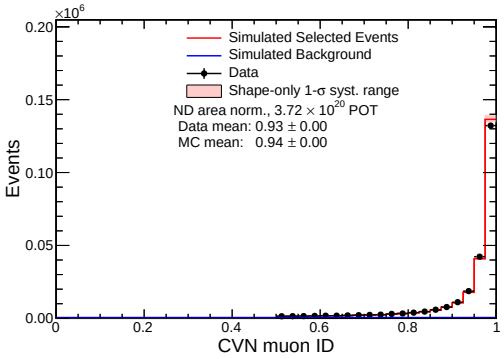

(b) Lowest E_{had}/E_{ν} quantile.

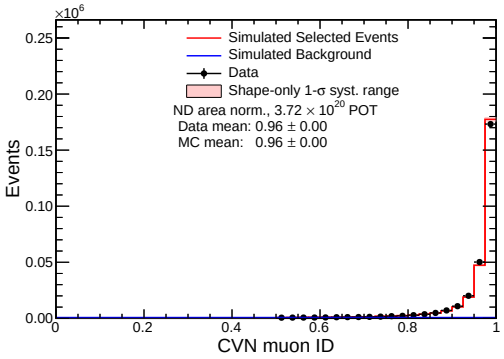

(c) Second lowest E_{had}/E_{ν} quantile.

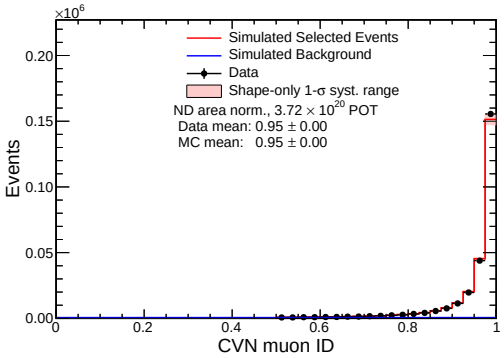

(d) Second highest E_{had}/E_{ν} quantile.

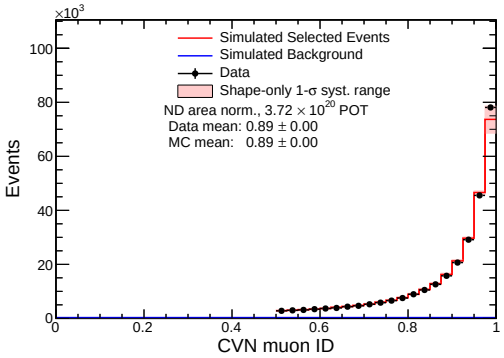

(e) Highest E_{had}/E_{ν} quantile.

Figure 6.7: Plots showing the number of events vs. the CVN muon identification score for each E_{had}/E_{ν} quantile. The CVN score is found using NOvA's Convolutional Visual Network described in Section 4.3. The events passing selection for simulation and data are shown by the red histogram and the black data-points respectively. The systematic uncertainty in the distribution of the simulated events is shown by the shaded red region enclosing the red histogram. The simulated background events passing the selection are shown by the blue histogram.

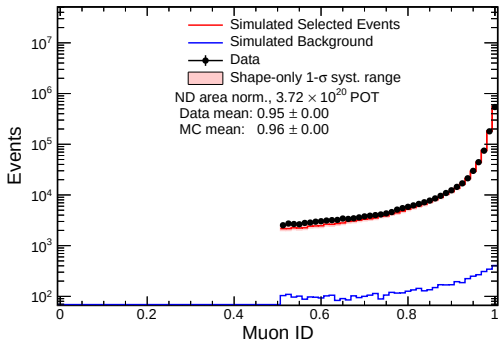

(a) All E_{had}/E_{ν} quantiles combined.

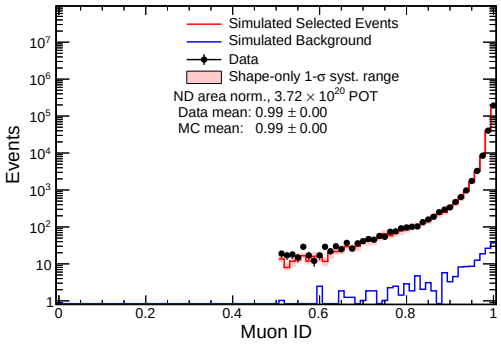

(b) Lowest E_{had}/E_{ν} quantile.

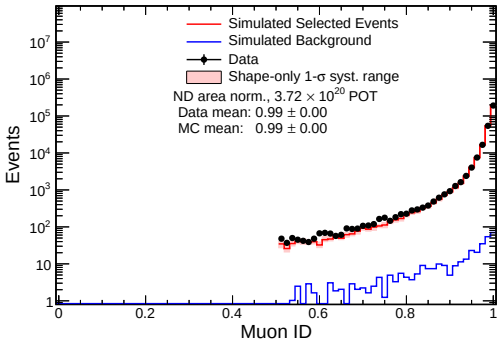

(c) Second lowest E_{had}/E_{ν} quantile.

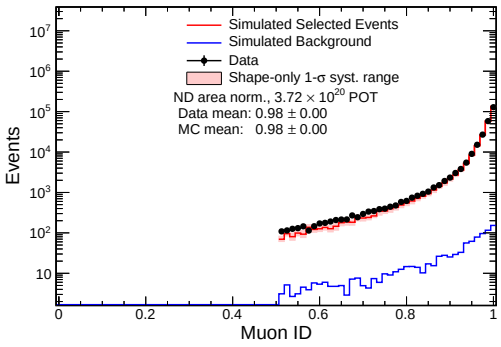

(d) Second highest E_{had}/E_{ν} quantile.

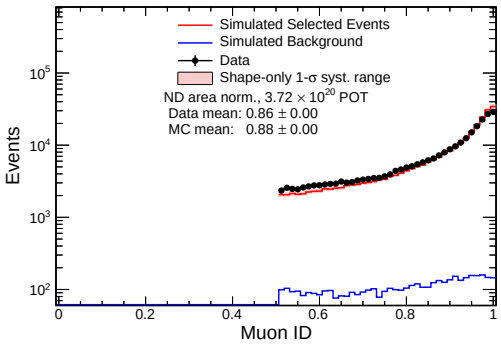

(e) Highest E_{had}/E_{ν} quantile.

Figure 6.8: Plots showing the number of events vs. the ReMId muon identification score for each E_{had}/E_{ν} quantile. The muon identification algorithm is described in Section 4.3. The events passing selection for simulation and data are shown by the red histogram and the black data-points respectively. The systematic uncertainty in the distribution of the simulated events is shown by the shaded red region enclosing the red histogram. The simulated background events passing the selection are shown by the blue histogram.

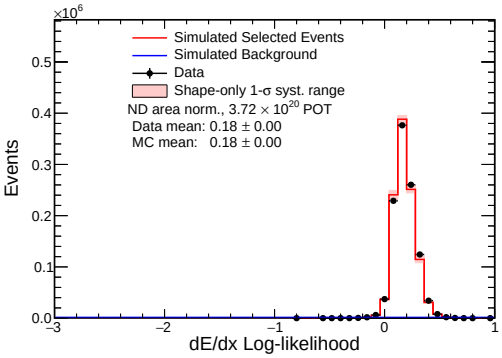

(a) All E_{had}/E_{ν} quantiles combined.

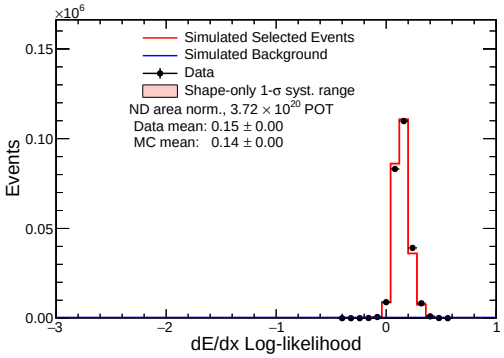

(b) Lowest E_{had}/E_{ν} quantile.

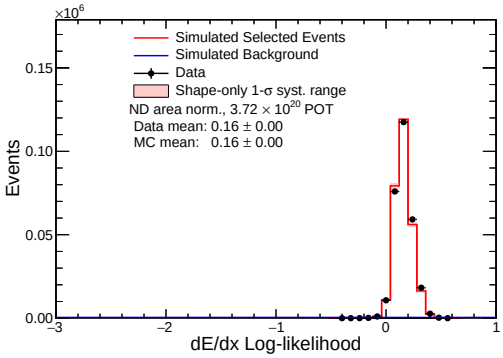

(c) Second lowest E_{had}/E_{ν} quantile.

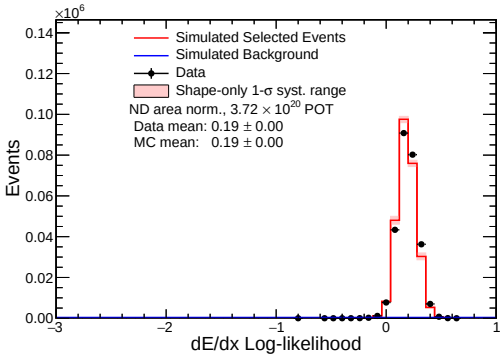

(d) Second highest E_{had}/E_{ν} quantile.

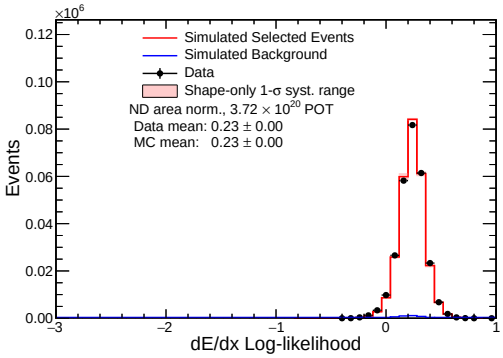

(e) Highest E_{had}/E_{ν} quantile.

Figure 6.9: Plots showing the number of events vs. dE/dx log-likelihood for each E_{had}/E_{ν} quantile. The dE/dx log-likelihood is an input to the muon identification called ReMId. The dE/dx log-likelihood is found by comparing the dE/dx vs. distance to track end of a candidate event with true signal and background events. The events passing selection for simulation and data are shown by the red histogram and the black data-points respectively. The systematic uncertainty in the distribution of the simulated events is shown by the shaded red region enclosing the red histogram. The simulated background events passing the selection are shown by the blue histogram.

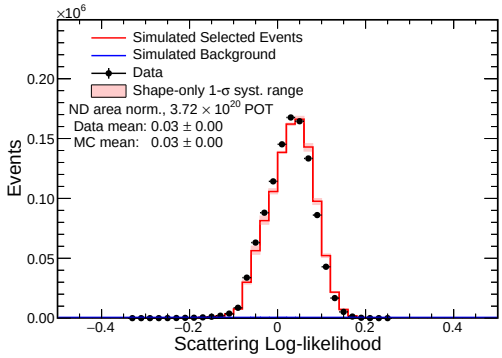

(a) All E_{had}/E_{ν} quantiles combined.

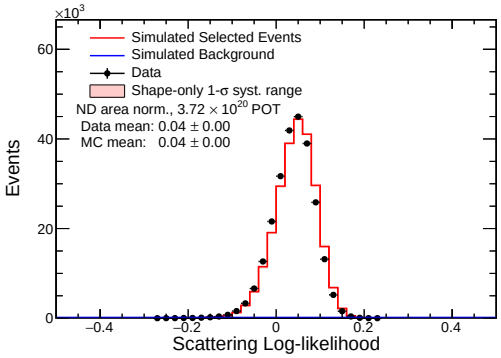

(b) Lowest E_{had}/E_{ν} quantile.

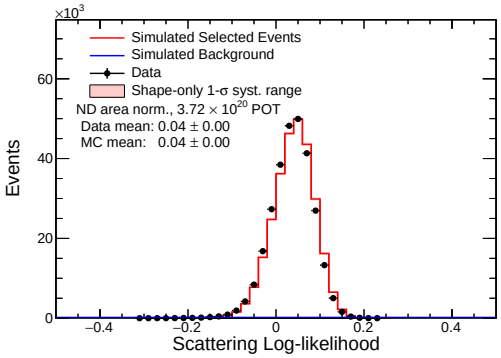

(c) Second lowest E_{had}/E_{ν} quantile.

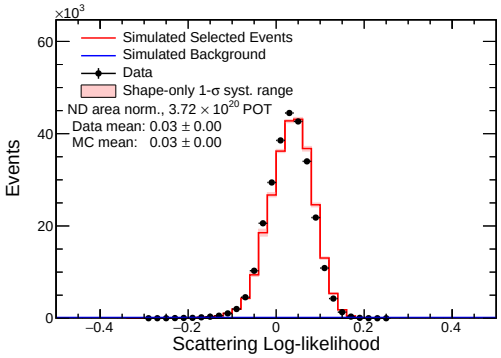

(d) Second highest E_{had}/E_{ν} quantile.

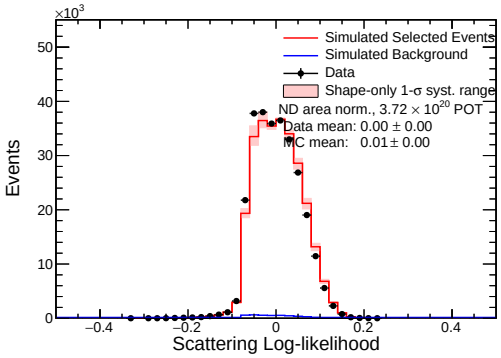

(e) Highest E_{had}/E_{ν} quantile.

Figure 6.10: Plots showing the number of events vs. the scattering log-likelihood for each E_{had}/E_{ν} quantile. The scattering log-likelihood is an input to the muon identification called ReMId. The scattering log-likelihood is found by comparing the scattering angle vs. distance to track end of a candidate event with true signal and background events. The events passing selection for simulation and data are shown by the red histogram and the black data-points respectively. The systematic uncertainty in the distribution of the simulated events is shown by the shaded red region enclosing the red histogram. The simulated background events passing the selection are shown by the blue histogram.

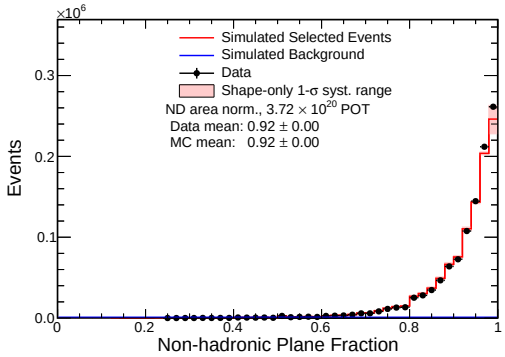

(a) All E_{had}/E_{ν} quantiles combined.

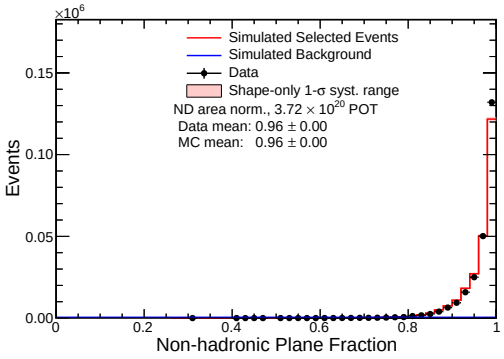

(b) Lowest E_{had}/E_{ν} quantile.

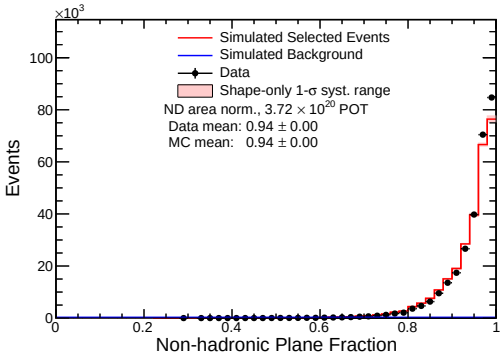

(c) Second lowest E_{had}/E_{ν} quantile.

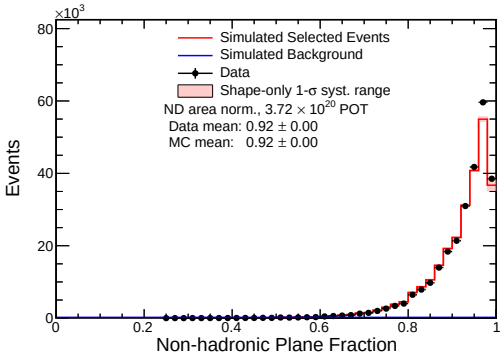

(d) Second highest E_{had}/E_{ν} quantile.

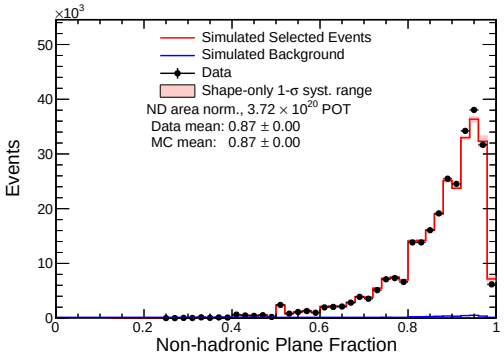

(e) Highest E_{had}/E_{ν} quantile.

Figure 6.11: Plots showing the number of events vs. fraction of planes within the event without hadronic activity for each E_{had}/E_{ν} quantile. The fraction of planes without hadronic activity is an input to the muon identification called ReMId. This is defined as the number of planes along the candidate muon track within the event that do not contain any off-track energy deposits. The events passing selection for simulation and data are shown by the red histogram and the black data-points respectively. The systematic uncertainty in the distribution of the simulated events is shown by the shaded red region enclosing the red histogram. The simulated background events passing the selection are shown by the blue histogram.

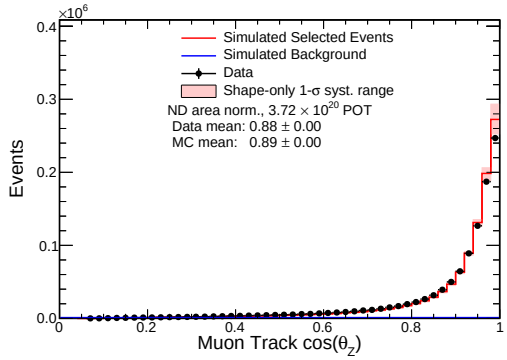

(a) All E_{had}/E_{ν} quantiles combined.

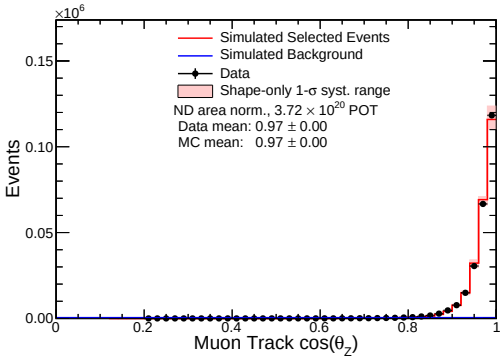

(b) Lowest E_{had}/E_{ν} quantile.

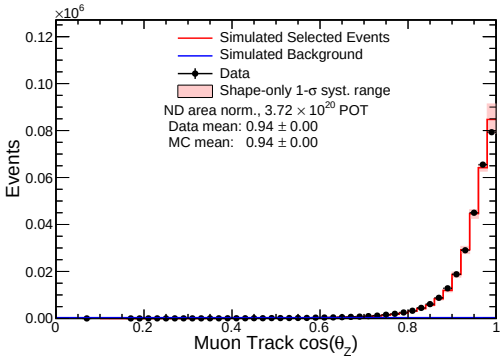

(c) Second lowest E_{had}/E_{ν} quantile.

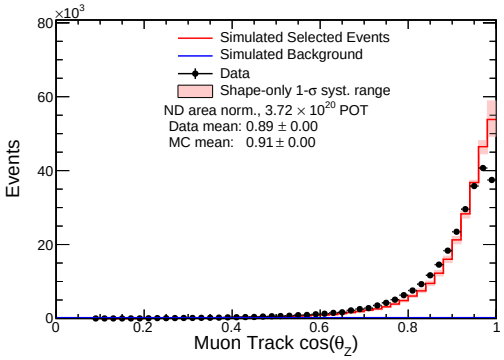

(d) Second highest E_{had}/E_{ν} quantile.

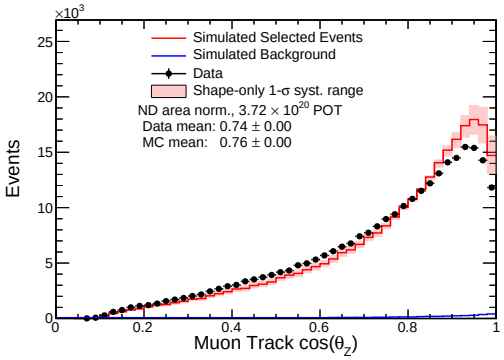

(e) Highest E_{had}/E_{ν} quantile.

Figure 6.12: Plots showing the number of events vs. $\cos\theta_Z$ (where θ_Z is the angle of the leading track relative to the beam direction) for each E_{had}/E_{ν} quantile. The events passing selection for simulation and data are shown by the red histogram and the black data-points respectively. The systematic uncertainty in the distribution of the simulated events is shown by the shaded red region enclosing the red histogram. The simulated background events passing the selection are shown by the blue histogram.

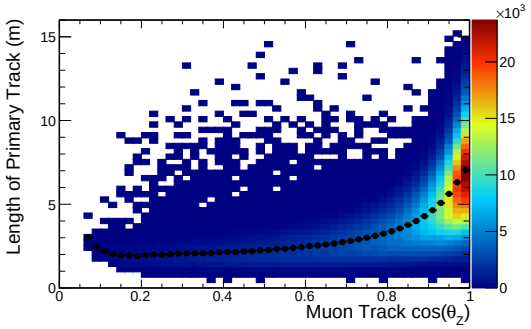

(a) All E_{had}/E_{ν} quantiles combined.

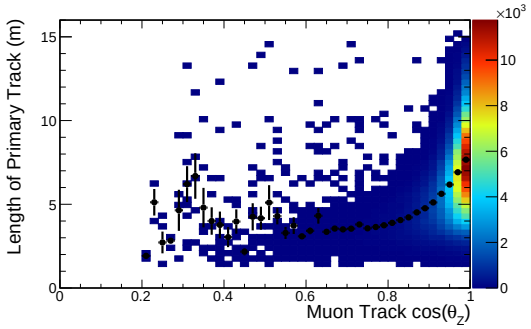

(b) Lowest E_{had}/E_{ν} quantile.

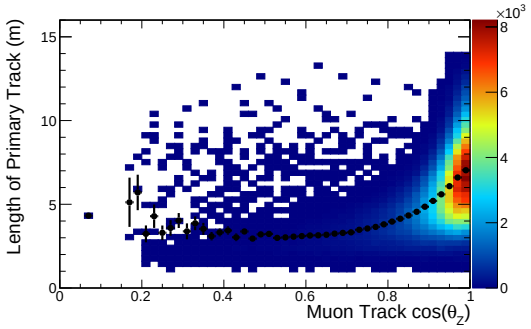

(c) Second lowest E_{had}/E_{ν} quantile.

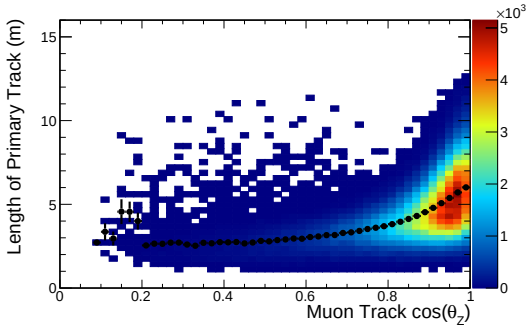

(d) Second highest E_{had}/E_{ν} quantile.

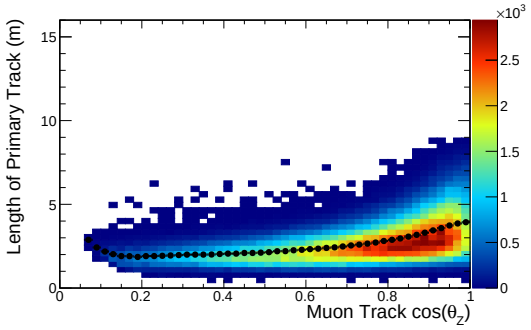

(e) Highest E_{had}/E_{ν} quantile.

Figure 6.13: Plots showing the length of the leading track vs. the $\cos\theta_Z$ (where θ_Z is the angle of the leading track relative to the beam direction) for each E_{had}/E_{ν} quantile. The number of events within each bin is displayed by the bin colour. For each $\cos\theta_Z$ bin the mean of the profile along the track length axis is shown by the black circles with statistical error bars.

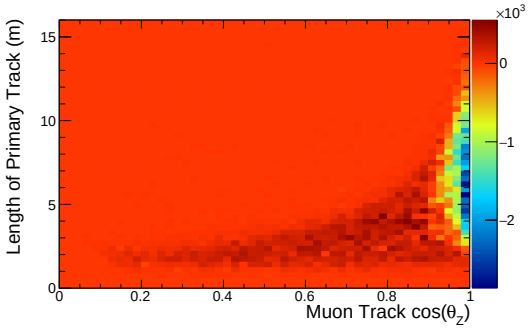

(a) All E_{had}/E_{ν} quantiles combined.

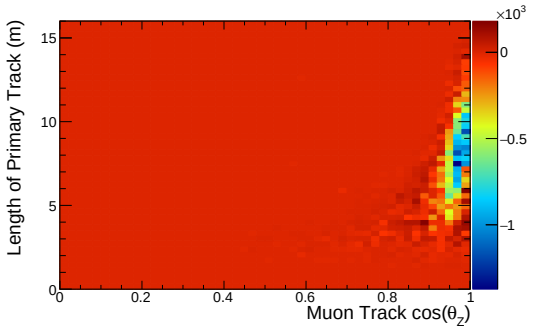

(b) Lowest E_{had}/E_{ν} quantile.

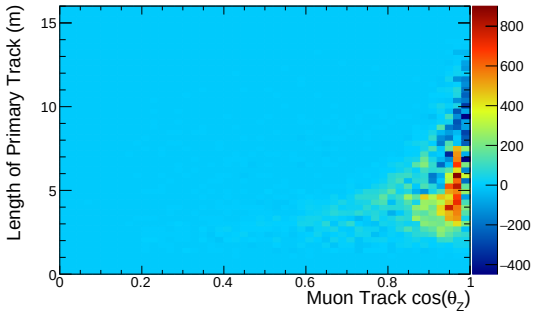

(c) Second lowest E_{had}/E_{ν} quantile.

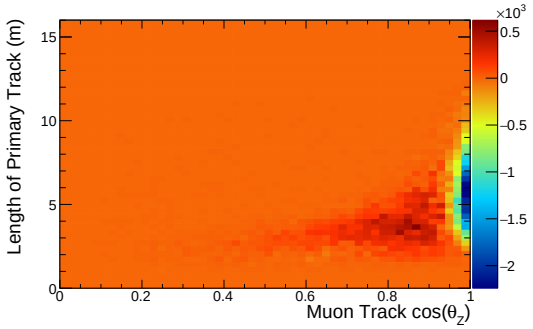

(d) Second highest E_{had}/E_{ν} quantile.

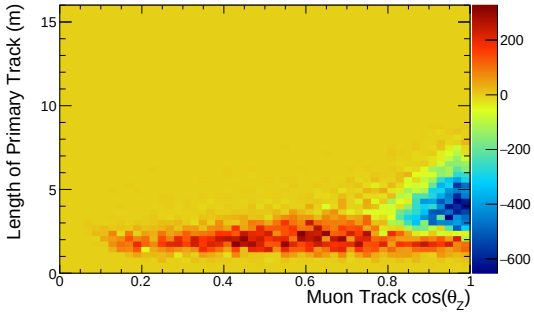

(e) Highest E_{had}/E_{ν} quantile.

Figure 6.14: Plots showing the difference between data and MC entries in the length of the leading track vs. $\cos\theta_Z$ (where θ_Z is the angle of the leading track relative to the beam direction) distributions for each E_{had}/E_{ν} quantile. For each bin the colour displays the number of events in MC subtracted from the number of events in data.

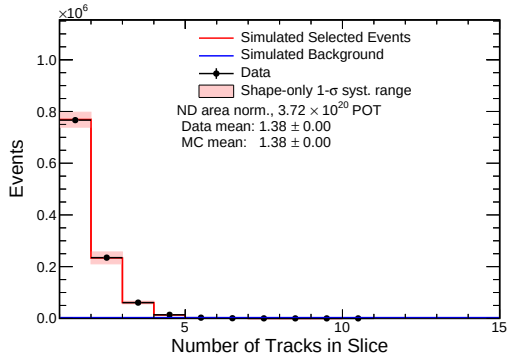

(a) All E_{had}/E_{ν} quantiles combined.

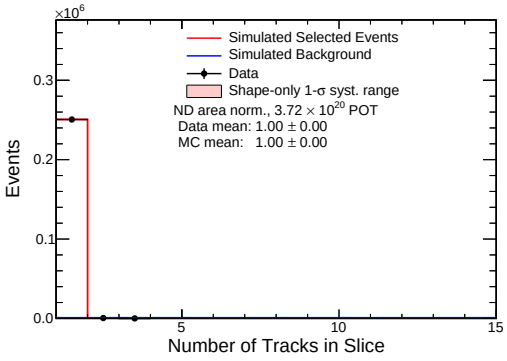

(b) Lowest E_{had}/E_{ν} quantile.

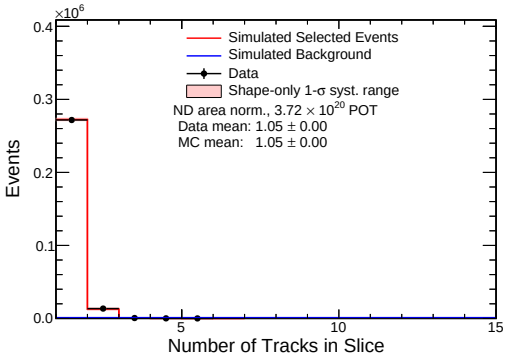

(c) Second lowest E_{had}/E_{ν} quantile.

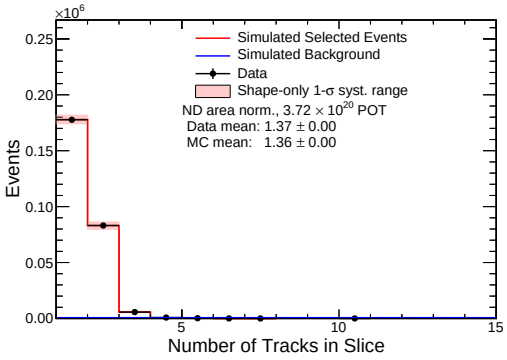

(d) Second highest E_{had}/E_{ν} quantile.

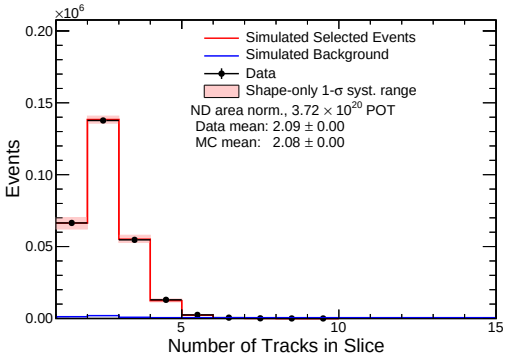

(e) Highest E_{had}/E_{ν} quantile.

Figure 6.15: Plots showing the number of events vs. the number of Kalman tracks for each E_{had}/E_{ν} quantile. The events passing selection for simulation and data are shown by the red histogram and the black data-points respectively. The systematic uncertainty in the distribution of the simulated events is shown by the shaded red region enclosing the red histogram. The simulated background events passing the selection are shown by the blue histogram.

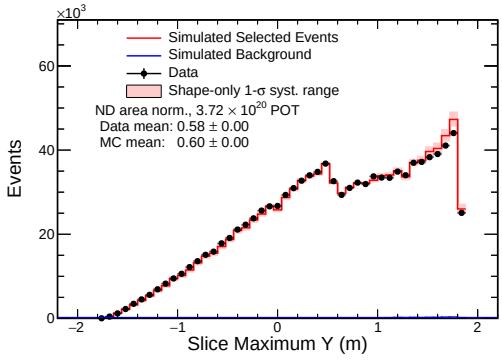

(a) All E_{had}/E_{ν} quantiles combined.

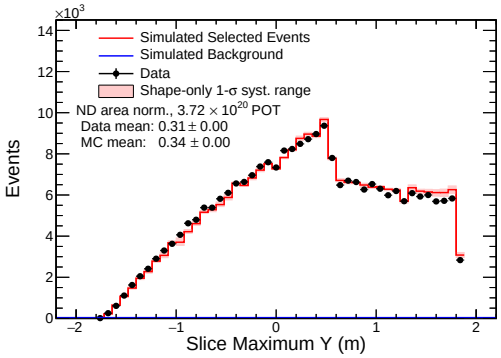

(b) Lowest E_{had}/E_{ν} quantile.

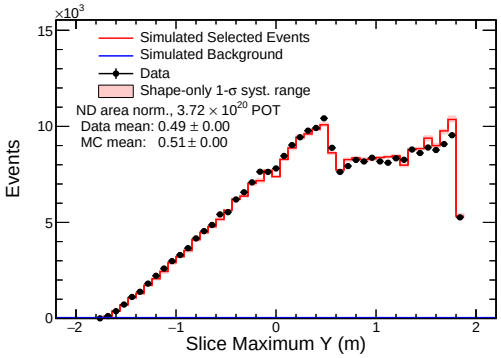

(c) Second lowest E_{had}/E_{ν} quantile.

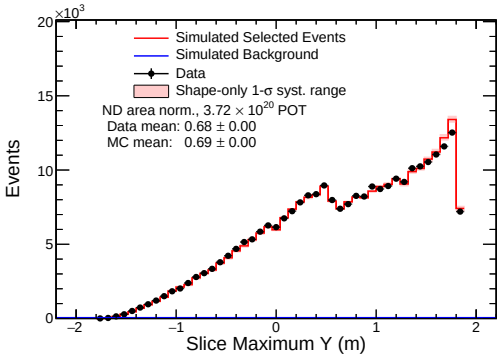

(d) Second highest E_{had}/E_{ν} quantile.

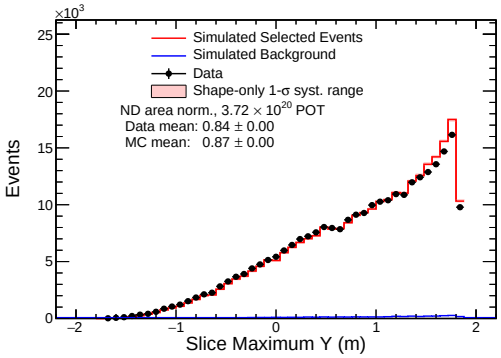

(e) Highest E_{had}/E_{ν} quantile.

Figure 6.16: Plots showing the number of events vs. the maximum height of activity associated with the event within the detector for each E_{had}/E_{ν} quantile. The events passing selection for simulation and data are shown by the red histogram and the black data-points respectively. The systematic uncertainty in the distribution of the simulated events is shown by the shaded red region enclosing the red histogram. The simulated background events passing the selection are shown by the blue histogram.

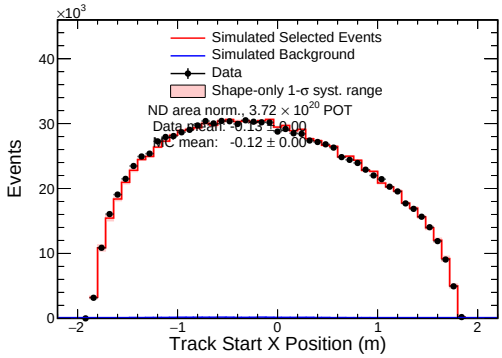

(a) All E_{had}/E_{ν} quantiles combined.

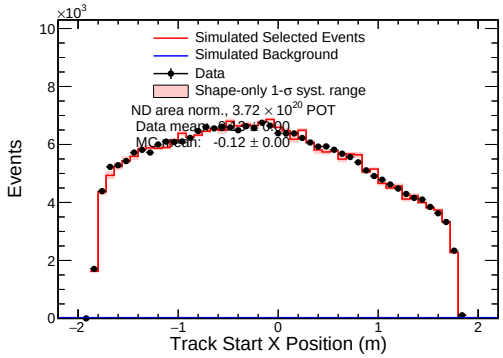

(b) Lowest E_{had}/E_{ν} quantile.

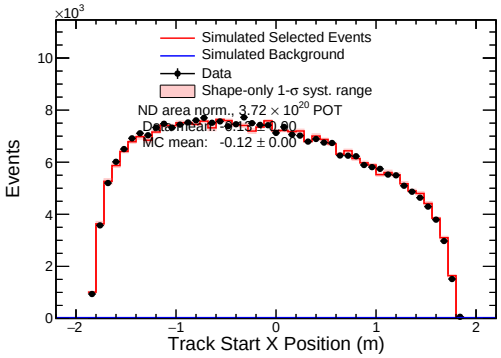

(c) Second lowest E_{had}/E_{ν} quantile.

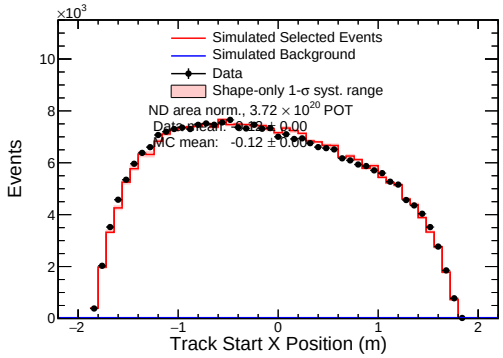

(d) Second highest E_{had}/E_{ν} quantile.

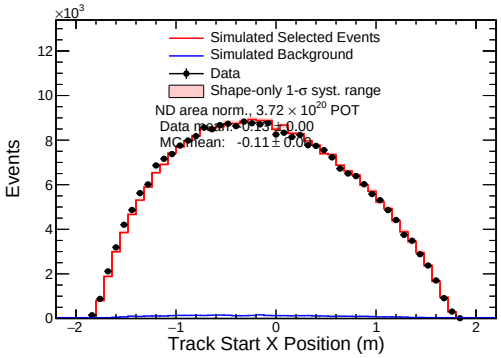

(e) Highest E_{had}/E_{ν} quantile.

Figure 6.17: Plots showing the number of events vs. the starting position in the x direction (horizontal) of the leading track for each E_{had}/E_{ν} quantile. The events passing selection for simulation and data are shown by the red histogram and the black data-points respectively. The systematic uncertainty in the distribution of the simulated events is shown by the shaded red region enclosing the red histogram. The simulated background events passing the selection are shown by the blue histogram.

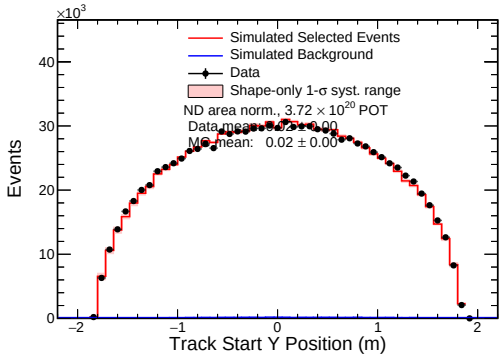

(a) All E_{had}/E_{ν} quantiles combined.

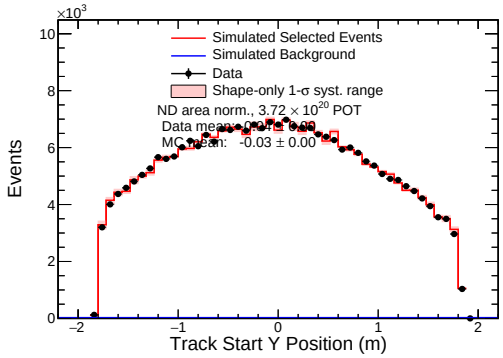

(b) Lowest E_{had}/E_{ν} quantile.

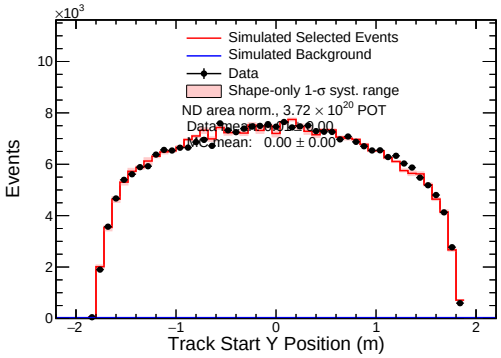

(c) Second lowest E_{had}/E_{ν} quantile.

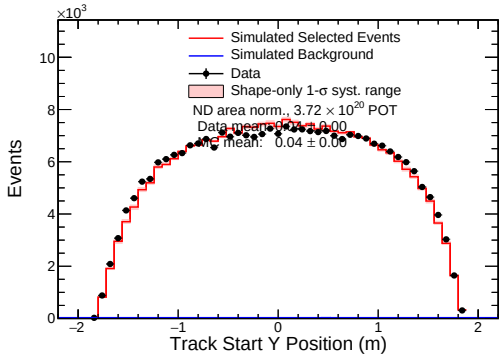

(d) Second highest E_{had}/E_{ν} quantile.

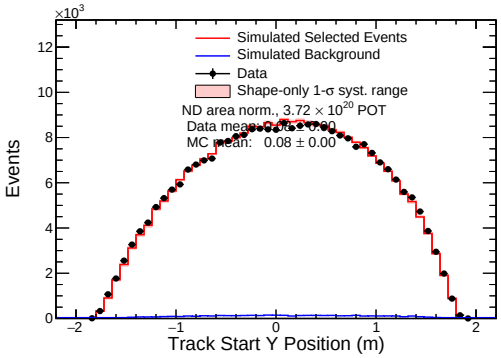

(e) Highest E_{had}/E_{ν} quantile.

Figure 6.18: Plots showing the number of events vs. the starting position in the y direction (vertical) of the leading track for each E_{had}/E_{ν} quantile. The events passing selection for simulation and data are shown by the red histogram and the black data-points respectively. The systematic uncertainty in the distribution of the simulated events is shown by the shaded red region enclosing the red histogram. The simulated background events passing the selection are shown by the blue histogram.

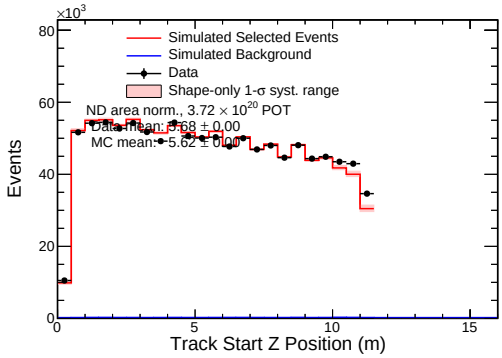

(a) All E_{had}/E_{ν} quantiles combined.

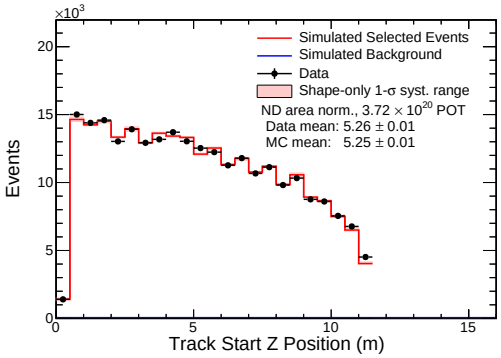

(b) Lowest E_{had}/E_{ν} quantile.

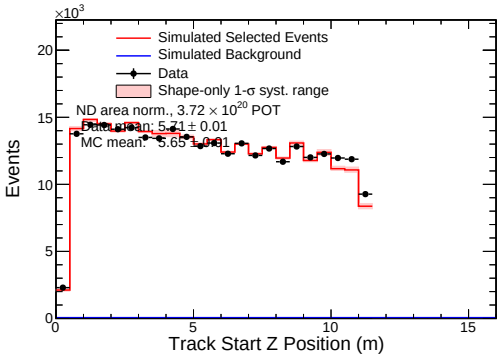

(c) Second lowest E_{had}/E_{ν} quantile.

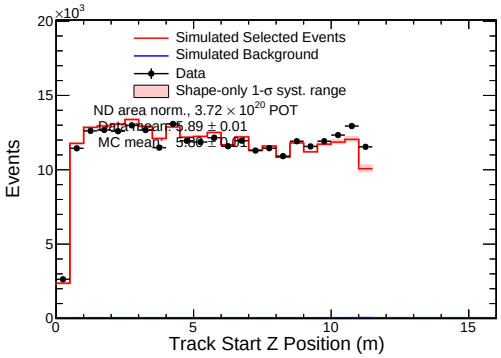

(d) Second highest E_{had}/E_{ν} quantile.

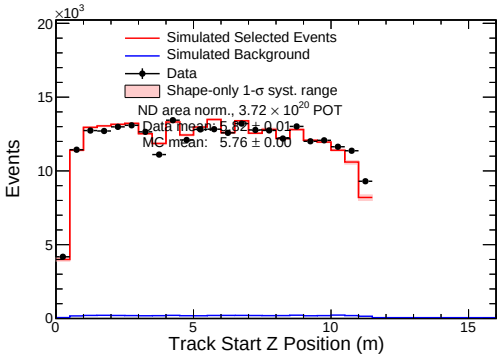

(e) Highest E_{had}/E_{ν} quantile.

Figure 6.19: Plots showing the number of events vs. the starting position in the z direction (depth along the length of the detector) of the leading track for each E_{had}/E_{ν} quantile. The events passing selection for simulation and data are shown by the red histogram and the black data-points respectively. The systematic uncertainty in the distribution of the simulated events is shown by the shaded red region enclosing the red histogram. The simulated background events passing the selection are shown by the blue histogram.

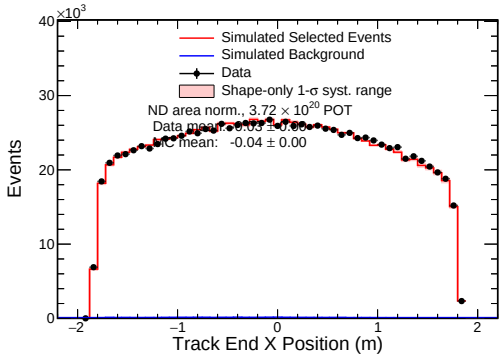

(a) All E_{had}/E_{ν} quantiles combined.

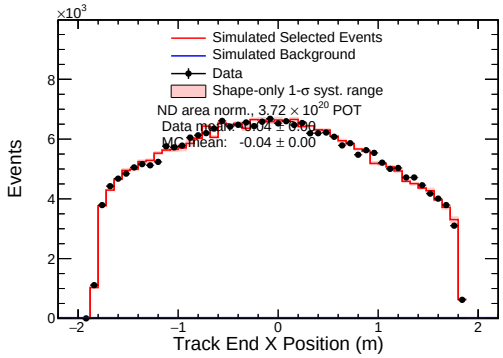

(b) Lowest E_{had}/E_{ν} quantile.

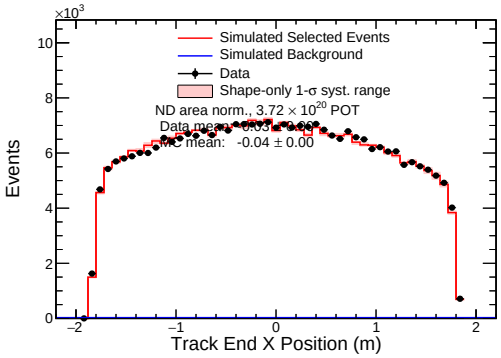

(c) Second lowest E_{had}/E_{ν} quantile.

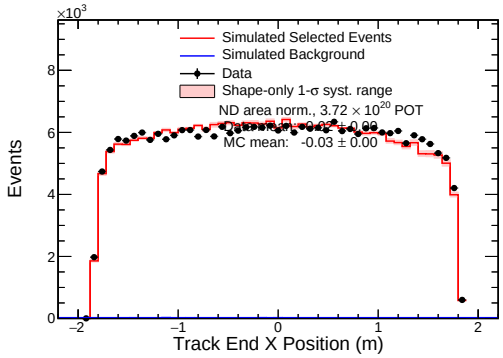

(d) Second highest E_{had}/E_{ν} quantile.

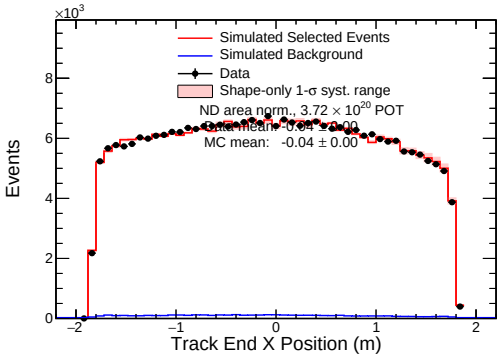

(e) Highest E_{had}/E_{ν} quantile.

Figure 6.20: Plots showing the number of events vs. the stopping position in the x direction of the leading track for each E_{had}/E_{ν} quantile. The events passing selection for simulation and data are shown by the red histogram and the black data-points respectively. The systematic uncertainty in the distribution of the simulated events is shown by the shaded red region enclosing the red histogram. The simulated background events passing the selection are shown by the blue histogram.

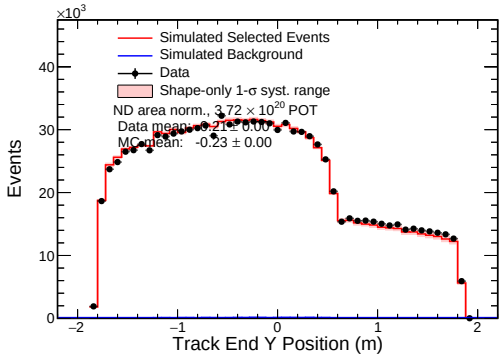

(a) All E_{had}/E_{ν} quantiles combined.

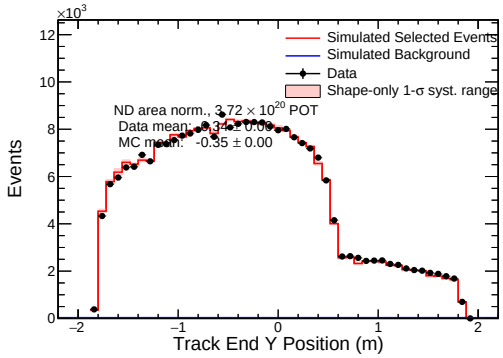

(b) Lowest E_{had}/E_{ν} quantile.

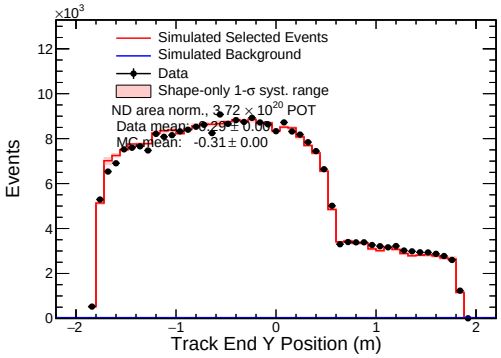

(c) Second lowest E_{had}/E_{ν} quantile.

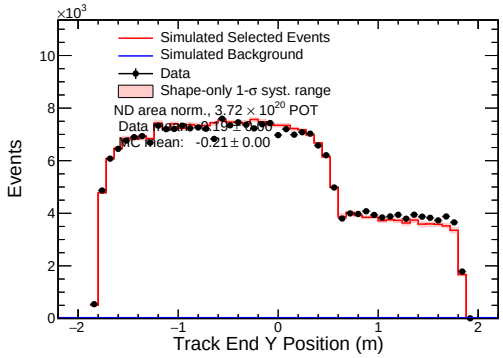

(d) Second highest E_{had}/E_{ν} quantile.

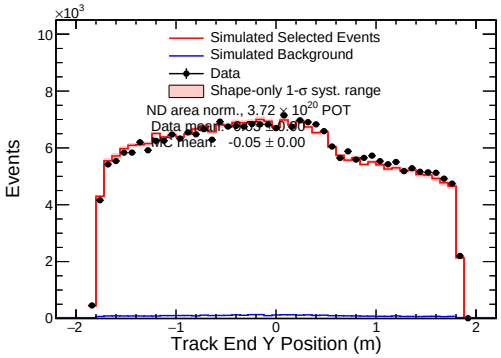

(e) Highest E_{had}/E_{ν} quantile.

Figure 6.21: Plots showing the number of events vs. the stopping position in the y direction of the leading track for each E_{had}/E_{ν} quantile. The events passing selection for simulation and data are shown by the red histogram and the black data-points respectively. The systematic uncertainty in the distribution of the simulated events is shown by the shaded red region enclosing the red histogram. The simulated background events passing the selection are shown by the blue histogram.

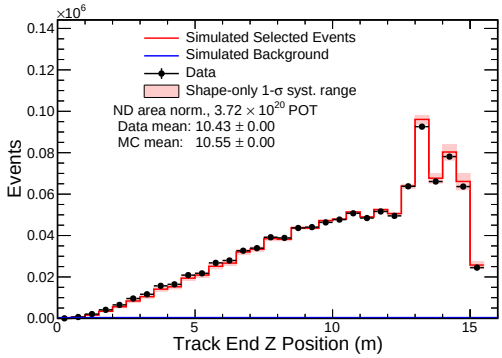

(a) All E_{had}/E_{ν} quantiles combined.

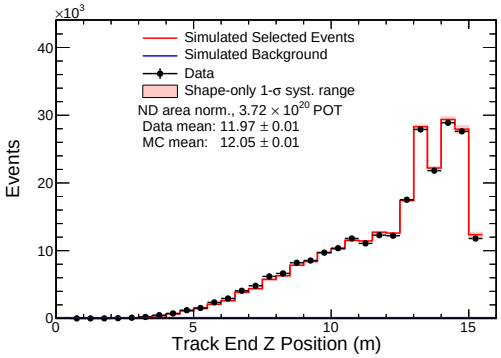

(b) Lowest E_{had}/E_{ν} quantile.

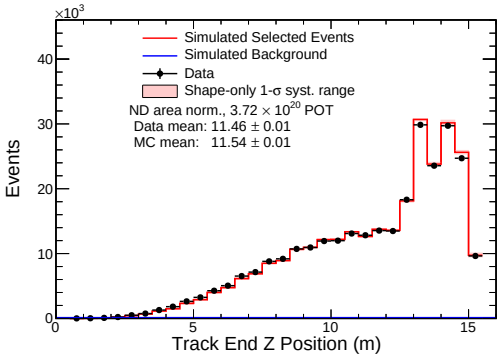

(c) Second lowest E_{had}/E_{ν} quantile.

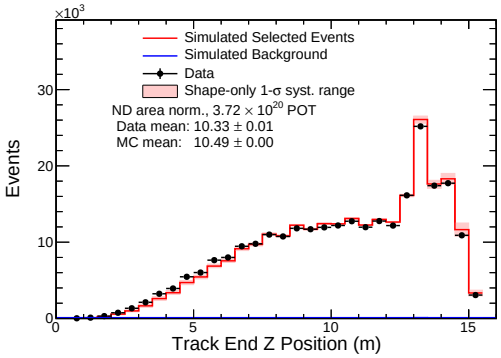

(d) Second highest E_{had}/E_{ν} quantile.

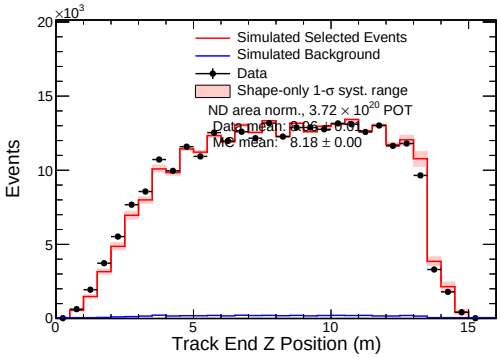

(e) Highest E_{had}/E_{ν} quantile.

Figure 6.22: Plots showing the number of events vs. the stopping position in the z direction of the leading track for each E_{had}/E_{ν} quantile. The events passing selection for simulation and data are shown by the red histogram and the black data-points respectively. The systematic uncertainty in the distribution of the simulated events is shown by the shaded red region enclosing the red histogram. The simulated background events passing the selection are shown by the blue histogram.

6.1.1 Improvements with a New Simulation

At the time of writing, an updated MC simulation is being introduced which improves the agreement between data and MC[1]. This updated MC provides better descriptions of the detector geometry, detector response and represents the best estimate for the values of the muon and hadronic energy. In particular, the simulation updates include modelling of the Cherenkov light produced by charged particles travelling through the detector, changes to the interior width and height (both reduced by about 0.9%) of the cells and a decrease in the stopping power of the scintillator (0.3% and 0.8% in the near and far detector respectively) [99]. For this section, upgraded MC and data refers to the updated simulation and calibration. Whilst default MC and data refers to the MC and data used in the rest of this thesis.

To make a fair comparison of the two simulations, careful consideration of the weights applied to each neutrino interaction to modify their cross section and underlying flux is required. First, the default MC has weights applied to correct the non-resonance single pion cross section and an incorrect ratio of neutron-neutron to proton-neutron events. It is also adjusted to achieve a more constant cross section for 2p2h-MEC processes above 1 GeV. Second, the upgraded MC has weights applied to correct the non-resonance single pion cross section and the flux due to hadron production. The details of these weights and corrections is as follows:

- Due to the recent reanalysis of bubble chamber data [55], the rate of non-resonant single pion events in GENIE is reduced via weighting deep inelastic-scattering events with an invariant mass of $W < 1.7$ GeV down by 35%. In light of this new evidence, both the upgraded and default MC have weights applied to correct the non-resonant single pion cross section.

- The default simulation is adjusted to achieve a sensible cross section for 2p2h-MEC processes with neutrino energies greater than 1 GeV. These 2p2h events are also reweighted as function of three-momentum transfer and hadronic energy such that the MC matches the data in the near detector.

- The default MC uses GENIE v2.10.4 which contained an error where the 4:1 ratio of neutron-neutron and neutron-proton initial dinucleon targets should have been the reverse [41]. This ratio is inverted via reweighting of the events in the default MC.

[1] A study [98] has shown that data and MC distributions in the near detector agree within errors when using the new simulation and data.

- The hadron production from the NuMI target is simulated with GEANT4 in the upgraded simulation rather than FLUKA. Weights obtained from a careful analysis of all available hadron production are used to re-weight the GEANT4 simulation. The new beam flux has small normalisation difference and smaller uncertainties but does not affect the mean neutrino energy in the 1.5 GeV region.

The reconstructed energy variables are found using conversions from reconstructed quantities (such as track length) to the true energy in the simulation. In particular, the muon energy was reconstructed using a spline fit of the true muon energy to the track length. Similarly, the total energy of the hadronic recoil system was reconstructed from a spline fit of the true hadronic energy to the visible energy in the scintillator. These spline fits used the default MC for all the variables shown in this section.

Figure 6.23 shows the distributions of muon, neutrino and hadronic energy in the default MC and data alongside the upgraded MC and data. The data shows slight shifts in all three variables, this is due to the calibration of the data depending on the MC simulation. These comparisons of the three energy variables will be discussed in turn. First, for the neutrino energy distributions both sets of data show good agreement with the upgraded MC but the default MC is shifted to higher energies relative to the data. Specifically, the mean in the default MC is about 2.35% higher than the data. Second, the upgraded MC has a muon energy 1.5% lower than the default MC and the data-MC agreement is improved, except between approximately 0.8 and 1.6 GeV where there is no change. Additionally, the mean muon energy in both sets of data is about 2.3% lower than the default MC. Third, for the hadronic energy, the upgraded MC shows better agreement with both sets of data than the default MC. In the default files the mean hadronic energy in the MC is 5% higher than the data. However, in the upgraded files the mean energy in the MC is 2% lower than the data. The upgraded data shows a small divergence from the default data because the upgraded files use an updated calibration of the detector response.

The upgraded MC represents the best estimate for the values of muon and hadronic energy and so a correction is applied to the default data for use in this analysis. As mentioned above, the upgraded MC includes a Cherenkov effect previously missing and this lowers the amount of visible energy produced by a hadron shower in the MC. In the default MC there was too much visible hadronic energy for a given true energy. The hadronic energy is reconstructed from a spline fit of visible hadronic energy to the true total energy of the hadronic recoil system. This spline fit is created using the default

MC. This meant that the hadronic energy in data was reconstructed too low and should be shifted to higher energy. Comparison between the upgraded data and MC using the double ratio $(\mathrm{MC}_{upgrade}/\mathrm{MC}_{default})/(\mathrm{data}_{upgrade}/\mathrm{data}_{default})$ suggests shifting the data up by 5%.

Now let us consider the muon energy. The updated MC is 1.5% lower than the default MC. However, the muon energy is the same in the new and old data, as expected. Reconstructed muon energy is found using a spline fit between track length and true muon energy. Therefore, the difference between the simulations indicates that a change was introduced in the upgraded MC which caused tracks to be 1.5% shorter for a given energy. In the default MC the conversion between muon track length and energy is correct by construction. For the default data the track length required to reconstruct a given energy is too large. Therefore, our best estimate is that data was reconstructed with too little muon energy and needs to be shifted up by 1.5%.

No new systematic uncertainties were introduced to cover the two shifts described above. This is because the shifts introduced are within the bounds of the uncertainty already placed on the muon and hadronic energy. The hadronic energy has a 5% uncertainty and is now shifted by 5% in the data. The muon energy has an uncertainty of 2% and is now shifted by 1.5% in the data. Plots comparing the distribution of muon, hadronic, neutrino energy and hadronic energy fraction in data and MC (with the energy shifts discussed above) are shown in Figures 6.24, 6.26, 6.28 and 6.30. The corresponding data/MC ratio plots are shown in Figures 6.25, 6.27, 6.29 and 6.31. For the muon energy distributions, the data-MC agreement is now good, with the data lying mostly within the systematic error band. Relative to the unshifted distributions shown in Figure 6.2, the agreement is improved in the low energy region, before the shift to the muon energy the MC had a significant deficit below 1 GeV. This deficit is now greatly reduced and is almost contained within the systematic error band. The hadronic energy shows better data-MC agreement relative to the distributions shown in Figure 6.1 which were made without shifts to the muon and hadronic energy. In particular, the agreement in the third and fourth quantiles is better and any discrepancies are now almost all covered by the 1 σ systematic uncertainty band. In addition, the means in each quantile in data and MC now agree within 1%. The distributions of E_{had}/E_{ν} in data and MC are compared in Figure 6.30. With the shifts described above there is good agreement in each of the E_{had}/E_{ν} quantiles. After the shifts, the neutrino energy distributions show good data-MC agreement in each quantile. Specifically, for the first and second quantile data closely matches the central

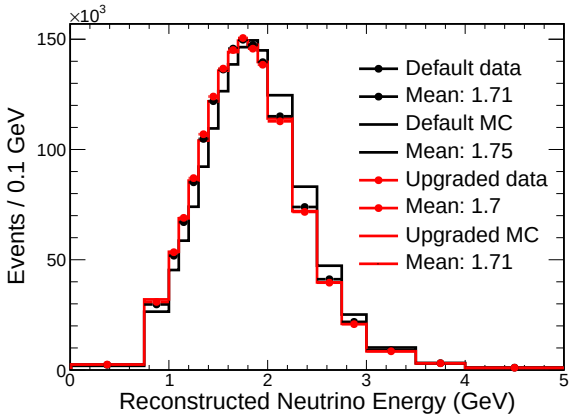

(a)

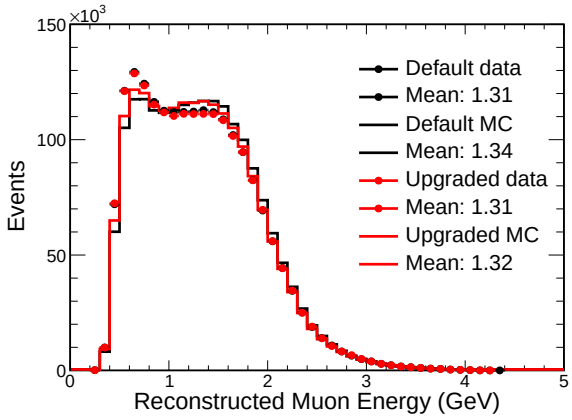

(b)

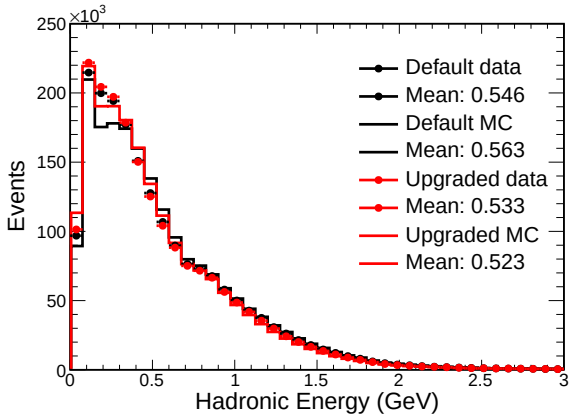

(c)

Figure 6.23: The MC and data used for this thesis is shown by the black histogram and black full circles respectively. The updated MC and corresponding data are shown by the red histogram and red full circles respectively. Subfigures (a), (b) and (c) show the neutrino, muon and hadronic energy respectively.

	Events per quantile		Events per quantile / total events	
E_{had}/E_{ν} quantile	Data	MC	Data	MC
Lowest	432922	486715	0.222894	0.248734
Second lowest	508759	487345	0.26194	0.249056
Second highest	491133	488234	0.252865	0.24951
Highest	509460	494473	0.262301	0.252699
Total	1.94228e+06	1.95677e+06	1	1

Table 6.2: Events and share of total events within each quantile in data and MC. The muon and hadronic energy in data have been shifted by 1.5% and 5% respectively.

value in the MC. In the third and fourth quantile the data has slightly lower neutrino energy than the MC but the difference is almost completely covered by the systematic uncertainty band.

Shifting the muon and hadronic energy in data to higher values can cause events previously in one quantile to migrate to another. This effect could cause each quantiles share of the events in data to shift away from the desired 25%. Any shift away from a 25% share of the events must be covered by the systematic uncertainties. Table 6.2 shows the total number of candidate neutrino events and fractional share of events per quantile in data and MC (after the shifts to the muon and hadronic energy described above). The data shows some deviation from 25%, particularly in the lowest E_{had}/E_{ν} quantile which contains 22.3% of the events. This deviation is covered by the systematics, for example the MEC-scale systematics alone produces a larger change Deviations seen in the other three quantiles are covered by 1 σ shifts to either the charged current quasi-elastic normalisation or the charged current resonance axial mass systematic uncertainties.

6.2 Analysis of the Far Detector Data

This section discusses an analysis of the far detector data using the analysis improvements described in Chapter 5. Confidence limit contours are used to present the regions in the Δm^2_{32} vs. $\sin^2\theta_{23}$ plane allowed by a fit to the far detector data. One dimensional distributions of χ^2 vs. Δm^2_{32} and $\sin^2\theta_{23}$ are made by marginalising over the other oscillation parameter.

This section proceeds in several stages. First, a count of the muon neutrino charged current candidate events is presented. Second, the far detector distributions of the vari-

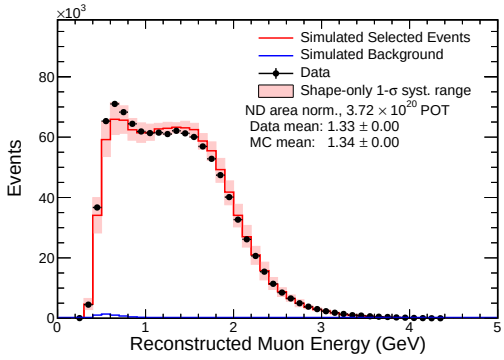

(a) All E_{had}/E_{ν} quantiles combined.

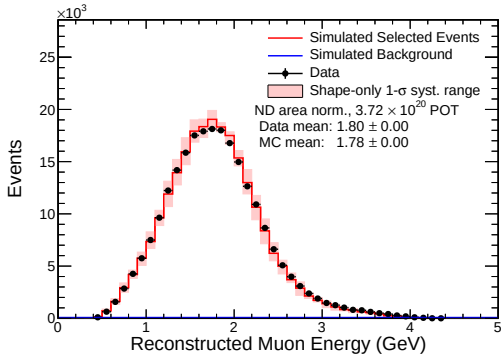

(b) Lowest E_{had}/E_{ν} quantile.

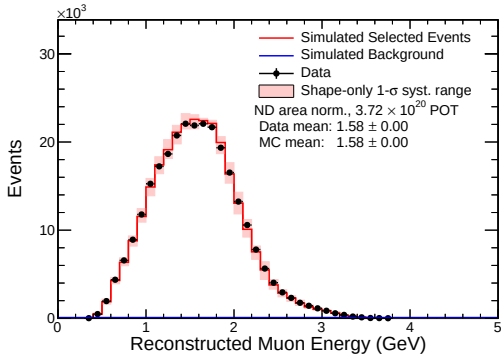

(c) Second lowest E_{had}/E_{ν} quantile.

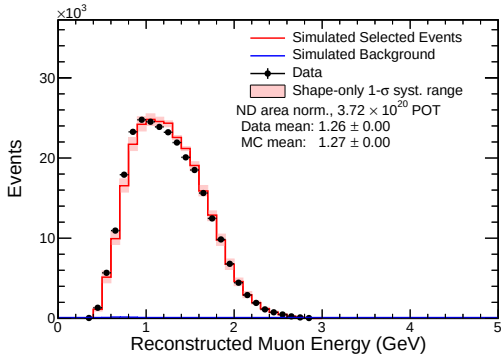

(d) Second highest E_{had}/E_{ν} quantile.

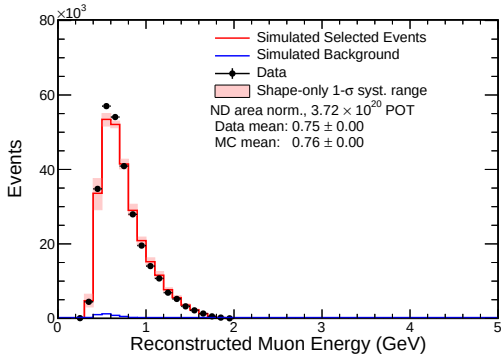

(e) Highest E_{had}/E_{ν} quantile.

Figure 6.24: Plots showing the number of events vs. the muon energy for each E_{had}/E_{ν} quantile. The events passing selection for simulation and data are shown by the red histogram and the black data-points respectively. The systematic uncertainty in the distribution of the simulated events is shown by the shaded red region enclosing the red histogram. The simulated background events passing the selection are shown by the blue histogram. The muon and hadronic energy have been shifted in the data by 1.5% and 5% respectively. The reason for these shifts are described in Section 6.1.1.

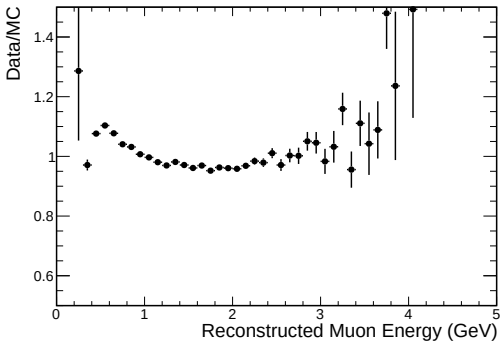

(a) All E_{had}/E_{ν} quantiles combined.

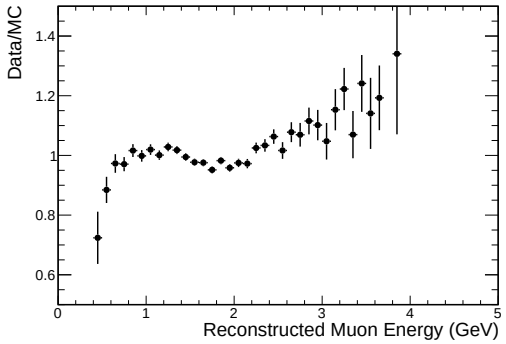

(b) Lowest E_{had}/E_{ν} quantile.

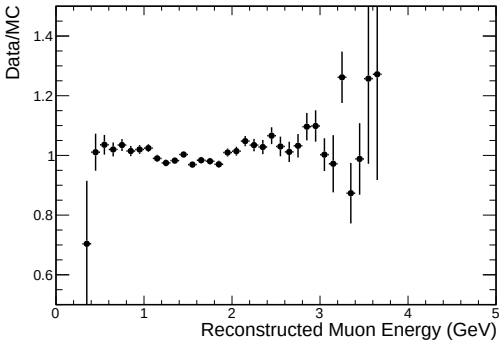

(c) Second lowest E_{had}/E_{ν} quantile.

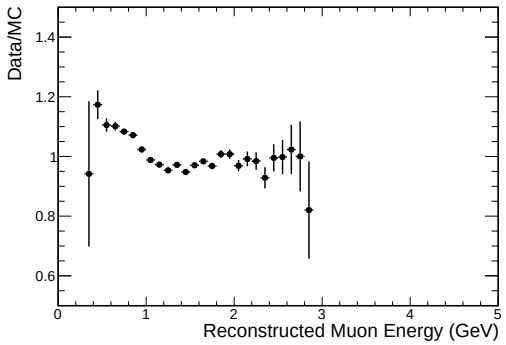

(d) Second highest E_{had}/E_{ν} quantile.

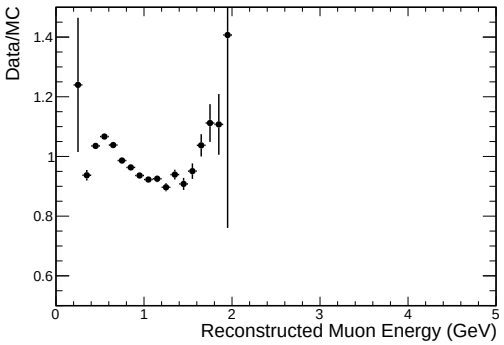

(e) Highest E_{had}/E_{ν} quantile.

Figure 6.25: Near detector data/MC ratio for muon energy for each E_{had}/E_{ν} quantile. The ratios are made from the data and MC distributions shown in Figure 6.24. The muon and hadronic energy have been shifted in the data by 1.5% and 5% respectively. The reason for these shifts are described in Section 6.1.1.

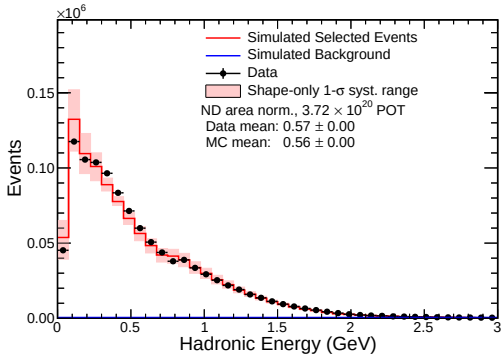

(a) All E_{had}/E_{ν} quantiles combined.

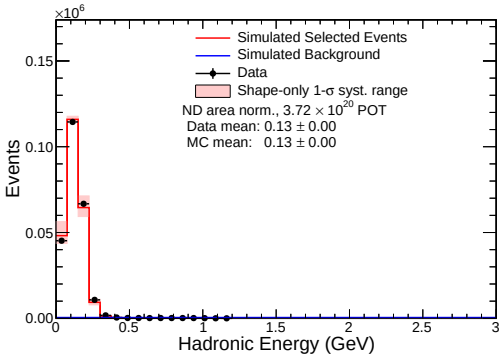

(b) Lowest E_{had}/E_{ν} quantile.

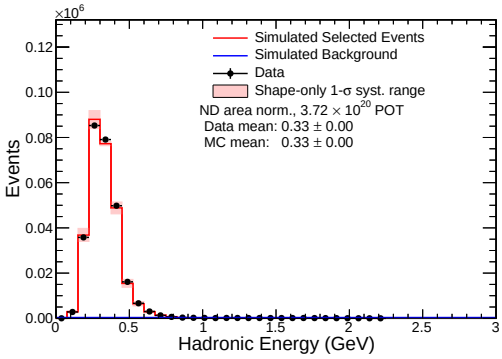

(c) Second lowest E_{had}/E_{ν} quantile.

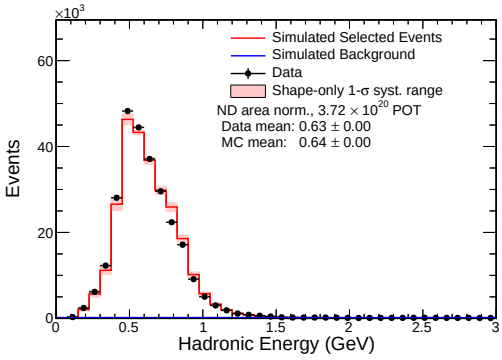

(d) Second highest E_{had}/E_{ν} quantile.

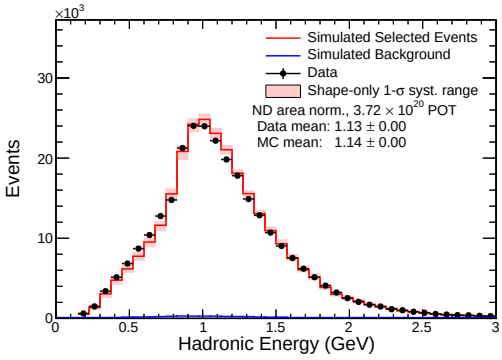

(e) Highest E_{had}/E_{ν} quantile.

Figure 6.26: Plots showing the number of events vs. the hadronic energy for each E_{had}/E_{ν} quantile. The events passing selection for simulation and data are shown by the red histogram and the black data-points respectively. The systematic uncertainty in the distribution of the simulated events is shown by the shaded red region enclosing the red histogram. The simulated background events passing the selection are shown by the blue histogram. The muon and hadronic energy have been shifted in the data by 1.5% and 5% respectively. The reason for these shifts are described in Section 6.1.1.

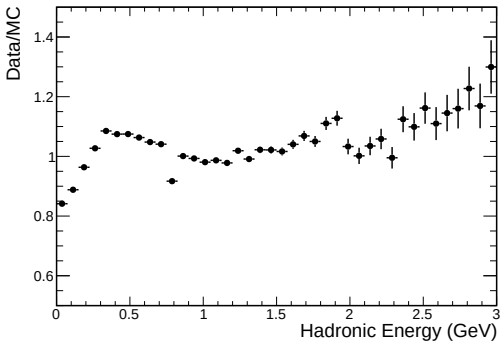

(a) All E_{had}/E_{ν} quantiles combined.

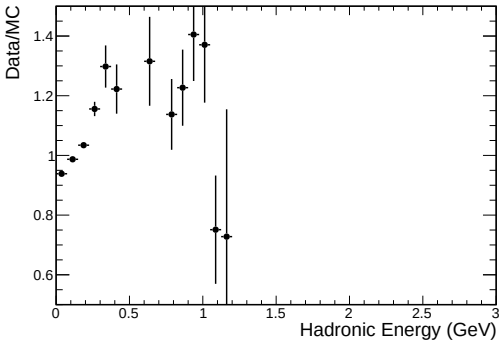

(b) Lowest E_{had}/E_{ν} quantile.

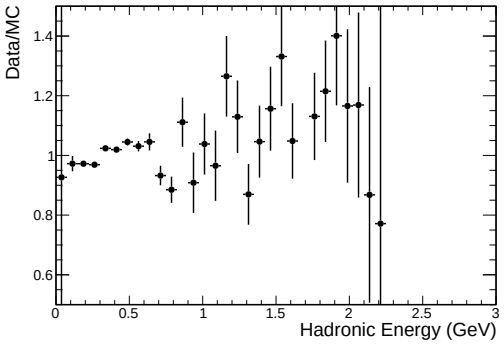

(c) Second lowest E_{had}/E_{ν} quantile.

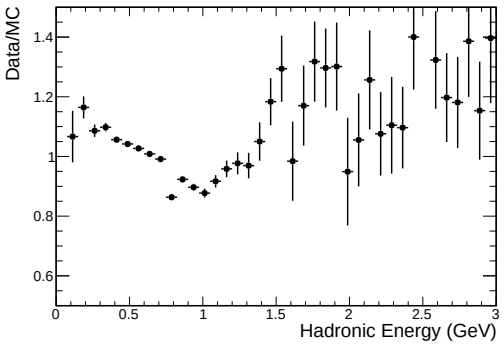

(d) Second highest E_{had}/E_{ν} quantile.

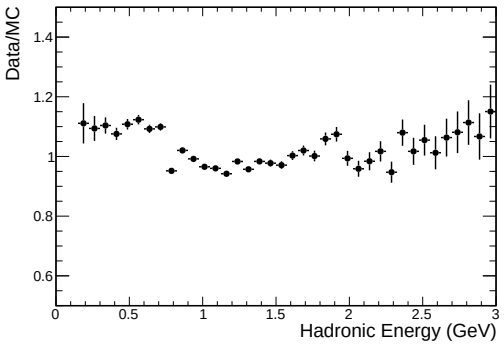

(e) Highest E_{had}/E_{ν} quantile.

Figure 6.27: Near detector data/MC ratio for hadronic energy for each E_{had}/E_{ν} quantile. The ratios are made from the data and MC distributions shown in Figure 6.26. The muon and hadronic energy have been shifted in the data by 1.5% and 5% respectively. The reason for these shifts are described in Section 6.1.1.

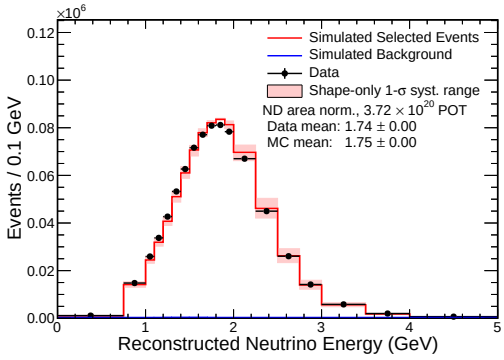

(a) All E_{had}/E_{ν} quantiles combined.

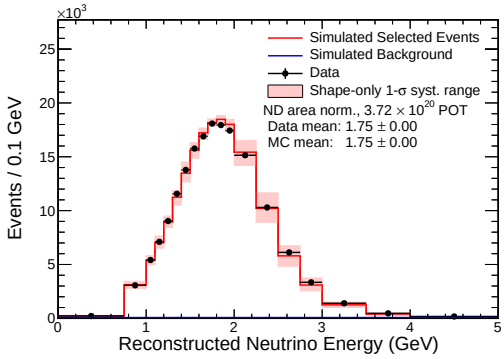

(b) Lowest E_{had}/E_{ν} quantile.

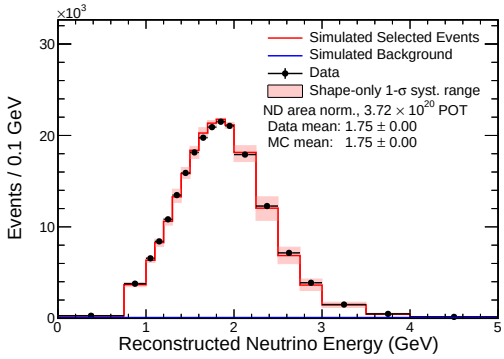

(c) Second lowest E_{had}/E_{ν} quantile.

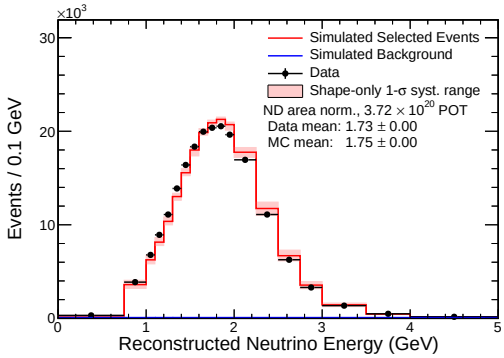

(d) Second highest E_{had}/E_{ν} quantile.

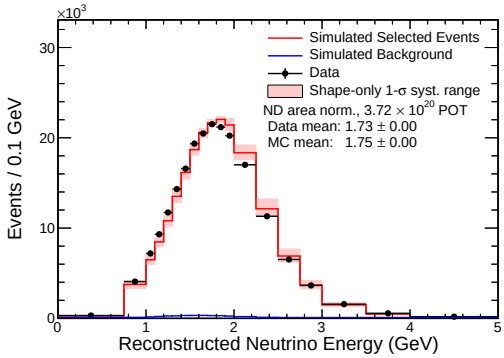

(e) Highest E_{had}/E_{ν} quantile.

Figure 6.28: Plots showing the number of events vs. the muon neutrino energy for each E_{had}/E_{ν} quantile. The events passing selection for simulation and data are shown by the red histogram and the black data-points respectively. The systematic uncertainty in the distribution of the simulated events is shown by the shaded red region enclosing the red histogram. The simulated background events passing the selection are shown by the blue histogram. The muon and hadronic energy have been shifted in the data by 1.5% and 5% respectively. The reason for these shifts are described in Section 6.1.1.

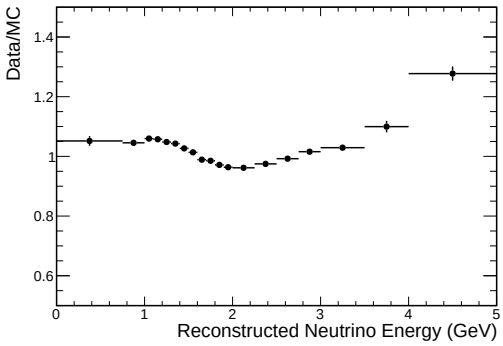

(a) All E_{had}/E_{ν} quantiles combined.

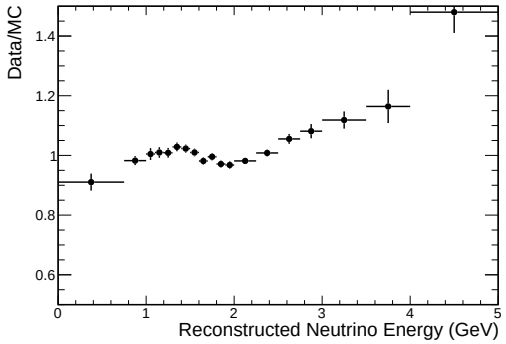

(b) Lowest E_{had}/E_{ν} quantile.

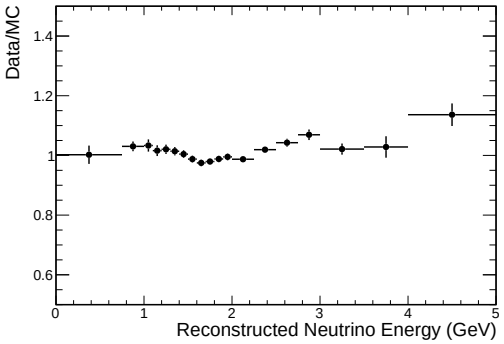

(c) Second lowest E_{had}/E_{ν} quantile.

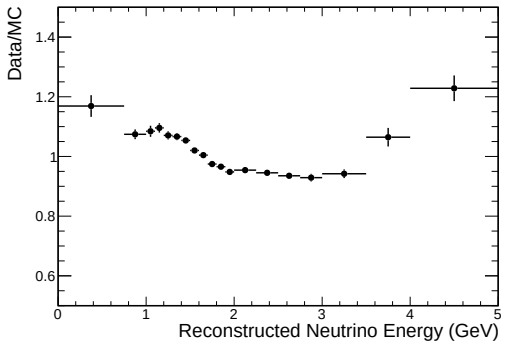

(d) Second highest E_{had}/E_{ν} quantile.

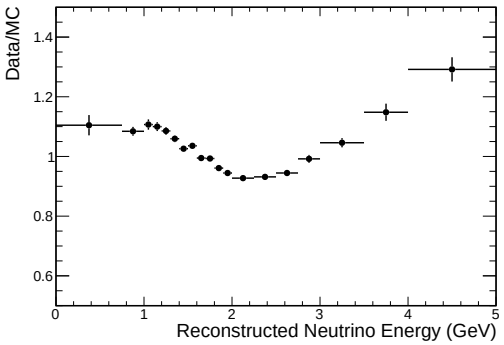

(e) Highest E_{had}/E_{ν} quantile.

Figure 6.29: Near detector data/MC ratio for muon neutrino energy for each E_{had}/E_{ν} quantile. The ratios are made from the data and MC distributions shown in Figure 6.28. The muon and hadronic energy have been shifted in the data by 1.5% and 5% respectively. The reason for these shifts are described in Section 6.1.1.

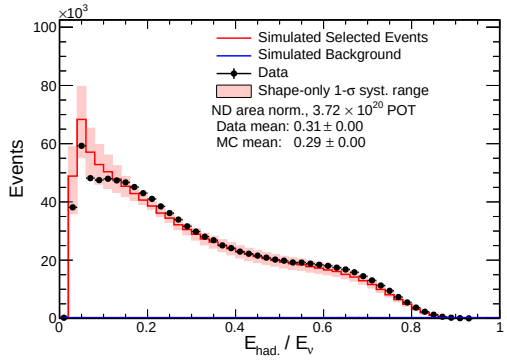

(a) All E_{had}/E_ν quantiles combined.

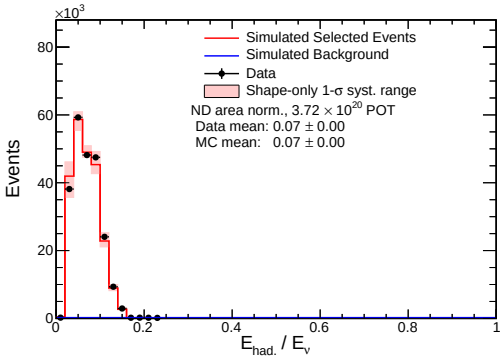

(b) Lowest E_{had}/E_ν quantile.

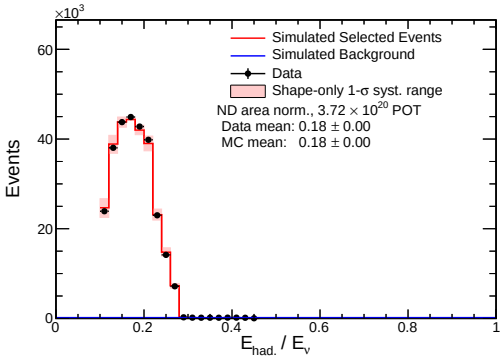

(c) Second lowest E_{had}/E_ν quantile.

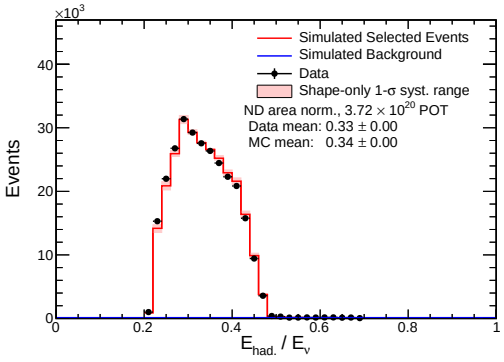

(d) Second highest E_{had}/E_ν quantile.

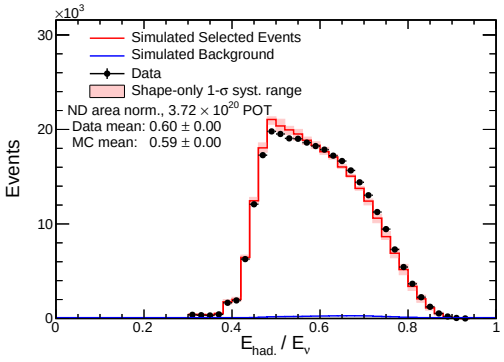

(e) Highest E_{had}/E_ν quantile.

Figure 6.30: Plots showing the number of events vs. the hadronic energy fraction (E_{had}/E_ν) for each E_{had}/E_ν quantile. The events passing selection for simulation and data are shown by the red histogram and the black data-points respectively. The systematic uncertainty in the distribution of the simulated events is shown by the shaded red region enclosing the red histogram. The simulated background events passing the selection are shown by the blue histogram.

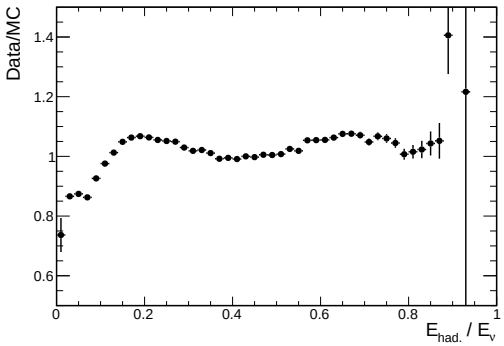

(a) All E_{had}/E_ν quantiles combined.

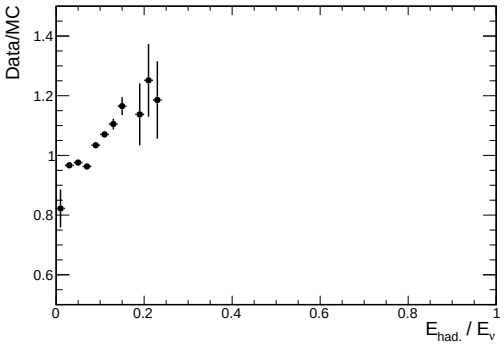

(b) Lowest E_{had}/E_ν quantile.

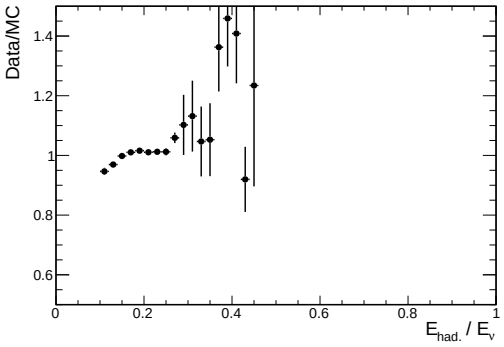

(c) Second lowest E_{had}/E_ν quantile.

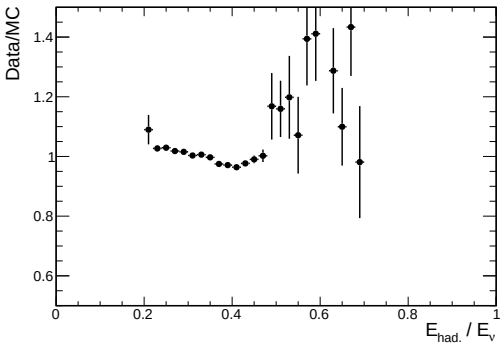

(d) Second highest E_{had}/E_ν quantile.

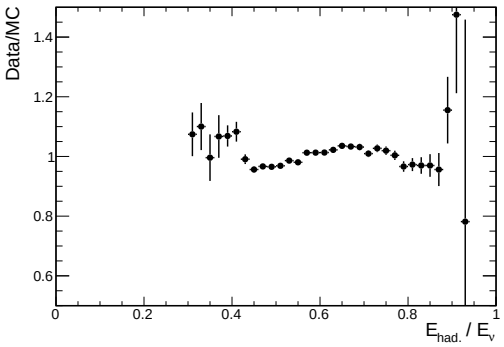

(e) Highest E_{had}/E_ν quantile.

Figure 6.31: Near detector data/MC ratio for E_{had}/E_ν for each E_{had}/E_ν quantile. The ratios are made from the data and MC distributions shown in Figure 6.30. The muon and hadronic energy have been shifted in the data by 1.5% and 5% respectively. The reason for these shifts are described in Section 6.1.1.

E_{had}/E_{ν} quantile	Events	Predicted ν_{μ} CC candidate events
Lowest	21	21.3
Second lowest	18	21.0
Second highest	21	21.4
Highest	21	23.0
Total	81	86.7

Table 6.3: Muon neutrino candidate events within each E_{had}/E_{ν} quantile in the far detector data and MC. The predicted events are calculated assuming neutrino oscillations at NOvA's 2017 [41] best fit point. The predicted events include both the beam and the cosmic ray background. The muon and hadronic energy in the data have been shifted up by 1.5% and 5% respectively.

ables important to the analysis are compared in data and MC. Finally, the neutrino energy spectrum is shown along with the contours. A blind analysis procedure was followed. The whole analysis as described in previous sections and chapters was finalised before the far detector data was examined and fit.

6.2.1 Muon Neutrino Charged Current Candidate Event Count

Table 6.3 lists the event count within each E_{had}/E_{ν} quantile in the far detector data and in an oscillated prediction created at NOvA's 2017 [41] best fit point. In the data, the lowest, second highest and highest quantiles each contain 21 muon neutrino candidate events. Meanwhile, the second lowest quantile contains 18 muon neutrino candidates. Each of these counts is consistent, within the Poisson error, with the expectation from the simulation. In addition, the number of candidates in the data within each quantile is slightly lower than the number predicted assuming oscillations at NOvA's 2017 [41] best fit point.

6.2.2 Far Detector Distributions

This section discusses comparisons between the far detector data and an oscillated prediction for the variables important to the analysis. The oscillated prediction is created by extrapolating the near detector data-MC distributions to the far detector and applying oscillations at NOvA's 2017 [41] best fit point. In the following plots, the estimated beam background is shown by the blue line and the estimated cosmic ray background is shown by the dotted magenta line.

Figures 6.32 and 6.33 show the hadronic and muon energy distributions for all E_{had}/E_{ν} quantiles combined as well as the distributions for each quantile individually. The distributions show reasonable data-MC agreement.

The number of tracks in the event is shown in Figure 6.34. There is good agreement between the data and the oscillated prediction in all the quantiles. The direction of the track relative to the z-axis of the detector is given in terms of $\cos\theta_Z$ in Figure 6.35. Again, data shows reasonable agreement with the oscillated prediction at NOvA's 2017 [41] best fit point within the limits of the large statistical uncertainties.

The distributions of the scores for event selectors CVN and ReMId are shown in Figure 6.36 and 6.37. For both selectors, the data shows reasonable agreement with the oscillated prediction. With increasing E_{had}/E_{ν} quantiles the ReMId distributions, in both the data and the prediction, shift to lower scores of ReMId. A sample of the input variables used to create the ReMId selection score are the dE/dx log-likelihood, the scattering log-likelihood and the non-hadronic plane fraction which are shown in Figures 6.38, 6.39 and 6.40 respectively. All the distributions show reasonable agreement between data and the oscillated prediction.

The starting and stopping position of the candidate muon track for each event is shown in Figure 6.41 in terms of the three detector coordinates X, Y and Z. For each of the distribution the data shows reasonable agreement with the oscillated prediction.

6.2.3 Fitting the Far Detector Neutrino Energy Spectrum

We observe 81 candidate events in the far detector data with an expected background of 2.8 cosmic events and 1.3 neutral current events. At NOvA's 2017 [41] best fit point we expect 90.7 candidate events and at the new best fit point we expect 89.5 candidates. Breakdowns of the expected event count from each oscillation channel for neutrinos and antineutrinos are shown for NOvA's 2017 [41] best fit point and the new best fit point in Tables 6.4 and 6.5 respectively.

The energy spectrum of the muon neutrino charged current candidate events selected by this analysis is shown in Figure 6.42. The data is shown by the black points and the prediction that provides the best fit to the data is shown by the red line. The systematic uncertainty on the best fit prediction is shown by the shaded red band. For comparison, the prediction oscillated at NOvA's 2017 [41] best fit point is shown by the dotted green line. Similar plots are also shown for the muon and hadronic energy in Figures 6.43 and 6.44. A comparison between the energy spectrum in the far detector data and a predicted

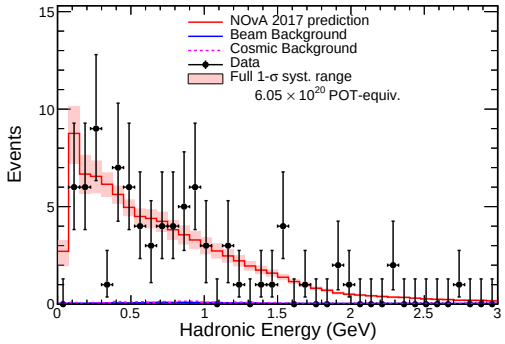

(a) All E_{had}/E_{ν} quantiles combined.

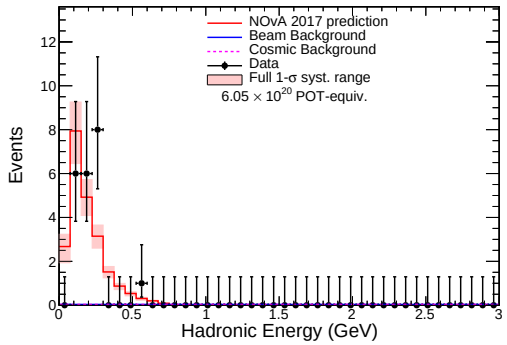

(b) Lowest E_{had}/E_{ν} quantile.

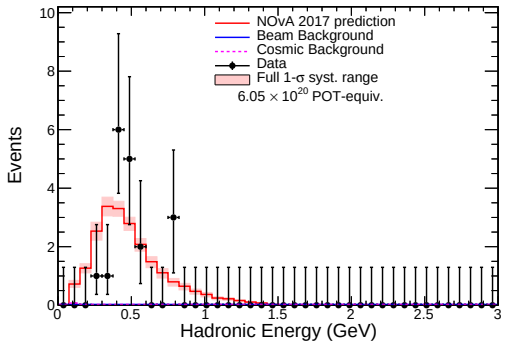

(c) Second lowest E_{had}/E_{ν} quantile.

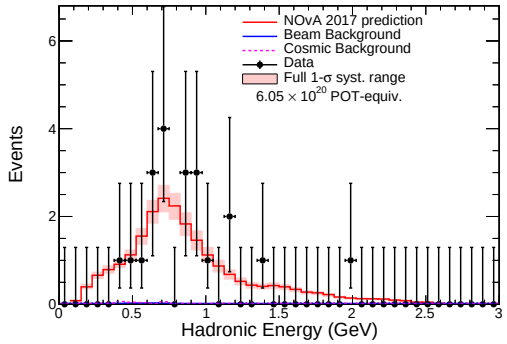

(d) Second highest E_{had}/E_{ν} quantile.

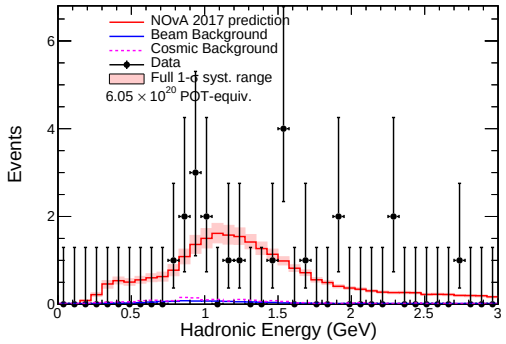

(e) Highest E_{had}/E_{ν} quantile.

Figure 6.32: Plots showing the number of events vs. the hadronic energy for each E_{had}/E_{ν} quantile in the far detector. The events passing selection for simulation and data are shown by the red histogram and the black data-points respectively. The simulation is created using an oscillated (at NOvA's 2017 [41] best fit point) extrapolation from the near to the far detector. The systematic uncertainty in the distribution of the simulated events is shown by the shaded red region enclosing the red histogram. The two sources of background to the analysis are also shown. The simulated background events are shown by the blue histogram. The data estimated cosmic background is shown by the dotted magenta histogram. The muon and hadronic energy have been shifted in the data by 1.5% and 5% respectively. The reason for these shifts are described in Section 6.1.1.

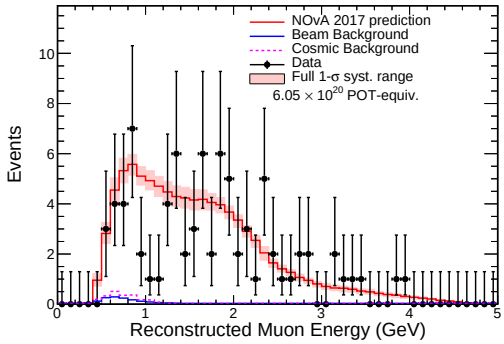

(a) All E_{had}/E_{ν} quantiles combined.

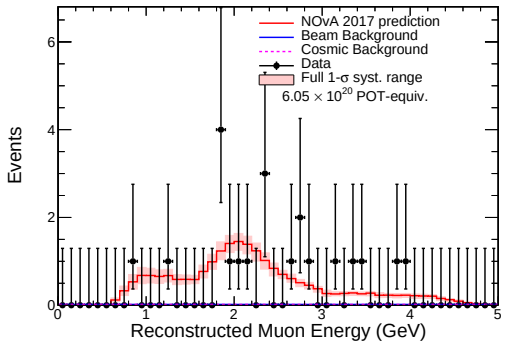

(b) Lowest E_{had}/E_{ν} quantile.

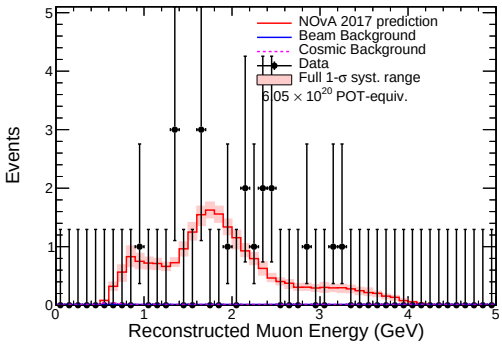

(c) Second lowest E_{had}/E_{ν} quantile.

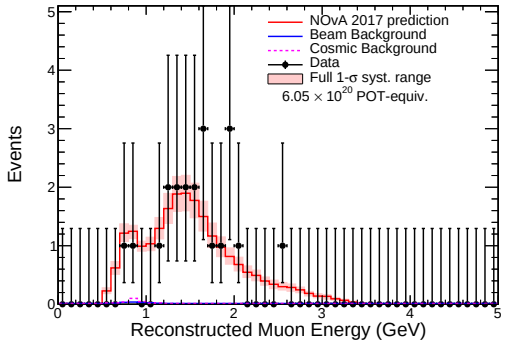

(d) Second highest E_{had}/E_{ν} quantile.

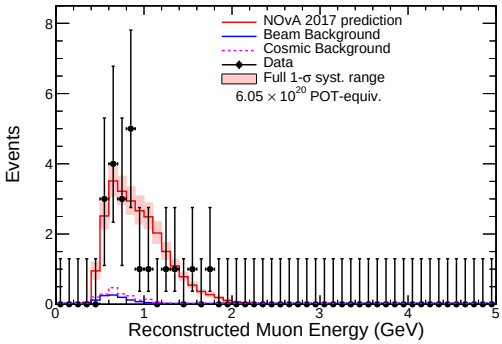

(e) Highest E_{had}/E_{ν} quantile.

Figure 6.33: Plots showing the number of events vs. the muon energy for each E_{had}/E_{ν} quantile in the far detector. The events passing selection for simulation and data are shown by the red histogram and the black data-points respectively. The simulation is created using an oscillated (at NOvA's 2017 [41] best fit point) extrapolation from the near to the far detector. The systematic uncertainty in the distribution of the simulated events is shown by the shaded red region enclosing the red histogram. The two sources of background to the analysis are also shown. The simulated background events are shown by the blue histogram. The data estimated cosmic background is shown by the dotted magenta histogram. The muon and hadronic energy have been shifted in the data by 1.5% and 5% respectively. The reason for these shifts are described in Section 6.1.1.

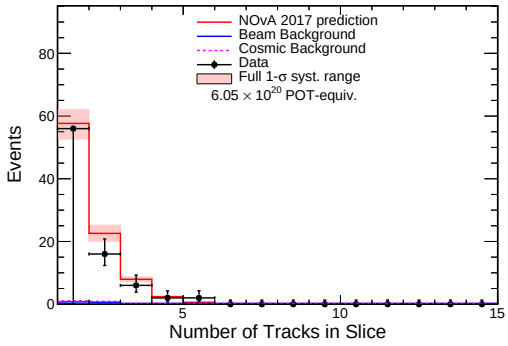

(a) All E_{had}/E_{ν} quantiles combined.

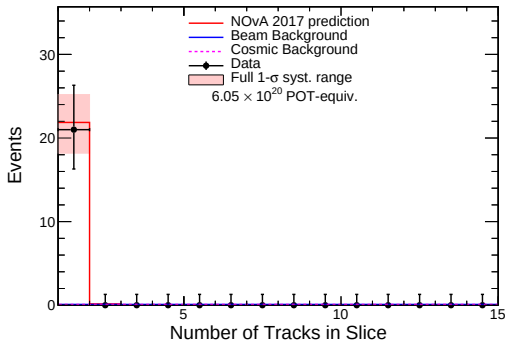

(b) Lowest E_{had}/E_{ν} quantile.

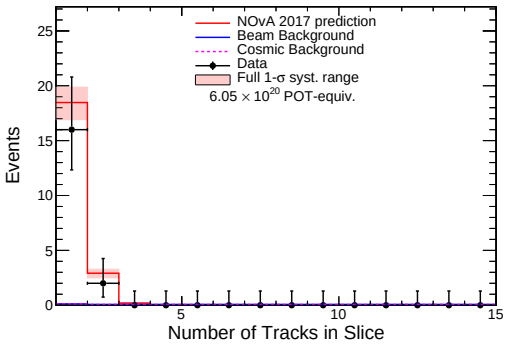

(c) Second lowest E_{had}/E_{ν} quantile.

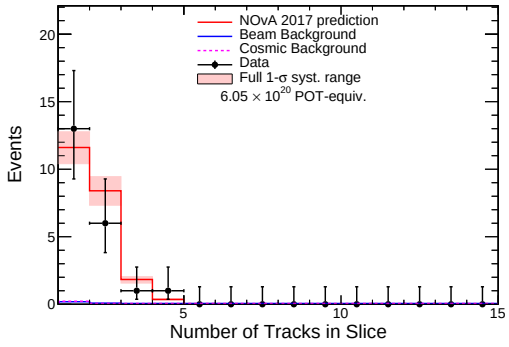

(d) Second highest E_{had}/E_{ν} quantile.

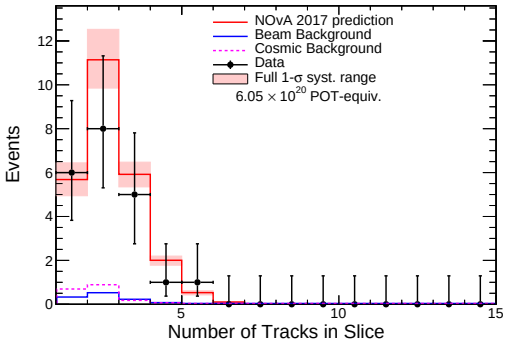

(e) Highest E_{had}/E_{ν} quantile.

Figure 6.34: Plots showing the number of events vs. the number of Kalman tracks for each E_{had}/E_{ν} quantile in the far detector. The events passing selection for simulation and data are shown by the red histogram and the black data-points respectively. The simulation is created using an oscillated (at NOvA's 2017 [41] best fit point) extrapolation from the near to the far detector. The systematic uncertainty in the distribution of the simulated events is shown by the shaded red region enclosing the red histogram. The two sources of background to the analysis are also shown. The simulated background events are shown by the blue histogram. The data estimated cosmic background is shown by the dotted magenta histogram. The muon and hadronic energy have been shifted in the data by 1.5% and 5% respectively. The reason for these shifts are described in Section 6.1.1.

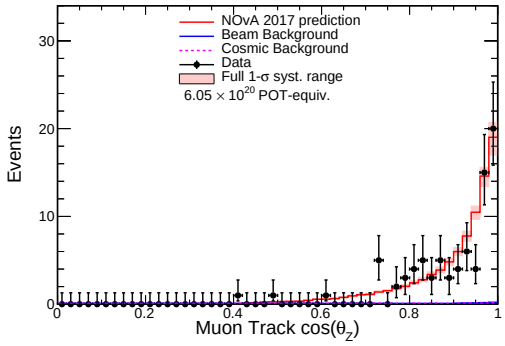

(a) All E_{had}/E_{ν} quantiles combined.

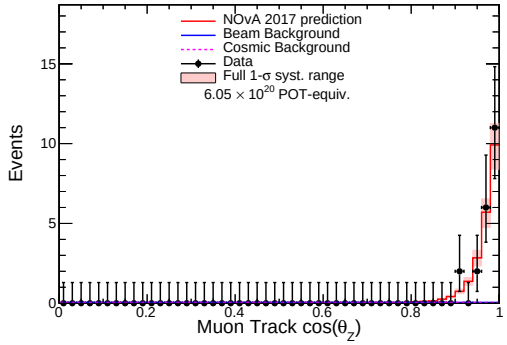

(b) Lowest E_{had}/E_{ν} quantile.

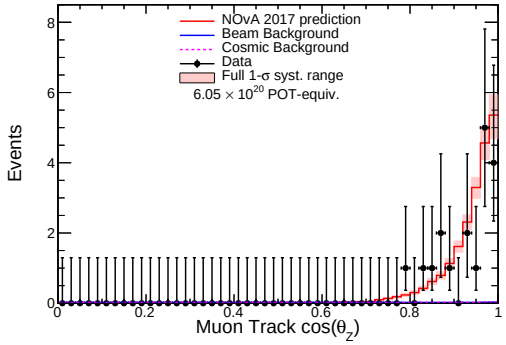

(c) Second lowest E_{had}/E_{ν} quantile.

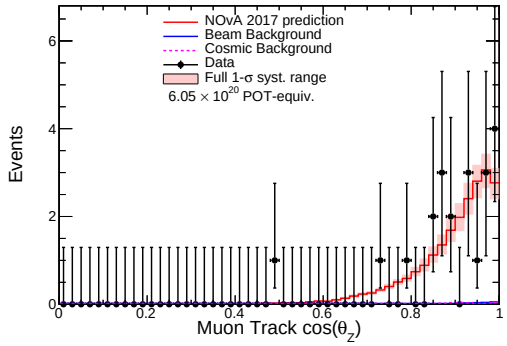

(d) Second highest E_{had}/E_{ν} quantile.

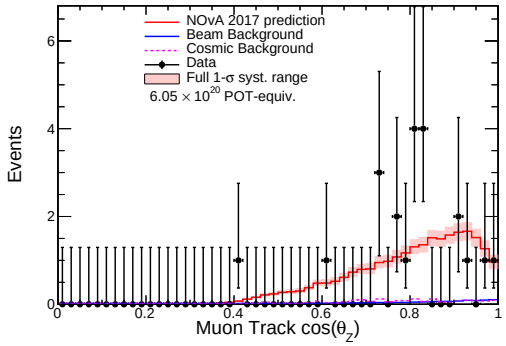

(e) Highest E_{had}/E_{ν} quantile.

Figure 6.35: Plots showing the number of events vs. $\cos\theta_Z$ (where θ_Z is the angle of the leading track relative to the beam direction) for each E_{had}/E_{ν} quantile in the far detector. The events passing selection for simulation and data are shown by the red histogram and the black data-points respectively. The simulation is created using an oscillated (at NOvA's 2017 [41] best fit point) extrapolation from the near to the far detector. The systematic uncertainty in the distribution of the simulated events is shown by the shaded red region enclosing the red histogram. The two sources of background to the analysis are also shown. The simulated background events are shown by the blue histogram. The data estimated cosmic background is shown by the dotted magenta histogram. The muon and hadronic energy have been shifted in the data by 1.5% and 5% respectively. The reason for these shifts are described in Section 6.1.1.

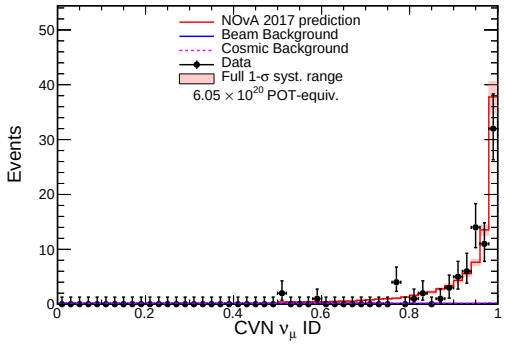

(a) All E_{had}/E_{ν} quantiles combined.

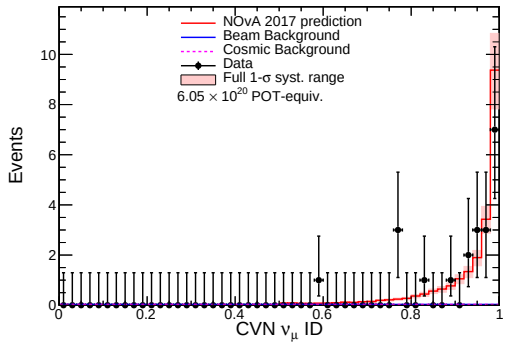

(b) Lowest E_{had}/E_{ν} quantile.

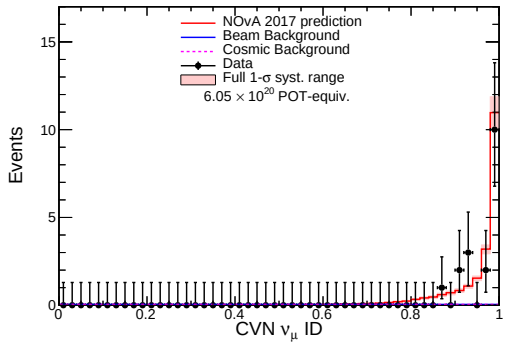

(c) Second lowest E_{had}/E_{ν} quantile.

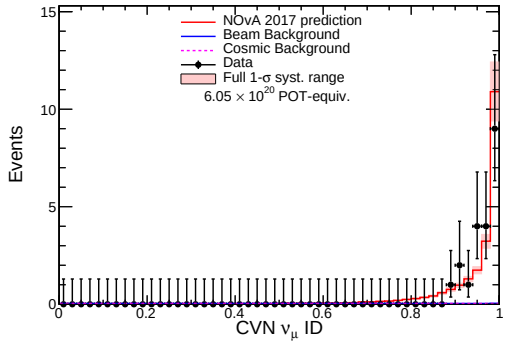

(d) Second highest E_{had}/E_{ν} quantile.

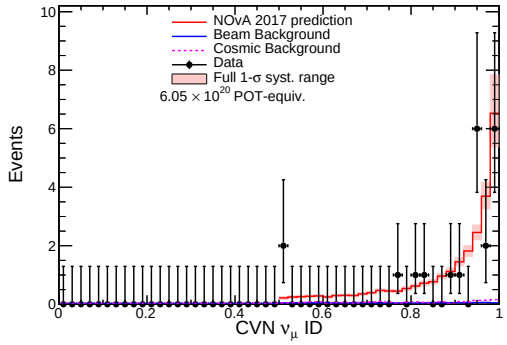

(e) Highest E_{had}/E_{ν} quantile.

Figure 6.36: Plots showing the number of events vs. the CVN score in each E_{had}/E_{ν} quantile in the far detector. The events passing selection for simulation and data are shown by the red histogram and the black data-points respectively. The simulation is created using an oscillated (at NOvA's 2017 [41] best fit point) extrapolation from the near to the far detector. The systematic uncertainty in the distribution of the simulated events is shown by the shaded red region enclosing the red histogram. The two sources of background to the analysis are also shown. The simulated background events are shown by the blue histogram. The data estimated cosmic background is shown by the dotted magenta histogram. The muon and hadronic energy have been shifted in the data by 1.5% and 5% respectively. The reason for these shifts are described in Section 6.1.1.

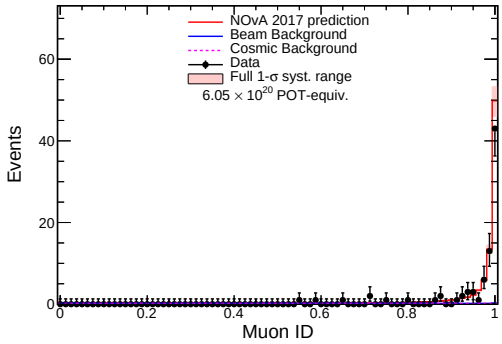

(a) All E_{had}/E_{ν} quantiles combined.

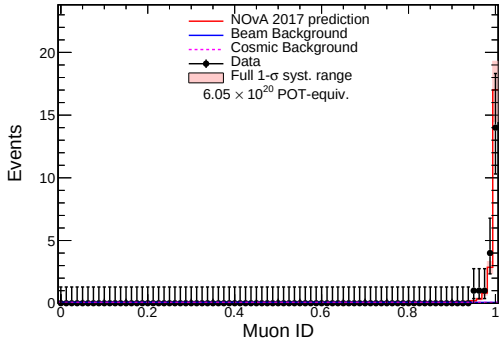

(b) Lowest E_{had}/E_{ν} quantile.

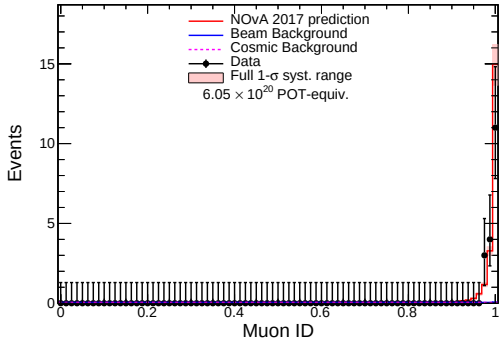

(c) Second lowest E_{had}/E_{ν} quantile.

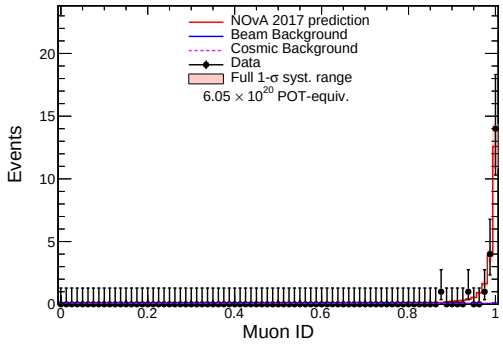

(d) Second highest E_{had}/E_{ν} quantile.

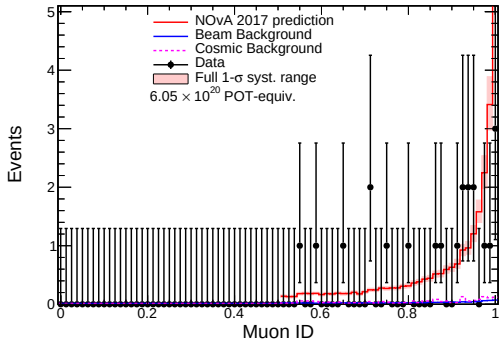

(e) Highest E_{had}/E_{ν} quantile.

Figure 6.37: Plots showing the number of events vs. ReMId score for each E_{had}/E_{ν} quantile in the far detector. The events passing selection for simulation and data are shown by the red histogram and the black data-points respectively. The simulation is created using an oscillated (at NOvA's 2017 [41] best fit point) extrapolation from the near to the far detector. The systematic uncertainty in the distribution of the simulated events is shown by the shaded red region enclosing the red histogram. The two sources of background to the analysis are also shown. The simulated background events are shown by the blue histogram. The data estimated cosmic background is shown by the dotted magenta histogram. The muon and hadronic energy have been shifted in the data by 1.5% and 5% respectively. The reason for these shifts are described in Section 6.1.1.

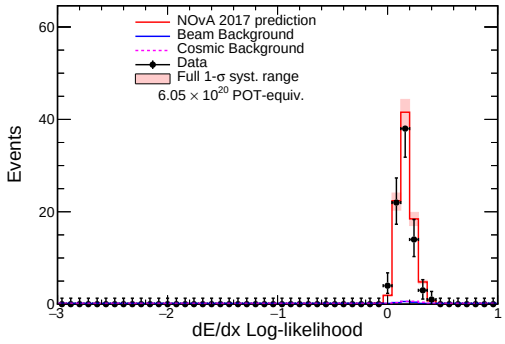

(a) All E_{had}/E_{ν} quantiles combined.

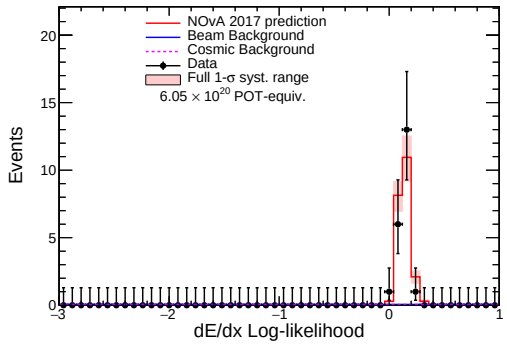

(b) Lowest E_{had}/E_{ν} quantile.

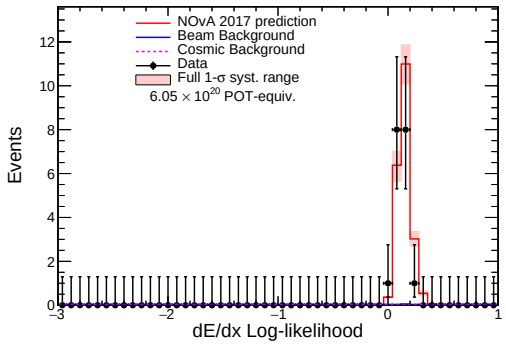

(c) Second lowest E_{had}/E_{ν} quantile.

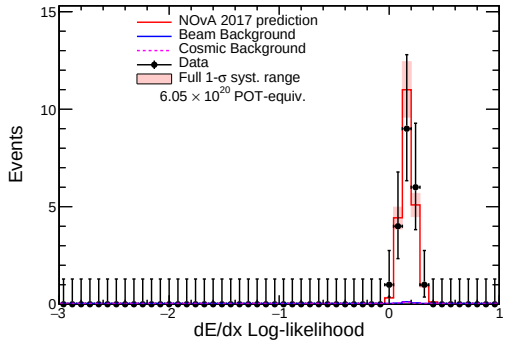

(d) Second highest E_{had}/E_{ν} quantile.

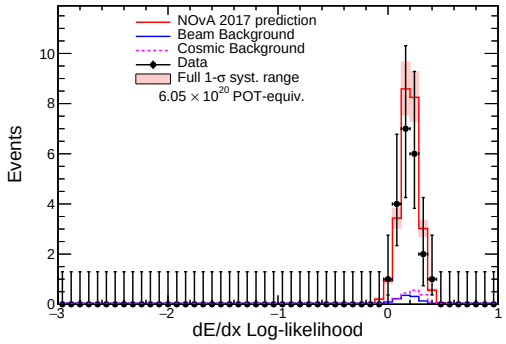

(e) Highest E_{had}/E_{ν} quantile.

Figure 6.38: Plots showing the number of events vs. the dE/dx for each E_{had}/E_{ν} quantile in the far detector. The events passing selection for simulation and data are shown by the red histogram and the black data-points respectively. The simulation is created using an oscillated (at NOvA's 2017 [41] best fit point) extrapolation from the near to the far detector. The systematic uncertainty in the distribution of the simulated events is shown by the shaded red region enclosing the red histogram. The two sources of background to the analysis are also shown. The simulated background events are shown by the blue histogram. The data estimated cosmic background is shown by the dotted magenta histogram. The muon and hadronic energy have been shifted in the data by 1.5% and 5% respectively. The reason for these shifts are described in Section 6.1.1.

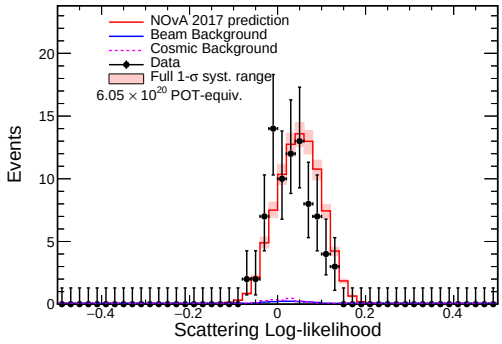

(a) All E_{had}/E_{ν} quantiles combined.

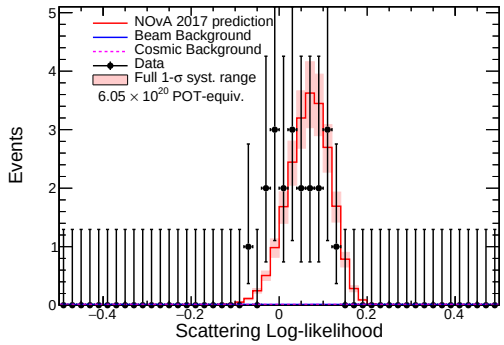

(b) Lowest E_{had}/E_{ν} quantile.

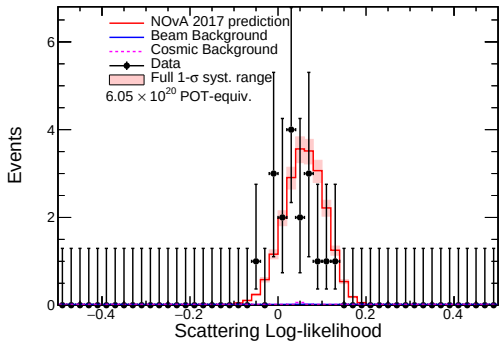

(c) Second lowest E_{had}/E_{ν} quantile.

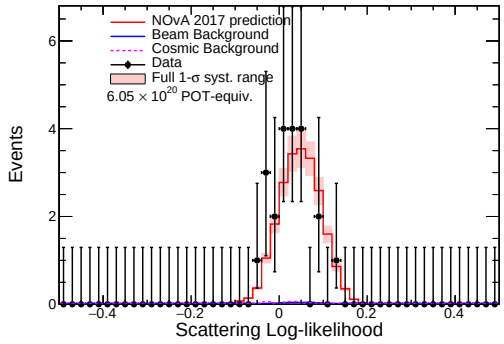

(d) Second highest E_{had}/E_{ν} quantile.

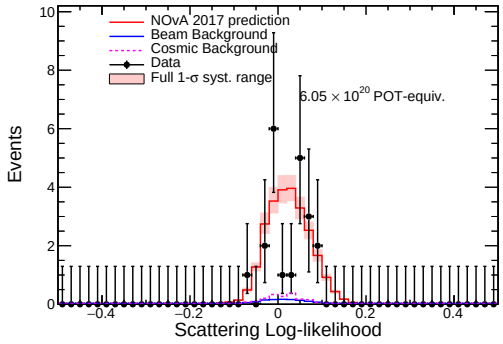

(e) Highest E_{had}/E_{ν} quantile.

Figure 6.39: Plots showing the number of events vs. the scattering Log-Likelihood for each E_{had}/E_{ν} quantile in the far detector. The events passing selection for simulation and data are shown by the red histogram and the black data-points respectively. The simulation is created using an oscillated (at NOvA's 2017 [41] best fit point) extrapolation from the near to the far detector. The systematic uncertainty in the distribution of the simulated events is shown by the shaded red region enclosing the red histogram. The two sources of background to the analysis are also shown. The simulated background events are shown by the blue histogram. The data estimated cosmic background is shown by the dotted magenta histogram. The muon and hadronic energy have been shifted in the data by 1.5% and 5% respectively. The reason for these shifts are described in Section 6.1.1.

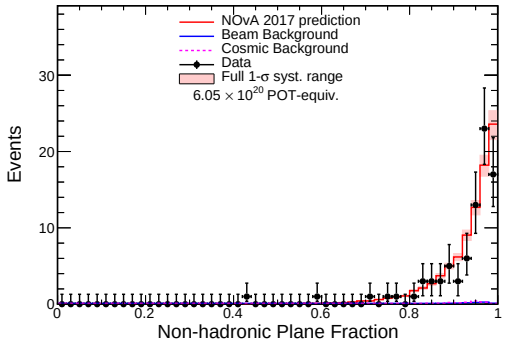

(a) All E_{had}/E_{ν} quantiles combined.

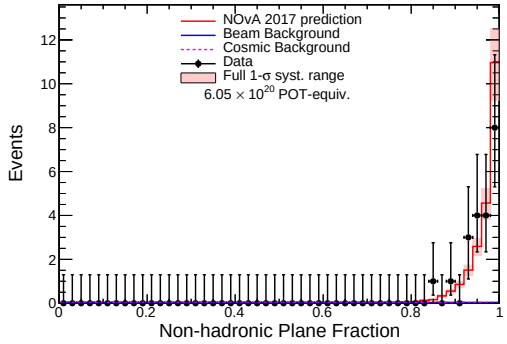

(b) Lowest E_{had}/E_{ν} quantile.

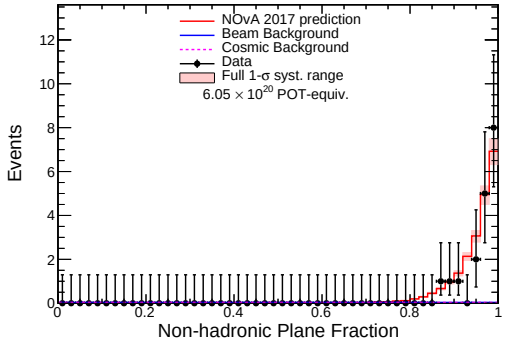

(c) Second lowest E_{had}/E_{ν} quantile.

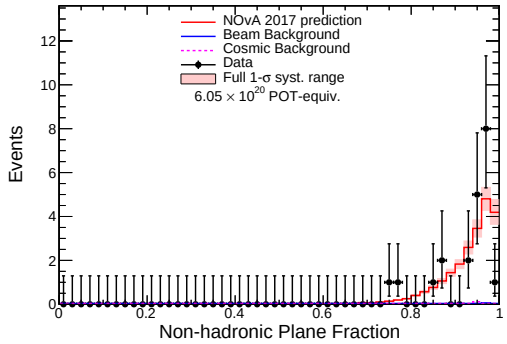

(d) Second highest E_{had}/E_{ν} quantile.

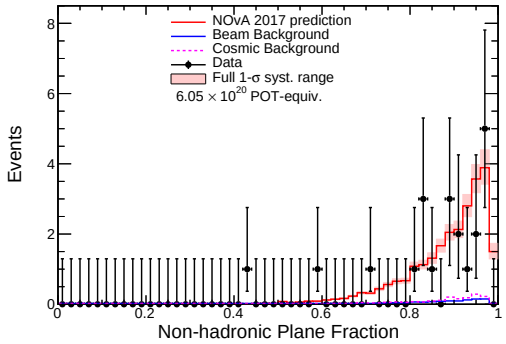

(e) Highest E_{had}/E_{ν} quantile.

Figure 6.40: Plots showing the number of events vs. the number of planes within an event without hadronic activity for each E_{had}/E_{ν} quantile in the far detector. The events passing selection for simulation and data are shown by the red histogram and the black data-points respectively. The simulation is created using an oscillated (at NOvA's 2017 [41] best fit point) extrapolation from the near to the far detector. The systematic uncertainty in the distribution of the simulated events is shown by the shaded red region enclosing the red histogram. The two sources of background to the analysis are also shown. The simulated background events are shown by the blue histogram. The data estimated cosmic background is shown by the dotted magenta histogram. The muon and hadronic energy have been shifted in the data by 1.5% and 5% respectively. The reason for these shifts are described in Section 6.1.1.

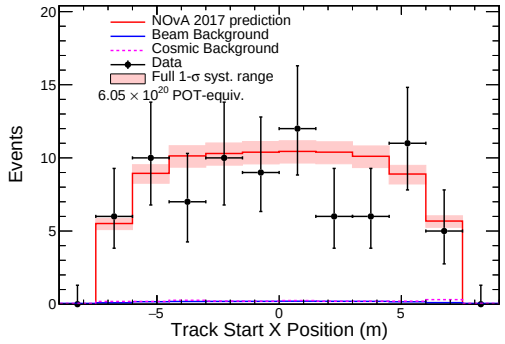

(a) X-position of track start.

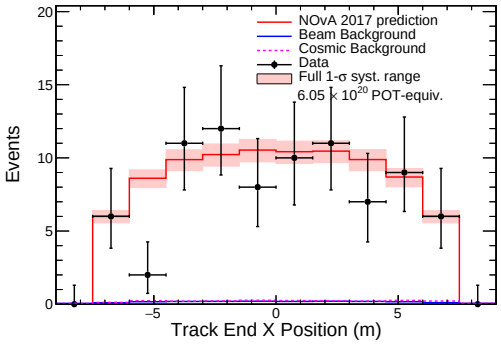

(b) X-position of track end.

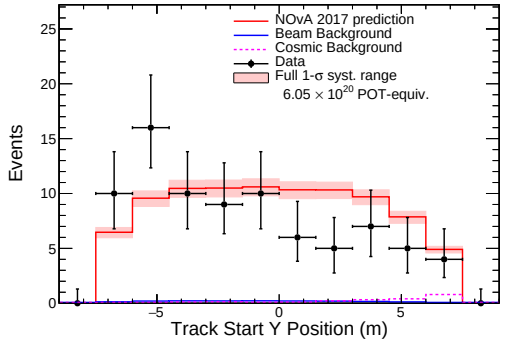

(c) Y-position of track start.

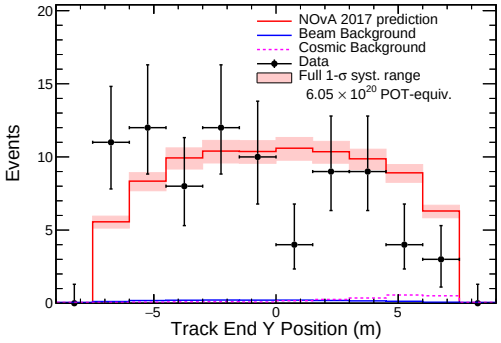

(d) Y-position of track end.

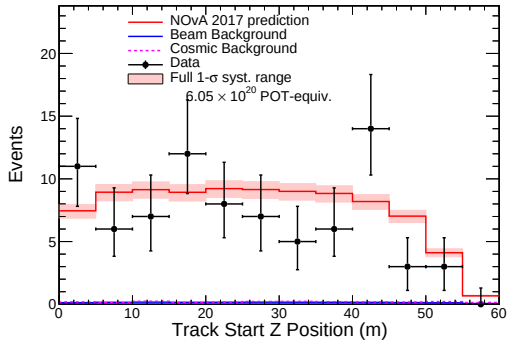

(e) Z-position of track start.

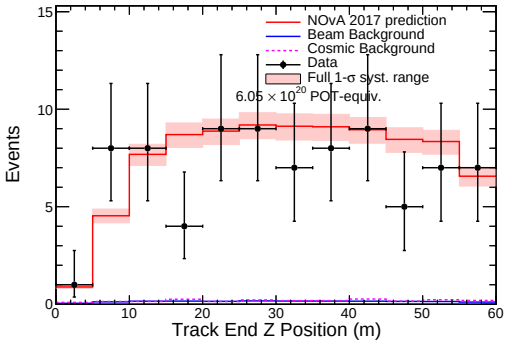

(f) Z-position of track end.

Figure 6.41: Plots showing the start and end points of the candidate neutrino event's leading track. The events passing selection for simulation and data are shown by the red histogram and the black data-points respectively. The simulation is created using an oscillated (at NOvA's 2017 [41] best fit point) extrapolation from the near to the far detector. The systematic uncertainty in the distribution of the simulated events is shown by the shaded red region enclosing the red histogram. The two sources of background to the analysis are also shown. The simulated background events are shown by the blue histogram. The data estimated cosmic background is shown by the dotted magenta histogram. The muon and hadronic energy have been shifted in the data by 1.5% and 5% respectively. The reason for these shifts are described in Section 6.1.1.

Channel	CC events
$\nu_\mu \to \nu_\mu$	83.2
$\nu_\mu \to \nu_e$	0.0963
$\nu_\mu \to \nu_\tau$	0.244
$\overline{\nu}_\mu \to \overline{\nu}_\mu$	5.65
$\overline{\nu}_\mu \to \overline{\nu_e}$	0.000695
$\overline{\nu}_\mu \to \overline{\nu_\tau}$	0.0347
$\nu_e \to \nu_\mu$	0.144
$\nu_e \to \nu_e$	0.0293
$\nu_e \to \nu_\tau$	0.00122
$\overline{\nu_e} \to \overline{\nu}_\mu$	0.0100
$\overline{\nu_e} \to \overline{\nu_e}$	0.00112
$\overline{\nu_e} \to \overline{\nu_\tau}$	0.000160
All ν_μ CC	89.0
	NC events
All	1.29

Table 6.4: Expected events at NOvA's 2017 best fit point

Channel	CC events
$\nu_\mu \to \nu_\mu$	81.9
$\nu_\mu \to \nu_e$	0.119
$\nu_\mu \to \nu_\tau$	0.213
$\overline{\nu}_\mu \to \overline{\nu}_\mu$	5.69
$\overline{\nu}_\mu \to \overline{\nu_e}$	0.00081
$\overline{\nu}_\mu \to \overline{\nu_\tau}$	0.0303
$\nu_e \to \nu_\mu$	0.174
$\nu_e \to \nu_e$	0.0295
$\nu_e \to \nu_\tau$	0.000775
$\overline{\nu_e} \to \overline{\nu}_\mu$	0.012
$\overline{\nu_e} \to \overline{\nu_e}$	0.00113
$\overline{\nu_e} \to \overline{\nu_\tau}$	0.000101
All ν_μ CC	87.8
	NC events
All	1.29

Table 6.5: Expected events at the new best fit point

Parameter	best fit value
$\sin^2\theta_{23}$	0.547 (0.553)
Δm^2_{32}	2.45×10^{-3} eV^2 (-2.50×10^{-3} eV^2)

Marginalised parameter	Central value at best fit
δ_{CP}	$3\pi/2$ (manually set)
$\sin^2 2\theta_{13}$	0.0860
$\sin^2 2\theta_{12}$	0.846
Δm^2_{21}	7.53×10^{-5} eV^2

Table 6.6: Table showing the oscillation parameters that produce the best fit to the data. The top portion of the table shows the measured values of $\sin^2\theta_{23}$ and Δm^2_{32}. Meanwhile, the bottom portion lists the central values taken by the marginalised parameters at the best fit. If a different value is preferred under the assumption of inverted ordering then it is shown within parentheses.

spectrum in the absence of neutrino oscillations is shown in Figure 6.45.

The contours resulting from a fit to the data are shown in Figure 6.46. The blue line shows shows the 90% C.L. contour when accounting for only the statistical errors. The red lines show the 68% (dashed line), 90% (solid line) and 99% (dotted line) C.L. contours when including the systematic uncertainties. Figures 6.47 and 6.48 show the $\Delta\chi^2$ vs. Δm^2_{32} and $\sin^2\theta_{23}$ respectively. These 1D plots are produced by marginalising over the other measured oscillation parameter.

Table 6.6 lists the measured values of the $\sin^2\theta_{23}$ and Δm^2_{32} along with the values taken by the other oscillation parameters which are marginalised over. For the normal hierarchy, the measurements and 1 σ bounds of the mixing angle and the mass splitting are $\sin^2\theta_{23} = 0.547^{+0.046}_{-0.118}$ and $\Delta m^2_{32} = 2.45^{+0.087}_{-0.079} \times 10^{-3}$ eV^2. The 1 σ bounds quoted are the combined systematic and statistical uncertainty bounds. The best fit is found with the parameter δ_{CP} set to $3\pi/2$. The χ^2 between the data and the best fit prediction is 84.4. The analysis uses 19 neutrino energy bins, 4 E_{had}/E_ν bins and the fit is performed in $\sin^2\theta_{23}$ vs. Δm^2_{32} space. Therefore, the best fitting prediction has χ^2/n.d.o.f = 84.4/74 = 1.14 and the corresponding Gaussian p-value is 19.2%. A comparison of the result contour with the sensitivity at the new best fit, shown in Figure 6.49, displays reasonable agreement with the result contour.

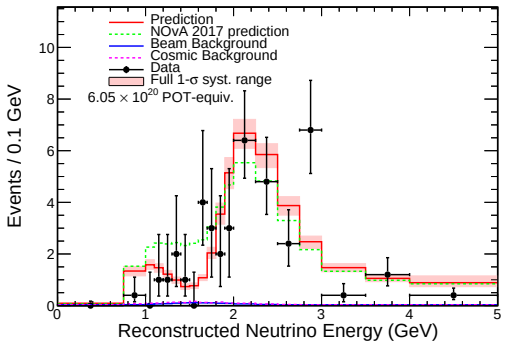

(a) All E_{had}/E_{ν} quantiles combined.

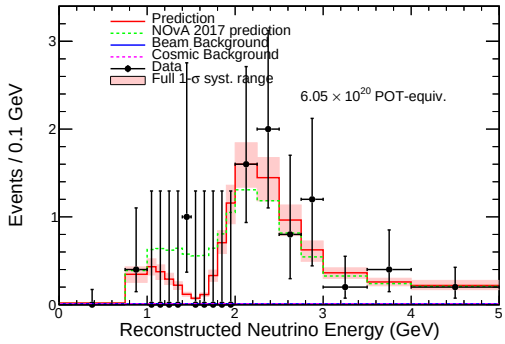

(b) Lowest E_{had}/E_{ν} quantile.

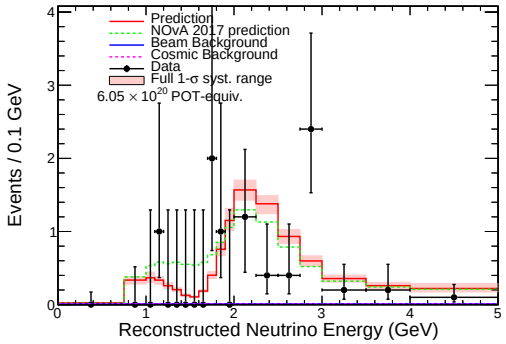

(c) Second lowest E_{had}/E_{ν} quantile.

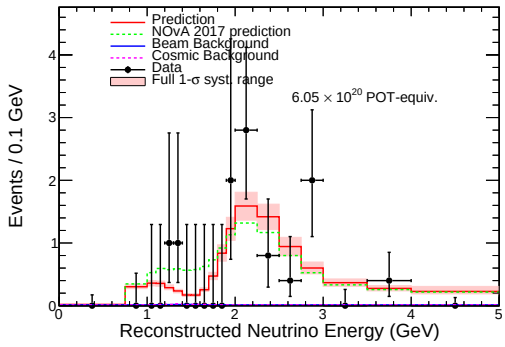

(d) Second highest E_{had}/E_{ν} quantile.

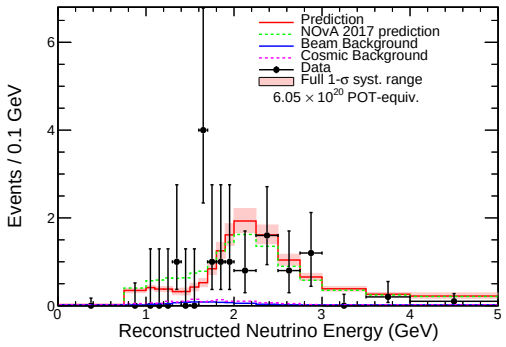

(e) Highest E_{had}/E_{ν} quantile.

Figure 6.42: Plots showing the number of events vs. the muon neutrino energy for each E_{had}/E_{ν} quantile in the far detector. The data are shown by the black points with Poisson error bars. The prediction that best fits the data is shown by the red histogram and the associated systematic uncertainty is shown by the red shaded band. The prediction at NOvA's 2017 [41] best fit point is shown by the dotted green line. The two sources of background to the analysis are also shown. The simulated beam background events are shown by the blue histogram. The data estimated cosmic background is shown by the dotted magenta histogram. The muon and hadronic energy have been shifted in the data by 1.5% and 5% respectively. The reason for these shifts are described in Section 6.1.1.

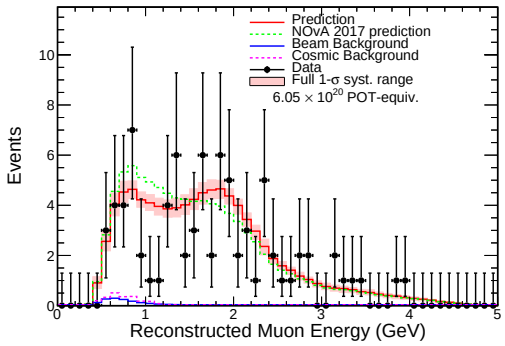

(a) All E_{had}/E_{ν} quantiles combined.

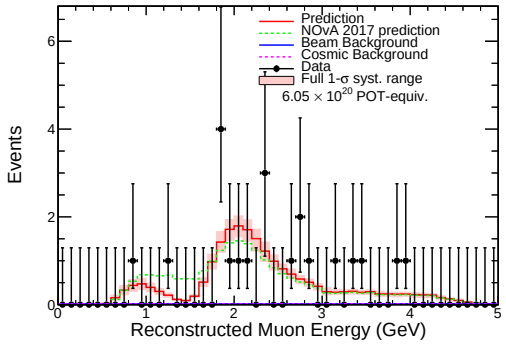

(b) Lowest E_{had}/E_{ν} quantile.

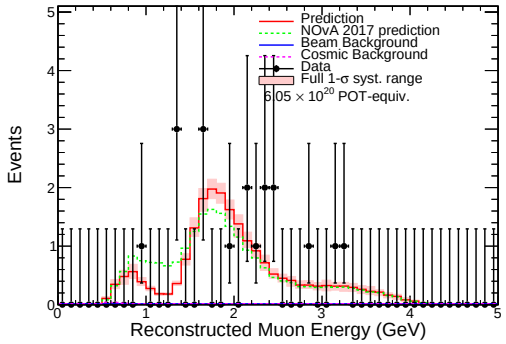

(c) Second lowest E_{had}/E_{ν} quantile.

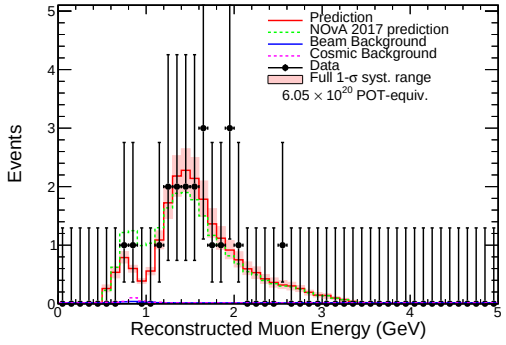

(d) Second highest E_{had}/E_{ν} quantile.

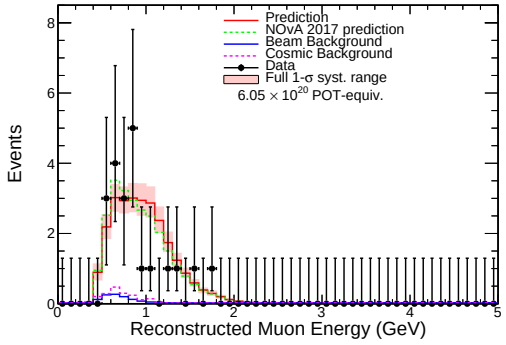

(e) Highest E_{had}/E_{ν} quantile.

Figure 6.43: Plots showing the number of events vs. the muon energy for each E_{had}/E_{ν} quantile in the far detector. The data are shown by the black points with Poisson error bars. The prediction that best fits the data is shown by the red histogram and the associated systematic uncertainty is shown by the red shaded band. The prediction at NOvA's 2017 [41] best fit point is shown by the dotted green line. The two sources of background to the analysis are also shown. The simulated beam background events are shown by the blue histogram. The data estimated cosmic background is shown by the dotted magenta histogram. The muon and hadronic energy have been shifted in the data by 1.5% and 5% respectively. The reason for these shifts are described in Section 6.1.1.

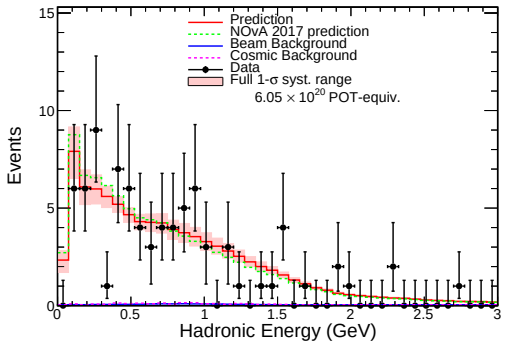

(a) All E_{had}/E_{ν} quantiles combined.

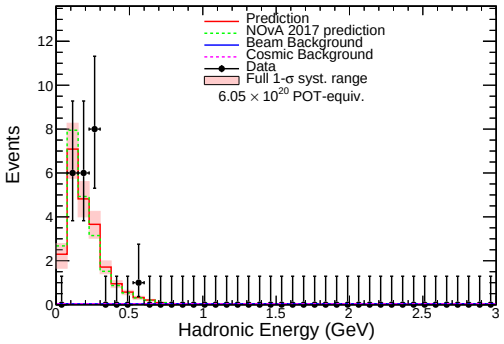

(b) Lowest E_{had}/E_{ν} quantile.

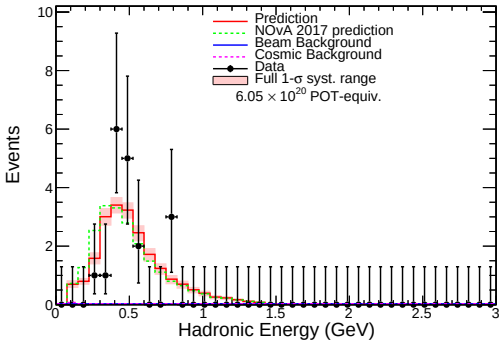

(c) Second lowest E_{had}/E_{ν} quantile.

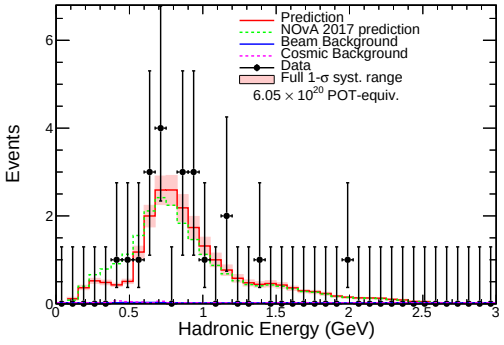

(d) Second highest E_{had}/E_{ν} quantile.

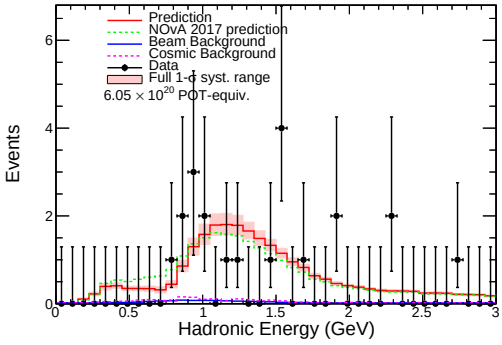

(e) Highest E_{had}/E_{ν} quantile.

Figure 6.44: Plots showing the number of events vs. the hadronic energy for each E_{had}/E_{ν} quantile in the far detector. The data are shown by the black points with Poisson error bars. The prediction that best fits the data is shown by the red histogram and the associated systematic uncertainty is shown by the red shaded band. The prediction at NOvA's 2017 [41] best fit point is shown by the dotted green line. The two sources of background to the analysis are also shown. The simulated beam background events are shown by the blue histogram. The data estimated cosmic background is shown by the dotted magenta histogram. The muon and hadronic energy have been shifted in the data by 1.5% and 5% respectively. The reason for these shifts are described in Section 6.1.1.

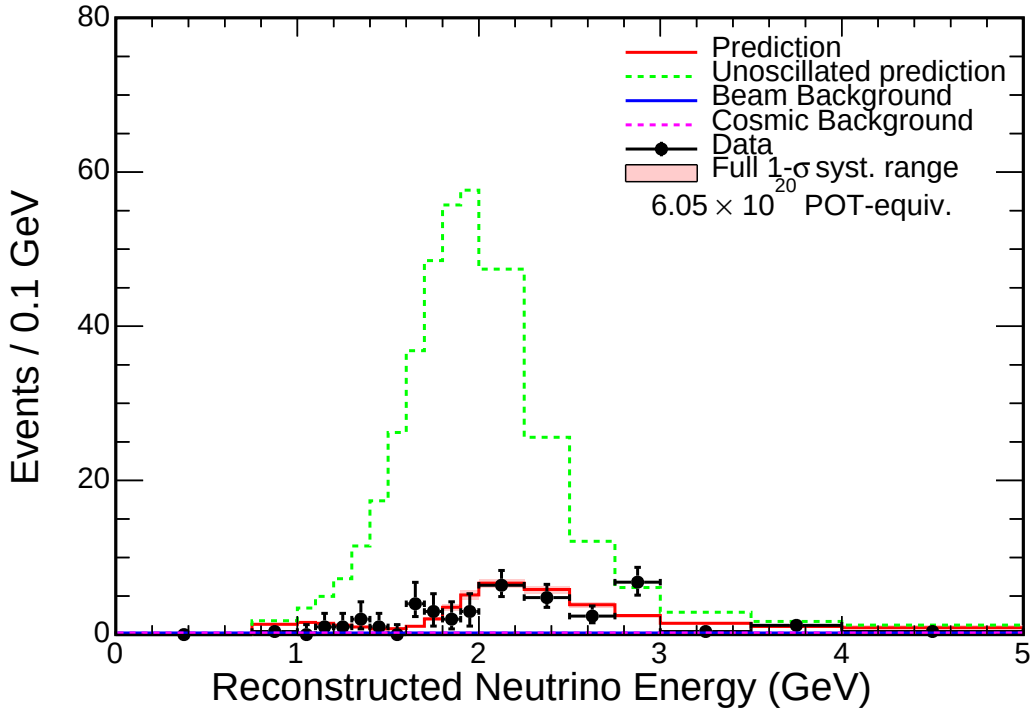

Figure 6.45: Events vs. muon neutrino energy in the far detector. The data are shown by the black points with Poisson error bars. The prediction that best fits the data is shown by the red histogram and the associated systematic uncertainty is shown by the red shaded band. The predicted energy spectrum in absence of neutrino oscillations is shown by the dotted green line. The two sources of background to the analysis are also shown. The simulated beam background events are shown by the blue histogram. The data estimated cosmic background is shown by the dotted magenta histogram. The muon and hadronic energy have been shifted in the data by 1.5% and 5% respectively. The reason for these shifts are described in Section 6.1.1.

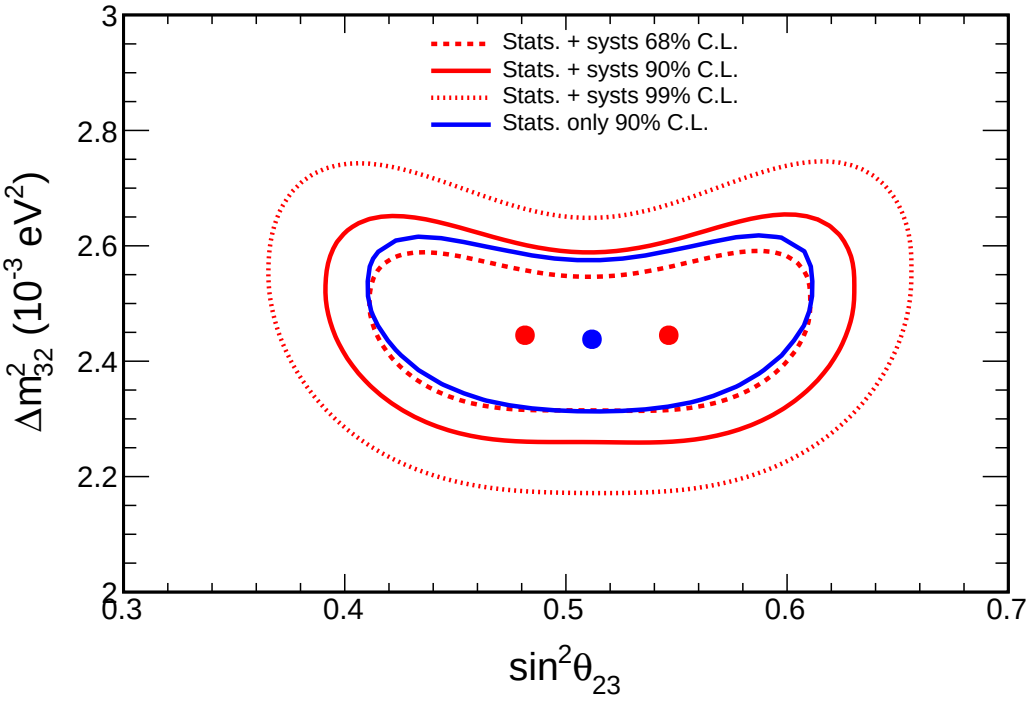

Figure 6.46: The 90% stats. only (blue line) and full systematic (red lines) result contours produced by this analysis using a data set with a far detector exposure of 6.05×10^{20} POT-equiv..

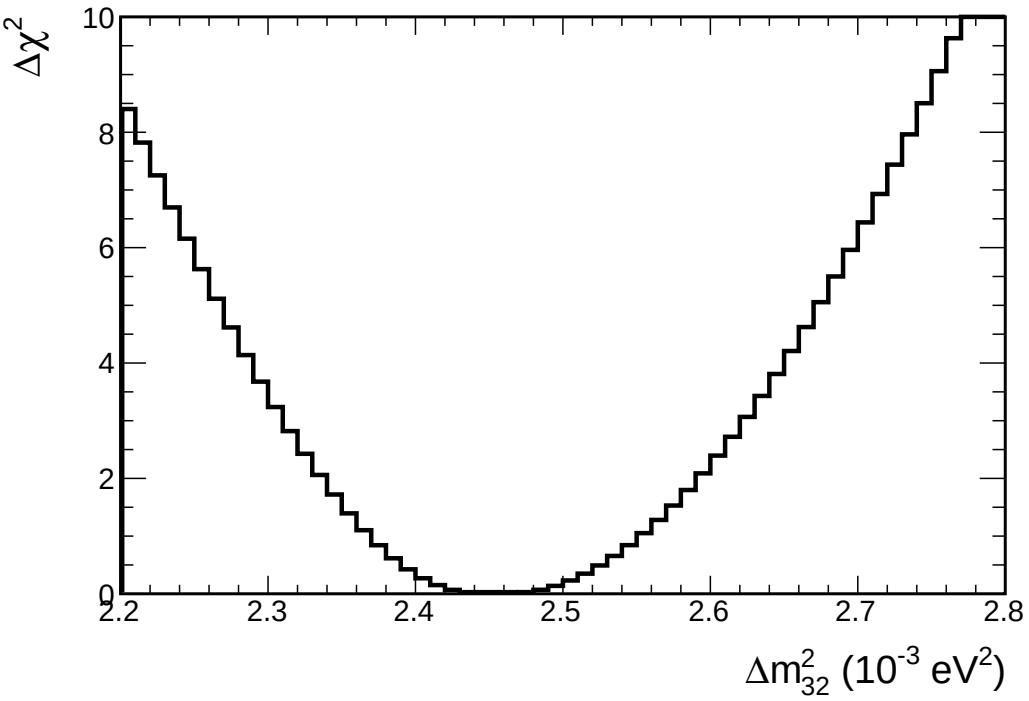

Figure 6.47: Plot showing the $\Delta\chi^2$ vs. the mass splitting Δm^2_{32} produced by this analysis using a data set with a far detector exposure of 6.05×10^{20} POT-equiv..

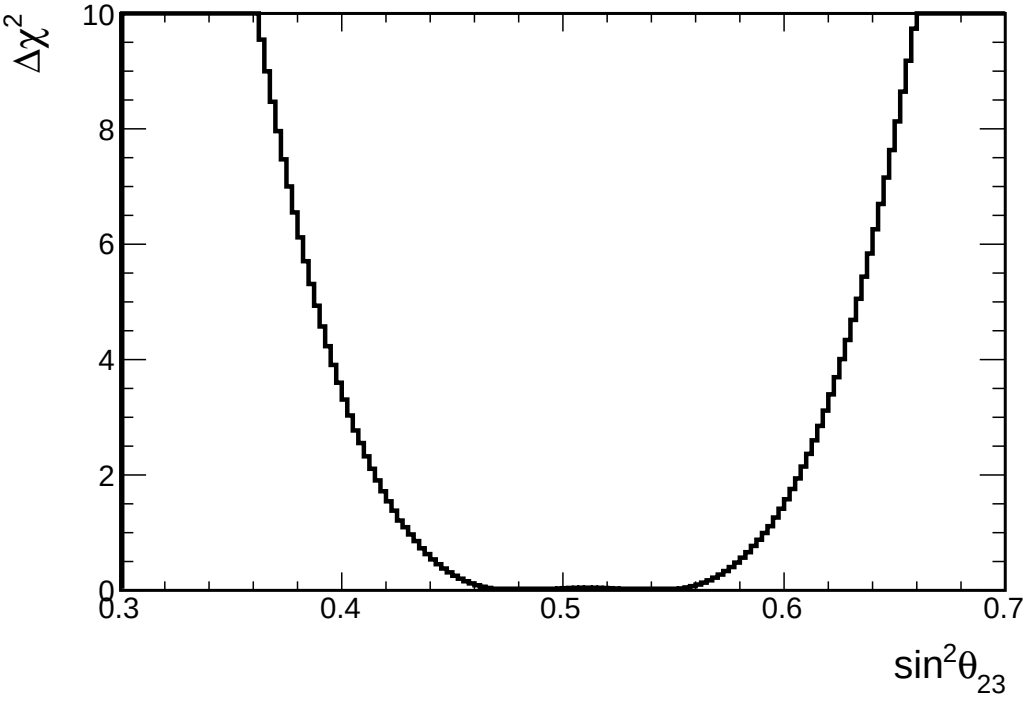

Figure 6.48: Plot showing the $\Delta\chi^2$ vs. the mixing angle $\sin^2\theta_{23}$ produced by this analysis using a data set with a far detector exposure of 6.05×10^{20} POT-equiv..

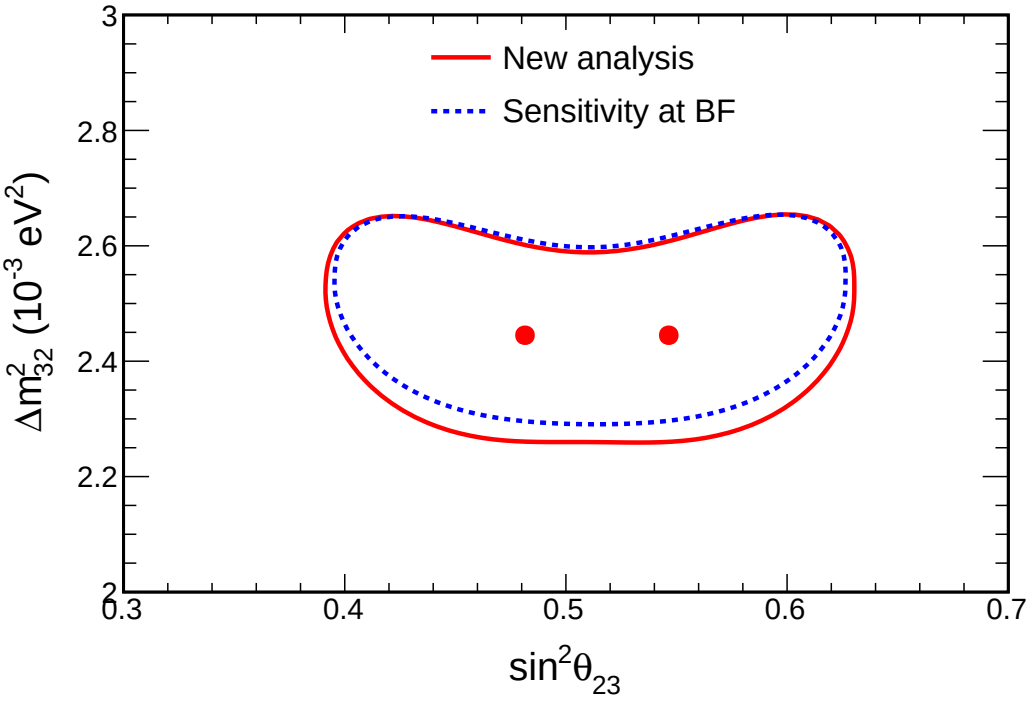

Figure 6.49: Comparison of the result contour (red line) and the sensitivity at the new best fit (dashed blue line) produced by this analysis using a data set with a far detector exposure of 6.05×10^{20} POT-equiv..

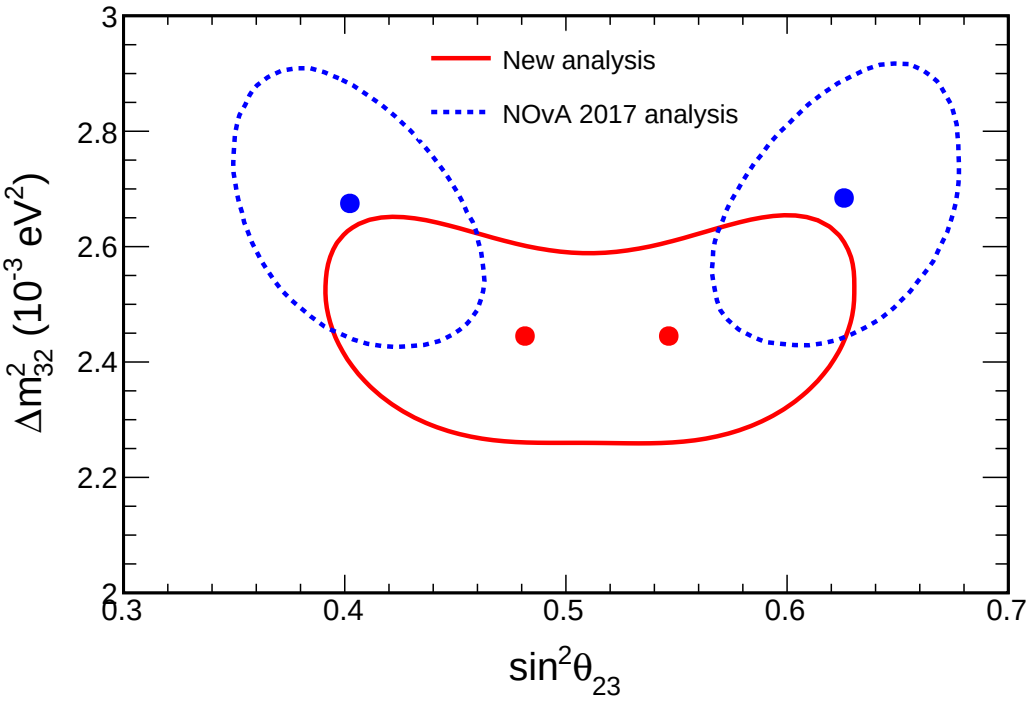

Figure 6.50: Comparison of the 90% result contour produced by this analysis (red contour) with that produced by the NOvA 2017 [41] analysis (dashed blue contour). Both analyses use the same data set with a far detector exposure of 6.05×10^{20} POT-equiv..

Table 6.7 shows the extent to which the prediction is systematically shifted to improve the fit to the data at the best fit point. These shifts, called systematic pulls, are shown for each source of systematic uncertainty and quoted as fractions of σ. The pulls represent the extent to which the prediction was systematically shifted to improve the fit to the data for each systematic uncertainty at the best fit point. The uncertainties pulled the most are the absolute and relative muon and hadronic energy scales which are pulled by -0.56, -0.67, -0.60 and -0.44 units of σ respectively.

Figure 6.50 shows a comparison between the new result contour and NOvA's 2017 [41] result contour. The new result is consistent with maximal mixing, whereas NOvA's 2017 [41] result disfavoured maximal mixing at 2.6 σ. This new analysis excludes NOvA's 2017 [41] best fit point by $\Delta\chi^2 = 5.70$ which corresponds to 2.4 σ. The reasons behind the differences in the two results are analysed in Section 6.3.

A comparison of the result with MINOS's 2014 [40] and T2K's 2015 joint ν_μ and $\overline{\nu}_\mu$ [27] 90% C.L. contours is shown in Figure 6.51. The result contour produced by this thesis sits between the T2K and MINOS contours. In addition, Figure 6.52 shows a comparison between this result and the following three T2K results: the 2015 joint ν_μ+$\overline{\nu}_\mu$ analysis [27],

Source of uncertainty	pull (σ)
norm	0.00061
relNorm	0.33
numuNCScale	0.074
TransportPlusNA49	-0.30
mecScale	-0.041
RPA	-0.016
SAMuEScale	-0.56
FDSAMuEScale	-0.67
SACalibXY	-0.60
SACalibYFunc	0.26
SABirks	-0.36
SARelHadE	-0.44
numuSumSmallGENIE	-0.018
MaNCEL	-0.00043
NormCCQE	0.059
MaCCQEshape	-0.011
MaCCRES	0.059
MvCCRES	0.030
MaNCRES	0.0036
MvNCRES	0.0014
CCQEPauliSupViaKF	-0.052
cosmicScale	0.043

Table 6.7: Table showing the pull terms for each source of uncertainty that produces the best fit to the data.

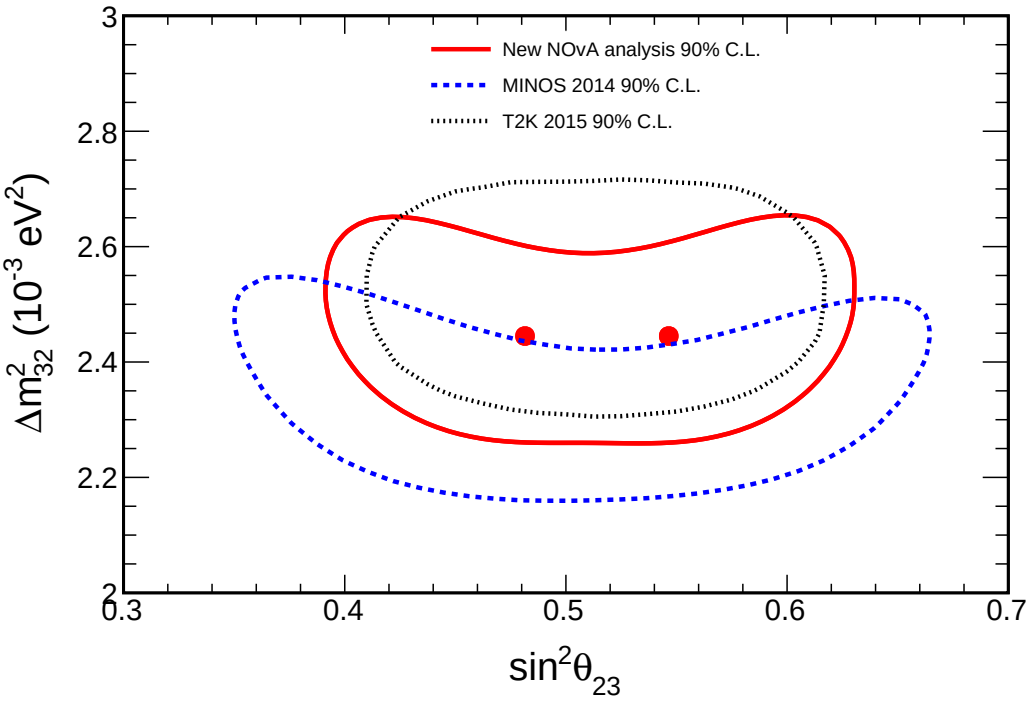

Figure 6.51: Comparison of the 90% result contour produced by this analysis (red contour) with that produced by the MINOS 2014 [40] analysis (dashed blue contour) and the T2K 2015 [27] analysis (dotted black contour).

the 2016 ν_μ analysis [100] and the 2016 combined $\nu_\mu + \nu_e$ analysis [101]. The new result is consistent with the T2K results but prefers a slightly lower value of the mass splitting. Figure 6.53 shows a comparison with Daya Bay's world leading measurement of the mass splitting Δm^2_{32}. The 1D 1 σ confidence limit measurements of the mass splitting are overlaid on the result contour plot for both Daya Bay (blue band) and the new NOvA result (hatched red). These C.L. bands show that the new result provides approximately the same resolution on the mass splitting measurement.

6.3 Analysis of the Result

The result shown in Section 6.2.3 represents a significant shift away from NOvA's previous result while using exactly the same data set. This section discusses the difference between NOvA's 2017 [41] result and the result produced by this thesis. In particular, the contributions of the individual analysis changes are investigated.

The result contours produced by each E_{had}/E_ν quantile independently are compared in Figure 6.54. The highest E_{had}/E_ν quantile (shown by the dashed black line) produces

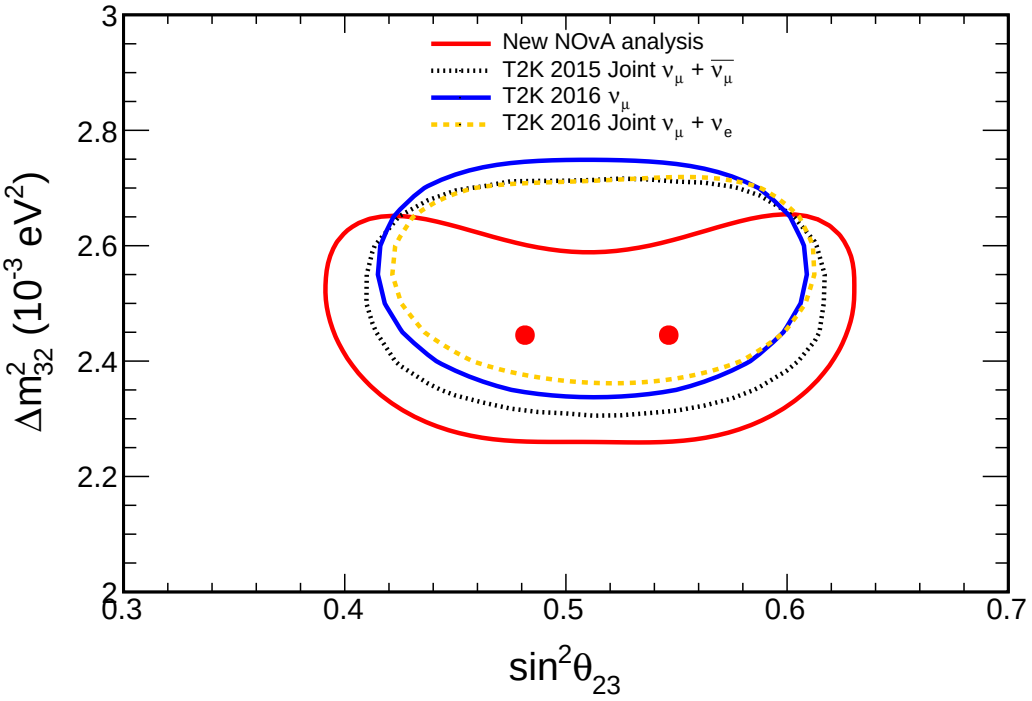

Figure 6.52: Comparison of the result of this thesis (red line) compared with three T2K result contours. T2K's 2015 [27] joint ν_μ plus $\overline{\nu}_\mu$, 2016 ν_μ [100] and 2016 joint ν_μ plus ν_e [101] results are shown by the dotted black, solid blue, and dashed orange lines respectively.

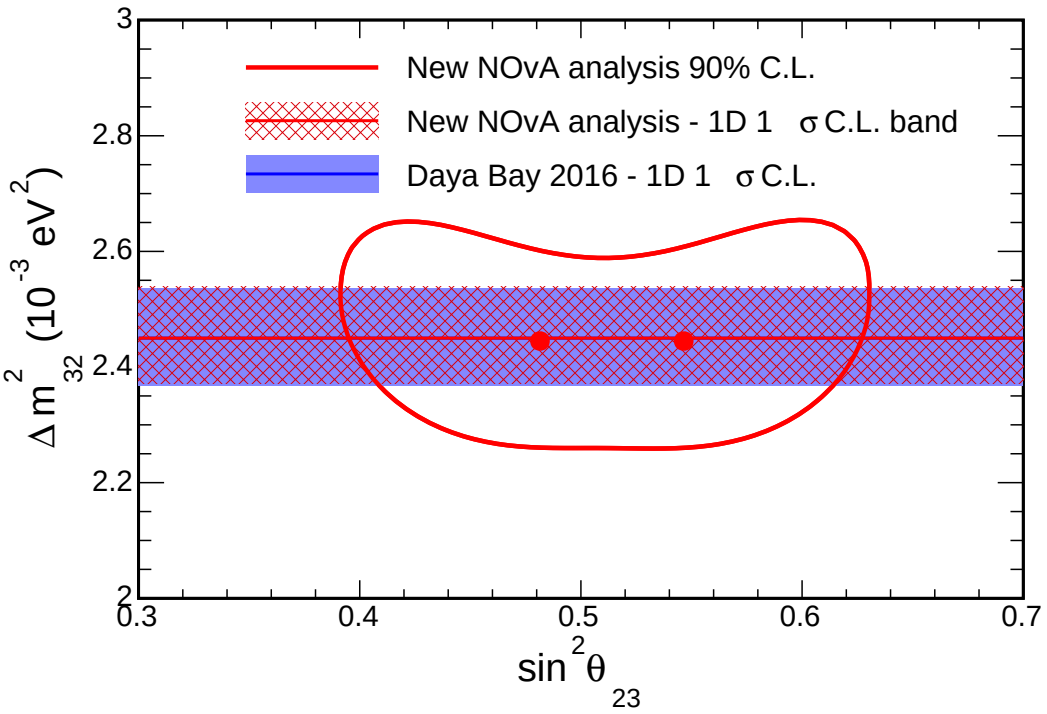

Figure 6.53: Comparison between the new 1D 1 σ C.L. Δm^2_{32} measurement and Daya Bay's 2017 [102] measurement overlaid on the new result contour. The measurement of Δm^2_{32} found in this thesis is shown by the red line and the uncertainty is shown by the shaded red region. Daya Bay's 2017 [102] measurement with uncertainty ($\Delta m^2_{32} = (2.45 \pm 0.06(stat.) \pm 0.06(syst.)) \times 10^{-3}$ eV^2) is shown by the blue line and shaded blue region. Note that Daya Bay's best fit line is hidden as it lies beneath the new result best fit.

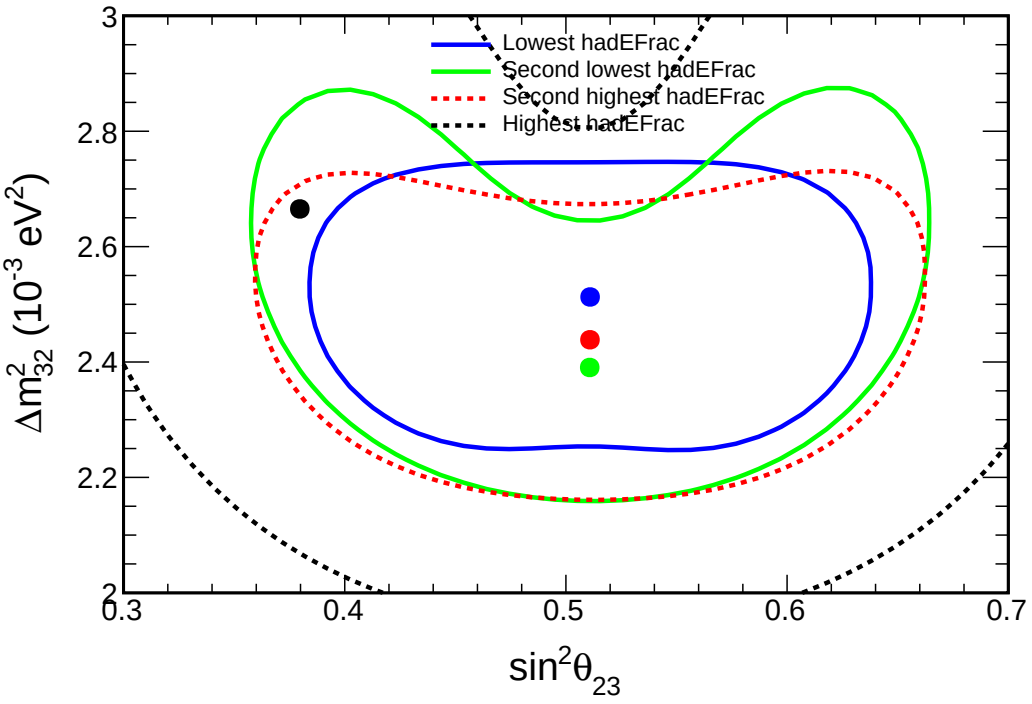

Figure 6.54: Comparison of the 90% result contours for each individual E_{had}/E_ν quantile.

the largest contour with a non-maximal mixing best fit. On the other hand, the other three quantiles that have better energy resolution produce smaller, more precise, contours with best fit values at the maximum disappearance value of $\sin^2\theta_{23} = 0.514$.

A comparison between the results produced by implementing each of the improvements individually is shown in Figure 6.55. For every one of the changes the contour shifts towards maximal mixing. The largest changes in the contour are seen for the hybrid selection and the E_{had}/E_ν binning, for these two changes the result contour no longer excludes maximal mixing. The effect of the four changes to the analysis will now be discussed in turn. First, the result produced using the hybrid selection and shown by the green line. In NOvA's 2017 analysis most of the rejection of maximal mixing came from the 1.5-1.75 GeV neutrino energy bin (the so-called "dip bin") containing 8 events [103]. The hybrid selector is 10% more efficient, twice as pure and selects one less event in the dip bin [66, 65]. We expected about 0.8 background events in the dip bin in the NOvA 2017 [41] analysis but three of the events previously selected are now rejected as background by the new analysis. Two events previously rejected are now selected (in NOvA's 2017 [41] analysis one of these events marginally failed the muon ID selection and the other marginally failed the cosmic rejection). This suggests an upward fluctuation in the number of background events in the dip bin in NOvA's 2017 [41] analysis. The

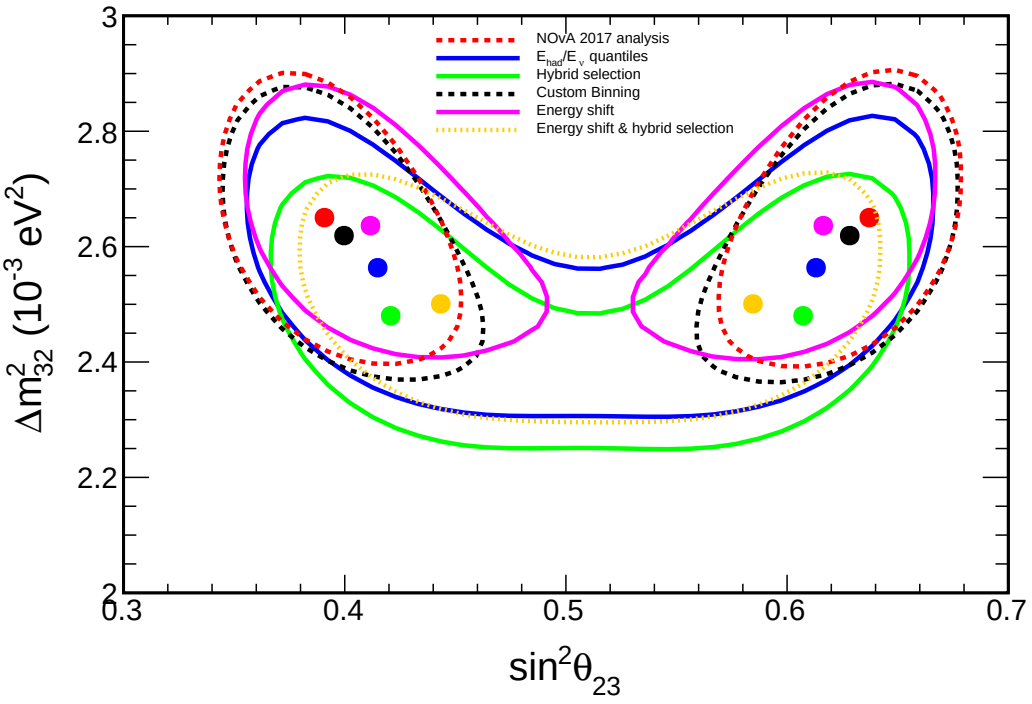

Figure 6.55: Comparison of the 90% result contour produced by each separate change introduced for this analysis.

dashed yellow contour shows the 90% C.L. contour produced when combining the hybrid selection and the energy shift. The contour is shifted towards maximal mixing (more so than when using the just hybrid selection) and to a lower value of the mass splitting. A study of the individual events shows that one event previously at the upper edge of the "dip bin" migrates to the next energy bin when the energy shift is applied. Third, the blue line shows the 90% C.L. contour produced using separating events in into quantiles of E_{had}/E_ν. This E_{had}/E_ν binning places the vast majority of the predicted background events within the highest two E_{had}/E_ν quantiles. In NOvA's 2017 [41] analysis, the events within the dip had higher hadronic energy than expected [103] and mostly fall into the two high E_{had}/E_ν bins. These events are effectively deweighted in the fit due to the greater number of background events in these quantiles and their low energy resolution. Fourth, the finer binning (dotted black line) reduces the rejection of maximal mixing. In NOvA's 2017 analysis we expected events to have a reasonably uniform distribution across the width of the dip bin (1.5-1.75 GeV) but they didn't, 7 of the 8 events had energies in the range 1.65-1.75 GeV. The introduction of finer binning in this energy region has more precisely allocated events to higher energy bins and reduced the rejection of maximal mixing.

Figure 6.56a shows the energy spectrum when using the hybrid selection and applying the energy shift. The data is shown alongside predictions at T2K's 2015 [40] best fit point, NOvA's 2017 [41] best fit point and the best fit to the data shown. Note, the best fit to the data shown is created from a fit using just the hybrid selection and the energy shift, it is not the same as the best fit quoted as the final result. The χ^2 (strictly Log-Likelihood, LL) distributions for comparisons of the data with each prediction are shown in Figure 6.57a. The total χ^2 is quoted in the legend and a comparison between the total χ^2 produced by predictions at the new best fit and NOvA's 2017 best fit provides $\Delta\chi^2 = 3.89$. The χ^2 for the new best fit prediction is lower than the NOvA 2017 [41] prediction across most of the neutrino energy bins, the largest differences occur between 1 and 1.5 GeV and between 1.75 and 3 GeV.

Figures 6.56b, 6.56c, 6.56d and 6.56e show the energy spectra for each E_{had}/E_ν quantile when applying all of the analysis improvements. The data is shown alongside predictions at T2K's 2015 [40] best fit point, NOvA's 2017 [41] best fit point and the new result best fit. The corresponding χ^2 distributions formed from comparisons of the data with the above predictions are shown in Figures 6.57b, 6.57c, 6.57d and 6.57e. The $\Delta\chi^2$ between predictions made using the NOvA 2017 [41] best fit and the new best fit is printed on the plot. These $\Delta\chi^2$ values show that the new best fit prediction provides a better fit to the data in all of the E_{had}/E_ν quantiles except the fourth quantile where the NOvA 2017 [41] prediction provides a slightly better fit to the data.

6.4 Systematic Uncertainty

The contributions of each systematic uncertainty to the measurement uncertainty at the new best fit point is shown in Table 6.8. The contribution of each source of systematic uncertainty to the measurement uncertainty is found in the same way as described in Section 5.9.

The largest sources of uncertainty in the measurement of Δm^2_{32} are the absolute and relative muon and hadronic energies, scintillation model (birks'), normalisation and the combined GENIE and MEC and RPA (largely due to the MaCCRES uncertainty) systematic uncertainties. By far the largest source of systematic uncertainty for Δm^2_{32} is the absolute muon energy. For $\sin^2\theta_{23}$ the largest contributors to the measurement uncertainty are the absolute and relative muon energy, normalisation, absolute hadronic energy and the neutral current background. The relative muon and hadronic energy are the largest source of systematic uncertainty in the $\sin^2\theta_{23}$ measurement.

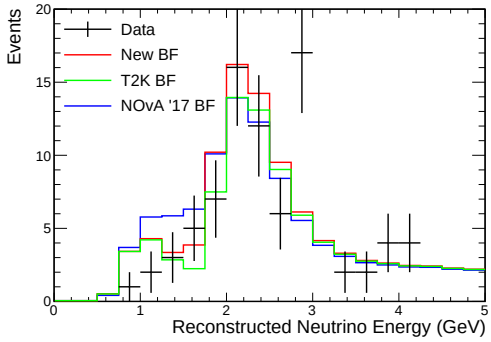

(a) Hybrid selection and energy shift.

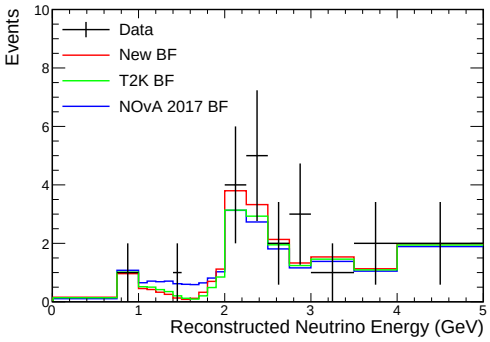

(b) Improved analysis, 1st E_{had}/E_{ν}.

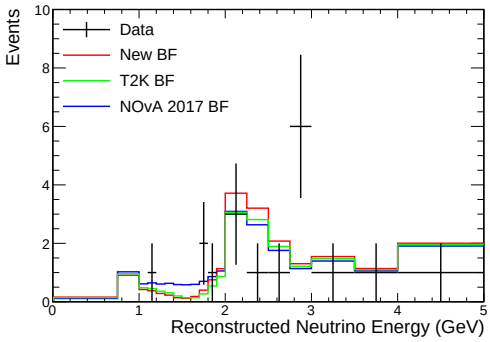

(c) Improved analysis, 2nd E_{had}/E_{ν}.

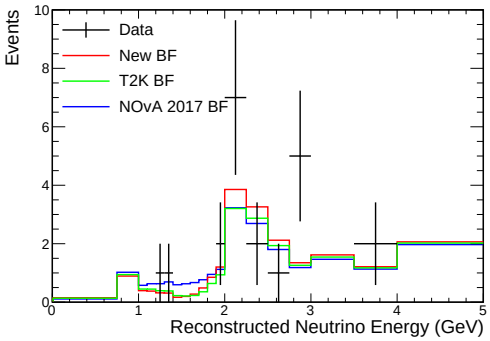

(d) Improved analysis, 3rd E_{had}/E_{ν}.

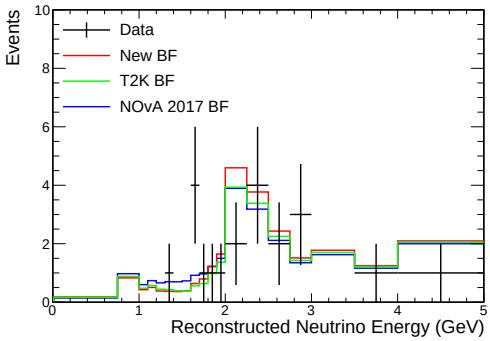

(e) Improved analysis, 4th E_{had}/E_{ν}.

Figure 6.56: The energy spectrum of muon neutrino charged current candidates. The black points show the data. The prediction at NOvA's 2017 [41], T2K's 2015 [27] best fit points are shown by the blue and green histograms respectively. The prediction that best fits the data is shown by the red histogram. The top plot shows the result of combining the hybrid selection and the energy shift. The bottom four plots show the distribution within each E_{had}/E_{ν} quantile when using all the analysis improvements and the energy shift.

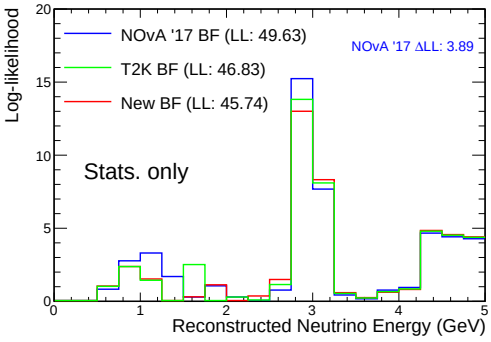

(a) Hybrid selection and energy shift.

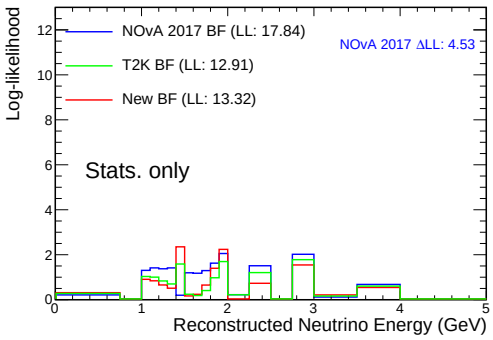

(b) Improved analysis, 1st E_{had}/E_{ν}.

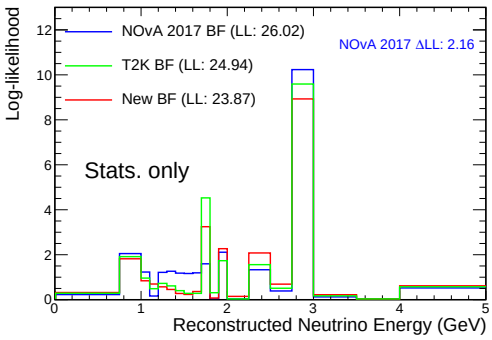

(c) Improved analysis, 2nd E_{had}/E_{ν}.

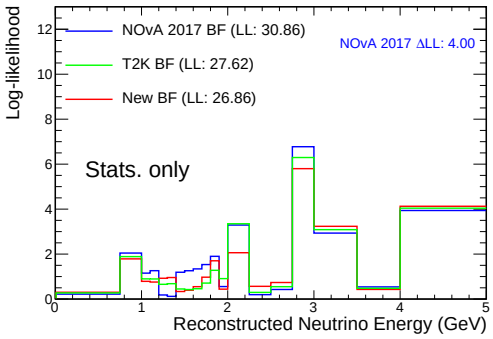

(d) Improved analysis, 3rd E_{had}/E_{ν}.

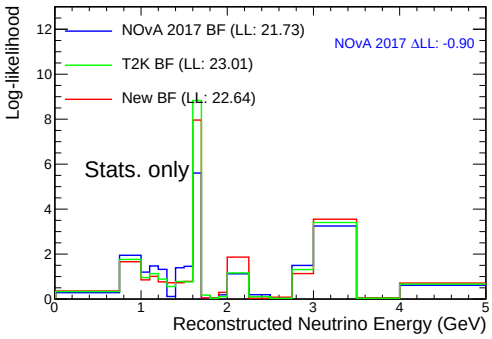

(e) Improved analysis, 4th E_{had}/E_{ν}.

Figure 6.57: The log-likelihood vs. the energy of muon neutrino charged current candidates. The plots are made by comparing each of the predictions with the data shown in Figure 6.56. Comparisons between the data and the prediction at NOvA's 2017 [41], T2K's 2015 [27] best fit points are shown by the blue and green histograms respectively. The comparison between the data and the prediction that best fits the data is shown by the red histogram. The top plot shows the result of combining the hybrid selection and the energy shift. The bottom four plots show the log-likelihood distribution within each E_{had}/E_{ν} quantile when using all the analysis improvements and the energy shift.

Table 6.8: Table of uncertainty in $\sin^2\theta_{23}$ and Δm^2_{32} due to each source of systematic uncertainty when using the improved analysis and new best fit point ($\sin^2\theta_{23} = 0.547$, $\Delta m^2_{32} = 2.45 \times 10^{-3}$ eV^2). The uncertainty is quoted as if the best fit was at the point of maximal disappearance ($\sin^2\theta_{23} = 0.514$). The existence of a degenerate best fit point at 0.481 means that the uncertainties are otherwise highly asymmetric, which is not very meaningful. The largest contributions to the systematic uncertainty in the measurement of Δm^2_{32} and $\sin^2\theta_{23}$ are given in bold text.

Source of uncertainty	Uncertainty in $\sin^2\theta_{23}(\times 10^{-3})$	Uncertainty in $\Delta m^2_{32}\left(10^{-6}\text{ eV}^2\right)$
Normalisations	**±7.1**	**+9.5 / -15**
Absolute muon energy	**±6.7**	**+22 / -29**
Relative muon energy	**±11**	**+3.6 / -14**
Absolute hadronic energy	**±5.8**	**+4.5 / -11**
Relative hadronic energy	**±12**	**+0.47 / -11**
Birks'	±1.5	**+14 / -14**
Summed small GENIE	±0.78	+0.59 / -0.39
NormCCQE	±1.2	+1.6 / -0.52
MaCCQEshape	±0.0	+2.3 / -2.9
MaCCRES	±0.48	**+11 / -12**
MvCCRES	±0.34	+7.4 / -7.3
MaNCRES	±0.71	+0.82 / -0.35
CCQEPauliSupViaKF	±0.59	+2.8 / -3.5
MEC scale	±2.1	+8.3 / -6.5
RPA	±0.27	+3.2 / -2.7
Comb. GENIE+MEC+RPA	±1.9	**+15 / -14**
NC background	**±4.9**	+4.2 / -1.1
Cosmic background	±1.9	+1.5 / -0.43
TransportPlusNA49	±3.0	+4.1 / -2.2
δ_{CP}	±0.51	**+13 / -13**
Statistical uncertainty	±76	+74 / -63
Total systematic uncertainty	±24	+50 / -57
Total uncertainty	±80	+98 / -87

Chapter 7

Conclusion

This thesis has outlined three methods to improve the sensitivity of NOvA's muon neutrino disappearance analysis. First, events are separated into four quantiles of E_{had}/E_{ν} to separate well resolved events from events that are not so well resolved. Second, an optimised neutrino energy binning is implemented that uses finer binning in the region of maximum muon neutrino disappearance. Third, a hybrid selection is introduced that selects muon neutrino events with greater efficiency and purity. The combination of these improvements produces an increase to the sensitivity of the analysis equivalent to collecting 40-100% more data across the range of possible values of Δm^2_{32} and $\sin^2\theta_{23}$. This thesis produces new results using a 14 ktonne detector equivalent exposure of 6.05×10^{20} protons on target. A fit to the far detector data, assuming normal hierarchy, produces measurements of $\Delta m^2_{32} = 2.45^{+0.087}_{-0.079} \times 10^{-3}$ eV^2 and $\sin^2\theta_{23}$ in the range 0.429 - 0.593 with two statistically degenerate best fit points at 0.481 and 0.547. This result has the same world leading sensitivity to Δm^2_{32} as Daya Bay [102] and the measurement of $\sin^2\theta_{23}$ is competitive with T2K [27].

The far detector data used for this thesis is only 1/6 of the data expected during NOvA's full running period. NOvA's future measurement of $\sin^2\theta_{23}$ will remain statistically limited at the current best fit point. In contrast, the future measurement of Δm^2_{32} will start to be systematically limited with double the exposure (12×10^{20}) unless the systematic uncertainties are reduced. Around half the total systematic uncertainty arises from the absolute muon energy scale and efforts are under way to reduce this.

Bibliography

[1] J. Chadwick. Distribution in intensity in the magnetic spectrum of the β-rays of radium. *Ver. Dtsch. Physik. Ges*, 16:383–391, 1914. pages 3

[2] W. Pauli. Letter to the physical society of Tubingen, 1930. pages 3

[3] E. Fermi. Tentativo di una teoria dei raggi β. *Il Nuovo Cimento (1924-1942)*, 11(1):1–19, 1934. pages 3

[4] H. Bethe and R. Peierls. The 'neutrino'. *Nature*, 133(3362):532, 1934. pages 3

[5] F. Reines and C. L. Cowan. The neutrino. *Nature*, 178:446–449, 1956. pages 3

[6] G. Danby et al. Observation of High-Energy Neutrino Reactions and the Existence of Two Kinds of Neutrinos. *Phys. Rev. Lett.*, 9:36–44, Jul 1962. pages 4

[7] D. Decamp et al. Determination of the Number of Light Neutrino Species. *Phys. Lett.*, B231:519–529, 1989. pages 4

[8] S. Schael et al. Precision electroweak measurements on the Z resonance. *Phys. Rept.*, 427:257–454, 2006. pages 4

[9] K. Kodama et al. Observation of tau neutrino interactions. *Phys. Lett.*, B504:218–224, 2001. pages 4

[10] P. Anselmann et al. Solar neutrinos observed by GALLEX at Gran Sasso. *Phys. Lett.*, B285:376–389, 1992. pages 4

[11] R. Davis, D. S. Harmer, and K. C. Hoffman. Search for Neutrinos from the Sun. *Phys. Rev. Lett.*, 20:1205–1209, May 1968. pages 4

[12] J. N. Bahcall, N. A. Bahcall, W. A. Fowler, and G. Shaviv. Solar neutrinos and low-energy nuclear cross sections. *Physics Letters B*, 26(6):359 – 361, 1968. pages 4

[13] K. S. Hirata et al. Observation of ^{8}B solar neutrinos in the Kamiokande-II detector. *Phys. Rev. Lett.*, 63:16–19, Jul 1989. pages 4

[14] A. I. Abazov et al. Search for neutrinos from the Sun using the reaction ^{71}Ga(ν_e,e^-)^{71}Ge. *Phys. Rev. Lett.*, 67:3332–3335, Dec 1991. pages 4

[15] B. Pontecorvo. Neutrino Experiments and the Problem of Conservation of Leptonic Charge. *Sov. Phys. JETP*, 26:984–988, 1968. [Zh. Eksp. Teor. Fiz.53,1717(1967)]. pages 5

[16] V. N. Gribov and B. Pontecorvo. Neutrino astronomy and lepton charge. *Phys. Lett.*, B28:493, 1969. pages 5

[17] Z. Maki, M. Nakagawa, and S. Sakata. Remarks on the unified model of elementary particles. *Prog. Theor. Phys.*, 28:870–880, 1962. pages 5

[18] Y. Fukuda et al. Evidence for Oscillation of Atmospheric Neutrinos. *Phys. Rev. Lett.*, 81:1562–1567, Aug 1998. pages 5

[19] Q. R. Ahmad, R. C. Allen, T. C. Andersen, J. D. Anglin, J. C. Barton, E. W. Beier, M. Bercovitch, J. Bigu, S. D. Biller, R. A. Black, et al. Direct evidence for neutrino flavor transformation from neutral-current interactions in the Sudbury Neutrino Observatory. *Physical review letters*, 89(1):011301, 2002. pages 5

[20] C. Patrignani et al. Chin. Phys. C, 40, 100001. *Particle Data Group*, 2016. pages 6, 8, 9, 11, 29, 54, 66, 67, 68

[21] R. N. Mohapatra et al. Theory of neutrinos: A White paper. *Rept. Prog. Phys.*, 70:1757–1867, 2007. pages 6

[22] S. F. King. Models of neutrino mass, mixing and CP violation. *Journal of Physics G: Nuclear and Particle Physics*, 42(12):123001, 2015. pages 7

[23] M. Thomson. *Modern particle physics*. Cambridge University Press, 2013. pages 8

[24] H. Nunokawa, S. Parke, and J. W. F. Valle. CP Violation and Neutrino Oscillations. *Prog. Part. Nucl. Phys*, 2007. pages 8, 12, 13

[25] B. Kayser. On the quantum mechanics of neutrino oscillation. *Physical Review D*, 24(1):110, 1981. pages 9

[26] P. Adamson et al. First measurement of electron neutrino appearance in NOvA. *Phys. Rev. Lett.*, 116(15):151806, 2016. pages 10

[27] K. Abe et al. Measurements of neutrino oscillation in appearance and disappearance channels by the T2K experiment with 6.6× 1 0 20 protons on target. *Physical Review D*, 91(7):072010, 2015. pages 10, 20, 21, 68, 71, 75, 76, 79, 84, 87, 88, 90, 91, 92, 96, 162, 164, 165, 170, 171, 173

[28] K. Fukuura, T. Miura, E. Takasugi, and M. Yoshimura. Large CP violation, large mixings of neutrinos, and a democratic-type neutrino mass matrix. *Phys. Rev. D*, 61:073002, Feb 2000. pages 10

[29] Z. Xing and Z. Zhao. A review of μ-τ flavor symmetry in neutrino physics. *Reports on Progress in Physics*, 79(7):076201, 2016. pages 10

[30] S. Morisi, S. F. King, A. Merle, Y. Shimizu, and M. Tanimoto. Neutrino mass and mixing: from theory to experiment. *New Journal of Physics*, 16(4):045018, 2014. pages 10

[31] S. P. Mikheyev and A. Y. Smirnov. Resonant amplification of ν oscillations in matter and solar-neutrino spectroscopy. *Il Nuovo Cimento C*, 9(1):17–26, 1986. pages 12

[32] L. Wolfenstein. Neutrino oscillations in matter. *Phys. Rev. D*, 17:2369–2374, May 1978. pages 12

[33] P. Adamson et al. NOvA Official Plots and Figures. `http://www-nova.fnal.gov/plots_and_figures/plots_and_figures.html`. pages 14

[34] T. Araki et al. Measurement of Neutrino Oscillation with KamLAND: Evidence of Spectral Distortion. *Phys. Rev. Lett.*, 94:081801, Mar 2005. pages 15

[35] M. V. Diwan, V. Galymov, X. Qian, and A. Rubbia. Long-Baseline Neutrino Experiments. *Ann. Rev. Nucl. Part. Sci.*, 66:47–71, 2016. pages 15

[36] A. Gando et al. Reactor On-Off Antineutrino Measurement with KamLAND. *Phys. Rev.*, D88(3):033001, 2013. pages 15, 16

[37] F. P. An et al. Observation of electron-antineutrino disappearance at Daya Bay. *Phys. Rev. Lett.*, 108:171803, 2012. pages 17

[38] F. P. An et al. Spectral measurement of electron antineutrino oscillation amplitude and frequency at Daya Bay. *Phys. Rev. Lett.*, 112:061801, 2014. pages 17

[39] F. P. An et al. New Measurement of Antineutrino Oscillation with the Full Detector Configuration at Daya Bay. *Phys. Rev. Lett.*, 115:111802, Sep 2015. pages 17, 18

[40] P. Adamson et al. Combined analysis of ν_μ disappearance and $\nu_\mu \rightarrow \nu_e$ appearance in MINOS using accelerator and atmospheric neutrinos. *Physical review letters*, 112(19):191801, 2014. pages 19, 67, 68, 71, 74, 76, 80, 83, 86, 88, 89, 91, 92, 95, 162, 164, 169

[41] P. Adamson et al. Measurement of the Neutrino Mixing Angle θ_{23} in NOvA. *Phys. Rev. Lett.*, 118:151802, Apr 2017. pages 20, 22, 23, 43, 45, 47, 53, 54, 56, 62, 65, 66, 67, 68, 69, 70, 71, 73, 74, 75, 76, 77, 78, 79, 80, 81, 82, 83, 84, 85, 86, 87, 88, 89, 90, 91, 92, 93, 94, 95, 96, 97, 99, 100, 101, 127, 140, 141, 142, 143, 144, 145, 146, 147, 148, 149, 150, 151, 155, 156, 157, 162, 164, 167, 168, 169, 170, 171

[42] P. Adamson et al. Constraints on Oscillation Parameters from ν_e Appearance and ν_μ Disappearance in NOvA. *Phys. Rev. Lett.*, 2017. pages 20, 24

[43] D. S. Ayres et al. The NOvA Technical Design Report. *Fermilab Publication*, 2007. pages 25, 30, 31, 35, 36, 37

[44] P. Adamson et al. The NuMI Neutrino Beam. *Nucl. Instrum. Meth.*, A806:279–306, 2016. pages 25, 27, 28, 39

[45] S. L. Mufson. Scintillator update. *Internal (Private) NOvA document, DocDB-8541*, 2013. pages 33

[46] J. A. Formaggio and G. P. Zeller. From eV to EeV: Neutrino cross sections across energy scales. *Rev. Mod. Phys.*, 84:1307–1341, Sep 2012. pages 41

[47] T. T. Böhlen, F. Cerutti, M. P. W. Chin, A. Fassò, A. Ferrari, P. G. Ortega, A. Mairani, P. R. Sala, G. Smirnov, and V. Vlachoudis. The FLUKA Code: Developments and Challenges for High Energy and Medical Applications. *Nuclear Data Sheets*, 120:211–214, June 2014. pages 41

[48] A. Ferrari, P. R. Sala, A. Fasso, and J. Ranft. FLUKA: A multi-particle transport code (Program version 2005), 2005. pages 41

[49] S. Agostinelli et al. GEANT4—a simulation toolkit. *Nuclear instruments and methods in physics research section A: Accelerators, Spectrometers, Detectors and Associated Equipment*, 506(3):250–303, 2003. pages 41

[50] C. Andreopoulos et al. The GENIE neutrino monte carlo generator. *Nuclear Instruments and Methods in Physics Research Section A: Accelerators, Spectrometers, Detectors and Associated Equipment*, 614(1):87–104, 2010. pages 41, 42, 66, 103

[51] C. Hagmann, D. Lange, and D. Wright. Cosmic-ray shower generator (CRY) for Monte Carlo transport codes. In *2007 IEEE Nuclear Science Symposium Conference Record*, volume 2, pages 1143–1146. IEEE, 2007. pages 42

[52] P. A. Rodrigues, J. Demgen, E. Miltenberger, L. Aliaga, O. Altinok, L. Bellantoni, A. Bercellie, M. Betancourt, A. Bodek, A. Bravar, et al. Identification of nuclear effects in neutrino-carbon interactions at low three-momentum transfer. *Physical review letters*, 116(7):071802, 2016. pages 43

[53] O. Benhar, D. Day, and I. Sick. Inclusive quasielastic electron-nucleus scattering. *Reviews of Modern Physics*, 80(1):189, 2008. pages 43

[54] J. Wolcott. GENIE tune and uncertainty band for Second Analysis. NOvA Internal (Private) Document, DocDB-15214, 2016. pages 43, 44

[55] C. Wilkinson, P. Rodrigues, S. Cartwright, L. Thompson, and K. McFarland. Reanalysis of bubble chamber measurements of muon-neutrino induced single pion production. *Phys. Rev. D*, 90:112017, Dec 2014. pages 43, 127

[56] J. Hartnell and G. Pawloski. Summary of the 2016 (Second Analysis) ν_μ Disappearance Analysis. NOvA Internal (Private) Document, DocDB-15232, May 2016. pages 45, 48, 62

[57] C. Backhouse. The CAFAna framework - technote. NOvA Internal (Private) Document, DocDB-9222, 2014. pages 45

[58] F. James and M. Roos. Minuit-a system for function minimization and analysis of the parameter errors and correlations. *Computer Physics Communications*, 10(6):343–367, 1975. pages 45

[59] M. D. Baird. *An Analysis of Muon Neutrino Disappearance from the NuMI Beam Using an Optimal Track Fitter*. PhD thesis, Indiana U., 2015. pages 46, 62

[60] M. Ester, H. Kriegel, J. Sander, X. Xu, et al. A density-based algorithm for discovering clusters in large spatial databases with noise. In *Kdd*, volume 96, pages 226–231, 1996. pages 46

[61] R. E. Kalman et al. A new approach to linear filtering and prediction problems. *Journal of basic Engineering*, 82(1):35–45, 1960. pages 46

[62] N. Raddatz. KalmanTrack Technical Note. NOvA Internal (Private) Document, DocDB-13545. pages 46

[63] N. S. Altman. An introduction to kernel and nearest-neighbor nonparametric regression. *The American Statistician*, 46(3):175–185, 1992. pages 48

[64] N. Raddatz. *Measurement of Muon Neutrino Disappearance with Non-Fiducial Interactions in the NOvA Experiment*. PhD thesis, University of Minnesota, 2016. pages 48

[65] N. Raddatz. ReMId Technical Note. NOvA Internal (Private) Document, DocDB-11206. pages 48, 49, 167

[66] A. Aurisano, A. Radovic, D. Rocco, A. Himmel, M. D. Messier, E. Niner, G. Pawloski, F. Psihas, A. Sousa, and P. Vahle. A convolutional neural network neutrino event classifier. *Journal of Instrumentation*, 11(09):P09001, 2016. pages 48, 50, 77, 167

[67] L. Suter and J. Musser. SA Data Quality updates. NOvA Internal (Private) Document, DocDB-15307, April 2016. pages 49

[68] S. R. Phan-Budd and L. Goodenough. Technical Note on the NOvA Beam Monitoring for 2015 Summer Analysis. NOvA Internal (Private) Document, DocDB-13572, July 2015. pages 49

[69] S. Lein. DCM Edge Metric. NOvA Internal (Private) Document, DocDB-13527, June 2015. pages 49

[70] K. Sachdev and X. Bu. Spill level data quality. NOvA Internal (Private) Document, DocDB-12437, July 2015. pages 49

[71] K. Bays. NOvA Cosmic Rejection package and algorithms technical note. NOvA Internal (Private) Document, DocDB-11205. pages 49

[72] P. Adamson et al. NOvA NuMu blessed plots. `http://nusoft.fnal.gov/nova/blessedplots/Numu_SA.html`, February 2017. pages 51

[73] C. Backhouse and A. Radovic. The Attenuation and Threhold Correction of the NOvA detectors. NOvA Internal (Private) Document, DocDB-13579, 2015. pages 52

[74] C. Backhouse, A. Radovic, and P. Singh. The Attenuation and Threhold Correction of the NOvA detectors. NOvA Internal (Private) Document, DocDB-13579, 2016. pages 52

[75] L. Vinton. Calorimetric Energy Scale Calibration of the NOvA Detectors. NOvA Internal (Private) Document, DocDB-13579, 2015. pages 53

[76] P. Adamson et al. First measurement of muon-neutrino disappearance in NOvA. *Phys. Rev. D*, 93:051104, Mar 2016. pages 53, 71, 77

[77] D. P. Mendez. Second Analysis Calorimetric Energy Scale Calibration of the NOvA detectors. NOvA Internal (Private) Document, DocDB-13579, 2016. pages 53, 57

[78] E. Niner. Timing Calibration Technical Note. NOvA Internal (Private) Document, DocDB-13579, 2015. pages 53

[79] S. Lein. Summary of dE/dx plots for Muons/Protons. NOvA Internal (Private) Document, DocDB-15028, 2016. pages 57

[80] L. Vinton. Tech note on the calibration systematics for the muon neutrino disappearance analysis. NOvA Internal (Private) Document, DocDB-15215, 2016. pages 57

[81] J. Davies. NuMu Calibration Systematic - Normalisation Shift, NOvA internal document, docDB 15219, April 2016. pages 58

[82] C. N. Chou. The nature of the saturation effect of fluorescent scintillators. *Physical Review*, 87(5):904, 1952. pages 58

[83] D. Pershey. Birks-Chou Post Tuning. NOvA Internal (Private) Document, DocDB-13233, 2015. pages 62

[84] A. Aurisano. Detector Simulations, NOvA internal document, docDB 20717, June 2017. pages 62

[85] L. Vinton. Birks' systematic uncertainties for the second muon neutrino disappearance analysis. NOvA Internal (Private) Document, DocDB-15347, 2016. pages 62

[86] L. Vinton. Near detector normalisation with rock muons. NOvA Internal (Private) Document, DocDB-15292, 2016. pages 62

[87] A. Aurisano. The NOvA Detector Simulation, NOvA internal document, docDB 13577, June 2015. pages 62

[88] L. Vinton. Noise systematics for the second muon neutrino disappearance analysis. NOvA Internal (Private) Document, DocDB-15216, 2016. pages 65

[89] G. J. Feldman and R. D. Cousins. Unified approach to the classical statistical analysis of small signals. *Physical Review D*, 57(7):3873, 1998. pages 68

[90] K. Bays. Numu SA FC NH result. NOvA Internal (Private) Document, DocDB-15814, 2016. pages 70

[91] J. S. Marshall. *A study of muon neutrino disappearance with the MINOS detectors and the NuMI neutrino beam.* PhD thesis, Cambridge U., 2008. pages 72

[92] K. Bays. Quick plots regarding CVN and ReMId. NOvA Internal (Private) Document, DocDB-15120, 2016. pages 77, 81

[93] L. Vinton. Sensitivity studies. Hybrid selection and number of neutrino energy bins. NOvA Internal (Private) Document, DocDB-16292, 2016. pages 81

[94] L. Vinton. Effect of Systematics on hadEFrac bin values. NOvA Internal (Private) Document, DocDB-17854, 2017. pages 97

[95] B. Zamorano. Update on effect of delta-CP. NOvA Internal (Private) Document, DocDB-16555, 2016. pages 98

[96] B. Zamorano. Summary on effect of delta-CP. NOvA Internal (Private) Document, DocDB-16599, 2016. pages 98

[97] L. Vinton. Improved analysis: ND data-MC plots. NOvA Internal (Private) Document, DocDB-18954, 2017. pages 103

[98] T. Blackburn. ND Data/MC and Resolution Bins - SA vs 3A FHC. NOvA Internal (Private) Document, DocDB-19895, June 2017. pages 127

[99] A. Adam. Detector Simulations. NOvA Internal (Private) Document, DocDB-17082, 2017. pages 127

[100] K. Abe et al. Updated T2K measurements of muon neutrino and antineutrino disappearance using 1.5 e21 protons on target. *arXiv preprint arXiv:1704.06409*, 2017. pages 164, 165

[101] K. Abe et al. Combined analysis of neutrino and antineutrino oscillations at T2K. *Physical Review Letters*, 118(15):151801, 2017. pages 164, 165

[102] F. P. An et al. Measurement of electron antineutrino oscillation based on 1230 days of operation of the Daya Bay experiment. *Physical Review D*, 95(7):072006, 2017. pages 166, 173

[103] L. Vinton and B. Zamorano. Numu Second analysis results and cross-checks. NOvA Internal (Private) Document, DocDB-15581, 2016. pages 167, 168